# PIEZOELECTRIC AND ELECTROSTRICTIVE MATERIALS

## FOR TRANSDUCER APPLICATIONS.

Period February 1, 1989 to January 31, 1990

Annual Report.

VOLUME II

OFFICE OF NAVAL RESEARCH
Contract No. N00014-89-J-1689

APPROVED FOR PUBLIC RELEASE--DISTRIBUTION UNLIMITED.

Reproduction in whole or in part is permitted for any purpose
of the United States Government.

L. E. Cross
R.E. Newnham
A.S. Bhalla
J.P. Dougherty
J.H. Adair
V.K. Varadan
V.V. Varadan

# PENNSTATE

1855

## THE MATERIALS RESEARCH LABORATORY
### UNIVERSITY PARK, PA

90 07 3 203

# DISCLAIMER NOTICE
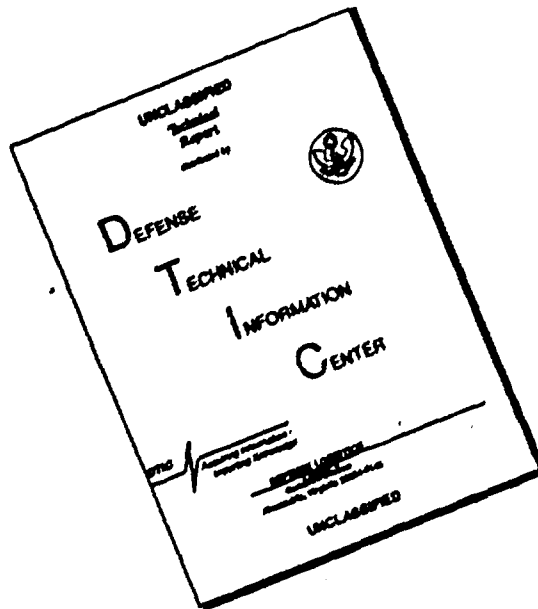
# REPORT DOCUMENTATION PAGE

Form Approved
OMB No. 0704-0188

| 1a. REPORT SECURITY CLASSIFICATION | 1b. RESTRICTIVE MARKINGS |
|---|---|
| 2a. SECURITY CLASSIFICATION AUTHORITY | 3. DISTRIBUTION/AVAILABILITY OF REPORT Reproduction in whole or in part is permitted for any purpose of the United States Government |
| 2b. DECLASSIFICATION/DOWNGRADING SCHEDULE | |

| 4. PERFORMING ORGANIZATION REPORT NUMBER(S) | 5. MONITORING ORGANIZATION REPORT NUMBER(S) |
|---|---|
| N00014-89-J-1689 | |

| 6a. NAME OF PERFORMING ORGANIZATION | 6b. OFFICE SYMBOL (If applicable) | 7a. NAME OF MONITORING ORGANIZATION |
|---|---|---|
| Materials Research Laboratory | | |

| 6c. ADDRESS (City, State, and ZIP Code) | 7b. ADDRESS (City, State, and ZIP Code) |
|---|---|
| The Pennsylvania State University University Park, PA 16802 | |

| 8a. NAME OF FUNDING/SPONSORING ORGANIZATION | 8b. OFFICE SYMBOL (If applicable) | 9. PROCUREMENT INSTRUMENT IDENTIFICATION NUMBER |
|---|---|---|
| | | |

| 8c. ADDRESS (City, State, and ZIP Code) | 10. SOURCE OF FUNDING NUMBERS | | | |
|---|---|---|---|---|
| | PROGRAM ELEMENT NO. | PROJECT NO. | TASK NO. | WORK UNIT ACCESSION NO. |
| | | | | |

11. TITLE (Include Security Classification)
Electrostrictive Materials For Transducer Applications

12. PERSONAL AUTHOR(S)
L.E. Cross, R.E. Newnham, A.S. Bhalla, J.P. Dougherty, J.H. Adair, V.K. Varadan, V.V. Varadan

| 13a. TYPE OF REPORT | 13b. TIME COVERED | 14. DATE OF REPORT (Year, Month, Day) | 15. PAGE COUNT |
|---|---|---|---|
| annual | FROM 2/89 TO 1/90 | | |

16. SUPPLEMENTARY NOTATION

| 17. | COSATI CODES | | 18. SUBJECT TERMS (Continue on reverse if necessary and identify by block number) |
|---|---|---|---|
| FIELD | GROUP | SUB-GROUP | |
| | | | |
| | | | |

19. ABSTRACT (Continue on reverse if necessary and identify by block number)

This report documents work carried out in the Materials Research Laboratory of the Pennsylvania State University over the first year of a new three year Grant No. N00014-89-J-1689 on "Piezoelectric and Electrostrictive Materials for Transducer Applications". The program in MRL has been supplemented by an associated program in the Center for Engineering of Electronic and Acoustic Materials under V.V. and V.J. Varadan.

| 20. DISTRIBUTION/AVAILABILITY OF ABSTRACT ☐ UNCLASSIFIED/UNLIMITED ☐ SAME AS RPT. ☐ DTIC USERS | 21. ABSTRACT SECURITY CLASSIFICATION |
|---|---|
| 22a. NAME OF RESPONSIBLE INDIVIDUAL | 22b. TELEPHONE (Include Area Code) | 22c. OFFICE SYMBOL |

DD Form 1473, JUN 86    Previous editions are obsolete.    SECURITY CLASSIFICATION OF THIS PAGE

Over the current year studies of the 3.0 type composite have evolved a new structure for a much more effective stress transforming composite. The device uses cavities in the electrode structure which are simple, inexpensive and robust. The sensitivity is higher than that of the end capped cylinder for equivalent PZT volume and we believe this will be a most important development for towed array hydrophones.

For agile transducer structures, the very high piezoelectric coefficients induced by DC bias in the lead magnesium niobate:lead titanate electrostrictors have been confirmed using both resonance and ultra-dilatometer methods. In parallel studies of aging in these systems a rather complete understanding of the aging process has been obtained and methods for fabricating PMN:PT systems with no aging developed, an essential need for the agile transducer.

The phenomenology of the PZT system has been completed and published and the equations are now being applied to studies of the properties of PZT compositions at the lead titanate end of the system. We expect that the phenomenology will be particularly valuable for the future evaluation of thin film PZTs where the breakdown field are such that $E_B.P_S$ is a large perturbation to the total energy.

In high strain actuators for surface modification and flow control antiferroelectric:ferroelectric systems have been explored which yield strains up to 0.85%. Effort is now being dedicated to understanding and eliminating fatigue effects in these charge switching systems.

In the associated program a detailed modeling of the 1:3 type PZT:polymer composite has now been completed.

TABLE OF CONTENTS

Appendices:

1.  R.E. Newnham, "Electroceramics," Reports on the Progress in Physics 52:123-156 (1989).

2.  L.E. Cross, "Piezoelectric and Electrostrictive Sensors and Actuators for Adaptive Structures and Smart Materials," Proc. AME 110th Annual Mtg., San Fransisco (December 1989).

3.  R.E. Newnham, Q.C. Xu, S. Kumar and L.E. Cross, "Smart Ceramics." Ferroelectrics 102:77-89 (1990).

4.  W.Y. Pan and L. Eric Cross, "A Sensitive Double Beam Laser Interferometer for Studying High Frequency Piezoelectric and Electrostrictive Strains," Rev. Sci. Inst. 60:2701 (1989).

5.  Q.M. Zhang, S.J. Jang and L.E. Cross, "High Frequency Strain Response in Ferroelectrics and Its Measurement Using a Modified Mach-Zehnder Interferometer," J. Appl. Phys. 65:2807 (1989).

6.  W.Y. Pan, H. Wang and L.E. Cross, "Laser Interferometer for Studying Phase Delay in Piezoelectric Response."

7.  Dragon Damjanovic, "An Equivalent Electrical Circuit of a Piezoelectric Bar Resonator with a Large Piezoelectric Phase Angle," Ferroelectrics.

8.  A.D. Hilton, C.A. Randall, D.J. Barber and T.R. Shrout, "TEM Studies of $Pb(Mg_{1/3}Nb_{2/3})O_3$-$PbTiO_3$ Ferroelectric Relaxtors," Ferroelectrics 93:379 (1989).

9.  S.W. Choi, T.R. Shrout, S.J. Jang and A.S. Bhalla, "Dielectric and Pyroelectric Properties in the $Pb(Mg_{1/3}Nb_{2/3})O_3$-$PbTiO_3$ system," Ferroelectrics 100:29 (1989).

10. Q. Zhang, W. Pan, A. Bhalla and L.E. Cross, "Electrostrictive and Dielectric Response in Lead Magnesium Niobate-Lead Titanate (0.9PMN:0.1PT) and Lead Lanthanum Zirconate Titanate (PZT 9.5/65/35) Under Variation of Temperature and Electric Field," J. Am. Ceram. Soc. 72(4):599 (1989).

11. Q.M. Zhang, W.Y. Pan, S.J. Jang and L.E. Cross, "The Pressure Dependence of the Dielectric Response and Its Relation to Electrostriction," Ferroelectrics 88:147 (1989).

12. W.Y. Pan, W.Y. Gu, D.J. Taylor and L.E. Cross, "Large Piezoelectric Effect Induced by Direct Current Bias in PMN:PT Relaxor Ferroelectric Ceramics," Japanese J. Appl. Phys. 4:653 (1989).

13. D.J. Taylor, D. Damjanovic, A.S. Bhalla and L.E. Cross, "Complex Piezoelectric Elastic and Dielectric Coefficients of La doped $Pb(Mg_{1/3}Nb_{2/3})O_3:0.07PbTiO_3$ under DC Bias," Ferroelectric Letters.

14. W.Y. Gu, W.Y. Pan and L.E. Cross, "Effects of Thermal Treatment and DC Bias on Dielectric Aging in the PLZT 9.5:65:35 Relaxor Ferrolectric Ceramic," Ferroelectrics 89:47 (1989).

15. T.R. Shrout, W. Huebner, C.A. Randall and A.D. Hilton, 'Aging Mechanisms in $Pb(Mg_{1/3}Nb_{2/3})O_3$-Based Relaxor Ferroelectrics," Ferroelectrics 93:361 (1989).

16. W.Y. Pan, T.R. Shrout and L.E. Cross, "Modelling the Aging Phenomenon in 0.9PMN:0.1PT Relaxor Ferroelectric Ceramic," J. Mat. Sci. 8:771 (1989).

17. Q.Y. Jiang, S.B. Krupanidhi and L.E. Cross, "Effects of the Lapped Surface Layer and Surface Stress on the Dielectric Properties of PLZT Ceramics," Proc. Symp. on Ceramic Dielectrics," Ed. H.C. Ling, Ceramic Soc. (1989).

18. S.W. Choi, T.R. Shrout, S.J. Jang and A.S. Bhalla, "Morphotropic Phase Boundary in $PbMg_{1/3}Nb_{2/3}O_3$-$PbTiO_3$ System," Materials Letters 8:253 (1989).

19. N. Kim, W. Huebner, S.J. Jang and T.R. Shrout, "Dielectric and Piezoelectric Properties of Lanthanum Modified Lead Magnesium Niobate-Lead Titanate Ceramics," Ferroelectrics 93:341 (1989).

20. M.T. Lanagan, N. Yang, D. Dube and S.J. Jang, "Dielectric Behaviour of the Relaxor $PbMg_{1/3}Nb_{2/3}O_3$-$PbTiO_3$ Solid Solution System in the Microwave Region," J. Am. Ceram. Soc. 72:481 (1989).

21. D.C. Dube, S.J. Jang and A. Bhalla, "Studying a Ferroelectric at Microwave Frequency," Ferroelectrics 87:303 (1988).

22. T.R. Shrout and J P. Dougherty, "Lead Based $Pb(B_1B_2)O_3$ Relaxors vs. $BaTiO_3$ Dielectrics for Multilayer Capacitors," Proc. Symp. on Ceramic Dielectrics, Ed. H.C. Ling, Am. Ceram. Soc. (1989).

VOLUME II: $Conti tir$ )

23. M.J. Haun, T.J. Harvin, M.T. Lanagan, Z.Q. Zhuang, S.J. Jang and L.E. Cross, "Thermodynamic Theory of $PbZrO_3$," J. Appl. Phys. 65:3173 (1989).

24. M.J. Haun, E. Furman, S.J. Jang and L.E. Cross, "Thermodynamic Theory of the Lead Zirconate-Titanate Solid Solution System, Part I. Phenomenlogy," Ferroelectrics 99:13 (1989).

25. M.J. Haun, E. Furman, H.A. McKinstry and L.E. Cross, "Thermodynamic Theory of the Lead Zirconate-Titanate Solid Solution System, Part II. Tricritical Behavior," Ferroelectrics 99:27 (1989).

26. M.J. Haun, Z.Q. Zhuang, E. Furman, S.J. Jang and L.E. Cross, "Thermodynamic Theory of the Lead Zirconate-Titanate Solid Solution System, Part III. Curie Constant and Sixth Order Polarization Interaction Dielectric Stiffness Coefficients," Ferroelectrics 99:45 (1989).

27. M.J. Haun, E. Furman, T.R. Halemane and L.E. Cross, "Thermodynamic Theory of the Lead Zirconate-Titanate Solid Solution System, Part IV. Tilting of the Oxygen Octahedra," Ferroelectrics 99:55 (1989).

28. M.J. Haun, E. Furman, S.J. Jang and L.E. Cross, "Thermodynamic Theory of the Lead Zirconate-Titanate Solid Solution System Part V. Theoretical Calculations," Ferroelectrics 99:63 (1989).

29. M.J. Haun, Z.Q. Zhuang, E. Furman, S.J. Jang and L.E. Cross, "Electrostrictive Properties of the Lead Zirconate-Titanate Solid-Solution System," J. Am. Ceram. Soc. 72:1140 (1989).

30. M.J. Haun, E. Furman, S.J. Jang and L.E. Cross, "Modeling of the Electrostrictive, Dielectric and Piezoelectric Properties of Ceramic $PbTiO_3$," IEEE Trans. on Ultrasonics, Ferroelectrics and Frequency Control, 36:393 (1989).

31. J.R. Oliver, R.R. Neurgaonkar and L.E. Cross, "Ferroelectric Properties of Tungsten Bronze Morphotropic Phase Boundary Systems," J. Am. Ceram. Soc. 72:202 (1989).

32. J.R. Oliver, R.R. Naugaonkar and L.E. Cross, "A Thermodynamic Phenomenology for Ferroelectric Tungsten Bronze $Sr_{0.6}Ba_{0.4}Nb_2O_6$ (SBN60);" J. Appl. Phys. 64:37 (1988).

33. Z.Q. Zhuang, M.J. Haun, S.J. Jang and L.E. Cross, "Composition and Temperature Dependence of the Dielectric, Piezoelectric and Elastic Properties of Pure PZT Ceramics," IEEE Transactions on Ultrasonics Ferroelectrics and Frequency Control 36:413 (1989).

34. J.N. Kim, M.J. Haun, S.J. Jang, L.E. Cross and X.R. Xue, "Temperature Behavior of Dielectric and Piezoelectric Properties of Samarium-Doped Lead Titanate Ceramics," IEEE Transactions on Ultrasonics Ferroelectrics and Frequency Control 36:389 (1989).

35. T.W. Dekleva, J.M. Hayes, L.E. Cross and G.L. Geoffroy, "Sol-Gel Processing of Lead Titanate in Two Methoxyethanol Investigation into the Nature of the Prehydrolized Solutions," Comm. to Am. Ceram. Soc. 71:C280 (1988).

36. W.Y. Pan, Q. Zhuang, A. Bhalla and L.E. Cross, "Field Forces Antiferroelectrics to Ferroelectric Switching in Modified Lead Zirconate Titanate Stannate Ceramics," J. Am. Ceram. Soc. 72:571 (1989).

37. W.Y. Pan, W.Y. Gu and L.E. Cross, "Transition Speed on Switching From a Field Induced Ferroelectric State to an Antiferroelectric Upon the Release of the Applied Field in $(PbLa)(ZrTiSn)O_3$ Antiferroelectric Ceramics," Ferroelectrics 99:185 (1989).

12. ASSOCIATED PROGRAM

APPENDICES

38. J.H. Jeng, V.V. Varadan and V.K. Varadan, "Design and Analysis of the Performance of PZT/Polymer Composite Transducers," (in press).

39. J.H. Jeng, X. Bao, V.V. Varadan and V.K. Varadan, "Finite Element-Eigenmode Analysis for the Design of 1-3 Composite Transducers Including the Effect of Fluid Loading" (in press).

APPENDIX 23

# Thermodynamic theory of PbZrO₃

M. J. Haun,[a] T. J. Harvin, M. T. Lanagan,[b] Z. Q. Zhuang,[c] S. J. Jang,
and L. E. Cross
*Materials Research Laboratory, The Pennsylvania State University, University Park, Pennsylvania 16802*

A thermodynamic theory is presented to model the phase transitions and properties of lead zirconate. The free energy $\Delta G$ is expressed as a power series in terms of the ferroelectric polarization ($P_i = P_{a_i} + P_{b_i}$) and antiferroelectric polarization ($p_i = P_{a_i} - P_{b_i}$) including all possible terms up to the sixth power, but only first-order cross coupling terms and couplings to elastic stress. Under the assumption that only the lowest-order coefficients of $P_i$ and $p_i$ are linearly temperature dependent (Curie–Weiss behavior) and all other constants are temperature independent, experimental data are used to define the constants and permit calculation of ferroelectric and antiferroelectric free energies as a function of temperature. Use of the function to define the averaged dielectric permittivity at room temperature in the antiferroelectric phase gives a value of $\epsilon_R = 120$ in good agreement with recent microwave measurements. A simplified technique for modifying the function to explore solid solution with lead titanate is examined, and shown to lead to excellent agreement with the known phase diagram.

## I. INTRODUCTION

Lead zirconate is an end member of the technologically important lead zirconate-titanate (PZT) solid solution system.[1] At room temperature, PbZrO₃ has an antiferroelectric orthorhombic ($A_O$) perovskite structure with an antipolar arrangement along the {110} direction. The $A_O$ phase remains stable up to $\approx 200\,°C$, where a transition occurs to a ferroelectric rhombohedral ($F_R$) phase with a polarization along the {111} direction.[2] The $F_R$ phase is only stable over a narrow temperature range and transforms to a paraelectric cubic ($P_C$) phase as $\approx 232\,°C$.[3]

Lead zirconate has been recently studied as a possible dielectric material for high-frequency applications.[4,5] In this study a dielectric relaxation was found to occur at microwave frequencies. To further the understanding of the dielectric properties of lead zirconate, a thermodynamic theory has been developed to calculate the intrinsic dielectric response. The development of a thermodynamic theory of lead zirconate was also needed to complete the theory that was developed for the PZT solid-solution system.[6–10]

Whatmore and Glazer[11] used a one-dimensional energy function to model the Pb ion displacement in lead zirconate. Uchino et al.[12] included stress terms in the energy function to determine the hydrostatic electrostrictive coefficient. However, in these papers not enough coefficients were determined to calculate the energies and dielectric properties of the phases.

In this paper a more complete thermodynamic theory of lead zirconate will be developed using a three-dimensional energy function. In the next section the energy function will be presented, along with the solutions and property relations that can be derived from this energy function. Values of the coefficients will be determined from experimental data in Sec. III and used to calculate the theoretical properties in Sec. IV. The calculated dielectric properties will be compared with experimental high-frequency data. In Sec. V a procedure will be presented to calculate the energy of the antiferroelectric orthorhombic phase into the PZT system. Finally a summary of this paper will be given in Sec. VI.

## II. PHENOMENOLOGICAL THERMODYNAMIC THEORY

The following energy function for lead zirconate was derived from the two-sublattice theory that was previously developed to model antiferroelectric materials.[13–16] The coefficients were limited by the symmetry of the paraelectric phase ($m3m$). By assuming isothermal conditions, using reduced notation, and expanding the energy function in powers of the ferroelectric ($P_i$) and antiferroelectric ($p_i$) polarizations, and including couplings between these order parameters, and between the stress ($X_m$) and the order parameters the following energy function resulted:

$$\Delta G = \alpha_1(P_1^2 + P_2^2 + P_3^2) + \alpha_{11}(P_1^4 + P_2^4 + P_3^4) + \alpha_{12}(P_1^2 P_2^2 + P_2^2 P_3^2 + P_3^2 P_1^2) + \alpha_{111}(P_1^6 + P_2^6 + P_3^6)$$

$$+ \alpha_{112}[P_1^4(P_2^2 + P_3^2) + P_2^4(P_1^2 + P_3^2) + P_3^4(P_1^2 + P_2^2)] + \alpha_{123}P_1^2 P_2^2 P_3^2$$

$$+ \sigma_1(p_1^2 + p_2^2 + p_3^2) + \sigma_{11}(p_1^4 + p_2^4 + p_3^4) + \sigma_{12}(p_1^2 p_2^2 + p_2^2 p_3^2 + p_3^2 p_1^2) + \sigma_{111}(p_1^6 + p_2^6 + p_3^6)$$

$$+ \sigma_{112}[p_1^4(p_2^2 + p_3^2) + p_2^4(p_1^2 + p_3^2) + p_3^4(p_1^2 + p_2^2)] + \sigma_{123}p_1^2 p_2^2 p_3^2 + \mu_{11}(P_1^2 p_1^2 + P_2^2 p_2^2 + P_3^2 p_3^2)$$

[a] Now at E. I. du Pont de Nemours & Co., Electronics Dept., Experimental Station. P O Box 80334, Wilmington, DE 19880-0334.
[b] Now at Argonne National Lab., Materials and Components Technology Div., Argonne, IL 60439.
[c] Visiting Scientist from the Department of Inorganic Materials Science and Engineering, South China Institute of Technology, Guangzhou, The People's Republic of China.

$$+ \mu_{1-1} P_1^2(p_2^2 + p_3^2) + F_2^2(p_1^2 + p_3^2) + P_3^2(p_1^2 + p_2^2)] + \mu_{44}(P_1 P_2 p_1 p_2 + P_2 P_3 p_2 p_3 + P_3 P_1 p_3 p_1)$$

$$- 1/2 S_{11}(X_1^2 + X_2^2 + X_3^2) - S_{12}(X_1 X_2 + X_2 X_3 + X_3 X_1) - 1/2 S_{44}(X_4^2 + X_5^2 + X_6^2)$$

$$- Q_{11}(X_1 P_1^2 + X_2 P_2^2 + X_3 P_3^2) - Q_{12}[X_1(P_2^2 + P_3^2) + X_2(P_1^2 + P_3^2) + X_3(P_1^2 + P_2^2)]$$

$$- Q_{44}(X_4 P_2 P_3 + X_5 P_1 P_3 + X_6 P_1 P_2) - Z_{11}(X_1 p_1^2 + X_2 p_2^2 + X_3 p_3^2) - Z_{12}[X_1(p_2^2 + p_3^2)$$

$$+ X_2(p_1^2 + p_3^2) + X_3(p_1^2 + p_2^2)] - Z_{44}(X_4 p_2 p_3 + X_5 p_1 p_3 + X_6 p_1 p_2). \tag{1}$$

The coefficients of this energy function are defined in Table I. The energy function includes all possible ferroelectric and antiferroelectric polarization terms up to the sixth-order and the first-order coupling terms.

The following solutions to the energy function [Eq. (1)] are of interest in the lead zirconate system:

*Paraelectric cubic* $(P_C)$:

$$P_1 = P_2 = P_3 = 0, \quad p_1 = p_2 = p_3 = 0; \tag{2}$$

*Ferroelectric rhombohedral* $(F_R)$:

$$P_1^2 = P_2^2 = P_3^2 \neq 0, \quad p_1 = p_2 = p_3 = 0; \tag{3}$$

*Antiferroelectric orthohombic* $(A_O)$:

$$P_1 = P_2 = P_3 = 0, \quad p_1 = 0, \quad p_2^2 = p_3^2 \neq 0 \tag{4}$$

Applying these solutions to Eq. (1) under zero stress conditions results in the following relations for the energies of each solution:

$$P_C: \quad \Delta G = 0; \tag{5}$$

$$F_R: \quad \Delta G = 3\alpha_1 P_3^2 + 3(\alpha_{11} + \alpha_{12})P_3^4 + (3\alpha_{111} + 6\alpha_{112}$$
$$+ \alpha_{123})P_3^6; \tag{6}$$

$$A_O: \quad \Delta G = 2\sigma_1 p_3^2 + (2\sigma_{11} + \sigma_{12})p_3^4 + 2(\sigma_{111} + \sigma_{112})p_3^6. \tag{7}$$

The spontaneous ferroelectric and antiferroelectric polarizations $(P_3$ and $p_3)$ in the above equations can be found from the first partial derivative stability conditions $(\partial \Delta G / \partial P_3$ and $\partial \Delta G / \partial p_3)$ as shown below.

$$F_R: \quad \frac{\partial \Delta G}{\partial P_3} = 0 = (3\alpha_{111} + 6\alpha_{112} + \alpha_{123})P_3^4$$
$$+ 2(\alpha_{11} + \alpha_{12})P_3^2 + \alpha_1; \tag{8}$$

$$A_O: \quad \frac{\partial \Delta G}{\partial p_3} = 0 = 3(\sigma_{111} + \sigma_{112})p_3^4$$
$$+ (2\sigma_{11} + \sigma_{12})p_3^2 + \sigma_1. \tag{9}$$

The polarizations can be calculated by solving these quadratic equations. Equations (6)–(9) relate the energies

| | |
|---|---|
| $\alpha, \alpha_{i,}\alpha_{ik}$ | Ferroelectric dielectric stiffnesses at constant stress |
| $\sigma, \sigma_{i,}\sigma_{ik}$ | Antiferroelectric dielectric stiffnesses at constant stress |
| $\mu_i$ | Coupling between the ferroelectric and antiferroelectric polarizations |
| $s$ | Elastic compliances at constant polarization |
| $Q_{ij}$ | Electrostrictive coupling between the ferroelectric polarization and stress |
| $Z_i$ | Electrostrictive coupling between the antiferroelectric polarization and stress |

of each solution to the coefficients of the energy function. Thus, by determining these coefficients, the energies of each phase can be calculated.

The spontaneous elastic strains $x_i = (= \partial \Delta G / \partial X_i)$ under zero stress conditions can be derived from Eq. (1), as follows:

$$P_C: \quad x_1 = x_2 = x_3 = x_4 = x_5 = x_6 = 0; \tag{10}$$

$$F_R: \quad x_1 = x_2 = x_3 = (Q_{11} + 2Q_{12})P_3^2,$$
$$x_4 = x_5 = x_6 = Q_{44}P_3^2; \tag{11}$$

$$A_O: \quad x_1 = 2Z_{12}p_3^2, \quad x_2 = x_3 = (Z_{11} + Z_{12})p_3^2,$$
$$x_4 = Z_{44}p_3^2, \quad x_5 = x_6 = 0. \tag{12}$$

Relations for the relative dielectric stiffnesses $\chi_{ij}(= \partial^2 \Delta G / \partial P_i \partial P_j)$ were derived from Eq. (1) for the solutions

$$P_C: \quad \chi_{11} = \chi_{22} = \chi_{33} = 3\epsilon_0 \alpha_1, \quad \chi_{12} = \chi_{23} = \chi_{31} = 0. \tag{13}$$

$$F_R: \quad \chi_{11} = \chi_{22} = \chi_{33} = 2\epsilon_0[\alpha_1 + (6\alpha_{11} + 2\alpha_{12})P_3^2$$
$$+ (15\alpha_{111} + 14\alpha_{112} + \alpha_{123})P_3^4],$$
$$\chi_{12} = \chi_{23} = \chi_{31} = 4\epsilon_0[\alpha_{12}P_3^2 + (4\alpha_{112} + \alpha_{123})P_3^4]; \tag{14}$$

$$A_O: \quad \chi_{11} = 2\epsilon_0[\alpha_1 + 2\mu_{12}p_3^2],$$
$$\chi_{22} = \chi_{33} = 2\epsilon_0[\alpha_1 + (\mu_{11} - \mu_{12})p_3^2],$$
$$\chi_{12} = \chi_{31} = 0, \quad \chi_{23} = \epsilon_0 \mu_{44} p_3^2. \tag{15}$$

The multiplication by the permittivity of free space $\epsilon_0$ in these equations was required to convert from absolute to relative dielectric stiffnesses. Equations (14) and (15) can be used to calculate the relative dielectric stiffnesses for each phase based on the original cubic axes.

In the orthorhombic state the polarization can be along any of the $\langle 110 \rangle$ directions of the original cubic axes. The polarization of the rhombohedral state can be along any of the $\langle 111 \rangle$ directions. By rotating these axes so that for both states the new $x_3$ axis is along the polar directions, diagonalized matrices will result. The new dielectric stiffness coefficients (indicated by a prime) can be related to the old coefficients [defined by Eqs. (14) and (15)] with the following relations:

$$F_R: \quad \chi'_{11} = \chi'_{22} = \chi_{11} - \chi_{12}, \quad \chi'_{33} = \chi_{11} + 2\chi_{12},$$
$$\chi'_{12} = \chi'_{23} = \chi'_{31} = 0; \tag{16}$$

$$A_O: \quad \chi'_{11} = \chi_{11}, \quad \chi'_{22} = \chi_{33} - \chi_{23},$$
$$\chi'_{33} = \chi_{33} + \chi_{23}, \quad \chi'_{12} = \chi'_{23} = \chi'_{31} = 0. \tag{17}$$

These equations can be used to calculate the dielectric

stiffnesses of the orthorhombic and rhombohedral phases parallel and perpendicular to the polar axes.

## III. EVALUATION OF THE COEFFICIENTS

In this section, coefficients of the energy function will be determined from experimental data. All of the coefficients were assumed to be independent of temperature, except for the ferroelectric ($\alpha_1$) and antiferroelectric ($\sigma_1$) dielectric stiffness coefficients which were given a linear temperature dependence based on the Curie–Weiss law.

$$\alpha_1 = (T - \theta)/(2\epsilon_0 C), \tag{18}$$

$$\sigma_1 = (T - \theta_A)/(2\epsilon_0 C_A). \tag{19}$$

$C$ is the Curie constant, $\epsilon_0$ is the permittivity of free space, $\theta$ is the Curie–Weiss temperature, and $C_A$ and $\theta_A$ are antiferroelectric constants analogous to $C$ and $\theta$.

By combining Eqs. (13) and (18), $C$ and $\theta$ can be determined from a linear fit of experimental dielectric stiffness data in the paraelectric cubic state (the Curie–Weiss law). The dielectric stiffness is the inverse of the dielectric susceptibility $\eta_{ij}$, which will be assumed to be equal to the relative dielectric permittivity $\epsilon_{ij}$ (actually $\epsilon_{ij} = \eta_{ij} + 1$). Values of $C$ and $\theta$ for lead zirconate were previously found to be equal to $1.5 \times 10^5$ °C and 190 °C by fitting the Curie–Weiss law to single-crystal dielectric data.[2,3] These constants will be used to calculate the $\alpha_1$ coefficient versus temperature. A different procedure was used to determine the antiferroelectric $C_A$ and $\theta_A$ constants, as will be described later in this section.

The ferroelectric rhombohedral spontaneous polarization ($P_3$) can be related to the coefficients of the energy function by solving the quadratic relation formed from the first partial derivative stability condition [Eq. (8)]:

$$P_3^2 = [-\zeta + (\zeta^2 - 9\alpha_1\xi)^{1/2}]/(3\xi), \tag{20}$$

where

$$\zeta = 3(\alpha_{11} + \alpha_{12})$$

and

$$\xi = 3\alpha_{111} + 6\alpha_{112} + \alpha_{123}. \tag{21}$$

At $T_c$, the transition temperature between the ferroelectric rhombohedral and paraelectric cubic phases, two relations must be satisfied:

$$0 = 3\alpha_{1C} + \zeta P_{3C}^2 + \xi P_{3C}^4 \tag{22}$$

and

$$0 = \alpha_{1C} + 2/3\zeta P_{3C}^2 + \xi P_{3C}^4, \tag{23}$$

where $\alpha_{1C}$ and $P_{3C}$ are $\alpha_1$ and $P_3$ at $T_C$. Equation (22) was derived from the requirement that the $\Delta G$'s of the cubic and rhombohedral phases [Eqs. (5) and (6)] must be equal at $T_C$. Equation (23) is the first partial derivative stability condition [Eq. (8)], which must be satisfied so that the stable state corresponds to the minima of the energy function.

When the transition at $T_C$ is first order, the spontaneous polarization in the ferroelectric state will develop discontinuously at the transition, and thus $P_{3C}$ will be nonzero. In this case Eq. (18) can be substituted into Eqs. (22) and (23) to obtain relations for the $\zeta$ and $\xi$ coefficients:

$$\zeta = \frac{-3(T_C - \theta)}{\epsilon_0 C P_{3C}^2}, \quad \xi = \frac{3(T_C - \theta)}{2\epsilon_0 C P_{3C}^4}. \tag{24}$$

By assuming that the $\zeta$ and $\xi$ coefficients are independent of temperature and then substituting Eqs. (24) and (18) into Eq. (20), the following relation results for the spontaneous polarization of the ferroelectric rhombohedral phase:

$$P_3^2 = \Psi P_{C3}^2,$$

where

$$\Psi = \frac{2}{3} \cdot \left[ 1 + \left( 1 - \frac{3(T - \theta)}{4(T_C - \theta)} \right)^{1/2} \right]. \tag{25}$$

Now if $P_{3C}, T_C$, and $\theta$ can be determined, the spontaneous polarization of the ferroelectric rhombohedral phase can be calculated versus temperature. Note that $P_3$ is the $x_3$ component of the resultant spontaneous polarization ($P_S$) along the [111] direction, and thus $P_S = 3^{1/2}P_3$.

Using the value of $\theta$ given above, with $T_C$ equal to 232 °C,[3] a value of $P_{3C}$ was found from the best least-squares fit of Eq. (25) to experimental spontaneous polarization data (from curve 2 in Fig. 3 of Ref. 17), as shown in the insert of Fig. 1. The resulting $P_{3C}$ value is listed in Table II with the values of the other constants that were used in the calculations. These values were used to calculate the ferroelectric rhombohedral spontaneous polarization versus temperature down to $-273$ °C as shown in Fig. 1. However, over most of this temperature region the rhombohedral phase is metastable to the stable antiferroelectric orthorhombic phase.

A similar relation to Eq. (25) can be derived for the spontaneous strain $x_4$ by substituting Eq. (25) into Eq. (11):

$$x_4 = \Psi x_{4C},$$

where

$$x_{4C} = Q_{44} P_{3C}^2. \tag{26}$$

This equation was used with the values of the constants listed in Table II to determine a value of $x_{4C}$ ($x_4$ at $T_C$) that gave the best least-squares fit of experimental $x_4$ data, as shown in the insert of Fig. 2. The experimental $x_4$ data was calculated from rhombohedral range $\alpha_R$ data from Ref. 11 using the relation: $x_4 = (90 - \alpha_R)/90$. A value of the electrostrictive
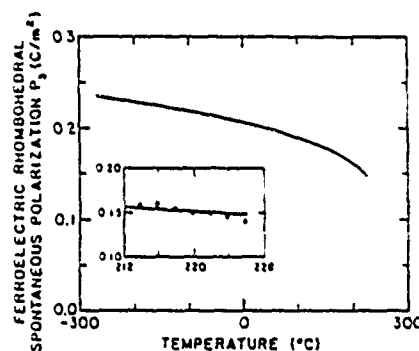


FIG. 1 Spontaneous polarization as a function of temperature calculated for the stable and metastable regions of the ferroelectric rhombohedral form. Inset: Comparison with measured polarization over the stable range of the phase.

| | |
|---|---|
| $T_C (°C)$ | 232.0[a] |
| $\theta (°C)$ | 190.0[a] |
| $C (10^5 °C)$ | 1.5[a] |
| $P_{3C} (C/m^2)$ | 0.1428[b] |
| $Q_{44} (m^4/C^2)$ | 0.059 |
| $T_{AF} (°C)$ | 220.0[c] |
| $T_N (°C)$ | 226.0 |
| $\theta_A (°C)$ | 216.5 |
| $x_{4N} (10^{-4})$ | 2.63 |
| $Z_{44}C_A (m^4 °C/C^2)$ | 683.35 |
| $\lambda (10^{11} m/F)$ | 6.0184 |

[a] From Refs. 2 and 3.
[b] From Ref. 17.
[c] Average of the heating and cooling DTA data from Ref. 2.

$Q_{44}$ constant was calculated from $x_{4C}$ and $P_{3C}$ using Eq. (26) This value is listed in Table II. The ferroelectric rhombohedral spontaneous strain $x_4$ was calculated versus temperature into the antiferroelectric region as shown in Fig. 2 using Eq. (26) and the constants listed in Table II.

The constants determined above will be used to calculate the $\Delta G$ of the ferroelectric rhombohedral phase in the next section. The procedure used to determine values of the antiferroelectric constants, which are needed to calculate the $\Delta G$ of the antiferroelectric orthorhombic phase, will now be presented.

The antiferroelectric measure of the polarization $p_3$ for the orthorhombic solution can be related to the antiferroelectric $\sigma$ coefficients by solving the quadratic relation formed from the first partial derivative stability condition [Eq. (9)]:

$$p_3^2 = [ -\delta + (\delta^2 - 6\sigma_1\gamma)^{1/2}]/(3\gamma), \tag{27}$$

where

$$\delta = 2\sigma_{11} + \sigma_{12}$$

and

$$\gamma = 2(\sigma_{111} + \sigma_{112}). \tag{28}$$

The Néel temperature ($T_N$) is the transition temperature from an antiferroelectric phase to a paraelectric phase. In lead zirconate this is a metastable phase transition, be-
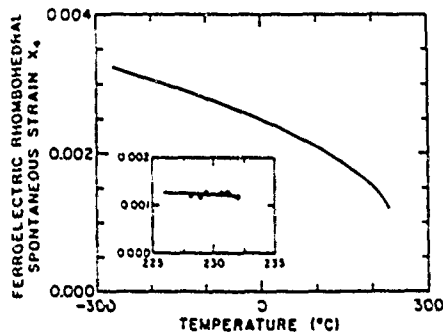


FIG. 2. Spontaneous lattice strain $x_4$ as a function of temperature calculated for the stable and metastable regions of the ferroelectric rhombohedral form Inset Comparison of calculated and measured strain over the stable region of the phase.

cause it occurs in the ferroelectric rhombohedral stability region. As in the rhombohedral case at $T_C$, two equations must be satisfied at $T_N$:

$$0 = 2\sigma_{1N} + \delta p_{3N}^2 + \gamma p_{3N}^4. \tag{29}$$

$$0 = \sigma_{1N} + \delta p_{3N}^2 + 3/2\gamma p_{3N}^4. \tag{30}$$

$\sigma_{1N}$ and $p_{3N}$ are $\sigma_1$ and $p_3$ at $T_N$. Equation (29) was derived from the requirement that the $\Delta G$s of the two phases (Eqs. (5) and (7)] must be equal at $T_N$. Equation (30) is the first partial derivative stability condition [Eq. (9)].

Substituting Eq. (19) into Eqs. (29) and (30), and solving for the $\delta$ and $\gamma$ coefficients results in

$$\delta = \frac{-2(T_N - \theta_A)}{\epsilon_0 C_A p_{3N}^2}, \quad \gamma = \frac{T_N - \theta_A}{\epsilon_0 C_A p_{3N}^4}, \tag{31}$$

where $p_{3N}$ is $p_3$ at $T_N$.

By assuming that the $\delta$ and $\gamma$ coefficients are independent of temperature, and then substituting Eqs. (19) and (31) into Eq. (27) yields

$$p_3^2 = \Psi p_{3N}^2,$$

where

$$\Psi = \frac{2}{3}\left[1 + \left(1 - \frac{3(T - \theta_A)}{4(T_N - \theta_A)}\right)^{1/2}\right]. \tag{32}$$

Unfortunately, there is not any experimental antiferroelectric polarization $p_3$ data available, and thus $p_{3N}$ will not be determined in this paper.

However, antiferroelectric spontaneous strain data can be calculated from cell constant data and used to determine two of the antiferroelectric constants. By substituting Eq. (32) into Eq. (12) the following relation results for the antiferroelectric spontaneous strain $x_4$:

$$x_4 = \Psi x_{4N},$$

where

$$x_{4N} = Z_{44}p_{3N}^2. \tag{33}$$

$x_{4N}$ is $x_4$ at $T_N$. Values of $T_N, \theta_A$, and $x_{4N}$ are needed to calculate $x_4$ using Eqs. (32) and (33).

Spontaneous strain $x_4$ data were calculated from cell constant data from Ref. 11 [interaxial $\gamma_p$ data from Fig. 5 in Ref. 11 was related to $x_4$ with the relation: $x_4 = (90 - \gamma_p)/90$]. By fitting these data with all three constants ($T_N, \theta_A$, and $x_{4N}$) as unknowns many combinations of the values of these constants gave similar fits of the data. For this reason the value of one of these constants had to be determined from additional data. Without additional data, it was necessary to make an assumption.

$T_N$ must occur between the antiferroelectric-ferroelectric transition temperature ($T_{AF}$) and the ferroelectric-paraelectric transition temperature ($T_C$). $T_{AF}$ occurs at $\approx 220 °C$ (average of the heating and cooling DTA data in Ref. 2), and $T_C$ at $\approx 232 °C$. Thus since $T_N$ must occur between 220 and 232 °C, it was assumed to be equal to 226 °C. the average of the two extremes. This was a good assumption, because the constants were not significantly affected even if $T_N$ was varied a few degrees. With $T_N$ fixed at 226 C values of $\theta_A$ and $x_{4N}$ were found that gave the best least-

squares fit of the $x_4$ data as shown in Fig. 3. These values are listed in Table II.

Substituting Eqs. (19), (28), (31), (32), and (33) into Eq. (7) results in the following relation for the $\Delta G$ of the antiferroelectric orthorhombic phase:

$$\Delta G = \Psi x_{4N}/(\epsilon_0 Z_{44} C_4)$$
$$\times [T - T_4 - 2\Psi(T_N - T_4)(1 - 1/2\Psi)]. \quad (34)$$

All of the constants needed to calculate the $\Delta G$ of the antiferroelectric orthorhombic phase using this equation have been determined, except for the $Z_{44}$ and $C_4$ constants. At this point there is not enough experimental data available to determine values of both of these constants. However, the product of these constants can be determined by equating the $\Delta G$s of the $A_O$ and $F_R$ phases at the transition between these phases:

$$\text{At } T_{AF}: \quad \Delta G_{F_R} = \Delta G_{4_O}. \quad (35)$$

The rhombohedral $\Delta G$ at $T_{AF}$ can be calculated from Eqs. (6), (19), (21), (24), and (25) using the constants listed in Table II. This value can then be used with Eqs. (34) and (35) and the constants from Table II to calculate a value of the $Z_{44} C_4$ product. This value is listed in Table II. By assuming that $Z_{44} C_4$ is independent of temperature, all of the constants necessary to calculate the $\Delta G$ of the antiferroelectric orthorhombic phase versus temperature have been determined. Calculations of the $\Delta G$'s of the ferroelectric and antiferroelectric phases will be presented in the next section.

All of the $\alpha$ coefficients must be determined to calculate the dielectric stiffness $\chi_{ij}$ coefficients of the ferroelectric rhombohedral phase [see Eq. (14)]. The constants determined earlier in this section can be used in Eq. (24) to calculate the $\zeta[ = 3(\alpha_{11} + \alpha_{12})]$ and $\xi( = 3\alpha_{111} + 6\alpha_{112} + \alpha_{123})$ coefficients, which can be used to calculate the spontaneous polarization, strain, and $\Delta G$ of the $F_R$ phase. At this time there are not enough lead zirconate data present to determine values of $\alpha_{11}$, $\alpha_{12}$, $\alpha_{111}$, $\alpha_{112}$, and $\alpha_{123}$. However, these coefficients were determined in the PZT system, and extrapolated to lead zirconate.[6-10]

To calculate the dielectric stiffness $\chi_{ij}$ coefficients of the antiferroelectric orthorhombic phase, the $\mu_{ij}$ antiferroelectric-ferroelectric coupling coefficients must be determined. Unfortunately the data necessary to determine these coeffi-



FIG. 3. Antiferroelectric orthorhombic strain $x_4$ as a function of temperature: Comparison of calculated and measured values.

cients has not been measured. One goal of this project was to compare calculations from this theory with polycrystalline high-frequency dielectric data. To accomplish this a procedure was used to combine the unknown constants in the dielectric relations into one constant that could be determined from low-temperature polycrystalline dielectric data. This procedure will be described below.

By combining Eqs. (15) and (17) dielectric stiffness relations based on the normal orthorhombic axes result

$$\chi'_{11} = 2\epsilon_0(\alpha_1 + 2\mu_{12}p_3^2),$$
$$\chi'_{22} = 2\epsilon_0[\alpha_1 + (\mu_{11} + \mu_{12} - 1/2\mu_{44})p_3^2],$$
$$\chi'_{33} = 2\epsilon_0[\alpha_1 + (\mu_{11} + \mu_{12} + 1/2\mu_{44})p_3^2]. \quad (36)$$

These single-crystal coefficients were related to the polycrystalline dielectric stiffness $\chi$ (a bold-faced symbol will be used to refer to polycrystalline constants) using the following parallel averaging relation:

$$\chi = 1/3(\chi'_{11} + \chi'_{22} + \chi'_{33}). \quad (37)$$

By substituting Eq. (36) into Eq. (37) the following relation results:

$$\chi = 2\epsilon_0[\alpha_1 + 2/3(\mu_{11} + 2\mu_{12})p_3^2]. \quad (38)$$

Not enough experimental data were available to determine the constants necessary to calculate $p_3$. However, the constants needed to calculate the antiferroelectric spontaneous strain $x_4$ were determined. By substituting Eq. (12) into Eq. (38) $p_3$ can be replaced by $x_4$

$$1/\epsilon \approx \chi = 2\epsilon_0(\alpha_1 + \lambda x_4),$$

where

$$\lambda = 2(\mu_{11} + 2\mu_{12})/(3Z_{44}). \quad (39)$$

Since $\alpha_1$ and $x_4$ can be determined from Eqs. (18) and (33) using the constants listed in Table II, the new constant $\lambda$ can be calculated from an experimental polycrystalline dielectric constant ($\epsilon$) measurement ($\epsilon \approx 1/\chi$).

To provide experimental data for evaluation of the constant $\lambda$, the dielectric constant was measured at 1 kHz from $-268.8$ °C to room temperature on polycrystalline lead zirconate. The procedure used to fabricate the lead zirconate samples was described in Refs. 4 and 5. The low-temperature measurement apparatus and technique that was used was described in Ref. 18. At low temperatures ($-268.8$ °C) the extrinsic contributions to the polycrystalline dielectric properties, such as domain wall motion or thermally activated defect motions, were assumed to "freeze out." The remaining dielectric properties would then represent the intrinsic contribution, or averaging of the single-domain properties.

A dielectric constant of 95 was measured at $-268.8$ °C, and used to calculate the value of the $\lambda$ constant listed in Table II. By assuming that this constant is independent of temperature the intrinsic polycrystalline dielectric constant could be calculated versus temperature using Eq. (39) and the constants listed in Table II. These calculations will be compared with experimental high-frequency dielectric measurements in the next section.
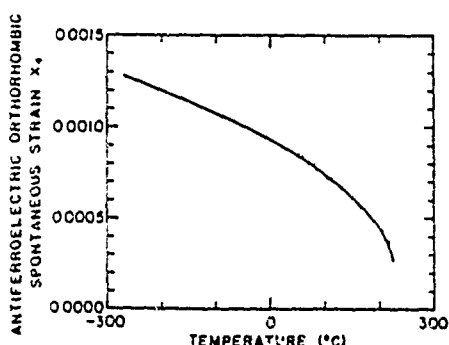
3177     J. Appl. Phys., Vol. 65, No. 8, 15 April 1989

Haun et al.     3177

## IV. THEORETICAL CALCULATIONS

In this section theoretical calculations will be made using the equations from Sec. II, and the constants that were determined in Sec. III. Figure 4 shows the energies $\Delta G$ of the antiferroelectric orthorhombic and ferroelectric high-temperature rhombohedral phases plotted versus temperature for lead zirconate. Above $T_C$ (232 °C) the energy of the ferroelectric rhombohedral phase is positive, and thus the cubic state with the reference energy set to zero is stable. At $T_C$ the energy of the $F_R$ phase decreases to zero, and then becomes negative below $T_C$ causing the rhombohedral phase to become stable. At $T_N$ the energy of the antiferroelectric orthorhombic phase is zero, and a metastable transition occurs from the cubic phase. As the temperature decreases, the larger temperature dependence of the $\Delta G$ of the $A_O$ phase compared to the $F_R$ phase causes the energies of these phases to become equal at the transition $T_{AF}$. Below $T_{AF}$ the $A_O$ phase becomes stable, and remains stable down to $-273$ °C.

The polycrystalline dielectric constant ($\epsilon$) of the antiferroelectric orthorhombic phase was calculated from Eq. (39) using the constants listed in Table II, and plotted in Fig. 5 versus temperature up to $T_{AF}$. The dielectric constant of the paraelectric cubic phase was also calculated using Eq. (13), and plotted in this figure above $T_C$. The ferroelectric rhombohedral dielectric properties were not investigated in this paper, but could be calculated from the values of the coefficients that were recently determined in Refs. 6–10.

The experimental data, measured at 1 kHz from $-268.8$ °C to room temperature, are plotted in the insert in Fig. 5. The data point at $-268.8$ °C was used to calculate the $\lambda$ constant, as described in Sec. III. By assuming that the theory is predicting the intrinsic response of the material, the difference that develops between the theoretical calculations and experimental data as the temperature is increased is due to the thermally activated (extrinsic) contributions to the polycrystalline dielectric constant. At room temperature the theoretical dielectric constant has a value of 120, compared to the experimental value of 167. This indicates that 72% of the experimentally measured polycrystalline dielectric constant is due to the intrinsic averaging of the single-domain constants, while 28% is from extrinsic contributions.

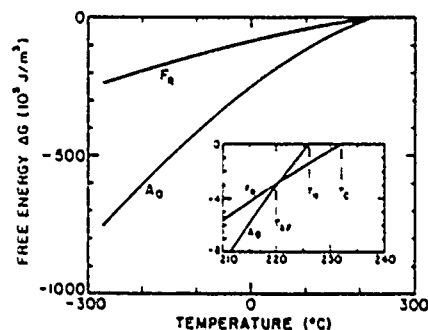Lanagan et al.[4,5] measured the dielectric constant of polycrystalline lead zirconate from 100 Hz to 26 GHz. Their
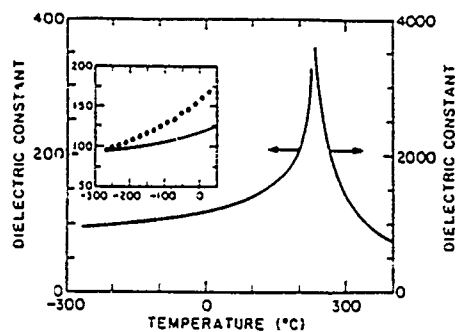
FIG. 5 Calculated dielectric permittivity in the antiferroelectric orthorhombic phase averaged for a polycrystalline sample. Inset: Comparison with low-frequency (1 kHz) data.

data are plotted versus the log of the frequency in Fig. 6. As can be seen by these data a relaxation occurred at microwave frequencies. Above this relaxation the dielectric constant agrees remarkably well with the calculation from the theory presented in this paper, indicating that the extrinsic contributions to the dielectric properties have "relaxed out" above $\approx 10$ GHz.

The data in Figs. 5 and 6 indicate that the extrinsic contributions to the polycrystalline dielectric constant of lead zirconate will "freeze out" at low temperatures and "relax out" at high frequencies, and that the remaining intrinsic contributions can be thermodynamically modeled. The theory provides a method of connecting the low-temperature data to the high-frequency data. It would now be useful to measure the high-frequency dielectric properties down to low temperatures.

The dielectric constant at 10 GHz was measured as a function of temperature as shown in Fig. 7. The 1-kHz data from Fig. 5 are also plotted in this figure along with the theoretical calculations. Unfortunately at this time the 10-GHz data was only measured down to $-100$ °C, and thus it is still not clear how the data would compare at lower temperatures. There is a slight difference between the temperature dependencies of the 10-GHz data and the theoretical calculations. This may indicate that at 10 GHz all of the extrinsic contributions had not completely "relaxed out," or that the actual temperature dependence was not completely

FIG 4 Calculated free energy $\Delta G$ for ferroelectric and antiferroelectric forms Inset Expanded scale to permit identification of the $A_O$ to $F_R$ and $F_R$ to paraelectric transitions.
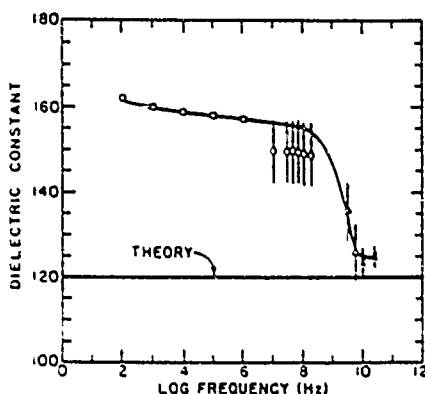
FIG. 6 Measured microwave relaxation in the dielectric permittivity of lead zirconate (Ref. 5) compared to the calculated room-temperature value for the antiferroelectric polycrystal.
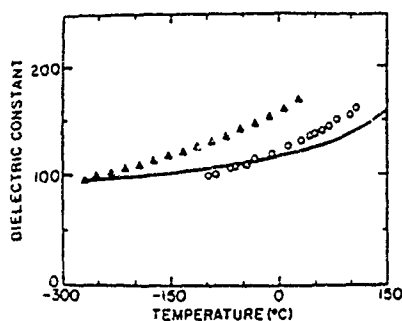
FIG. 7. Comparison of calculated permittivity as a function of temperature with measured values at low and at microwave frequencies.

accounted for in the theory (most of the coefficients of the energy function were assumed to be independent of temperature) In addition there is some experimental error in the measurements. The calibration for these measurements was only made at room temperature, and thus an error of $\pm 10\%$ has been estimated for the 10-GHz data.

## V. EXTENSION OF THE THEORY INTO THE PZT SYSTEM

In this section a procedure will be presented that can be used to calculate the compositional dependence of the $\Delta G$ of the antiferroelectric orthorhombic phase into the PZT system. This procedure was needed to complete the development of a thermodynamic theory to model all of the phase transitions of the PZT system.[6-10]

The $\Delta G$ of the antiferroelectric orthorhombic phase for lead ziconate was calculated in Sec. IV using Eq. (34). The constants needed for these calculations were determined from the available experimental data, as described in Sec. III. Unfortunately, similar experimental data are not available for PZT compositions in the antiferroelectric region, and thus the compositional dependence of each of the constants necessary to calculate the $\Delta G$ of the $A_O$ phase could not be determined. However, the following method was used to calculate the $\Delta G$ of the $A_O$ phase into the PZT system from the compositional dependence of a single constant, which was determined by equating the $\Delta G$'s of the $A_O$ and $F_R$ phases at the transition between these phases.

The $\Delta G$ of the antiferroelectric orthorhombic phase was determined from the following relation by multiplying the $\Delta G$ of lead zirconate (PZ) by a factor $\Xi$:

$$\Delta G_{4_O} = \Xi \Delta G_{4_O(\text{PZ})}. \tag{40}$$

The compositional dependence of $\Xi$ was then determined by combining this relation with Eq. (35).

$$\Xi = \Delta G_{F_R} (\text{at } T_{AF}) / \Delta G_{4_O(\text{PZ})}. \tag{41}$$

To calculate $\Xi$ using this equation, $\Delta G$ of the $F_R$ phase (high-temperature rhombohedral phase in PZT) at $T_{AF}$ was calculated from the PZT theory developed in Refs. 6–10. The antiferroelectric-ferroelectric transition temperature $T_{AF}$ was determined by fitting the following polynomial equation to the experimental phase diagram:[1]

$$T_{AF} = 220.84 - 706.15x - 26778.0x^2, \tag{42}$$

where $x$ is the mole fraction $PbTiO_3$ in PZT.

$\Delta G$ of the $A_O$ phase for lead zirconate was calculated from the equations and data presented in this paper, except that the value of the Curie constant was changed. The compositional dependence of the Curie constant that was used in the PZT theory[3] resulted in a value of $2.0 \times 10^5$ °C, instead of the value of $1.5 \times 10^5$ °C that was used in the previous calculations in this paper. To be consistent with the PZT calculations the value of the Curie constant was changed, which also caused the value of the $Q_{44} C_A$ constant to change to 889.27 m$^4$ °C/C$^2$, instead of the value listed in Table II.

Using the calculations described above in Eq. (41), the $\Xi$ constant was calculated versus composition, as plotted in Fig. 8. By then assuming the $\Xi$ constant to be independent of temperature, the $\Delta G$ of the antiferroelectric phase was calculated versus composition into the PZT system, as shown in Ref. 10. This method resulted in excellent agreement between the experimental and theoretical phase diagrams.[10]

## IV. SUMMARY

A two-sublattice theory was used to derive an energy function to account for the ferroelectic and antiferroelectric behavior of lead zirconate. Solutions and property relations were derived from this energy function corresponding to the stable solid phases of lead zirconate. The coefficients necessary to calculate the ferroelectric rhombohedral $\Delta G$, and spontaneous polarization and strain; and antiferroelectric $\Delta G$ and spontaneous strain were determined from the available experimental data in the literature.

Additional data were needed to model the intrinsic polycrystalline dielectric properties of lead zirconate. To provide these data the dielectric properties were measured down to low temperatures ($-268.8$ °C), where extrinsic contributions to the properties "freeze out." These data were then used to determine the value of a combination of constants, which could be used to calculate the intrinsic polycrystalline dielectric constant versus temperature. The calculations indicate that at room temperature 72% of the experimentally measured polycrystalline dielectric constant (measured at 1 kHz) is due to the intrinsic averaging of the single-domain constants, while 28% is from extrinsic contributions. The calculations were found to be in good agreement with experimental data at high frequencies ($> 10$ GHz), indicating that the extrinsic contributions had "relaxed out."
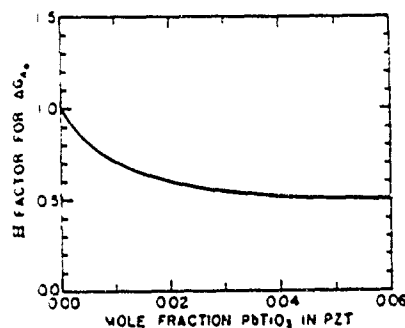


FIG 8 Values of $\Xi$ [ $= \Delta G_{F_R} (\text{At } T_{AF}) / \Delta G_{4_O(\text{PZ})}$ ] required to fit calculated and measured phase diagrams. $\Xi$ is assumed to be independent of temperature.

the antiferroelectric orthorhombic phase into the PZT system. This method was used to complete the development of a thermodynamic theory, which quantitatively accounts for all of the known phase transitions in the PZT system.[6-10]

Additional data are still needed to determine values of the coefficients of the energy function that were not determined in this paper. The effects of the application of electric field[19] or mechanical stress[20] may provide some of these data.

[1]B Jaffe, W J Cook, and H Jaffe, *Piezoelectric Ceramics* (Academic, London, 1971).
[2]Z. Ujma and J. Handerek, Phys. Status Solidi A **28**, 489 (1975).
[3]B. A. Scott and G. Burns, J. Am. Ceram. Soc. **55**, 331 (1972).
[4]M. T Lanagan, Ph.D. thesis, The Pennsylvania State University, 1987
[5]M. T. Lanagan, J. H. Kim, S. J. Jang, and R. E. Newnham, J. Am. Ceram. Soc. **71**, 311 (1988).
[6]M J Haun, E.Furman, H A McKinstry, and L. E. Cross (unpublished).
[7]M J Haun, Z Q Zhuang, E Furman, S J Jang, and L. E Cross (unpublished).
[8]M. J. Haun, E. Furman, T R. Halemane, and L. E. Cross (unpublished).
[9]M. J. Haun, E. Furman, S. J. Jang, and L. E. Cross (unpublished).
[10]R W Whatmore and A. M. Glazer, J. Phys. C. **12**, 1505 (1979)
[11]K Uchino, L E. Cross, R E Newnham, and S. Nomura, J Appl. Phys. **52**, 1455 (1981).
[12]C. Kittel, Phys. Rev **82**, 729 (1951).
[13]A. F Devonshire, Philos. Mag. **3**, 85 (1954).
[14]L. E. Cross, Philos. Mag. **1**, 76 (1956).
[15]C. N. W. Darlington, J. Appl. Phys. **43**, 4951 (1972).
[16]Z. Ujma and J. Handerek, Acta Phys. Polon. A **53**, 665 (1978).
[17]Z. Q. Zhuang, M. J. Haun, S. J. Jang, and L. E. Cross, *Proceedings of the 6th IEEE International Symposium on the Applications of Ferroelectrics,* Lehigh, PA, edited by Van Wood (IEEE, New York, 1986), pp. 394–397.
[18]O. E. Fesenko, V. G. Smotrakov, and N. G. Leontiev, Ferroelec. Lett. **2**, 33 (1984).
[19]G. A. Samara, Phys. Rev. B **1**, 3777 (1970).

APPENDIX 24

# THERMODYNAMIC THEORY OF THE LEAD ZIRCONATE-TITANATE SOLID SOLUTION SYSTEM, PART I: PHENOMENOLOGY

## M. J. HAUN,† E. FURMAN,‡ S. J. JANG and L. E. CROSS

*Materials Research Laboratory, The Pennsylvania State University, University Park, PA 16802, USA*

Compositions within the lead zirconate-titanate (PZT) solid solution system have been extensively used in polycrystalline ceramic form in a wide range of piezoelectric transducer applications. However, the growth of good quality PZT single crystals for compositions across the entire phase diagram has not been accomplished. Due to the lack of single-crystal data, an understanding of the properties of polycrystalline PZT has been limited. If the single domain (intrinsic) properties of PZT could be determined, then the extrinsic contributions (e.g. domain wall and defect motions) to the polycrystalline properties could be separated from the intrinsic contributions. The purpose of this research has been to develop a thermodynamic phenomenological theory to model the phase transitions and single-domain properties of the PZT system.

This paper is the first of a series of five papers describing the thermodynamic theory of PZT that has been developed for the entire solid solution system. In this paper the previous work that led to the present theory will first be reviewed, followed by the presentation of the energy function for PZT and the solutions and property relations that can be derived from this energy function

## I. INTRODUCTION

The lead zirconate-titanate (PZT) phase diagram[1] is shown in Figure 1. A cubic paraelectric phase ($P_C$) occurs at high temperatures and has the perovskite crystal structure $ABO_3$. On the lead titanate ($PbTiO_3$) side of the phase diagram, a ferroelectric tetragonal phase ($F_T$) exists with a spontaneous polarization along the pseudocubic [001] direction. A morphotropic boundary separates the tetragonal phase from a ferroelectric high-temperature rhombohedral phase ($F_{R(HT)}$).

Another ferroelectric to ferroelectric phase transition occurs between the high-temperature rhombohedral phase and a low-temperature rhombohedral phase ($F_{R(LT)}$). Both of these rhombohedral phases have a spontaneous polarization that occurs along the [111] direction. The low-temperature rhombohedral phase has a tilting or rotation of the oxygen octahedra about the [111] axis, which does not occur in the high-temperature phase.

On the lead zirconate side of the phase diagram antiferroelectric tetragonal ($A_T$) and orthorhombic ($A_O$) phases are present. These antiferroelectric phases are composed of two sublattices with equal and opposite polarization, resulting in zero net polarization.

More recent data[2] have shown that the $A_T$ phase does not occur in pure lead zirconate, but will occur with small dopants or impurities such as strontium. These data have also shown that the high-temperature rhombohedral phase extends over to lead zirconate. The theory described in this paper will be developed to model the phase diagram according to these recent data.
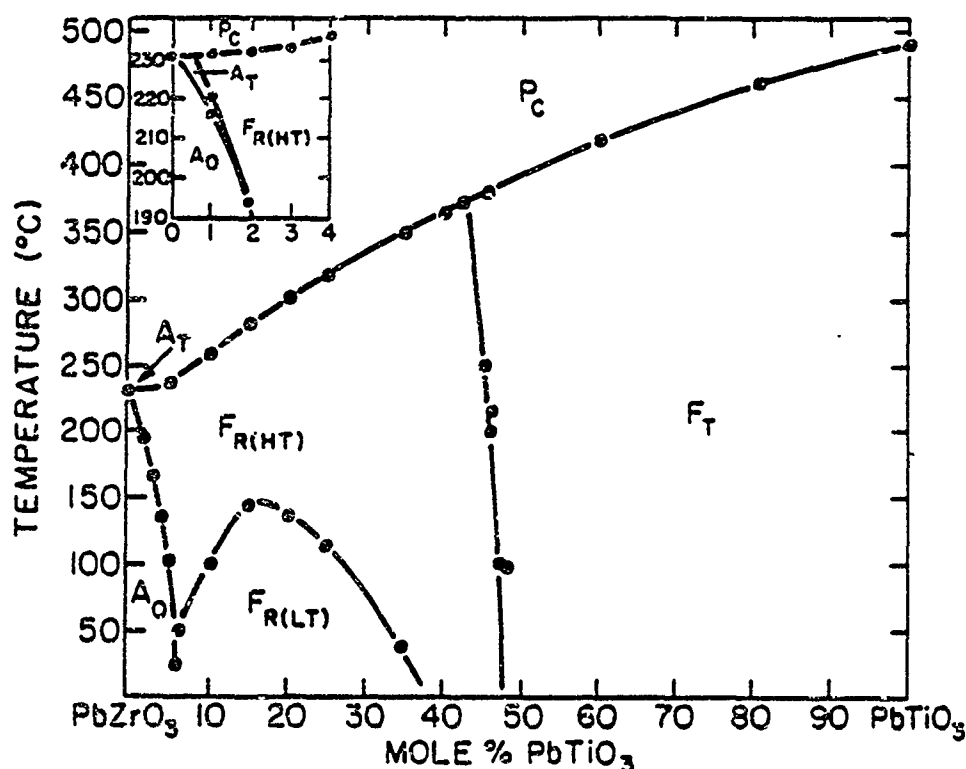
FIGURE 1    The PbZrO₃–PbTiO₃ Phase Diagram.[1]

PZT compositions have important technological applications as piezoelectric transducers, pyroelectric detectors, electro-optic devices, and explosively induced charge storage devices. The main application of PZT has been as piezoelectric transducers with compositions near the tetragonal-rhombohedral morphotropic boundary. These applications include phonograph pickups, buzzers, relays, accelerometers, igniters, micropositioners, hydrophones, sonar, wave filters, earphones, delay line welders, cutters, and high voltage sources.[1] Recently piezoelectric motors have even been made.[3,4]

Lead titanate has become important for possible application in hydrophones and medical ultrasonic imaging, because of the large electromechanical anisotropy that can be obtained in lead titanate polycrystalline ceramics.[5] The theory developed in this paper has been used to explain this large anisotropy, which occurs in lead titanate in polycrystalline form, but not in single-crystal form.[6]

PZT compositions with the high to low temperature rhombohedral phase transition have been used as pyroelectric detectors.[7] When cooling through this transition, the polarization increases suddenly due to a contribution from the tilting of the oxygen octahedra in the low-temperature phase. This results in a large pyroelectric coefficient. The dielectric constant is relatively low, and only has a very slight change when going through this transition. A large pyroelectric coefficient $p$ ($= dP_S/dT$) and small dielectric constant $K$ result in a large pyroelectric figure of merit ($= p/K^{1/2}$).

PZT is also an important material for electrooptic applications, when doped with lanthanum to form PLZT. According to Haertling and Land,[3] PLZT has advantages

in electrooptic applications because of "1) high transparency essentially independent of grain size, 2) ease of fabrication, and 3) electrically variable optical retardation, including electrooptic memory and linear or quadratic modulation capabilities."

Explosively induced charge storage devices have also been fabricated from PZT compositions utilizing the ferroelectric to antiferroelectric transition. In these applications a stress is applied to a poled ceramic sample with the ferroelectric structure, causing it to transform to the antiferroelectric state and to suddenly release the stored charge.

The applications described above show that PZT is an important material. These applications use PZT in polycrystalline ceramic form. The growth of good quality PZT single crystals for compositions across the entire phase diagram has not been accomplished.[9] Due to the lack of single-crystal data, an understanding of the properties of ceramic PZT has been limited. If the single-domain properties of PZT could be determined, then these intrinsic contributions to the ceramic properties could be separated from the extrinsic contributions (e.g. domain wall and defect motions). The purpose of this research has been to develop a thermodynamic phenomenological theory to predict the phase transitions and single-domain properties of the PZT system. This theory could then be used to further the understanding of the properties of polycrystalline materials.

This paper is the first of a series of five papers covering the details of the thermodynamic theory of PZT that has been developed for the entire solid solution system. In this paper the previous work that led to the present theory will first be reviewed, followed by the presentation of the energy function for PZT, and the solutions and property relations that can be derived from this energy function. In the next three papers[10-12] the coefficients of the energy function will be determined from experimental data. Finally in the last paper of the series[13] theoretical calculations of the PZT single-domain properties will be presented, along with a discussion of the applications of the theory.

## II. DEVELOPMENT OF A THERMODYNAMIC THEORY OF PZT

The Landau-Ginsburg-Devonshire type phenomenological theory was used to explain the transitions and properties at the tetragonal-rhombohedral morphotropic phase boundary in the PZT system.[14-21] However, due to the lack of single-crystal data the coefficients of the energy function could not be adequately determined.

Over the past several years at the Materials Research Laboratory of the Pennsylvania State University, the coefficients of an energy function for the PZT system have been determined using indirect methods. The development of this theory occurred in a series of steps, where different parts of the phase diagram were modeled separately. This development will be described below.

Amin[22] developed a modified Devonshire form of the elastic Gibbs free energy function for the simple proper ferroelectric phases of the PZT system. The spontaneous strain in the ferroelectric phases was determined using high-temperature x-ray diffraction, and used to calculate the spontaneous polarization through the electrostrictive constants. These data were used to determine the higher order

dielectric stiffness coefficients ($\alpha_{11}$ and $\alpha_{111}$). The morphotropic boundary between the tetragonal and rhombohedral phases was then used to determine the remaining higher-order dielectric stiffness coefficients ($\alpha_{12}$, $\alpha_{112}$, and $\alpha_{123}$), and allowed for the first time the calculation of the dielectric, piezoelectric, elastic, and thermal properties of the ferroelectric single-domain states. This theory was developed for the region of the PZT system from lead titanate over to the morphotropic boundary between the tetragonal and rhombohedral phases, and could be extrapolated into the high-temperature rhombohedral phase field.

In this initial theory the Curie constant was assumed to be independent of composition. Amin *et al.*[23] later found from a combination of calorimetric and phenomenological data that the Curie constant was dependent on composition with a peak forming near the morphotropic boundary. The theory was then modified to account for the compositional dependence of the Curie constant.[24] This resulted in better agreement between the theoretical and experimental dielectric data near the morphotropic boundary.

To account for the tilting of the oxygen octahedra in the low-temperature rhombohedral phase Halemane *et al.*[25] expanded the energy function in a one-dimensional power series of the polarization ($P$) and tilt angle ($\theta$) assuming isothermal and zero stress conditions. The possible phase transition sequences and solutions to the energy function were then investigated. This theory was applied to the $Pb(Zr_{0.9}Ti_{0.1})O_3$ composition, first by assuming 2nd order phase transitions,[25] and later by assuming 1st order transitions.[26,27]

The energy function was then expanded in a three-dimensional power series of $P$ and $\theta$ and used to describe all of the ferroelectric phases of the PZT system assuming 1st order phase transitions.[28] The coefficients of the energy function was determined from the phase boundary and equilibrium conditions combined with experimental data, resulting in smooth continuous functions across the phase diagram. The experimental and theoretical phase diagrams were shown to agree very well. Using this theory the spontaneous polarization and tilt angle were calculated as a function of composition and temperature.

A tricritical point, where a phase transition changes from first to second order, was found to occur between the cubic and rhombohedral phases at the PZT 94/6 composition (94% PZ and 6% PT).[29-31] From lead zirconate to the tricritical point the cubic-rhombohedral transition was shown to be first order, and then to change to second order from the tricritical point over to at least the PZT 88/12 composition.[30] Lead titanate has a first order transition from cubic to tetragonal, and thus a second tricritical point should occur between the PZT 88/12 and lead titanate compositions, where the transition would change back to first order.

To provide additional data to determine the coefficients of the energy function and to locate the second tricritical point, pure homogeneous sol-gel derived PZT powders were prepared for several compositions in the rhombohedral phase field.[32] The lattice parameters of these compositions were determined from high-temperature x-ray diffraction, and used to calculate the spontaneous strain.[33] By using these data to determine the higher-order dielectric stiffness coefficients of the energy function, the second order transition region was found to extend over to near or possibly at the morphotropic boundary.[34] Additional details of the tricritical behavior in PZT will be described in the second paper in this series.[10]

Using the x-ray data described above a phenomenological theory was developed to account for the 2nd order transition region of the PZT system.[34] In this theory additional terms were added to the energy function to account for the rotostrictive coupling between the stress and the square of the tilt angle (analogous to the electrostrictive coupling). A rotostrictive constant was determined from experimental spontaneous strain, polarization, and tilt angle data using a relation derived from the energy function for the low-temperature rhombohedral phase. The rotostrictive contribution to the spontaneous strain was found to be opposite in sign to the electrostrictive contribution.

A more complete phenomenological theory of lead titanate was recently developed independently of the PZT theory using the available single crystal data.[35] The theoretically predicted spontaneous polarization and strains, and dielectric and piezoelectric properties are in good agreement with the experimental data. The results of this theory were used to show that the large electromechanical anisotropy found in lead titanate ceramics, but not present in the single crystal properties, is simply due to the intrinsic averaging of the electrostrictive constants.[6,36]

A phenomenological theory for lead zirconate was also developed independently of the PZT theory using the available single-crystal data.[37] This theory was used to calculate the phase stability, antiferroelectric spontaneous strain, and ferroelectric polarization and strain. The polycrystalline ceramic dielectric constant was calculated from the single-crystal constants in this theory, and found to be in good agreement with dielectric data at microwave frequencies. This lead zirconate theory was also extended into the PZT system to account for the antiferroelectric region of the phase diagram.

As described above phenomenological theory has been developed for different sections of the PZT phase diagram. The purpose of this series of papers is to present the recent work that has been completed to combine these separate theories into a complete theory of PZT, where a single energy function and set of coefficients can be used to calculate the phase stability and properties of the entire PZT system. In the next section this energy function will be presented.

## III.  FREE ENERGY FUNCTION FOR PZT

In developing a phenomenological theory for the PZT system the order parameters that cause the phase transitions must be accounted for. The tetragonal and high-temperature rhombohedral phases undergo proper ferroelectric transitions from the paraelectric cubic state, where the spontaneous polarization is the order parameter causing the phase transition. An improper ferroelectric phase transition occurs between the high and low temperature rhombohedral phases, where the spontaneous tilting of the oxygen octahedra causes the phase transition and contributes to the spontaneous polarization. An antiferroelectric type polarization develops when a transition takes place from the ferroelectric to antiferroelectric phases, and is therefore the order parameter for the antiferroelectric state.

Thus to account for all of the phase transitions in the PZT system the energy function should include the ferroelectric and antiferroelectric measures of the polarization, and the tilting of the oxygen octahedra as order parameters. A two-

sublattice model[38] was used to derive the ferroelectric and antiferroelectric meas-
ures of the polarization. To account for the tilting of the oxygen octahedra an
additional term was added to the elastic Gibbs free energy as described in Ref
erences 25–28.

The following energy function for the PZT system was then derived from the
symmetry of the paraelectric phase (m3m) assuming isothermal conditions, using
reduced notation, and expanding the energy function in powers of the ferroelectric
($P_i$) and antiferroelectric ($p_i$) polarizations, oxygen octahedral tilt angle ($\theta_i$), and
including couplings between these order parameters, and between the stress ($X_m$)
and the order parameters:

$$
\begin{aligned}
\Delta G = {} & \alpha_1 \left[ P_1^2 + P_2^2 + P_3^2 \right] + \alpha_{11} \left[ P_1^4 + P_2^4 + P_3^4 \right] \\
& + \alpha_{12} \left[ P_1^2 P_2^2 + P_2^2 P_3^2 + P_3^2 P_1^2 \right] + \alpha_{111} \left[ P_1^6 + P_2^6 + P_3^6 \right] \\
& + \alpha_{112} \left[ P_1^4 (P_2^2 + P_3^2) + P_2^4 (P_1^2 + P_3^2) + P_3^4 (P_1^2 + P_2^2) \right] \\
& + \alpha_{123} P_1^2 P_2^2 P_3^2 + \sigma_1 \left[ p_1^2 + p_2^2 + p_3^2 \right] + \sigma_{11} \left[ p_1^4 + p_2^4 + p_3^4 \right] \\
& + \sigma_{12} \left[ p_1^2 p_2^2 + p_2^2 p_3^2 + p_3^2 p_1^2 \right] + \sigma_{111} \left[ p_1^6 + p_2^6 + p_3^6 \right] \\
& + \sigma_{112} \left[ p_1^4 (p_2^2 + p_3^2) + p_2^4 (p_1^2 + p_3^2) + p_3^4 (p_1^2 - p_2^2) \right] \\
& + \sigma_{123} p_1^2 p_2^2 p_3^2 + \mu_{11} \left[ P_1^2 p_1^2 + P_2^2 p_2^2 + P_3^2 p_3^2 \right] \\
& + \mu_{12} \left[ P_1^2 (p_2^2 + p_3^2) + P_2^2 (p_1^2 + p_3^2) + P_3^2 (p_1^2 + p_2^2) \right] \\
& + \mu_{44} \left[ P_1 P_2 p_1 p_2 + P_2 P_3 p_2 p_3 + P_3 P_1 p_3 p_1 \right] + \beta_1 \left[ \theta_1^2 + \theta_2^2 + \theta_3^2 \right] \\
& + \beta_{11} \left[ \theta_1^4 + \theta_2^4 + \theta_3^4 \right] + \gamma_{11} \left[ P_1^2 \theta_1^2 + P_2^2 \theta_2^2 + P_3^2 \theta_3^2 \right] \\
& + \gamma_{12} \left[ P_1^2 (\theta_2^2 + \theta_3^2) + P_2^2 (\theta_1^2 + \theta_3^2) + P_3^2 (\theta_1^2 + \theta_2^2) \right] \\
& + \gamma_{44} \left[ P_1 P_2 \theta_1 \theta_2 + P_2 P_3 \theta_2 \theta_3 + P_3 P_1 \theta_3 \theta_1 \right] \\
& - \tfrac{1}{2} S_{11} \left[ X_1^2 + X_2^2 + X_3^2 \right] - S_{12} \left[ X_1 X_2 + X_2 X_3 + X_3 X_1 \right] \\
& - \tfrac{1}{2} S_{44} \left[ X_4^2 + X_5^2 + X_6^2 \right] - Q_{11} \left[ X_1 P_1^2 + X_2 P_2^2 + X_3 P_3^2 \right] \\
& - Q_{12} \left[ X_1 (P_2^2 + P_3^2) + X_2 (P_1^2 + P_3^2) + X_3 (P_1^2 + P_2^2) \right] \\
& - Q_{44} \left[ X_4 P_2 P_3 + X_5 P_1 P_3 + X_6 P_1 P_2 \right] - Z_{11} \left[ X_1 p_1 + X_2 p_2 + X_3 p_3 \right] \\
& - Z_{12} \left[ X_1 (p_2^2 + p_3^2) + X_2 (p_1^2 + p_3^2) + X_3 (p_1^2 + p_2^2) \right] \\
& - Z_{44} \left[ X_4 p_2 p_3 + X_5 p_1 p_3 + X_6 p_1 p_2 \right] - R_{11} \left[ X_1 \theta_1^2 + X_2 \theta_2^2 + X_3 \theta_3^2 \right] \\
& - R_{12} \left[ X_1 (\theta_2^2 + \theta_3^2) + X_2 (\theta_1^2 + \theta_3^2) + X_3 (\theta_1^2 + \theta_2^2) \right] \\
& - R_{44} \left[ X_4 \theta_2 \theta_3 + X_5 \theta_1 \theta_3 + X_6 \theta_1 \theta_2 \right]
\end{aligned}
\tag{1}
$$

The coefficients of this energy function are defined in Table I. The energy function
includes all possible ferroelectric and antiferroelectric polarization terms up to the
sixth order, tilt angle terms up to the first fourth order term, and only the first
order coupling terms.

TABLE I

Coefficients of the PZT Energy Function

| | |
|---|---|
| $\alpha_i, \alpha_{ii}, \alpha_{iik}$ | ferroelectric dielectric stiffness at constant stress |
| $\sigma_i, \sigma_{ii}, \sigma_{ik}$ | antiferroelectric dielectric stiffness at constant stress |
| $\mu_{ij}$ | coupling between the ferroelectric and antiferroelectric polarizations |
| $\beta_i, \beta_{ij}$ | octahedral torsion coefficients |
| $\gamma_{ij}$ | coupling between the ferroelectric polarization and tilt angle |
| $s_{ij}$ | elastic compliances at constant polarization |
| $Q_{ij}$ | electrostrictive coupling between the ferroelectric polarization and stress |
| $Z_{ij}$ | electrostrictive coupling between the antiferroelectric polarization and stress |
| $R_{ij}$ | rotostrictive coupling between the tilt angle and stress |

## IV.  SOLUTIONS TO THE ENERGY FUNCTION

Considering zero stress conditions the following solutions to the energy function . (Equation 1) are of interest in the PZT system:

*Paraelectric Cubic (P_C)*

$$P_1 = P_2 = P_3 = 0, \qquad p_1 = p_2 = p_3 = 0, \qquad \theta_1 = \theta_2 = \theta_3 = 0 \qquad (2)$$

*Ferroelectric Tetragonal (F_T)*

$$P_1 = P_2 = 0, \qquad P_3^2 \neq 0, \qquad p_1 = p_2 = p_3 = 0, \qquad \theta_1 = \theta_2 = \theta_3 = 0 \qquad (3)$$

*Ferroelectric Orthorhombic (F_O)*

$$P_1 = 0, \qquad P_2^2 = P_3^2 \neq 0, \qquad p_1 = p_2 = p_3 = 0, \qquad \theta_1 = \theta_2 = \theta_3 = 0 \qquad (4)$$

*Ferroelectric High-temperature Rhombohedral (F_{R(HT)})*

$$P_1^2 = P_2^2 = P_3^2 \neq 0, \qquad p_1 = p_2 = p_3 = 0, \qquad \theta_1 = \theta_2 = \theta_3 = 0 \qquad (5)$$

*Ferroelectric Low-temperature Rhombohedral (F_{R(LT)})*

$$P_1^2 = P_2^2 = P_3^2 \neq 0, \qquad p_1 = p_2 = p_3 = 0, \qquad \theta_1^2 = \theta_2^2 = \theta_3^2 \neq 0 \qquad (6)$$

*Antiferroelectric Orthorhombic (A_O)*

$$P_1 = P_2 = P_3 = 0, \qquad p_1 = 0, \qquad p_2^2 = p_3^2 \neq 0, \qquad \theta_1 = \theta_2 = \theta_3 = 0 \qquad (7)$$

All of these solutions, except for the ferroelectric orthohombic solution. are stable in the PZT system. The ferroelectric orthorhombic solution was also included here, because the coefficients necessary to calculate the energy of this phase can be determined. An independent check of the calculated coefficients can then be made by confirming that this phase is metastable across the PZT system.

Applying these solutions to Equation (1) under zero stress conditions results in the following relations for the energies of each solution:

$$P_C \qquad \Delta G = 0 \tag{8}$$

$$F_T \qquad \Delta G = \alpha_1 P_3^2 + \alpha_{11} P_3^4 + \alpha_{111} P_3^6 \tag{9}$$

$$F_O \qquad \Delta G = 2\alpha_1 P_3^2 + (2\alpha_{11} + \alpha_{12})P_3^4 + 2(\alpha_{111} + \alpha_{112})P_3^6 \tag{10}$$

$$F_{R(HT)} \quad \Delta G = 3\alpha_1 P_3^2 - 3(\alpha_{11} + \alpha_{12})P_3^4 - (3\alpha_{111} - 6\alpha_{112} + \alpha_{123})P_3^6 \quad (11)$$

$$F_{R(LT)} \quad \Delta G = 3\alpha_1 P_3^2 + 3(\alpha_{11} + \alpha_{12})P_3^4 - (3\alpha_{111} + 6\alpha_{112} - \alpha_{123})P_3^6$$

$$+ 3\beta_1\theta_3^2 + 3\beta_{11}\theta_3^4 + 3(\gamma_{,1} - 2\gamma_{12} - \gamma_{44})P_3^2\theta_3^2 \quad (12)$$

$$A_O \quad \Delta G = 2\sigma_1 p_3^2 + (2\sigma_{11} + \sigma_{12})p_3^4 + 2(\sigma_{111} + \sigma_{112})p_3^6 \quad (13)$$

The spontaneous ferroelectric and antiferroelectric polarizations ($P_3$ and $p_3$) and tilt angle ($\theta_3$) in the above equations can be found from the first partial derivative stability conditions ($\partial\Delta G/\partial P_3$, $\partial\Delta G/\partial p_3$, and $\partial\Delta G/\partial\theta_3$) as shown below:

$$F_T \quad \partial\Delta G/\partial P_3 = 0 = 3\alpha_{111}P_3^4 + 2\alpha_{11}P_3^2 - \alpha_1 \quad (14)$$

$$F_O \quad \partial\Delta G/\partial P_3 = 0 = 3(\alpha_{111} - \alpha_{112})P_3^4 - (2\alpha_{11} - \alpha_{12})P_3^2 - \alpha_1 \quad (15)$$

$$F_{R(HT)} \quad \partial\Delta G/\partial P_3 = 0 = (3\alpha_{111} - 6\alpha_{112} + \alpha_{123})P_3^4$$

$$+ 2(\alpha_{11} - \alpha_{12})P_3^2 + \alpha_1 \quad (16)$$

$$F_{R(LT)} \quad \partial\Delta G/\partial P_3 = 0 = (3\alpha_{111} + 6\alpha_{112} + \alpha_{123})P_3^4$$

$$+ 2(\alpha_{11} + \alpha_{12})P_3^2 + \alpha_1 + \gamma_{11}\theta_3^2 \quad (17)$$

$$\partial\Delta G/\partial\theta_3 = 0 = \beta_1 + 2\beta_{11}\theta_3^2 + \gamma_{11}P_3^2 \quad (18)$$

$$A_O \quad \partial\Delta G/\partial p_3 = 0 = 3(\sigma_{111} - \sigma_{112})p_3^4 + (2\sigma_{11} + \sigma_{12})p_3^2 + \sigma_1 \quad (19)$$

The polarizations and tilt angle can be calculated by solving these quadratic equations. Equations (9)–(19) relate the energies of each solution to the coefficients of the energy function. Thus by determining these coefficients, the energies of each phase can be calculated.

## V. SPONTANEOUS ELASTIC STRAINS

The spontaneous elastic strains $x_i$ ( $\partial\Delta G/\partial X_i$) under zero stress conditions can be derived from Equation (1) as follows.

$$P_C \quad x_1 = x_2 = x_3 = x_4 = x_5 = x_6 = 0 \quad (20)$$

$$F_T \quad x_1 = x_2 = Q_{12}P_3^2, \quad x_3 = Q_{11}P_3^2, \quad x_4 = x_5 = x_6 = 0 \quad (21)$$

$$F_O \quad x_1 = 2Q_{12}P_3^2, \quad x_2 = x_3 = (Q_{11} + Q_{12})P_3^2,$$

$$x_4 = Q_{44}P_3^2, \quad x_5 = x_6 = 0 \quad (22)$$

$$F_{R(HT)} \quad x_1 = x_2 = x_3 = (Q_{11} + 2Q_{12})P_3^2, \quad x_4 = x_5 = x_6 = Q_{44}P_3^2 \quad (23)$$

$$F_{R(LT)} \quad x_1 = x_2 = x_3 = (Q_{11} + 2Q_{12})P_3^2 + (R_{11} + 2R_{12})\theta_3^2,$$

$$x_4 = x_5 = x_6 = Q_{44}P_3^2 + R_{44}\theta_3^2 \quad (24)$$

$$A_O \quad x_1 = 2Z_{12}p_3^2, \quad x_2 = x_3 = (Z_{11} + Z_{12})p_3^2,$$

$$x_4 = Z_{44}p_3^2, \quad x_5 = x_6 = 0 \quad (25)$$

In the next three papers of this series[10-12] these spontaneous strain relations will be shown to be very important in determining the coefficients of the energy function. Spontaneous strain data will be determined from x-ray diffraction of PZT powders, and used with the electrostrictive constants to calculate the spontaneous polarization, which is needed to determine coefficients of the energy function.

## VI. DIELECTRIC PROPERTIES

Relations for the relative dielectric stiffnesses $\chi_{ij}$ $(= \partial^2 \Delta G / \partial P_i \partial P_j)$ were derived from Equation (1) for the six solutions:

$$P_C \qquad \chi_{11} = \chi_{22} = \chi_{33} = 2\varepsilon_0\alpha_1, \qquad \chi_{12} = \chi_{23} = \chi_{31} = 0 \tag{26}$$

$$F_T \qquad \chi_{11} = \chi_{22} = 2\varepsilon_0[\alpha_1 - \alpha_{12}P_3^2 - \alpha_{112}P_3^4],$$

$$\chi_{33} = 2\varepsilon_0[\alpha_1 + 6\alpha_{11}P_3^2 + 15\alpha_{111}P_3^4], \qquad \chi_{12} = \chi_{23} = \chi_{31} = 0 \tag{27}$$

$$F_O \qquad \chi_{11} = 2\varepsilon_0[\alpha_1 + 2\alpha_{12}P_3^2 + (2\alpha_{112} + \alpha_{123})P_3^4],$$

$$\chi_{22} = \chi_{33} = 2\varepsilon_0[\alpha_1 + (6\alpha_{11} + \alpha_{12})P_3^2 + (15\alpha_{111} + 7\alpha_{112})P_3^4],$$

$$\chi_{12} = \chi_{31} = 0, \qquad \chi_{23} = 4\varepsilon_0[\alpha_{12}P_3^2 + 4\alpha_{112}P_3^4] \tag{28}$$

$$F_{R(HT)} \quad \chi_{11} = \chi_{22} = \chi_{33} = 2\varepsilon_0[\alpha_1 + (6\alpha_{11} + 2\alpha_{22})P_3^2$$

$$+ (15\alpha_{111} + 14\alpha_{112} + \alpha_{123})P_3^4,$$

$$\chi_{12} = \chi_{23} = \chi_{31} = 4\varepsilon_0[\alpha_{12}P_3^2 + (4\alpha_{112} + \alpha_{123})P_3^4] \tag{29}$$

$$F_{R(LT)} \quad \chi_{11} = \chi_{22} = \chi_{33} = 2\varepsilon_0[\alpha_1 + (6\alpha_{11} + 2\alpha_{12})P_3^2$$

$$+ (15\alpha_{111} + 14\alpha_{112} + \alpha_{123})P_3^4 + (\gamma_{11} - 2\gamma_{12})\theta_3^2],$$

$$\chi_{12} = \chi_{23} = \chi_{31} = 4\varepsilon_0[\alpha_{12}P_3^2 + (4\alpha_{112} + \alpha_{123})P_3^4 + \gamma_{44}\theta_3^2] \tag{30}$$

$$A_O \qquad \chi_{11} = 2\varepsilon_0[\alpha_1 + 2\mu_{12}p_3^2], \quad \chi_{22} = \chi_{33} = 2\varepsilon_0[\alpha_1 + (\mu_{11} + \mu_{12})p_3^2],$$

$$\chi_{12} = \chi_{31} = 0, \quad \chi_{23} = \varepsilon_0\mu_{44}p_3^2 \tag{31}$$

The multiplication by permittivity of free space $\varepsilon_0$ in these equations was required to convert from absolute to relative dielectric stiffnesses. Equations (26)–(31) can be used to calculate the relative dielectric stiffnesses for each phase based on the original cubic axes.

In the orthorhombic state the polarization can be along any of the (110) directions of the original cubic axes. The polarization of the rhombohedral state can be along any of the (111) directions. By rotating these axes so that for both states the new $x_3$ axis is along the polar directions, diagonalized matrices will result. The new dielectric stiffness coefficients (indicated by a prime) can be related to the old coefficients [defined by equations (28)–(31)] with the following relations:

$$F_O \text{ and } A_C \qquad \chi_{11}' = \chi_{11}, \qquad \chi_{22}' = \chi_{33} - \chi_{23} \tag{32}$$

$$\chi_{33}' = \chi_{33} + \chi_{23}, \qquad \chi_{12}' = \chi_{23}' = \chi_{31}' = 0$$

$F_{R(HT)}$ and $F_{R(LT)}$     $\chi'_{11} = \chi'_{22} = \chi_{11} - \chi_{12}$,     $\chi'_{33} = \chi_{11} - 2\chi_{12}$

$$\chi'_{12} = \chi'_{23} = \chi'_{31} = 0 \tag{33}$$

These equations can be used to calculate the dielectric stiffnesses of the orthorhombic and rhombohedral phases parallel and perpendicular to the polar axes.

The dielectric susceptibility coefficients ($\eta_{ij}$) can be determined from the reciprocal of the dielectric stiffness matrices ($\chi_{ij}$) using the following relation:[30]

$$\eta_{ij} = A_{ji}/\Delta. \tag{34}$$

where $A_{ji}$ and $\Delta$ are the cofactor and determinant of the $\chi_{ij}$ matrix. Using this relation results in the following relations for the dielectric susceptibility coefficients ($\eta_{ij}$):

$P_C$             $\eta_{11} = \eta_{22} = \eta_{33} = 1/\chi_{11}$,   $\eta_{12} = \eta_{23} = \eta_{31} = 0$          $(35)$

$F_T$             $\eta_{11} = \eta_{22} = 1/\chi_{11}$,   $\eta_{33} = 1/\chi_{33}$          $(36)$

$F_O$ and $A_O$          $\eta_{11} = 1/\chi_{11}$,   $\eta_{22} = \eta_{33} = \chi_{33}/(\chi_{33}^2 - \chi_{23}^2)$,

$$\eta_{12} = \eta_{31} = 0,   \eta_{23} = -\chi_{23}/(\chi_{33}^2 - \chi_{23}^2) \tag{37}$$

$$\eta'_{11} = 1/\chi'_{11},   \eta'_{22} = 1/\chi'_{22},   \eta'_{33} = 1/\chi'_{33}$$

$$\eta'_{12} = \eta'_{23} = \eta'_{31} = 0 \tag{38}$$

$F_{R(HT)}$ and $F_{R(LT)}$   $\eta_{11} = \eta_{22} = \eta_{33} = (\chi_{11}^2 - \chi_{12}^2)/(\chi_{11}^3 - 3\chi_{11}\chi_{12}^2 + 2\chi_{12}^3)$

$$\eta_{12} = \eta_{23} = \eta_{31} = (\chi_{12}^2 - \chi_{11}\chi_{12})/(\chi_{11}^3 - 3\chi_{11}\chi_{12}^2 - 2\chi_{12}^3)$$

$$\eta'_{11} = \eta'_{22} = 1/\chi'_{11},   \eta'_{33} = 1/\chi'_{33} \tag{39}$$

$$\eta'_{12} = \eta'_{23} = \eta'_{31} = 0 \tag{40}$$

These equations can be used to calculate the dielectric susceptibilities of each phase from the coefficients of the energy function.

## VII. PIEZOELECTRIC PROPERTIES

Relations for the piezoelectric $b_{ij}$ coefficients ($= \partial^2 \Delta G/\partial P_i \partial X_j$) were derived from Equation (1) for the tetragonal and rhombohedral states as shown below:

$F_T$                    $b_{33} = 2Q_{11}P_3$,   $b_{31} = b_{32} = 2Q_{12}P_3$,

$$b_{15} = b_{24} = Q_{44}P_3,   b_{11} = b_{12} = b_{13} = b_{14} = b_{16} = 0.$$

$$b_{21} = b_{22} = b_{23} = b_{25} = b_{26} = b_{34} = b_{35} = b_{36} = 0 \tag{41}$$

$F_{R(HT)}$ and $F_{R(LT)}$   $b_{11} = b_{22} = b_{33} = 2Q_{11}P_3$,   $b_{14} = b_{25} = b_{26} = 0$

$$b_{12} = b_{13} = b_{21} = b_{23} = b_{31} = b_{32} = 2Q_{12}P_3,$$

$$b_{15} = b_{16} = b_{24} = b_{26} = b_{34} = b_{35} = Q_{44}P_3, \tag{42}$$

Since a coupling term of type $X_tP_t\theta_t$ was not included in Equation (1), the $b_t$ relations [Equation (42)] for the high and low temperature rhombohedral phases are of the same form. However, the spontaneous polarizations $P_3$ are defined by different relations for the high and low temperature rhombohedral phases, and thus different values would result for these coefficients.

The piezoelectric $d_{ij}$ coefficients are defined by Reference 40:

$$d_{ij} = b_{kj}\eta_{ik} \tag{43}$$

Using this relation for the tetragonal and rhombohedral states results in the following relations:

$F_T$
$$d_{33} = 2\varepsilon_0\eta_{33}Q_{11}P_3, \quad d_{31} = d_{32} = 2\varepsilon_0\eta_{33}Q_{12}P_3,$$

$$d_{15} = d_{24} = \varepsilon_0\eta_{11}Q_{44}P_3, \quad d_{11} = d_{12} = d_{13} = d_{14} = d_{16} = 0,$$

$$d_{21} = d_{22} = d_{23} = d_{25} = d_{26} = d_{34} = d_{35} = d_{36} = 0 \tag{44}$$

$F_{R(HT)}$ and $F_{R(LT)}$
$$d_{11} = d_{22} = d_{33} = 2\varepsilon_0(\eta_{11}Q_{11} + 2\eta_{12}Q_{12})P_3,$$

$$d_{12} = d_{13} = d_{21} = d_{23} = d_{31} = d_{32}$$

$$= 2\varepsilon_0[\eta_{11}Q_{12} + \eta_{12}(Q_{11} + Q_{12})]P_3,$$

$$d_{14} = d_{25} = d_{36} = 2\varepsilon_0\eta_{12}Q_{44}P_3,$$

$$d_{15} = d_{16} = d_{24} = d_{26} = d_{34} = d_{35} = \varepsilon_0(\eta_{11} + \eta_{12})Q_{44}P_3, \tag{45}$$

The multiplication by the permittivity of free space $\varepsilon_0$ in these three equations was required to convert the dielectric susceptibilities from relative to absolute. Equations (41), (42), (44), and (45) can be used to calculate the piezoelectric $b_{ij}$ and $d_{ij}$ coefficients of the tetragonal and rhombohedral phases from the coefficients of the energy function.

## VII. SUMMARY

The applications of compositions of the PZT solid solution system as piezoelectric transducers, pyroelectric detectors, electro-optic devices, and explosively induced charge storage devices were described in the introduction to demonstrate the technological importance of PZT. These applications use PZT in polycrystalline ceramic form, and thus the properties of these ceramics are well established in the literature. However, the mechanisms contributing to these outstanding polycrystalline properties of PZT are not well understood, because of the complexity of the interactions within the polycrystalline material.

A first step in the analysis of a ferroelectric polycrystalline material is to separate the intrinsic and extrinsic contributions to the properties. The intrinsic contributions result from the averaging of the single-domain single-crystal properties, while the extrinsic contributions arise from the interactions at grain or phase boundaries and from the domain wall or thermal defect motions. Unfortunately, due to the difficulty of growing good quality single crystals of PZT, very little single crystal data is

available. Thus the goal of this project was to develop a thermodynamic phenomenological theory to calculate the single-domain properties of PZT This theory could then be used to separate the intrinsic and extrinsic contributions to the polycrystalline properties. In addition there are several other applications of this theory, which will be in the last paper of this series.[13]

A two-sublattice theory, where each sublattice has a separate polarization, was used to account for the ferroelectric and antiferroelectric phases of the PZT system. An additional order parameter was also included to account for the tilting of the oxygen octahedra in the low-temperature rhombohedral phase. The resulting energy function can be used to model the phase transitions and single-domain properties of the PZT system. Solutions to this energy function were used to derive relations for the energies: spontaneous polarizations, strains, and tilt angles, and dielectric and piezoelectric properties corresponding to the different phases in the PZT system.

The coefficients needed to calculate the energies and properties of the solutions will be determined in the next three papers in this series.[10-12] Theoretical calculations and comparisons with experimental data will then be presented in the final paper of this series.[13] Additional details of this theory, including tables of all the experimental data collected, can be found in Reference 41.

REFERENCES

1  B Jaffe. W J Cook and J Jaffe. Piezoelectric Ceramics (Academic Press, London, 1971)
2. R. W Whatmore and A. M. Glazer. J Phys C Solid State Phys , 12, 1505 (1979)
3  A. Kumada. Jpn J Appl Phys , 24 (Suppl 24-2), 739 (1985)
4  K. Uchino. Bull. Amer Ceram Soc , 65, 647 (1986)
5  H. Takeuchi. S. Jyomura and C. Nakaya. Jpn J Appl. Phys , 24 (Suppl 24-2) 36 (1985)
6  M J Haun. E. Furman. S. J Jang and L E. Cross. Trans. IEEE Ultrasonics, Ferroelectrics and Frequency Control Soc.. 36, 393 (1989)
7  R. Clarke. A. M. Glazer. F W Ainger. D Appleby. N J Poole and S G Porter. Ferroelectrics. 11, 359 (1976).
8  G. H. Haertling and C. E. Land. J Amer Ceram. Soc , 54, 1 (1971)
9  R. Clarke and R. W Whatmore. J of Crystal Growth. 33, 29 (1976).
10  M. J Haun. E. Furman. H. A. McKinstry and L. E. Cross. "Thermodynamic Theory of the Lead Zirconate-Titanate Solid Solution System. Part II. Tricritical Behavior." Ferroelectrics will be published together with this paper.
11  M. J. Haun. Z. Q. Zhuang. E. Furman. S. J. Jang and L. E. Cross. 'Thermodynamic Theory of the Lead Zirconate-Titanate Solid Solution System. Part III. Curie Constant and Sixth-Order Polarization Interaction Dielectric Stiffness Coefficients." Ferroelectrics will be published together with this paper.
12  M J Haun. E. Furman. T. R. Halemane and L E. Cross. 'Thermodynamic Theory of the Lead Zirconate-Titanate Solid State Solution System. Part IV Tilting of the Oxygen Octahedra. Ferroelectrics will be published together with this paper.
13  M. J Haun. E. Furman. S. J Jang and L. E. Cross. "Thermodynamic Theory of the Lead Zirconate-Titanate Solid Solution System. Part V Theoretical Calculations." Ferroelectrics will be published together with this paper
14  V A. Isupov. Fizika Tverdogo Tela. 12, 1380 (1970) [Soviet Physics—Solid State. 12, 1084 (1970)]
15  K. Carl and K. H. Hardtl. Phys. Stat. Sol (a). 8, 87 (1971).
16  V A. Isupov. Fizika Tverdogo Tela. 18, 92 (1976) [Soviet Physics—Solid State. 18, 529 (1976)]
17  V. A. Isupov. Ferroelectrics. 12, 141 (1976).
18. V A. Isupov. Fizika Tverdogo Tela. 19, 1347 (1977) [Soviet Physics–Solid State. 19, 783 (1977)
19  W Wersing. Proceedings 4th Int. Meeting Electro- and Magnetoceramics (1981) pp 162-182.
20. W Wersing. Ferroelectrics. 37, 611 (1981)
21. W Wersing. Ferroelectrics. 54, 207 (1984)

22  A  Amin. *Phenomenological and Structural Studies of Lead Zirconate-Titanate Piezoceramics*. Ph D Thesis in Solid State Science. The Pennsylvania State University (1979)

23  A  Amin. L. E. Cross and R  E  Newnham. *Ferroelectrics*. 37, 647 (1981)

24  A  Amin. M  J  Haun. B. Badger. H  A. McKinstry and L  E  Cross. *Ferroelectrics*. 65, 107 (1985)

25  T  R. Halemane. M  J  Haun. L. E  Cross and R. E. Newnham. *Ferroelectrics*. 62 149 (1985)

26  T  R  Halemane. M. J. Haun. L. E. Cross and R  E  Newnham. *Jpn. J  App  Phys*. 24 (Suppl 24-2). 212 (1985)

27  T  R. Halemane. M. J  Haun. L. E. Cross and R. E  Newnham. *Ferroelectrics*. 70, 153 (1986)

28  M. J  Haun. T  R. Halemane. R. E. Newnham and L. E. Cross. *Jpn. J  App. Phys* . 24 (Suppl 24-2). 209 (1985).

29  R. Clarke and A. M. Glazer. *Ferroelectrics*. 14, 695 (1976).

30  R. W  Whatmore. R. Clarke and A. M. Glazer. *J  Phys. C.Solid State Phys* . 11, 3089 (1978)

31. K. Roleder and J  Handerek. *Phase Transitions*. 2, 285 (1982).

32. Z  Q  Zhuang. M. J  Haun. S. J  Jang and L  E. Cross. *Proceedings of the 6th IEEE International Symposium on the Applications of Ferroelectrics*. Lehigh. PA. edited by Van Wood (IEEE. New York. 1986) pp 394-397

33  M. J  Haun. Y  H  Lee. H  A  McKinstry and L  E  Cross. *Advances in X-ray Analysis. Vol  30*. edited by C  S  Barrett. J  V  Gilfrich. R. Jenkins. D  E  Leyden. J  C  Russ and P  K  Predecki (Plenum Press. New York. 1987) pp 473-481

34  M  J  Haun. Z  Q  Zhuang. S. J  Jang. H  A  McKinstry and L  E. Cross. *Proceedings of the 6th IEEE International Symposium on the Applications of Ferroelectrics*. Lehigh. PA. edited by Van Wood (IEEE. New York. 1986) pp. 398-401

35  M  J  Haun. E. Furman. S. J. Jang. H. A. McKinstry and L. E. Cross. *J  Appl. Phys*  62, 333 (1987).

36  J  N  Kim. M. J  Haun. S. J  Jang. L  E. Cross and X. R. Xue. *Trans. IEEE Ultrasonics. Ferroelectrics and Frequency Control Soc*. 36, 389 (1989).

37  M. J  Haun. T  J  Harvin. M. T  Lanagan. Z. Q  Zhuang. S  J  Jang and L  E  Cross. *J  Appl  Phys*  65, 3173 (1989)

38  L. E. Cross. *Phil Mag.*. 1, 76 (1956)

39  J  F  Nye. *Physical Properties of Crystals*. (University Press. Oxford. 1957). p  156

40  A. F  Devonshire. *Phil. Mag* . 42. 1065 (1951)

41  M  J  Haun. *Thermodynamic Theory of the Lead Zirconate-titanate Solid Solution System*. Ph  D thesis in Solid State Science. The Pennsylvania State University (1988)

APPENDIX 25

# THERMODYNAMIC THEORY OF THE LEAD ZIRCONATE-TITANATE SOLID SOLUTION SYSTEM, PART II: TRICRITICAL BEHAVIOR

M. J. HAUN,† E. FURMAN,‡ H. A. McKINSTRY and L. E. CROSS

*Materials Research Laboratory, The Pennsylvania State University, University Park, PA 16802, USA*

Two tricritical points, where a phase transition changes from first to second order, were found to occur in the lead zirconate-titanate (PZT) solid solution system. High-temperature x-ray diffraction data on sol-gel derived PZT powders were used to calculate the cell parameters and spontaneous strain in the ferroelectric phases. These data were used with addition data from the literature to determine values of the higher-order dielectric stiffness coefficients, which were then used to locate the tricritical points. The values of the coefficients are also needed in the development of a thermodynamic theory of the PZT system.

## I. INTRODUCTION

Tricritical behavior, where a phase transition changes from first to second order, has been shown to occur in the lead zirconate-titanate (PZT) solid solution system.[1-4] The end members lead titanate ($PbTiO_3$) and lead zirconate ($PbZrO_3$) both have well defined first-order phase transitions from a paraelectric cubic phase at high temperatures to ferroelectric tetragonal and rhombohedral phases, respectively, at lower temperatures. By forming a solid solution between these first-order end members a second-order transition region develops in the middle of the phase diagram.[4]

The degree of first order behavior has been shown to decrease from lead zirconate to the PZT 94/6 (94% PZ and 6% PT) composition, where a tricritical point occurs and the transition changes to second order.[1,2] With increasing titanium content the second order transition region was found to extend from the tricritical point over to the PZT 88/12 composition.[2] Since lead titanate has a first order transition, a second tricritical point should occur between the PZT 88/12 and lead titanate compositions.

To provide additional data to locate the second tricritical point, pure homogeneous sol-gel derived powders were prepared for several PZT compositions.[5] The lattice parameters of these compositions were determined from high-temperature x-ray diffraction, and used to calculate the spontaneous strain.[6] By using these data to determine the higher order dielectric stiffness coefficients, the second-order

---

transition region was found to extend over to the morphotropic boundary between the tetragonal and rhombohedral phases.[4]

In this paper additional data will be presented to show that the second tricritical point occurs in the tetragonal phase field. The compositional dependence of the higher-order dielectric stiffness coefficients will be determined from high-temperature x-ray diffraction data, and used to locate the tricritical points. Values of the dielectric stiffness coefficients are also needed in the development of a thermodynamic theory to model the phase transitions and single-domain properties of the entire PZT system.[7-10]

In the next section experimental high-temperature x-ray diffraction data will be presented. This data will be used to calculate the spontaneous polarization for tetragonal and rhombohedral compositions in Sections III and IV, respectively. This polarization data will then be used to determine the higher-order dielectric stiffness coefficients, and to establish the location of the tricritical points. In Section V the morphotropic boundary will be used to complete the evaluation of these coefficients, followed by a summary of this paper in Section VI.


## II.   HIGH-TEMPERATURE X-RAY DIFFRACTION

High-temperature x-ray diffraction was used to determine the cell parameters of sol-gel derived lead titanate and PZT powders. The lead titanate data was previously presented in Reference 11, and used to develop a thermodynamic theory of lead titanate. X-ray data on PZT 90/10, 80/20, 70/30 and 60/40 were previously presented in Reference 6. In this section high-temperature x-ray diffraction data on sol-gel derived powder of PZT 32/68 will be presented. The sol-gel procedure used to prepare this powder was described in Reference 5. The x-ray diffractometer setup and data analysis procedure that were used were described in References 6 and 11.

The splitting of the 002/200 and 123/312/321 peaks for the PZT 32/68 composition are shown in Figure 1. These x-ray data were used to calculate the cell constants using the Cohen least-squares refinement method[12] as shown in Figure 2. The data in these figures indicate that the transition from cubic to tetragonal in the PZT 32/68 composition is either second order, or only slightly first order. This is more obvious when plotting the cell volume ($=a_T^2 c_T$) versus temperature as shown in Figure 3. A continuous change in the volume would indicate that the transition is second order. Additional data will be presented later in this paper to show that the cubic to tetragonal phase transition in PZT 32/68 is probably second order.

The spontaneous strains $x_1$ and $x_3$ can be calculated from the tetragonal cell constants $a_T$ and $c_T$ using the following relations:

$$x_1 = \frac{a_T - a'_C}{a'_C} \qquad x_3 = \frac{c_T - a'_C}{a'_C} \tag{1}$$

$a'_C$ is the cubic cell length extrapolated into the tetragonal region.

Different procedures have been used to calculate the spontaneous strains, depending on the procedure used to determine $a'_C$. Haun et al.[11] extrapolated the cubic cell constant into the tetragonal region by assuming that the electrostrictive
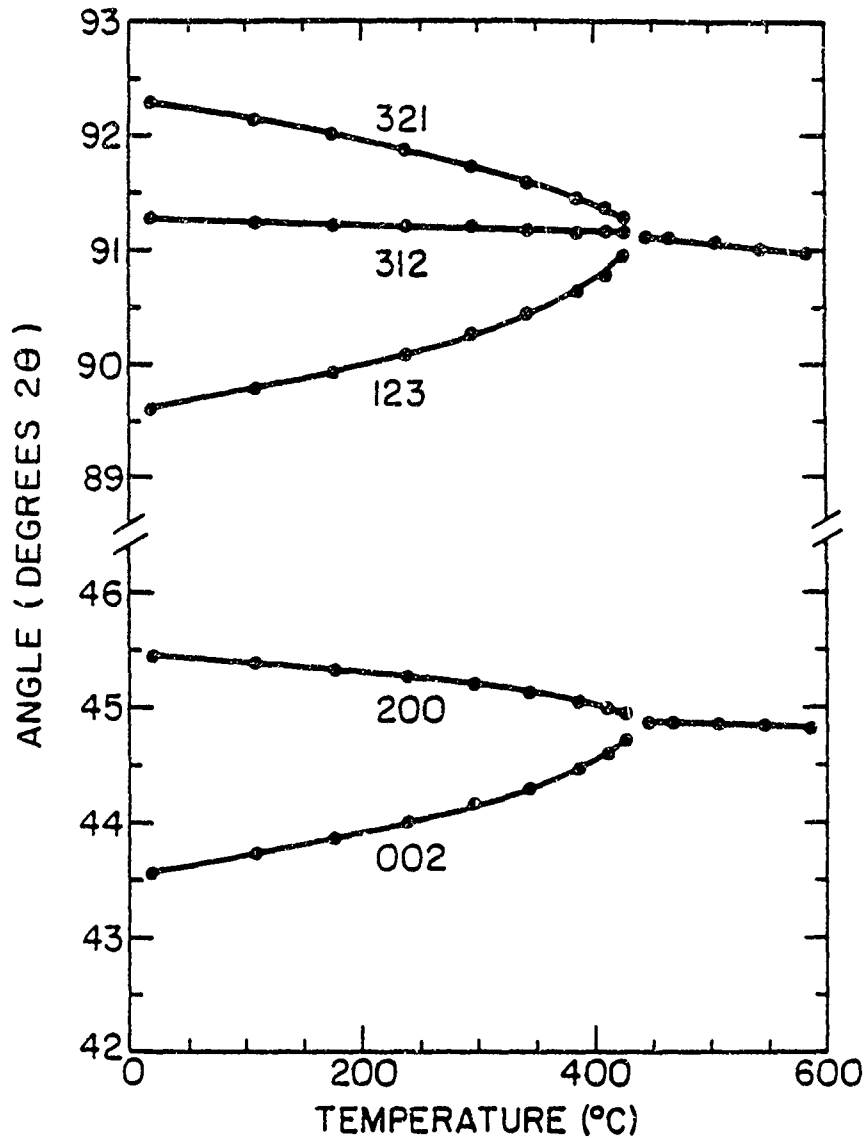
FIGURE 1 The angles of the 002/200 and 123/312/321 diffraction peaks of PZT 32.68 plotted versus temperature.

ratio $Q_{11}/Q_{12}$ is independent of temperature, which is a fairly good assumption in PZT.[13] This ratio can be determined from the ratio of the spontaneous strains $x_1$ and $x_3$ from Equation (21) in Reference 7:

$$\frac{x_3}{x_1} = \frac{Q_{11}}{Q_{12}} \tag{2}$$

If the $Q_{11}/Q_{12}$ ratio is known, then $a_C'$ can be determined by combining Equations (1) and (2):

$$a_C' = \frac{c_T - (Q_{11}/Q_{12})a_T}{1 - Q_{11}/Q_{12}} \tag{3}$$

By determining the $Q_{11}/Q_{12}$ ratio, $a_C'$ can be calculated and used with the cell
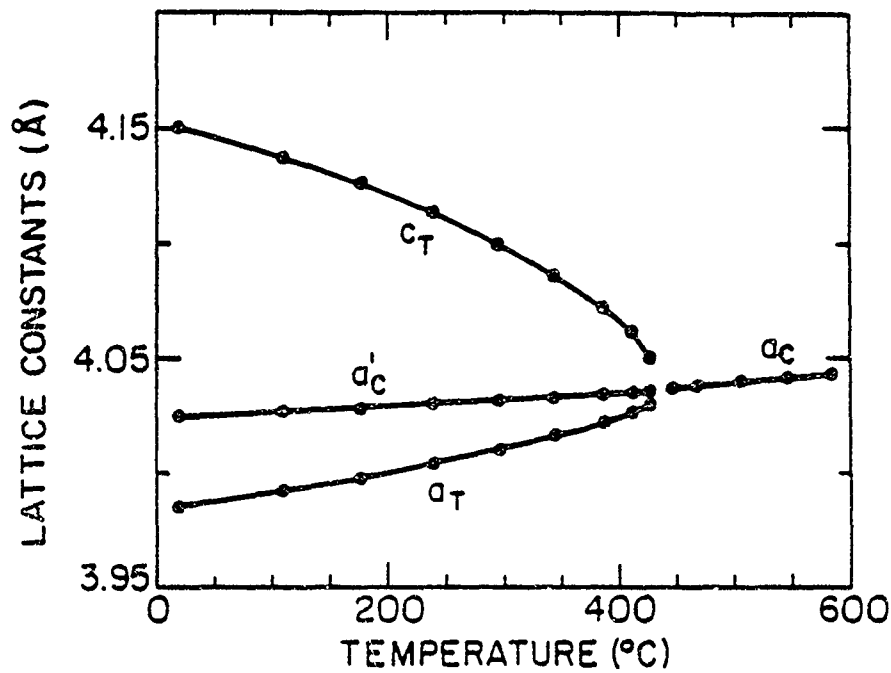
FIGURE 2  The lattice constants of PZT 32/68 plotted versus temperature. $a_T$ and $c_T$ are the lattice constants of the tetragonal structure. $a_c$ and $a_c$ are the lattice constants of the cubic structure above $T_c$ and extrapolated into the tetragonal region, respectively

constants to calculate the spontaneous strains. Haun et al.[11] used a procedure of extrapolating the cubic cell constant $a_c$ data to below the transition to calculate the $Q_{11}$ $Q_{12}$ ratio for PbTiO$_3$. Due to the second order transition behavior of the PZT 32/68 composition, this procedure was not possible. However, the electrostrictive constants of PZT have been recently approximated from a combination of single-crystal and polycrystalline data.[13] A value of $-3.166$ for the $Q_{11}$ $Q_{12}$ ratio
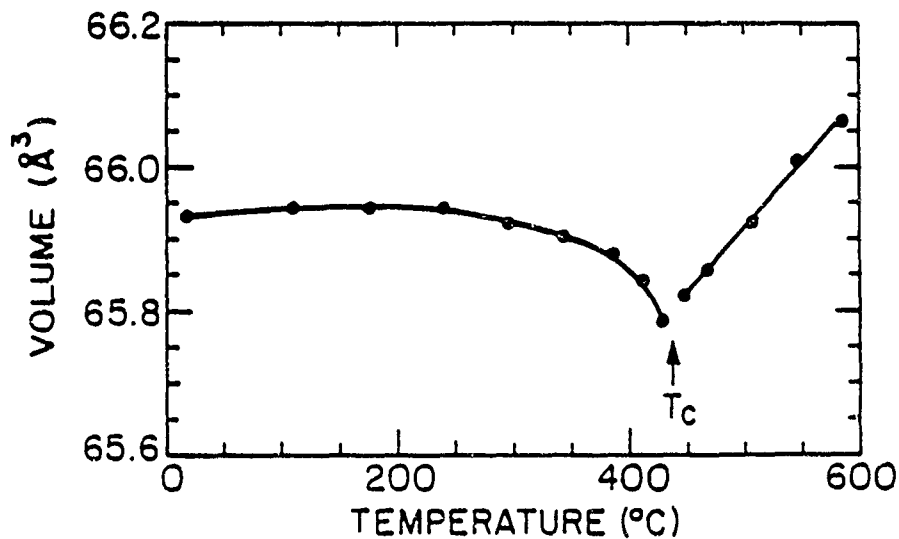


FIGURE 3  The unit cell volume of PZT 32/68 plotted versus temperature.

was determined for the PZT 32/68 composition.[13] This value was used in Equation (3) to calculate $a_C'$ as shown by the data plotted in Figure 2.

The spontaneous strains $x_1$ and $x_3$ were then calculated for the PZT 32/68 composition from the data in Figure 2 using Equation 1. The results are shown in Figure 4, along with the lead titanate strain data from Reference 11. The numerical values of these data are listed in Reference 14. These strain data will be used in the next section with the electrostrictive constants to calculate the spontaneous polarization, which will then be used to determine the higher-order dielectric stiffness coefficients.

## II.  TETRAGONAL COMPOSITIONS

All of the dielectric stiffness coefficients in the PZT energy function [Equation (1) in Reference 7] were assumed to be independent of temperature, except the dielectric stiffness constant $\alpha_1$ which was given a linear temperature dependence based on the Curie-Weiss law:

$$\alpha_1 = \frac{T - T_0}{2\,\varepsilon_0 C} \tag{4}$$

$C$ is the Curie constant, $\varepsilon_0$ is the permittivity of free space, and $T_0$ is the Curie-Weiss temperature. By finding values of $T_0$ and $C$, $\alpha_1$ can be calculated as a function of temperature.

The simplest and usual method of finding values of $T_0$ and $C$ is to fit the inverse of the dielectric constant in the paraelectric state using the Curie-Weiss law. Un-
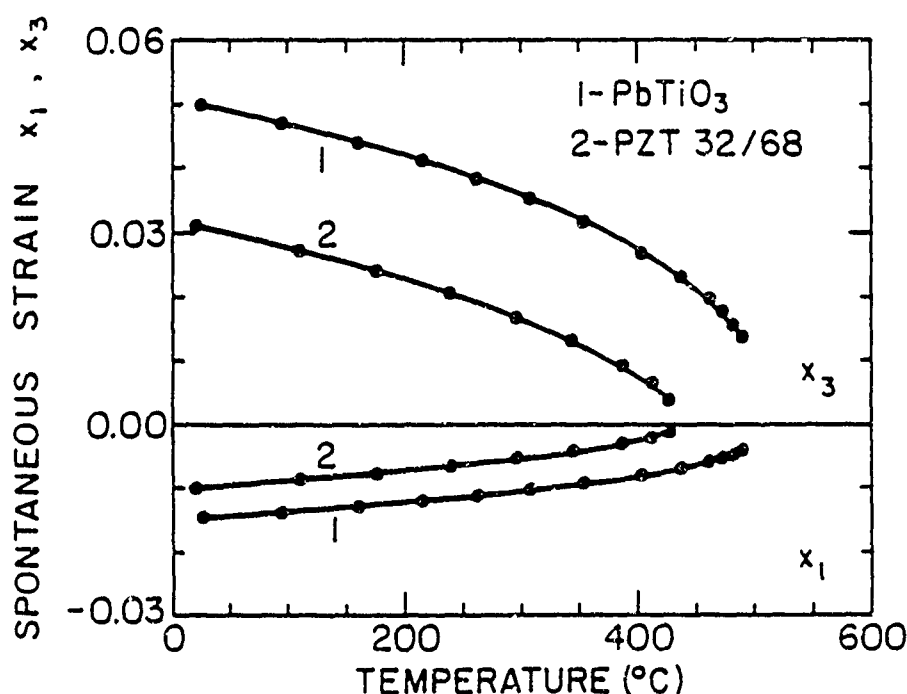


FIGURE 4   The spontaneous strains $x_1$ and $x_3$ plotted versus temperature for PbTiO. and PZT 32/68 The data points were calculated from the lattice constant data shown in Figure 2.

fortunately. very little dielectric data on PZT in the high temperature cubic state exists. due to the lack of good quality single crystals. Measurements on polycrystalline ceramic samples typically give similar values of $T_0$ and $C$ as single crystals. but these measurements are difficult in pure PZT due to the large electrical conductivity at high temperatures. In addition. considerable discrepancies exist in the measurements that have been made. For these reasons indirect methods were used to determine $T_0$ and $C$. $T_0$ will be determined by fitting spontaneous strain data as described later in this section. $C$ will be obtained from low-temperature dielectric data in the third paper of this series.[8]

The Curie constant acts as a scaling constant in the dielectric properties and energies of the phases. The dielectric stiffness coefficients are inversely proportional to the Curie constant. as shown in Equation (4) for $\alpha_1$. However. the spontaneous polarization. strain. and tilt angle are all independent of the Curie constant. Since the Curie constant was not known at this point. new constants were formed by multiplying the dielectric stiffness coefficients by the Curie constant. These new constants can be determined from the spontaneous polarization data independently of the Curie constant. Equation (4) then becomes:

$$\alpha_1 C = \frac{T - T_0}{2\varepsilon_0} \tag{5}$$

Now if $T_0$ can be determined. then the new constant $\alpha_1 C$ can be calculated.

The spontaneous polarization of the tetragonal state can be related to the dielectric stiffness coefficients by solving the quadratic relation formed from the first partial derivative stability condition [Equation (14) in Reference 7]:

$$P_3^2 = \frac{-\alpha_{11} = [\alpha_{11}^2 - 3\alpha_1\alpha_{111}]^{1\,2}}{3\alpha_{111}} \tag{6}$$

Only the solution involving a positive term in Equation (6) is considered here. because this solution corresponds to a free energy minimum. while the other solution corresponds to a maximum of the free energy.

Multiplying the numerator and denominator of Equation (6) by the Curie constant results in the following expression which relates $P_3$ to the new $\alpha_1 C$. $\alpha_{11} C$. and $\alpha_{111} C$ constants:

$$P_3^2 = \frac{-\alpha_{11}C + [(\alpha_{11}C)^2 - 3\alpha_1 C\,\alpha_{111}C]^{1\,2}}{3\alpha_{111}C} \tag{7}$$

If the cubic-tetragonal transition is second order then $T_0 = T_C$. and the following relation results from Equations (5) and (7):

$$P_3^2 = a\{1 - [1 - b(T - T_C)]^{1\,2}\}.$$

where $a = -\alpha_{11}C/(3\alpha_{111}C)$. and $b = 3\alpha_{111}C\,[2\varepsilon_0\,(\alpha_{11}C)^2] \tag{8}$

The $a$ and $b$ relations can also be rearranged in terms of the $\alpha_{11}C$ and $\alpha_{111}C$ constants:

$$\alpha_{11}C = -1/(2\varepsilon_0\,Cab) \qquad \alpha_{111}C = 1/(6\varepsilon_0 Ca^2 b) \tag{9}$$

Since $\alpha_{11}C$ and $\alpha_{111}C$ are assumed to be independent of temperature, $a$ and $b$ will also be independent of temperature. It can be deduced from equation (8) that for a second order transition the spontaneous polarization $P_3$ vanishes at the transition temperature $T_C$.

The spontaneous strains $x_1$ and $x_3$ of the tetragonal state are related to $P_3$ through the electrostrictive coefficients [see Equation (21) in Reference 7]. By substituting Equation (8) into Equation (21) from Reference 7 the following relations result:

$$x_1 = aQ_{12}\left\{1 - [1 - b(T - T_C)]^{1/2}\right\} \tag{10}$$

$$x_3 = aQ_{11}\left\{1 - [1 - b(T - T_C)]^{1/2}\right\} \tag{11}$$

These equations can be used to fit the tetragonal strain data, if the cubic-tetragonal transition is second order.

If the cubic-tetragonal transition is first order, then $T_0 = T_C$, and the spontaneous polarization changes discontinuously at the transition. At $T_C$ two relations must be satisfied:

$$0 = \alpha_{1C} + \alpha_{11}\ P_{3C}^2 + \alpha_{111}\ P_{3C}^4 \tag{12}$$

$$0 = \alpha_{1C} + 2\alpha_{11}\ P_{3C}^2 + 3\alpha_{111}\ P_{3C}^4 \tag{13}$$

where $\alpha_{1C}$ and $P_{3C}$ are $\alpha_1$ and $P_3$ at $T_C$. Equation (12) was derived from the requirement that the $\Delta G$'s of the cubic and tetragonal phases [Equations (8) and (9) in Reference 7] must be equal at $T_C$. Equation (13) is the first partial derivative stability condition [Equation (14) in Reference 7] at $T_C$, which must be satisfied so that the stable state corresponds to the minima of the energy function.

From Equation (4), $\alpha_1$ at $T_C$ is:

$$\alpha_{1C} = \frac{T_C - T_0}{2\varepsilon_0 C} \tag{14}$$

Substituting this equation into Equations (12) and (13), and solving for the temperature independent coefficients $\alpha_{11}$ and $\alpha_{111}$ results in:

$$\alpha_{11} = \frac{-(T_C - T_0)}{\varepsilon_0 C P_{3C}^2}, \qquad \alpha_{111} = \frac{T_C - T_0}{2\varepsilon_0 C P_{3C}^4} \tag{15}$$

Multiplying these relations by the Curie constant $C$, equations result for the new constants $\alpha_{11}C$ and $\alpha_{111}C$:

$$\alpha_{11}C = \frac{-(T_C - T_0)}{\varepsilon_0 P_{3C}^2}, \qquad \alpha_{111}C = \frac{T_C - T_0}{2\varepsilon_0 P_{3C}^4} \tag{16}$$

Substituting Equations (16) and (5) into Equation (7), or substituting Equations (15) and (4) into Equation (6), results in the following relation:

$$P_3^2 = \Psi P_{3C}^2, \qquad \text{where } \Psi = \frac{2}{3}\left\{1 + \left[1 - \frac{3(T - T_0)}{4(T_C - T_0)}\right]^{1/2}\right\} \tag{17}$$

This equation can be used to calculate the spontaneous polarization $P_3$ from $P_{3C}$, $T_0$, and $T_C - T_0$, when the paraelectric-ferroelectric transition is first order. Comparing this equation with the second order $P_3$ relation [Equation (8)] shows

that a change in sign occurred after the first term. This is because for a first-order transition $\alpha_{11}$ is negative.

Similar relations can be derived for the spontaneous strains $x_1$ and $x_3$ by substituting Equation (17) into Equation (21) from Reference 7:

$$x_1 = \Psi x_{1C}, \qquad \text{where } x_{1C} = Q_{12}P_{3C}^2 \tag{18}$$

$$x_3 = \Psi x_{3C}, \qquad \text{where } x_{3C} = Q_{11}P_{3C}^2 \tag{19}$$

The above equations were used to fit the experimental tetragonal spontaneous strain data that was determined from high-temperature x-ray diffraction data. In each equation there are three independent unknown constants [$x_{1C}$, $T_0$, and $T_C - T_0$ in Equation (18); and $x_{3C}$, $T_0$, and $T_C - T_0$ in Equation (19)]. With three unknown constants many combinations of the values of these constants will give similar fits of the experimental data. For this reason a value of $T_C$ was first determined from the experimental phase diagram, which reduced the number of unknown constants to two. With only two unknown constants, the combination of values that gave the best least squares fit of the data could be easily found.

Amin et al.[15] fit $T_C$ of the experimental phase diagram with the following polynomial equation:

$$T_C = (211.8 - 486.0x - 280.0x^2 + 74.42x^3)°C. \tag{20}$$

where $x$ is the mole fraction $PbTiO_3$ in PZT. This equation will be used to calculate $T_C$ versus composition for the evaluation of the dielectric stiffness constants in this section, but a new equation [Equation (42)] will be given in Section IV, which will be used to calculate $T_C$ in References 8-10.

Haun et al.[11] used a computer program to determine values of $x_{1C}$, $x_{3C}$, and $T_0$ that gave the best least-squares fit of the lead titanate strain data (shown in Figure 4) using Equations (18) and (19) with $T_C$ equal to 492.2°C [calculated from Equation (20)]. The electrostrictive constants of lead titanate were determined using Gavrilyachenko et al.[16] room temperature spontaneous polarization value of 0.75 C m$^2$, and used with the strain data to calculate the spontaneous polarization, as shown in Figure 5. The values of all of the constants used in these calculations are listed in Table I.

The same procedure was used to fit the PZT 32/68 spontaneous strain data from Figure 4. However, for this composition the least-squares error continually became smaller as the $T_C - T_0$ difference was reduced, indicating that the transition was actually second order. Therefore, Equations (10) and (11) were used to fit this data. Values of the constants $aQ_{11}$, $aQ_{12}$, and $b$ were then found that gave the best fit of the strain data. The spontaneous polarization was calculated by combining the strain data with the electrostrictive constants from Reference 13. The experimentally obtained polarization and theoretical fit of the data are shown in Figure 5. The values of the constants which give the best fit of the data are listed in Table I.
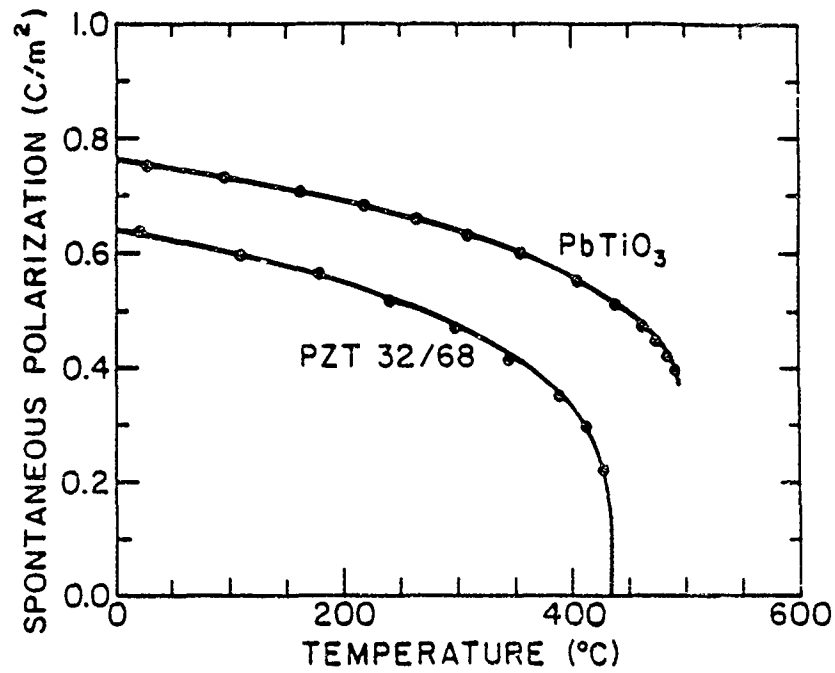
FIGURE 5  The spontaneous polarization $P_3$ ot $PbTiO_3$ and PZT 32 68 plotted versus temperature The data points were calculated from the experimental spontaneous strain data plotted in Figure 4. and the electrostrictive constants trom Reference 13  The solid curves are theoretical tits ot the data

TABLE I

Constants used to Fit the Spontaneous
Strain Data and to Calculate the
Spontaneous Polarization Data for the
Tetragonal Compositions

|  | $PbTiO_3$ |
|---|---|
| $T_C(^\circ C)$ | 492.2 |
| $T_0(^\circ C)$ | 478 8 |
| $T_c - T_0(^\circ C)$ | 13 4 |
| $r_{1c}(10^{-3})$ | $-0 362$ |
| $r_{3c}(10^{-3})$ | 1 24 |
| $Q_{11} (10^{-2} m^4/C^2)$ | 8 9 |
| $Q_{12} (10^{-2} m^4 C^2)$ | $-2 6$ |
| $P_{3c}(C m^2)$ | 0 373 |
| $\alpha_{11}C(10^{12} m^5 \,^\circ C\, C^2 F)$ | $-10 878$ |
| $\alpha_{111}C(10^{13} m^9 \,^\circ C\, C^4 F)$ | 3 909 |
|  | PZT 32 68 |
| $T_c = T_0(^\circ C)$ | 436 2 |
| $aQ_{11}$ | $-15 496$ |
| $aQ_{12}$ | 4 8904 |
| $b(^\circ C^{-1})$ | 1 0307 |
| $Q_{11} (10^{-2} m^4/C^2)$ | 7 70 |
| $Q_{12} (10^{-2} m^4 C^2)$ | $-2 43$ |
| $a (10^{-2} C^2 m^4)$ | $-2.0125$ |
| $\alpha_{11}C(10^{12} m^5 \,^\circ C\, C^2 F)$ | 2.7224 |
| $\alpha_{111}C(10^{13} m^9 \,^\circ C\, C^4 F)$ | 4 5091 |

## IV.   RHOMBOHEDRAL COMPOSITIONS

The spontaneous polarization of the high-temperature rhombohedral state can be solved from the quadratic first partial derivative stability condition [Equation (16) in Reference 7]:

$$P_3^2 = \frac{-\zeta + [\zeta^2 - 9\alpha_1\xi]^{1\,2}}{3\xi}, \tag{21}$$

where $\zeta = 3(\alpha_{11} + \alpha_{12})$,     and $\xi = 3\alpha_{111} + 6\alpha_{112} + \alpha_{123}$ $\qquad$ (22)

As in the tetragonal case the numerator and denominator of this equation were multiplied by the Curie constant $C$ to relate $P_3$ to the new constants:

$$P_3^2 = \frac{-\zeta C - [(\zeta C)^2 - 9\alpha_1 C\xi C]^{1\,2}}{3\xi C}. \tag{23}$$

where $\zeta C = 3(\alpha_{11}C + \alpha_{12}C)$,    and $\xi C = 3\alpha_{111}C - 6\alpha_{112}C + \alpha_{123}C$ $\qquad$ (24)

If the cubic-rhombohedral transition is second order then $T_0 = T_C$, and the following relation results from Equations (5) and (23):

$$P_3^2 = a\{1 - [1 - b(T - T_C)]^{1\,2}\}.$$
$$\text{where } a = -\zeta C (3\xi C). \qquad \text{and } b = 9\xi C [2\varepsilon_0(\zeta C)^2] \tag{25}$$

The $a$ and $b$ relations can also be rearranged in terms of $\zeta C$ and $\xi C$.

$$\zeta C = -3 (2\varepsilon_0 Cab) \qquad \xi C = 1 (2\varepsilon_0 Ca^2 b) \tag{26}$$

A similar relation can be found for the spontaneous strain $x_4$ by substituting Equation (25) into Equation (23) from Reference 7:

$$x_4 = aQ_{44} \{1 - [1 - b(T - T_C)]^{1\,2}\} \tag{27}$$

As in the tetragonal case at $T_C$, if the cubic-rhombohedral transition is first order, then a different procedure must be used to evaluate the coefficients. At $T_C$ the energies of the cubic and rhombohedral phases must be equal [Equations (8) and (10) in Reference 7], and the first partial derivative stability condition [Equation (16) in Reference 7] must be satisfied:

$$0 = 3\alpha_{1C} + \zeta P_{3C}^2 + \xi P_{3C}^4, \text{ and} \tag{28}$$

$$0 = \alpha_{1C} + \tfrac{1}{2} \zeta P_{3C}^2 + \xi P_{3C}^4. \tag{29}$$

where $\alpha_{1C}$ and $P_{3C}$ are $\alpha_1$ and $P_3$ at $T_C$.

Substituting Equation (14) into Equations (28) and (29) and solving for the temperature independent coefficients $\zeta$ and $\xi$ results in:

$$\zeta = \frac{-3(T_C - T_0)}{\varepsilon_0 C P_{3C}^2}. \qquad \xi = \frac{3(T_C - T_0)}{2\varepsilon_0 C P_{3C}^4} \tag{30}$$

Multiplying these relations by the Curie constant $C$, equations result for the new constants $\zeta C$ and $\xi C$:

$$\zeta C = \frac{-3(T_C - T_0)}{\varepsilon_0 P_{3C}^2}, \qquad \xi C = \frac{3(T_C - T_0)}{2\varepsilon^{-4}_{3C}} \qquad (31)$$

Substituting Equations (31) and (5) into Equation (23) or substituting Equations (30) and (4) into Equation (21) results in the following relation:

$$P_3^2 = \Psi P_{3C}^2, \quad \text{where } \Psi = \frac{2}{3}\left\{ 1 + \left[ 1 - \frac{3(T - T_0)}{4(T_C - T_0)} \right]^{1/2} \right\} \qquad (32)$$

This equation is the same as Equation (17) derived for the spontaneous polarization of the tetragonal state, except that $P_3$ and $P_{3C}$ in this case refer to the rhombohedral phase.

A similar relation can be derived for the spontaneous strain $x_4$ by substituting Equation (32) into Equation (23) from Reference 7:

$$x_4 = \Psi x_{4C}, \quad \text{where } x_{4C} = Q_{44}P_{3C}^2 \qquad (33)$$

Either Equation (27) or (33) was used to fit the experimental high-temperature rhombohedral spontaneous strain data from Reference 6. The transition temperature $T_C$ was first determined from the fit of the experimental phase diagram [Equation (20)], and then values of the remaining two unknown constants were found that gave the best least-squares fit of the data. The best fit of the PZT 90/10 data was found to be slightly first order, while the best fits of the PZT 80/20, 70/30, and 60/40 compositions were second order. The stain data was then used to calculate the spontaneous polarization through the electrostrictive constants from Reference 13, as shown in Figure 6. The values of the constants used in the calculations are listed in Table II.

## V.  FITTING THE MORPHOTROPIC PHASE BOUNDARY

In the last two sections constants involving the product of the Curie constant and the fourth and sixth order tetragonal ($\alpha_{11}C$ and $\alpha_{111}C$) and rhombohedral ($\zeta C$ and $\xi C$) dielectric stiffness constants were determined from spontaneous strain and electrostrictive data. $\alpha_{11}C$ and $\alpha_{111}C$ were determined for PbTiO$_3$ and PZT 32/68, and $\zeta C$ and $\xi C$ for PZT 90/10, 80/20, 70/30, and 60/40 compositions. In addition to these data, values of $\zeta C$ and $\xi C$ were calculated for PbZrO$_3$.[17] A value of $\zeta C$ was also determined for PbTiO$_3$.[11]

From the above data the compositional dependences could be estimated for $\zeta C$ from PbZrO$_3$ to PbTiO$_3$, for $\xi C$ only across the rhombohedral phase field, and for $\alpha_{11}C$ and $\alpha_{111}C$ only across the tetragonal phase field. Additional data were therefore needed to determine the compositional dependence of all of these constants across the entire PZT system.

The $\zeta C$ [$= 3(\alpha_{11} + \alpha_{12})C$] data was plotted in Figure 7 (c) versus composition. These data were fit with the following equation:

$$\zeta C = [(a + bx) \exp^{-cx} + dx + e]10^{14}, \qquad (34)$$
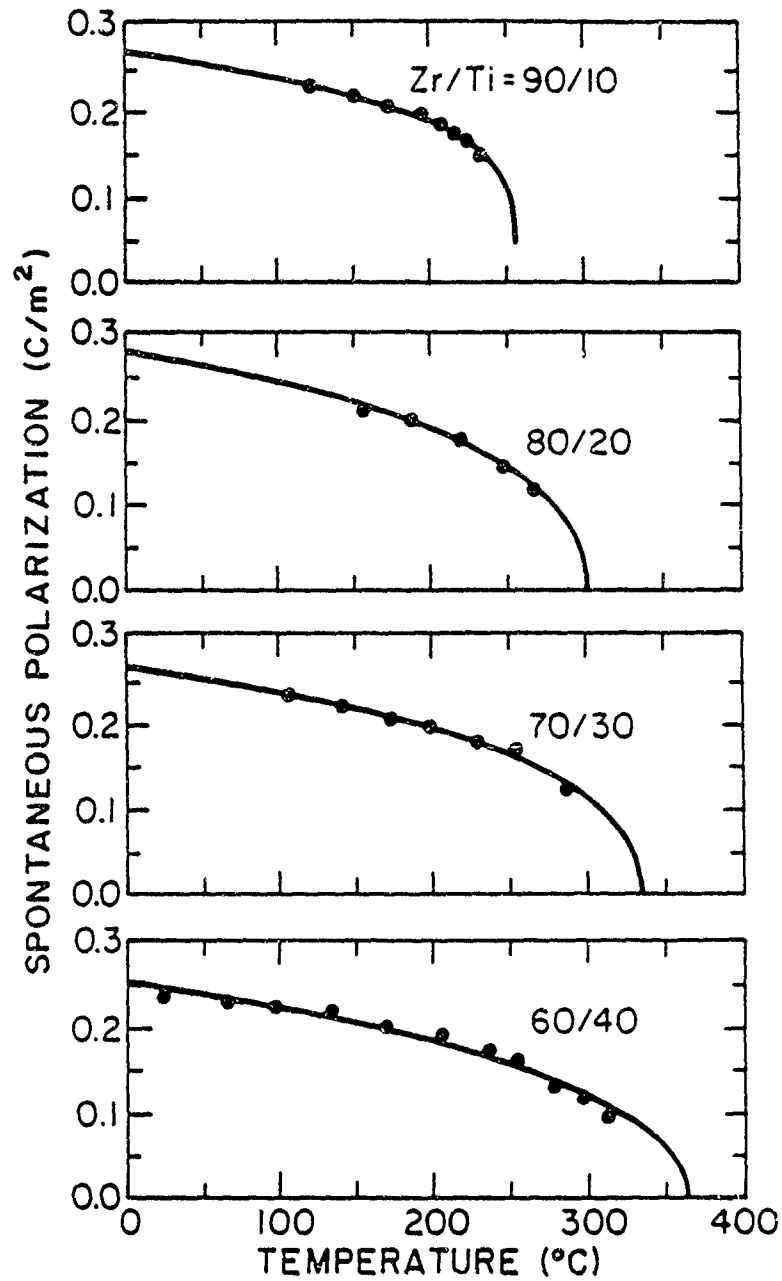
FIGURE 6   The spontaneous polarization $P_1$ (the component of $P_3$) of the high-temperature rhombohedral phase for the PZT 90/10, 80/20, 70/30, and 60/40 compositions plotted versus temperature. The data points were calculated from the experimental spontaneous strain data Reference 6 and the electrostrictive constants from Reference 16. The solid curves are theoretical fits of the data.

where $a = -9.6$, $b = -0.012501$, $c = 12.6$, $d = 0.42743$, $e = 2.6213$, exp is the exponential function, and $x$ is the mole fraction of $PbTiO_3$ in PZT. This equation was then used to calculate $\zeta C$ versus composition.

The rhombohedral sixth-order dielectric stiffness ($\xi$) cannot become negative when the rhombohedral phase is metastable, and the stable tetragonal phase undergoes a second-order transition to the cubic state. The $\xi C$ [$= 3\alpha_{111} + 6\alpha_{112} + \alpha_{123})C$] data from the last section showed that this constant does decrease across

TABLE II

Constants used to Fit the Spontaneous Strain Data and to Calculate
the Spontaneous Polarization Data for the Rhombohedral
Compositions

| | PZT 90/10 | | |
|---|---|---|---|
| $T_C(°C)$ | 257 674 | | |
| $T_0(°C)$ | 257 655 | | |
| $T_C - T_0 \,(°C)$ | 0.019 | | |
| $x_{4C}(10^{-5})$ | 3.5328 | | |
| $Q_{44} \,(10^{-2} \, m^4/C^2)$ | 4.9 | | |
| $P_{3C} \,(C/m^2)$ | 0 0329 | | |
| $\zeta C(10^{14} \, m^5 °C \cdot C^2 F)$ | −0 059390 | | |
| $\xi C \,(10^{15} \, m^9 °C \cdot C^4 F)$ | 2.7458 | | |
| | PZT 80/20 | PZT 70/30 | PZT 60/40 |
| $T_C = T_0(°C)$ | 298 40 | 334 41 | 366 16 |
| $a Q_{44} \,(10^{-1})$ | −2 2600 | −1 7487 | −5 4780 |
| $b(10^{-3} \, °C^{-1})$ | 2 2808 | 2.8542 | 0 55338 |
| $Q_{44} \,(10^{-2} \, m^4/C^2)$ | 5 17 | 5 52 | 6 29 |
| $a(10^{-2} \, C^2/m^4)$ | −4.3713 | −3.1679 | −8 7091 |
| $\zeta C(10^{14} \, m^5 °C/C^2 F)$ | 1 6992 | 1 8737 | 1 9715 |
| $\xi C(10^{15} \, m^9 °C/C^4 F)$ | 3 5153 | 3 5153 | 1 3454 |

the rhombohedral phase field towards the lead titanate composition, and may level
off without becoming negative. To keep this constant from becoming negative, $\xi C$
was assumed to be equal to $\alpha_{111} C$ at the lead titanate composition. This is the same
as assuming that $\alpha_{123} C$ is equal to six times $\alpha_{112} C$ for $PbTiO_3$. This data point was
plotted in Figure 8 (d) along with the rest of the $\xi C$ data, which were then fitted
with the following equation:

$$\xi C = [(a + bx) \exp^{-cx} + dx + e]10^{14}. \tag{35}$$

where $a = 16.225$, $b = -0.088651$, $c = 21.255$, $d = -0.76973$, $e = 0.887$, and
$x$ is the mole fraction of $PbTiO_3$ in PZT. This equation was then used to calculate
$\xi C$ versus composition.

The morphotropic phase boundary, where the energies of the tetragonal and
high-temperature rhombohedral phases must be equal, was used to extrapolate the
$\alpha_{11} C$ and $\alpha_{111} C$ constants into the rhombohedral phase field. The energies of the
tetragonal and high-temperature rhombohedral phases were defined by Equations
(9) and (11) in Reference 7. Multiplying these equations by the Curie constant
results in the following relations:

$$F_T \qquad \Delta G C = \alpha_1 C P_3^2 + \alpha_{11} C P_3^4 + \alpha_{111} C P_3^6 \tag{36}$$

$$F_{R(HT)} \; \Delta G C = 3\alpha_1 C P_3^2 + \zeta C P_3^4 + \xi C P_3^6 \tag{37}$$

Since the Curie constant is the same for the tetragonal and rhombohedral phases,
the product of $\Delta G$ and $C$ for these two phases should be equal at the morphotropic
boundary.

From the data presented in the last two sections, the paraelectric-ferroelectric
transition appears to be second order on both sides of the morphotropic boundary,
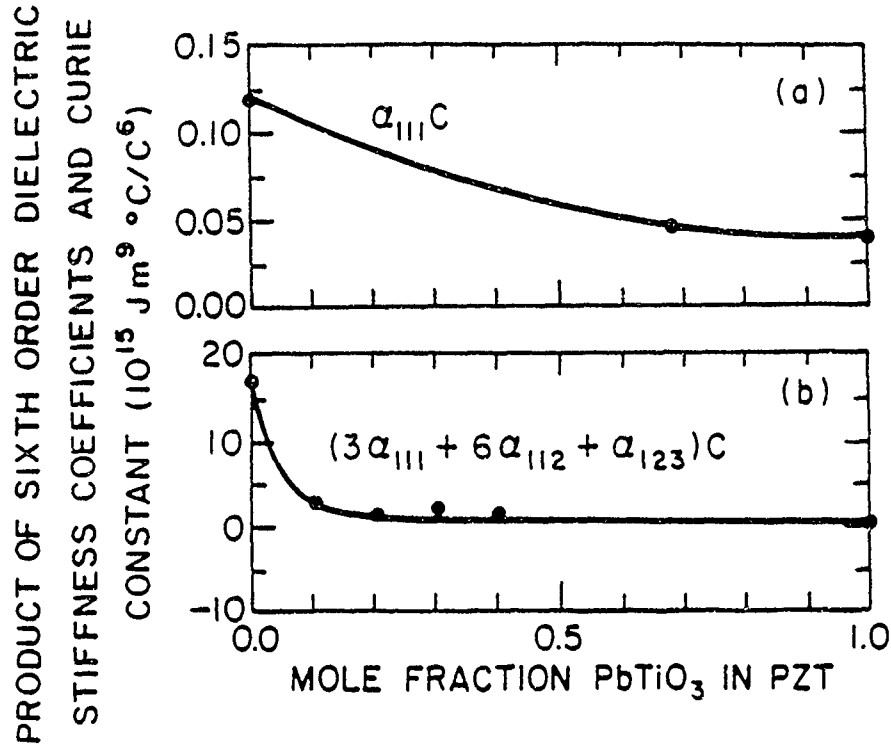and thus $T_0 = T_C$. The relation for $T_C$ [Equation (20)] was therefore used to
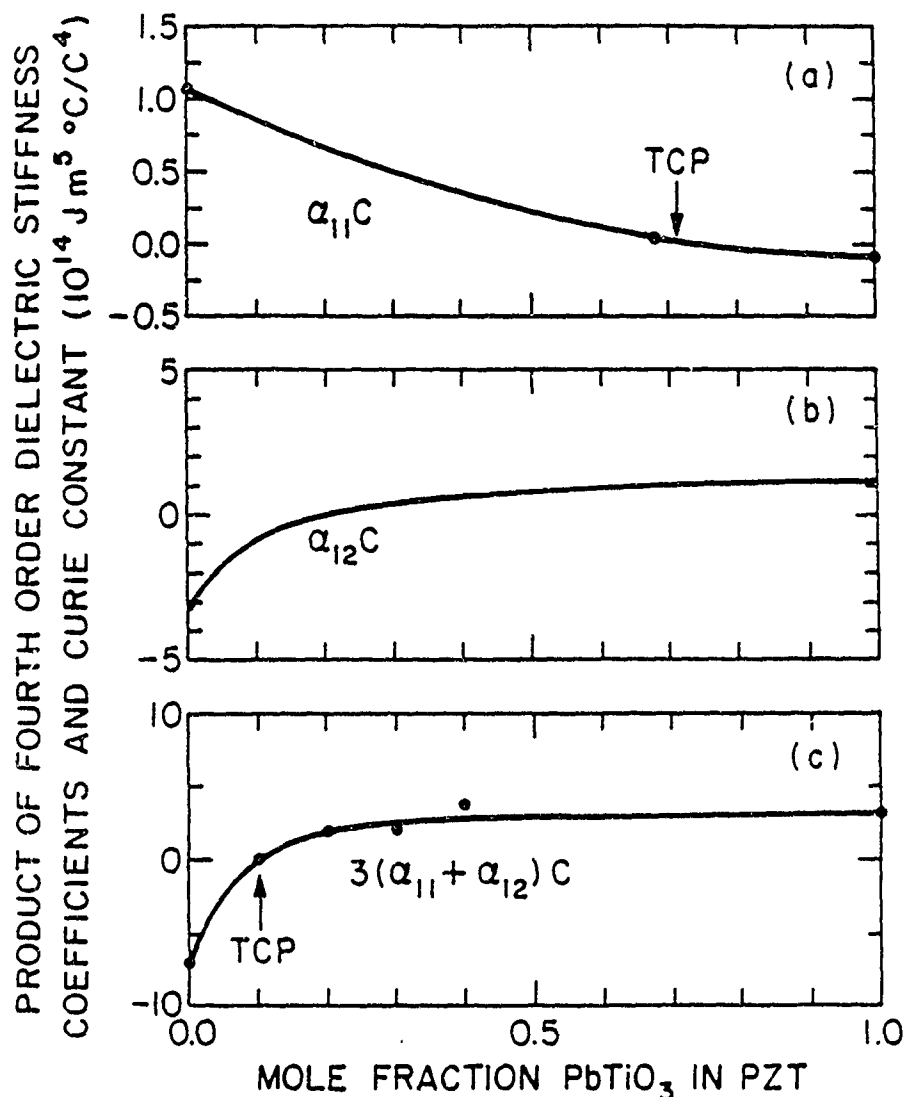
FIGURE 7   The product of the fourth-order dielectric stiffness coefficients and the Curie constant. The data points were determined from the experimental measurements. The solid curves are theoretical fits of the data.

calculate $T_0$, which is needed to determine $\alpha_1 C$ versus composition [see Equation (5)]. Using this procedure to calculate $\alpha_1 C$ with $\zeta C$ and $\xi C$ determined from Equations (34) and (35), the product of the energy $\Delta G$ and the Curie constant for the rhombohedral state could be calculated using Equation (37).

A computer program was written to extrapolate the $\alpha_{11} C$ and $\alpha_{111} C$ constants into the rhombohedral phase field by fitting the morphotropic boundary. The first step was to make initial guesses for the values of $\alpha_{11} C$ and $\alpha_{111} C$ for $PbZrO_3$. A quadratic fit of these data and the values of $\alpha_{11} C$ and $\alpha_{111} C$ determined in Section III for the PZT 32/68 and $PbTiO_3$ compositions were then made using the following equation:

$$\alpha_{11} C \text{ or } \alpha_{111} C = (a + bx + cx^2) \ 10^{13} \tag{38}$$

The product of the energy $\Delta G$ and the Curie constant of the tetragonal state could

FIGURE 8   The product of the sixth-order dielectric stiffness coefficients and the Curie constant  The data points were determined from the experimental measurements  The solid curves are theoretical fits of the data.

now be calculated using Equation (36). The morphotropic boundary was then calculated from the cross over of the ($\Delta GC$) products of the two phases, and a least-squares error with the experimental data was calculated. New values of $\alpha_{11}C$ and $\alpha_{111}C$ for PbZrO$_3$ were chosen, and the procedure repeated until the best least-squares fit of the morphotropic boundary was obtained. The final fit is shown in Figure 2 of Reference 10 by the solid curve. The values and final fittings of the $\alpha_{11}C$ and $\alpha_{111}C$ constants are plotted in Figures 7 and 8. In Equation (38) the final constants for $\alpha_{11}C$ were $a = 10.612$, $b = -22.655$, and $c = 10.955$; and for $\alpha_{111}C$ were $a = 12.026$, $b = -17.296$, and $c = 9.1790$.

This program visually demonstrated how the shape of the morphotropic boundary could be changed by varying the dielectric stiffness coefficients. Depending on the values of the coefficients chosen, the phase boundary could be shifted either towards PbZrO$_3$ or PbTiO$_3$, and the shape could be changed from vertical to curved. The bending of the boundary could also be made to go towards PbZrO$_3$ or PbTiO$_3$.

The $\alpha_{12}C$ constant can be calculated from the $\alpha_{11}C$ and $\zeta C[= 3(\alpha_{11} - \alpha_{12})C]$ constants:

$$\alpha_{12}C = \zeta C/3 - \alpha_{11}C \qquad (39)$$

Using this relation and Equations (34) and (38) for $\zeta C$ and $\alpha_{11}C$, $\alpha_{12}C$ was calculated versus composition as shown in Figure 7.

When $\alpha_{11}C$ or $\zeta C$ changes sign tricritical points occur, and the cubic-tetragonal or cubic-rhombohedral transition changes from first to second order. As shown in

Figure 7 tricritical points (labeled TCP) occur at the $Pb(Zr_{1-x}Ti_x)O_3$ compositions with values of $x$ equal to 0.102 and 0.717. Between these tricritical points the paraelectric-ferroelectric transition is second order. and first order regions exist near the end members $PbZrO_3$ and $PbTiO_3$. In the first order regions the $T_C - T_0$ difference and spontaneous polarization at $T_C$ ($P_{3C}$) can be calculated from the following relations derived from Equations (16) and (31):

$$F_T \qquad P_{3C} = [-\alpha_{11}C/(2\alpha_{111}C]^{1/2}, \qquad T_C - T_0 = \varepsilon_0(\alpha_{11}C)^2/(2\alpha_{111}C) \qquad (40)$$

$$F_{R(HT)} \qquad P_{3C} = [-\zeta C/(2\xi C)]^{1/2}, \qquad T_C - T_0 = \varepsilon_0(\zeta C)^2/(6\xi C) \qquad (41)$$

Using Equations (34), (35), and (38) to calculate the constants in these equations. $P_{3C}$ and $T_C - T_0$ were calculated as shown in Figure 9.

$T_C$ data from the experimental phase diagram were used with the preceding $T_C - T_0$ calculations to determine $T_0$ data in the first-order regions. These data were then combined with the $T_C$ data from the second-order region. which is equal to $T_0$, and fit with the following polynomial equation:

$$T_0 = a + bx^2 + cx^3 + dx^4 + ex^5 + fx^6, \qquad (42)$$

where $a = 189.48$. $b = 843.40$. $c = -2105.5$, $d = 4041.8$. $e = -3828.3$. $f = 1337.8$. and $x$ is the mole fraction of $PbTiO_3$ in PZT.

$T_C$ was then calculated from the following relation:

$$T_C = (T_C - T_0) + T_0, \qquad (43)$$
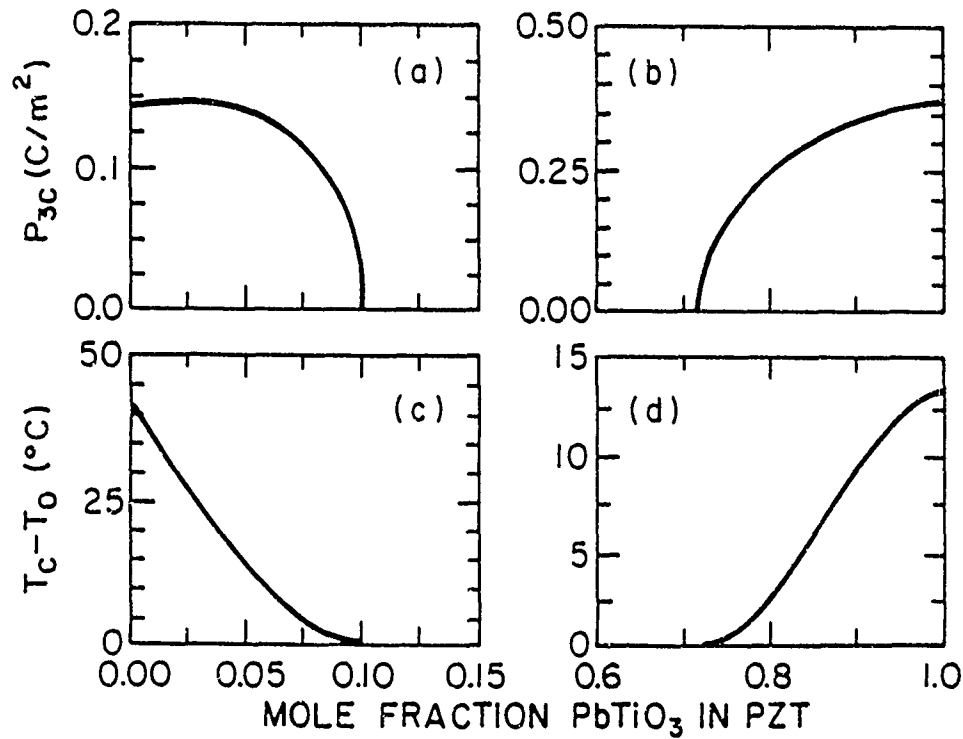


FIGURE 9   The spontaneous polarization at $T_C$($P_{3C}$) [(a) and (b)] and the $T_C - T_0$ difference [(c) and (d)] plotted versus composition in the first order regions of the phase diagram.

where $T_0$ and $T_C - T_0$ were calculated from Equations (40)–(42). $T_C$ was calculated from this equation and plotted in Figure 2 of Reference 10 along with the experimental data. Equation (42) and (43) were used to calculate $T_0$ and $T_C$ throughout the rest of this series of papers.

## VI. SUMMARY

High-temperature x-ray diffraction data on sol-gel derived PZT 32/68 powder were presented, and used with electrostrictive data to calculate the spontaneous polarization. These data were used with previously published data to determine the values of the higher-order dielectric stiffness coefficients at several compositions. The compositional dependence of each coefficient was determined by fitting these values with an equation. A set of equations was then established that can be used to calculate values of the coefficients at any composition.

All of the coefficients were assumed to be independent of temperature, except the dielectric stiffness coefficient $\alpha_1$, which was given a linear temperature dependence based on the Curie-Weiss law. The experimental phase diagram was extensively used in the evaluation of the coefficients, by requiring that the energies of the adjacent phases be equal at the boundaries. The first partial derivative stability conditions were also used as additional relations in the evaluation procedure.

The fourth-order tetragonal ($\alpha_{11}$) and rhombohedral ($\alpha_{11} - \alpha_{12}$) dielectric stiffness coefficients were found to change sign as a function of composition, indicating that two tricritical points occur in the PZT system, where the paraelectric-ferroelectric phase transition changes from first to second order. By extrapolating between the data points, the tricritical points were found to occur a: $Pb(Zr_{1-x}Ti_x)O_3$ compositions with $x$ equal to 0.102 and 0.717. The transition was first order from the end members to the tricritical points, and then a large second order region occurs across the phase diagram between the tricritical points.

The tricritical point on the lead zirconate side of the phase diagram was previously found to occur at the PZT 94/6 composition,[2] four percent closer to lead zirconate than indicated by this study. This difference may simply be due to the experimental error involved in the measurements and theoretical fitting, or may be related to differences in homogeneity of the powders used (mixed-oxide versus sol-gel).

Haun et al.[4] indicated that the second tricritical point occurred near or possibly at the morphotropic boundary. With the more recent data presented in this paper and a more careful analysis of the previous data, the second tricritical point appears to be located at the PZT 28/72 composition as described above. Differential Scanning Calorimetric (DSC) data on the sol-gel powders prepared in this project also indicated that the second tricritical point occurs near the PZT 28/72 composition. The shape of the DSC peaks at $T_C$ changed from sharp narrow peaks (first order) to very broad peaks (second order) at this composition. Additional work on preparing homogeneous PZT powders, and then determining the lattice constants as a function of temperature from high-temperature x-ray diffraction is needed to locate the tricritical points more precisely.

# REFERENCES

1 R. Clarke and A. M Glazer. *Ferroelectrics*. 14, 695 (1976).

2 R W Whatmore. R. Clarke and A M. Glazer. *J Phys C Solid State Phys*, 11, 3089 (1978)

3 K. Roleder and J Handerek. *Phase Transitions*. 2, 285 (1982).

4 M J Haun, Z Q Zhuang, S J Jang, H. A. McKinstry and L. E. Cross. *Proceedings of the 6th IEEE International Symposium on the Applications of Ferroelectrics*. Lehigh, PA, edited by Van Wood (IEEE, New York, 1986) pp. 398–401

5 Z G Zhuang, M. J Haun, S. J Jang and L. E Cross. *Proceedings of the 6th IEEE International Symposium on the Applications of Ferroelectrics*. Lehigh, PA, edited by Van Wood (IEEE, New York, 1986) pp. 394–397.

6. M. J. Haun, Y H. Lee, H. A. McKinstry and L. E. Cross. *Advances in X-ray Analysis, Vol 30*, edited by C. S. Barrett. J. V Gilfrich, R. Jenkins, D E. Leyden, J C Russ and P K Predecki, (Plenum Press, New York, 1987) pp. 473–481

7 M. J. Haun, E. Furman, S. J. Jang and L. E. Cross. 'Thermodynamic Theory of the Lead Zirconate-Titanate Solid Solution System, Part I. Phenomenology. *Ferroelectrics* to be published with this paper

8 M J Haun, Z. Q Zhuang, E. Furman, S J Jang and L. E. Cross. 'Thermodynamic Theory of the Lead Zirconate-Titanate Solid Solution System, Part III. Curie Constant and Sixth-Order Polarization Interaction Dielectric Stiffness Coefficients.' *Ferroelectrics* to be published with this paper

9 M. J Haun, E. Furman, T. R. Halemane and L. E. Cross. "Thermodynamic Theory of the Lead Zirconate-Titanate Solid Solution System, Part IV Tilting of the Oxygen Octahedra. ' *Ferroelectrics* to be published with this paper.

10. M J Haun, E. Furman, S. J Jang and L E. Cross. "Thermodynamic Theory of the Lead Zirconate-Titanate Solid Solution System, Part V Theoretical Calculations." *Ferroelectrics* to be published with this paper

11 M J Haun, E Furman, S. J Jang, H. A. McKinstry and L. E Cross. *J Appl Phys* 62, 333 (1987)

12. B Cullity, *Elements of X-ray Diffraction Second Edition* (Addison-Wesley, Reading, MA, 1978), pp 350–368

13 M J Haun, Z. Q Zhuang, E Furman, S J Jang and L E Cross. *J Am Ceram Soc* 72, 1140 (1989).

14 M J Haun, *Thermodynamic Theory of the Lead Zirconate-titanate Solid Solution System* Ph D thesis in Solid State Science, The Pennsylvania State University (1988)

15 A Amin, M J Haun, B Badger, H. A. McKinstry and L E Cross. *Ferroelectrics* 65, 107 (1985)

16 V G Gavrilvachenko, R. I. Spinko, M. A. Martynenko and E G Fesenko *Fiz. Tverd Tela*. 12, 1532 (1970) [*Sov Phys.-Solid State*, 12, 1203 (1970)]

17 M J Haun, T J Harvin, M. T Lanagan, Z. Q Zhuang, S. J. Jang, and L E Cross. *J Appl Phys* 65, 3173 (1989)

APPENDIX 26

# THERMODYNAMIC THEORY OF THE LEAD ZIRCONATE-TITANATE SOLID SOLUTION SYSTEM, PART III: CURIE CONSTANT AND SIXTH-ORDER POLARIZATION INTERACTION DIELECTRIC STIFFNESS COEFFICIENTS

M. J. HAUN,† Z. Q. ZHUANG,‡ E. FURMAN,§ S. J. JANG
and L. E. CROSS

*Materials Research Laboratory, The Pennsylvania State
University, University Park, PA 16802, USA*

Values of the Curie constant (C) and sixth-order polarization interaction dielectric stiffness coefficients ($\alpha_{112}$ and $\alpha_{123}$) are needed for the development of a thermodynamic theory for the entire lead zirconate-titanate (PZT) solid solution system. Low-temperature dielectric data measured on pure homogeneous polycrystalline PZT samples were used to determine values of these coefficients at several compositions across the phase diagram. Equations were then fitted to these data to determine the compositional dependence of the coefficients. The Curie constant was found to form a peak in the middle of the phase diagram at the PZT 50/50 composition.

## I. INTRODUCTION

This paper is the third paper in a series of five papers[1–4] describing the development of a thermodynamic theory for the entire lead zirconate-titanate (PZT) solid solution system. Values of the Curie constant (C) and sixth-order polarization interaction dielectric stiffness coefficients ($\alpha_{112}$ and $\alpha_{123}$) are needed for the development of this theory.

Due to the lack of experimental data, the Curie constant was originally assumed to be independent of composition in the theory developed for the single-cell region of the PZT system.[5] Amin *et al.*[6] later found from a combination of calorimetric and phenomenological data that the Curie constant was dependent on composition with a peak forming near the morphotropic boundary between the tetragonal and rhombohedral phases. The theory was then modified to account for the compositional dependence of the Curie constant.[7] The Curie constant data determined by Amin *et al.*[6] extends from lead titanate to the morphotropic boundary between the tetragonal and rhombohedral phases. Additional data were needed to complete

---

†Now at E. I. du Pont de Nemours & Co., Electronics Dept., Experimental Station, P O Box 80334, Wilmington, DE, 19880-0334.

‡Visiting Scientist from the Department of Inorganic Materials Science and Engineering, South China Institute of Technology, Guangzhou, The People's Republic of China.

§Now at Allied-Signal Inc., Metals and Ceramics Laboratory, P O Box 1021R, Morristown, NJ, 07960.

the compositional dependence of the Curie constant from the morphotropic boundary to lead zirconate.

In this paper values of $C$, $\alpha_{112}$, and $\alpha_{123}$ will be determined as a function of composition from low-temperature polycrystalline dielectric data. In the next section the results of the low-temperature dielectric measurements will be presented. These data will then be used in Section III to determine values of $C$, $\alpha_{112}$, and $\alpha_{123}$. A summary of this paper will be presented in Section IV.

## II.  LOW-TEMPERATURE DIELECTRIC MEASUREMENTS

Additional experimental data were needed to determine values of the Curie constant and $\alpha_{112}$ and $\alpha_{123}$ coefficients. Low-temperature polycrystalline dielectric data were chosen for this purpose. At low temperatures the thermally activated contributions to the dielectric properties should "freeze out". The remaining dielectric properties were assumed to be due to an averaging of the single-domain properties.

Zhuang et al.[3] fabricated pure homogeneous polycrystalline ceramic PZT samples from sol-gel derived powders. The same procedure was used to prepare disc shaped samples for use in this study. The samples were cut and polished, and sputtered with gold electrodes. The samples, with thermal-resistance wires attached as leads, were then shielded in a copper enclosure in an Air Products and Chemicals model LT-3-110 cryogenics system to cool the temperature to 4.2 K. The dielectric constant and loss were measured at 1 KHz on a Hewlett Packard 4270A automatic digital capacitance bridge.

After measuring the dielectric properties on the unpoled samples at 4.2 K, the same samples were poled with electric fields of 20 to 40 KV/cm for 4 to 30 minutes. The piezoelectric strain coefficient $d_{33}$ was measured using a Berlincourt Piezo-$d_{33}$ meter to determine the completeness of poling. The poled samples were then cooled back down to 4.2 K, and the dielectric properties were remeasured. The unpoled ($\varepsilon_{33}$), and poled ($\varepsilon_{33}^P$, parallel to the poling direction) dielectric constant data are listed in Table I.

The Bruggeman formula[9] was used to relate the poled ($\varepsilon_{33}^P$) and unpoled ($\varepsilon_{33}$) dielectric constants of the tetragonal and rhombohedral polycrystalline samples to the single-domain constants ($\varepsilon_{11}$ and $\varepsilon_{33}$):

$$\varepsilon_{33}^P = \tfrac{1}{4}(\varepsilon_{11} - 2\vartheta(\varepsilon_{11} + \varepsilon_{33}) + \{[\varepsilon_{11} - 2\vartheta(\varepsilon_{11} + \varepsilon_{33})]^2 + 8\varepsilon_{11}\varepsilon_{33}\}^{1/2}) \qquad (1)$$

$$\varepsilon_{33} = \tfrac{1}{4}(\varepsilon_{11} + \{\varepsilon_{11}^2 + 8\varepsilon_{11}\varepsilon_{33}\}^{1/2}) \qquad (2)$$

$\varepsilon_{11}$ and $\varepsilon_{33}$ are the dielectric constants perpendicular and parallel to the poling direction, and $\vartheta$ is the fraction of 90° or 71°(109°) domain alignment. $\varepsilon_{11}$ and $\varepsilon_{33}$ were assumed to be equal to the dielectric susceptibilities $\eta_{11}$ and $\eta_{33}$ (actually $\varepsilon_{ij} = \eta_{ij} + 1$) for the tetragonal compositions, and to $\eta_{11}'$ and $\eta_{33}'$ for the rhombohedral compositions [see Equations (27) and (29) in Reference 1].

In addition to the poled and unpoled ceramic dielectric constants, the fraction of 90° or 71°(109°) domain alignment $\vartheta$ is required in Equations (1) and (2) to calculate the single-domain constants. Turik et al.[9] used an x-ray method to determine $\vartheta$ as a function of composition. These data were used to approximate values of $\vartheta$ as listed in Table I.

The differences between the poled and unpoled ceramic dielectric constants at low temperatures (listed in Table I) showed a similar behavior as was seen at room

TABLE I

The dielectric constant at 4.2 K on poled ($\varepsilon^p_{jj}$) and unpoled ($\varepsilon_{jj}$) ceramic samples and the fraction of 90° (or 71, 109°) domain alignment $\vartheta$

| Zr/Ti | $\varepsilon_{jj}$ | $\varepsilon^p_{jj}$ | $\vartheta$ |
|-------|------|-------|------|
| 94/6  | 93 2  | 87 2  | 0.65 |
| 90/10 | 106.2 | 101.1 | 0.65 |
| 70/30 | 139.4 | 135.3 | 0.65 |
| 60/40 | 173.2 | 156.2 | 0.63 |
| 54/46 | 282.6 | 232.5 | 0.50 |
| 52/48 | 324.3 | 303.0 | 0.34 |
| 50/50 | 326 8 | 328.4 | 0.30 |
| 40/60 | 200 6 | 202.0 | 0.23 |

temperature.[9,10] By poling the samples the dielectric constant decreased for the rhombohedral compositions, and slightly increased for the tetragonal compositions. Turik et al.[9] attributed these changes from poling as being due to the reduction of the clamping effect from 180° domain walls. When 180° domains are present, the dielectric constant is lowered from a clamping effect between these domains. By poling a ceramic sample virtually all of the 180° domains reorient closest to the poling direction, and the clamping effect is reduced causing the dielectric constant to increase.

However, 90° or 71°(109°) domain reorientation also occurs during poling, which decreases the dielectric constant if $\varepsilon_{33}$ is less than $\varepsilon_{11}$. Thus the dielectric constant will increase or decrease after poling depending on which of these competing mechanisms dominates. In the tetragonal state the small fraction of the 90° domains that realign during poling does not quite cancel out the increase in dielectric constant from the reduction of the clamping effect of the 180° domains, and therefore the dielectric constant increases slightly. In the rhombohedral state a large fraction of the 71°(109°) domains align during poling and dominate the increase from the reduction of the clamping effect, causing the dielectric constant to decrease. In addition, a smaller fraction of 180° domains exist in a rhombohedral ceramic compared to a tetragonal one.[11]

Because of the clamping effect, as described above, Equations (1) and (2) were only used to calculate the single-domain dielectric susceptibilities $\eta'_{11}$ and $\eta'_{33}$ for the rhombohedral PZT 94/6 through 54/46 compositions using the data from Table I at 4.2 K. This data is listed in Table II. The single-domain dielectric susceptibilities of the PZT 52/48, 50/50, and 40/60 compositions will be calculated using a different procedure in the next section. The single-domain data will then be used to calculate values of the Curie constant, and the $\alpha_{112}$ and $\alpha_{123}$ coefficients.

## III.  EVALUATION OF THE CURIE CONSTANT AND SIXTH-ORDER POLARIZATION INTERACTION DIELECTRIC STIFFNESS COEFFICIENTS

In the second paper in this series[2] the compositional dependences of the $\alpha_{11}C$, $\alpha_{111}C$, $\zeta C$, and $\xi C$ constants were determined. These constants together with the $\alpha_1 C$ constant can be used to calculate the spontaneous polarization and $\Delta G\,C$ of

TABLE II

Calculations from the low temperature ceramic dielectric data

| Zr Ti | $\eta_{11}$ or $\eta_{11}'$ | $\eta_{33}$ or $\eta_{33}'$ | $C$ $(10^5\,°C)$ | $\alpha_{112}C$ $10^{14}\ m^{rc}C\ C^2F)$ | $\alpha_{12}\cdot C$ $(10^{14}\ m^{rc}C\ C^2F)$ |
|---|---|---|---|---|---|
| *Rhombohedral* | | | | | |
| 94/6 | 98.0 | 84.1 | 2.0031 | 13 905 | −3 3019 |
| 90/10 | 110.2 | 98.4 | 2.0823 | 7 0625 | −1 8033 |
| 70/30 | 142.6 | 133.1 | 2.1648 | 3 3549 | −1.5592 |
| 60/40 | 187.5 | 146.8 | 2.4243 | 3 1431 | −1 5008 |
| 54/46 | 338.4 | 189.4 | 3 1714 | 2.4256 | −1 1019 |
| 52/48 | 392.3 | 243 3 | 4 0965 | — | — |
| 50/50 | 429 7 | 254.1 | 4 2962 | — | — |
| *Tetragonal* | | | | | |
| 40/60 | 325 1 | 110 4 | 2 6951 | — | — |

the tetragonal and high temperature rhombohedral phases [Equations (7), (23), (36), and (37) in Reference 2]. In addition to these constants, the Curie constant $C$, and the polarization interactions coefficients $\alpha_{12}$, $\alpha_{112}$, and $\alpha_{123}$ are required to calculate the second derivative properties, such as the dielectric properties [see Equations (27) and (29) in Reference 1].

The $\alpha_{12}C$ constant was calculated from the $\alpha_{11}C$ and $\zeta C$ $[=3(\alpha_{11}-\alpha_{12})\ C]$ constants in Reference 2. A combination of the $\alpha_{112}C$ and $\alpha_{123}C$ constants can be calculated from the $\alpha_{111}C$ and $\xi C$ $[=(3\alpha_{111}+6\alpha_{112}+\alpha_{123})\ C]$ constants with the following relation:

$$(6\alpha_{112}+\alpha_{123})\ C = \xi C - 3\alpha_{111}C \tag{3}$$

Using this equation allowed $(6\alpha_{112}+\alpha_{123})\ C$ to be calculated from the values of the $\xi C$ and $\alpha_{111}C$ that were determined in Reference 2, but additional data were still needed to separate the $\alpha_{112}C$ and $\alpha_{123}C$ constants.

The low-temperature dielectric data presented in the last section were used to calculate the Curie constant and to separate the dielectric stiffness coefficients $\alpha_{112}$ and $\alpha_{123}$. To accomplish this the high-temperature rhombohedral equations were used at low temperatures, where actually the low-temperature rhombohedral phase is stable, because of the following reasons.

To calculate the dielectric susceptibility coefficients of the low-temperature rhombohedral phase, the polarization-tilt angle coupling coefficients must be determined, in addition to the dielectric stiffness coefficients [see Equation (30) in Reference 1]. The dielectric properties have been experimentally shown to only change very slightly at the transition between the high and low temperature rhombohedral phases.[12] A fairly good assumption can then be that the dielectric susceptibility coefficients of the high and low temperature rhombohedral phases are equal at the transition between these phases. Using this assumption with the methods described in this paper and the second and fourth papers of this series to determine the other coefficients, the constants needed to calculate the dielectric susceptibilities of the low-temperature rhombohedral phase can be solved for.

However, when using the low-temperature rhombohedral dielectric susceptibility

equations and the experimental ceramic data at low temperatures in the present theory (tilt angle coefficients are independent of temperature and only go up to the fourth order). the resulting values of the Curie constant will not agree with the available experimental data. A temperature dependence was added to the second order tilt angle related coefficient [$\beta_1$ in Equation (1) of Reference 1], but this still did not resolve the problem. Probably what is needed, in addition to this temperature dependence, is to add a sixth-order tilt angle term to the energy function. But if this is done the equations for the spontaneous polarization and tilt angle will change from quadratic to quartic. At this point the additional complexity resulting from a sixth-order tilt angle term is probably not warranted. and there is not enough experimental data available to properly determine these additional constants.

The question now is how can the low-temperature ceramic dielectric data be used to determine the Curie constant and to separate the sixth order polarization interaction coefficients, if the low-temperature rhombohedral equations will not give reasonable results with the present theory. The dielectric properties of the high and low temperature rhombohedral phases were experimentally found to be very similar at the transition between these phases. If the dielectric properties of these two phases remain similar down to low temperatures. then the high-temperature rhombohedral dielectric susceptibilities relations could be used at low temperatures.

Using the high-temperature rhombohedral relations at low temperatures produced very reasonable results. A Curie constant of $2 \times 10^5{}^\circ$C was obtained for the PZT 90/10 composition. which is in excellent agreement with experimental single-crystal measurements.[12] Thus this indicates that the high and low temperature rhombohedral dielectric properties are probably similar down to even very low temperatures (4 2 K). The high-temperature rhombohedral dielectric susceptibility relations were therefore used for the dielectric properties of both the high and low temperature rhombohedral phases, which appears to be a fairly good assumption.

The $\eta'_{11}$ and $\eta'_{33}$ data for the rhombohedral PZT 94/6 through 54/46 compositions were used to calculate the Curie constant, and to separate the $\alpha_{112}$ and $\alpha_{123}$ constants from the following high-temperature rhombohedral dielectric stiffness relations:

$$\eta'_{11} = C/\{\varepsilon_0[(T - T_0)/\varepsilon_0 + 12\alpha_{11}CP_3^2 + (30\alpha_{111}C + 12\alpha_{112}C - 2\alpha_{123}C)P_3^4]\} \qquad (4)$$

$$\eta'_{33} = C/\{\varepsilon_0[(T - T_0)/\varepsilon_0 + 4\zeta CP_3^2 + 10\xi CP_3^4]\} \qquad (5)$$

These equations were derived from Equations (29). (33). and (40) from Reference 1.

Equation (5) was used to calculate the Curie constant from the $\eta'_{33}$ data in Table II. and from values of the $\zeta C$ and $\xi C$ constants in Equations (34) and (35) listed in Reference 2. Equations (3). (4). and (5) were then combined to calculate the $\alpha_{112}C$ and $\alpha_{123}C$ constants using Equations (38) and (42) from Reference 2 determine values of $T_0$, $\alpha_{11}C$, and $\alpha_{111}C$. The $C$. $\alpha_{112}C$. and $\alpha_{123}C$ data are listed in Table II.

The $\alpha_{112}C$ data listed in Table II with the lead titanate value from Reference 13 were fit with the following relation:

$$\alpha_{112}C = a \exp^{-bx} + cx + d, \qquad (6)$$

where $a = 58.804$, $b = 29.397$, $c = -3.3754$, $d = 4.2904$, exp is the exponential function, and $x$ is the mole fraction $PbTiO_3$ in PZT.

The compositional dependence of the $\alpha_{123}C$ constant was determined from the following relation derived from equation (3):

$$\alpha_{123}C = \xi C - 3\alpha_{111}C - 6\alpha_{112},$$ 

(7)

where $\xi C$ and $\alpha_{111}C$ were determined from Equations (35) and (38) from Reference 2, and $\alpha_{112}C$ was determined from Equation (6) above. The data from Table II and the calculations from Equations (6) and (7) are shown in Figure 1.

The Curie constants of the PZT 52/48 and 50/50 compositions were determined by substituting Equations (4) and (5) into Equation (1), and using the $\varepsilon_{33}^P$ data from Table I, along with the dielectric stiffness constants calculated from the previously given equations. Values of $\eta_{11}'$ and $\eta_{33}'$ were then calculated from Equations (4) and (5) and are listed in Table II. This procedure was also used for the tetragonal PZT 40/60 composition using Equations (27) and (36) from Reference 1 for the tetragonal dielectric susceptibilities. The values of $C$, $\eta_{11}$, and $\eta_{33}$ are listed in Table II.
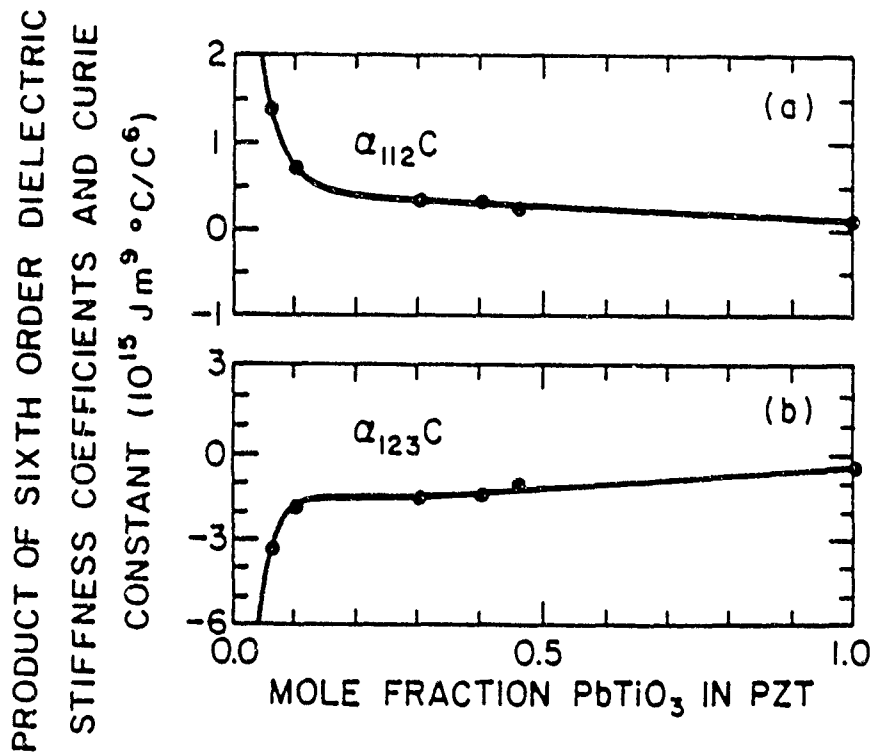


FIGURE 1  Product of the sixth-order polarization interaction dielectric stiffness coefficients and the Curie constant plotted versus composition. The data points were determined from experimental data. The solid curves are fits of the data using Equations (6) and (7)
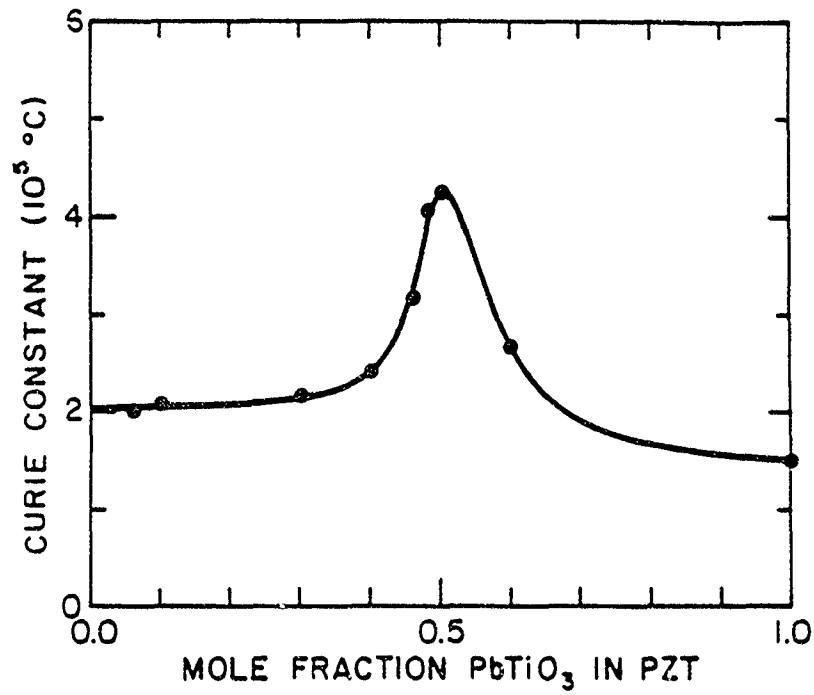
FIGURE 2 The Curie constant plotted versus composition. The data points are from Table II. The solid curve is a fitting of the data using Equation (8).
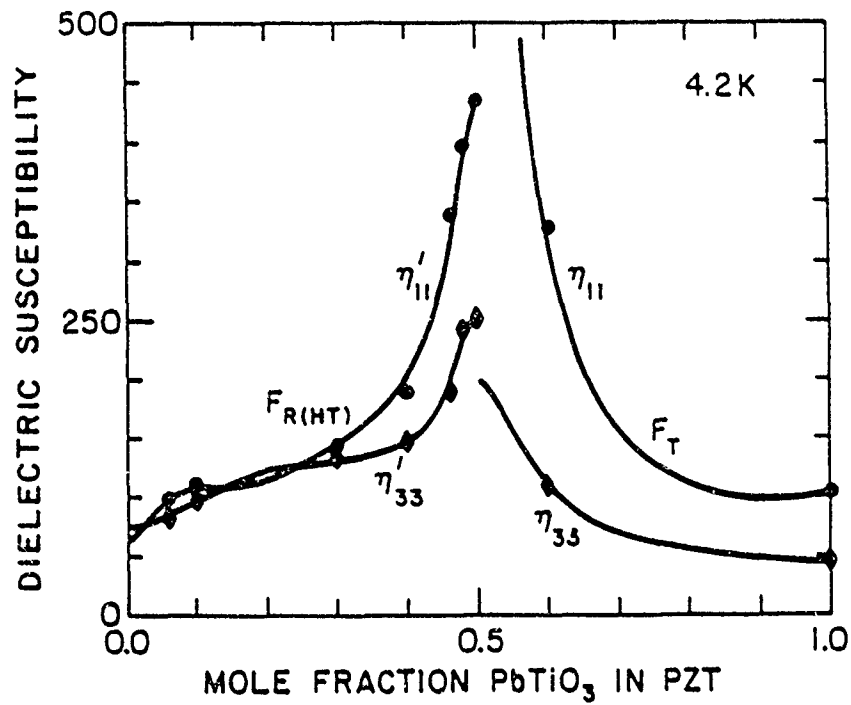


FIGURE 3 The dielectric susceptibility coefficients $\eta_{11}$ and $\eta_{33}$ in the tetragonal state and $\eta_{11}$ and $\eta_{33}$ in the rhombohedral state plotted versus composition at 4.2 K. The data points are from Table II. except for the points at PbTiO$_3$ which are from Reference 13 The solid curves are the theoretical calculations after determining the compositional dependence of the coefficients.

The best least-squares fit of the following relations were used to fit the compositional dependence of the Curie constant using the data listed in Table II along a value of $1.5 \times 10^{5}$°C for $PbTiO_3$:

For $x \leqslant 0.5$: $C = [2.1716/(1 + 500.05x)^2 + 0.131x + 2.01]10^5$

$$(8)$$

For $x \geqslant 0.5$: $C = [2.8339/(1 + 126.56x)^2 + 1.4132]10^5$

The Curie constant data and fitting from this equation are plotted in Figure 2. Amin et al.[7] also found a peak to occur in the Curie constant at the PZT 50/50 composition, although their peak value was somewhat larger than the results presented here (7.7 versus 4.3 $\times 10^{5}$°C). Tsuzuki et al.[14] experimentally found Curie constant values of 5.8 and 6.0 $\times 10^{5}$°C from single-crystal dielectric measurements on PZT 50/50 and 51/49 compositions.

The dielectric data listed in Table II are plotted in Figure 3, along with the theoretical calculations using the constants determined in this paper. The cross over of the $\eta'_{11}$ and $\eta'_{33}$ coefficients on the rhombohedral side of the diagram resulted from the extrapolation of the constants between the compositions where the data points occur, and may or may not be a real effect in the material. In any case the dielectric anisotropy becomes very small in this region. A more detailed discussion of the dielectric anisotropy will be provided Reference 4.

## IV  SUMMARY

The dielectric properties were measured on unpoled and poled polycrystalline samples at 4.2 K. These data were used to calculate the single-domain dielectric susceptibility coefficients using the Bruggeman relation. Values of the Curie constant and $\alpha_{112}$ and $\alpha_{123}$ coefficients were calculated from the single-domain data. Equations were then used to fit these values to determine the compositional dependence of the coefficients for use in the development of a thermodynamic theory for the PZT system. As a summary of this paper and the second paper of the series,[2] Table III gives values of the coefficients of the energy function.

The Curie constant was found to form a peak at the PZT 50/50 composition, similar to the compositional dependence of the electrostrictive constants.[15] This type of behavior is in agreement with earlier data in the literature,[7,14] but at this point it is not clear whether the peak is occurring due to the morphotropic boundary between the tetragonal and rhombohedral phases or due to some other effect. The Curie constant is a constant from the high-temperature cubic state, and thus should probably not be related to the morphotropic boundary. By studying the compositional dependence of these constants in other solid solution systems where a morphotropic boundary occurs away from the 50/50 composition [e.g. Pb-$(Mg_{1/3}Nb_{2/3})O_3$–$PbTiO_3$ system] may help to resolve some of these questions.

TABLE III

Values of the coefficients of the energy function at 25°C

| | Mole Fraction PbTiO₃ in PZT | | | | | | | | | | |
|---|---|---|---|---|---|---|---|---|---|---|---|
| | 0.0 | 0.1 | 0.2 | 0.3 | 0.4 | 0.5 | 0.6 | 0.7 | 0.8 | 0.9 | 1.0 |
| $T_c$ (°C) | 231.5 | 256.5 | 300.6 | 334.4 | 364.3 | 392.6 | 418.4 | 440.2 | 459.1 | 477.1 | 492.1 |
| $C$ ($10^5$ °C) | 2.027 | 2.050 | 2.083 | 2.153 | 2.424 | 4.247 | 2.664 | 1.881 | 1.642 | 1.547 | 1.500 |
| $Q_{11}$ ($10^{-2}$ m⁴/C²) | 4.620 | 5.080 | 5.574 | 6.175 | 7.260 | 9.660 | 8.116 | 7.887 | 8.142 | 8.504 | 8.900 |
| $Q_{12}$ ($10^{-2}$ m⁴/C²) | 1.391 | 1.540 | 1.720 | 1.997 | 2.708 | 4.600 | 2.950 | 2.480 | 2.446 | 2.507 | 2.600 |
| $Q_{44}$ ($10^{-2}$ m⁴/C²) | 4.464 | 4.900 | 5.165 | 5.522 | 6.293 | 8.190 | 6.710 | 6.356 | 6.417 | 6.569 | 6.750 |
| $a_1$ ($10^7$ m/f) at 25 °C | 4.582 | 6.376 | 7.470 | 8.116 | 7.904 | 4.887 | 8.340 | 12.47 | 14.84 | 16.17 | 17.08 |
| $a_{11}$ ($10^7$ m⁵/C⁴) | 52.35 | 41.25 | 31.29 | 22.30 | 13.62 | 4.764 | 3.614 | 0.6458 | 3.050 | 5.845 | 7.253 |
| $a_{12}$ ($10^8$ m⁵/C⁴) | 16.71 | 4.222 | 0.0345 | 1.688 | 2.391 | 1.735 | 3.233 | 5.109 | 6.320 | 7.063 | 7.500 |
| $\zeta$ ($10^6$ m⁵/C⁴) | 34.42 | 0.2897 | 9.284 | 11.75 | 11.26 | 6.634 | 10.78 | 15.52 | 18.05 | 19.44 | 20.32 |
| $a_{111}$ ($10^8$ m⁹/C⁴) | 5.932 | 5.068 | 4.288 | 3.560 | 2.713 | 1.336 | 1.859 | 2.348 | 2.475 | 2.518 | 2.606 |
| $a_{112}$ ($10^8$ m⁹/C⁴) | 311.2 | 34.45 | 18.14 | 15.27 | 12.13 | 6.128 | 8.503 | 10.25 | 9.684 | 8.099 | 6.100 |
| $a_{123}$ ($10^9$ m⁹/C⁴) | 104.1 | 8.797 | 7.545 | 7.052 | 5.690 | 2.894 | 4.063 | 5.003 | 4.901 | 4.359 | 3.660 |
| $\zeta$ ($10^9$ m⁹/C⁴) | 84.41 | 13.39 | 4.627 | 3.176 | 2.402 | 1.183 | 1.596 | 1.851 | 1.652 | 1.256 | 0.7818 |

# REFERENCES

1  M. J Haun, E. Furman, S. J Jang and L. E. Cross, "Thermodynamic Theory of the Lead Zirconate-Titanate Solid Solution System, Part I. Phenomenology," *Ferroelectrics* to be published with this paper.

2. M J Haun, E. Furman, H. A. McKinstry and L. E. Cross, "Thermodynamic Theory of the Lead Zirconate-Titanate Solid Solution System, Part II: Tricritical Behavior," *Ferroelectrics* to be published with this paper.

3  M J Haun, E. Furman, T R. Halemane and L. E. Cross, "Thermodynamic Theory of the Lead Zirconate-Titanate Solid Solution System, Part IV· Tilting of the Oxygen Octahedra," *Ferroelectrics* to be published with this paper.

4  M. J. Haun, E. Furman, S. J. Jang and L. E. Cross, "Thermodynamic Theory of the Lead Zirconate-Titanate Solid Solution System, Part V· Theoretical Calculations," *Ferroelectrics* to be published with this paper.

5  A Amin, *Phenomenological and Structural Studies of Lead Zirconate-Titanate Piezoceramics*, Ph D Thesis in Solid State Science, The Pennsylvania State University (1979)

6  A. Amin, L. E. Cross and R. E. Newnham, *Ferroelectrics*, 37, 647 (1981)

7  A Amin, M. J Haun, B Badger, H. A. McKinstry and L E Cross, *Ferroelectrics*, 65, 107 (1985)

8  Z. Q Zhuang, M. J Haun, S J. Jang and L E Cross, *Advanced Ceram. Mat.*, 3, 485 (1988)

9  A. V Turik, M. F Kupriyanov, E. N Sidorenko and S M Zaitsev, Zh. Tekh Fiz 50, 2146 (1980) [Sov. Phys. Tech. Phys. 25, 1251 (1980)].

10  Z. Q Zhuang, M. J. Haun, S. J. Jang and L. E. Cross, *Proceedings of the 6th IEEE International Symposium on the Applications of Ferroelectrics*, Lehigh, PA, edited by Van Wood (IEEE, New York, 1986) pp 394–397

11  D Berlincourt and H A. Krueger, *J Appl. Phys.* 30, 1804 (1959).

12. R. W Whatmore, R. Clarke and A. M. Glazer, *J Phys C Solid State Phys*, 11, 3089 (1978)

13  M J Haun, E. Furman, S J Jang, H. A. McKinstry and L. E. Cross, *J Appl. Phys* 62, 3331 (1987)

14  K. Tsuzuki, K. Sakata and M. Wada, *Ferroelectrics*, 8, 501 (1974)

15  M J Haun, Z. Q Zhuang, E. Furman, S J Jang and L E Cross, *J Am. Ceram Soc* 72, 1140 (1989)

APPENDIX 27

# THERMODYNAMIC THEORY OF THE LEAD ZIRCONATE-TITANATE SOLID SOLUTION SYSTEM, PART IV: TILTING OF THE OXYGEN OCTAHEDRA

## M. J. HAUN,† E. FURMAN,‡ T. R. HALEMANE§ and L. E. CROSS

*Materials Research Laboratory, The Pennsylvania State University, University Park, PA 16802, USA*

Values of coefficients related to the tilting of the oxygen octahedra in the low-temperature rhombohedral phase of the lead zirconate-titanate (PZT) solid solution system are needed in the development of a thermodynamic theory of the PZT system. In this paper these coefficients will be determined from experimental spontaneous strain and oxygen octahedral tilt angle data.

Values of the tilt angle related coefficients $\beta_1$, $\beta_{11}$, and $\phi$ are assumed to be independent of temperature, and are then related to $P_L$, $\theta_L$, and $T_R$, where $P_L$ and $\theta_L$ are the spontaneous polarization and tilt angle of the low-temperature rhombohedral phase at the transition temperature $T_R$ between tilted and untilted structures.

$P_L$ and $\theta_L$ are derived from experimental data for the PZT 90/10 composition, and used together with spontaneous strain values at this composition to determine electrostrictive ($Q_{ij}$) and rotostrictive ($R_{ij}$) constants. These constants are then in turn used to derive $P_L$ and $\theta_L$ values for other PZT compositions from spontaneous strain vs temperature at each composition, and in the final paper in this sequence to derive the $\beta_1$, $\beta_{11}$, and $\phi$ values for these compositions

## I. INTRODUCTION

This paper is the fourth paper in a series of five papers[1-4] describing the development of a thermodynamic theory for the entire lead zirconate-titanate (PZT) solid solution system. In the low-temperature rhombohedral phase in the PZT system the oxygen octahedra tilt or rotate about the polar axis. In the first paper of this series the oxygen octahedral tilt angle was included in the PZT energy function as an order parameter [see Equation (1) in Reference 1] to account for the low-temperature rhombohedral phase. In this paper the tilt angle related coefficients of the energy function will be determined.

## II. EVALUATION OF THE TILT ANGLE RELATED COEFFICIENTS

The tilt angle related coefficients will be determined from the available experimental low-temperature rhombohedral spontaneous strain and tilt angle data. Multiplying the energy of the low-temperature rhombohedral state [Equation (12) in

Reference 1] by the Curie constant results in the following relation:

$$F_{R(LT)} \quad \Delta GC = 3\alpha_1 CP_3^2 - \zeta CP_3^4 - \xi CP_3^6$$

$$+ 3\beta_1 C\theta_3^2 - 3\beta_{11} C\theta_3^4 - 3\phi CP_3^2\theta_3^2. \quad (1)$$

$$\text{where} \quad \phi C = (\gamma_{11} + 2\gamma_{12} + \gamma_{44})C \quad (2)$$

$\zeta C$ and $\xi C$ were defined by Equation (24) in Reference 2.

Equations for the spontaneous polarization $P_3$ and tilt angle $\theta_3$ can be found from the first partial derivative relations [Equations (17) and (18) in Reference 1]:

$$P_3^2 \text{ and } \theta_3^2 = \frac{-b + [b^2 - 4ac]^{1/2}}{2a}.$$

$$\text{where for } P_3^2: \quad a = \xi C$$

$$b = \tfrac{2}{3}\zeta C - (\phi C)^2/(2\beta_{11} C)$$

$$c = \alpha_1 C - \beta_1 C\phi C/(2\beta_{11} C) \quad (3)$$

$$\text{and for } \theta_3^2: \quad a = 4\xi c(\beta_{11} C)^2/(\phi C)^2$$

$$b = \phi C - \tfrac{4}{3}\beta_{11}C/(\phi C)[3\xi C\beta_1 C/(\phi C) - \zeta C]$$

$$c = \alpha_1 C - \beta_1 C/(\phi C)[\xi C\beta_1 C/(\phi C) - \tfrac{2}{3}\zeta C] \quad (4)$$

Values of the $\alpha_1 C$, $\zeta C$, and $\xi C$ coefficients were determined in the second paper in this series. Thus the tilt angle related coefficients $\beta_1 C$, $\beta_{11} C$, and $\phi C$ are the only unknown coefficients in these equations. These coefficients were assumed to be independent of temperature, and were related to three new constants at the high to low temperature rhombohedral transition temperature. $T_R$, using the first partial derivative stability conditions [Equations (17) and (18) in Reference 1], and by equating the energies of the two phases at the boundary [Equations (1) above and Equation (37) in Reference 2]. This resulted in the following equations:

$$\phi C = -1/\phi_L^2[2(3\alpha_{11}C + \alpha_{12}C)(P_H^2 - P_L^2)$$

$$+ (15\alpha_{111}C + 14\alpha_{12}C + \alpha_{123}C)(P_H^4 - P_L^4)] \quad (5)$$

$$\beta_1 C = -\phi CP_L^2 + 1/\theta_L^2[(T_R - T_0)/\varepsilon_0(P_H^2 - P_L^2)$$

$$+ \tfrac{2}{3}\zeta C(P_H^4 - P_L^4) - \tfrac{1}{3}\xi C(P_H^6 - P_L^6)] \quad (6)$$

$$\beta_{11}C = 1/\theta_L^4[(T_R - T_0)/(2\varepsilon_0)(P_H^2 - P_L^2)$$

$$+ \zeta C/3(P_H^4 - P_L^4) + \xi C/3(P_H^6 - P_L^6) - \beta_1 C\theta_L^2 - \phi CP_L^2\theta_L^2] \quad (7)$$

$P_H$ and $P_L$ are the spontaneous polarization of the high and low temperature rhombohedral states at $T_R$. $\theta_L$ is the tilt angle of the low-temperature rhombohedral state at $T_R$.

$P_H$ can be calculated from Equation (23) in Reference 2 using the constants determined in Reference 2. Thus by determining $T_R$, $P_L$, and $\theta_L$ the $\phi C$, $\beta_1 C$, and $\beta_{11} C$ constants can be calculated. When calculating these constants, the $\phi C$ constant

should be found first from Equation (5). This value should then be used in Equation (6) to calculate the $\beta_1 C$ constant. Finally the values of the $\phi C$ and $\beta_1 C$ constants should be used in Equation (7) to solve for the $\beta_{11} C$ constant.

The following least squares fit of the experimental phase diagram was used to determine the compositional dependence of $T_R$:

For $x \leqslant 0.15$:     $T_R = a + bx + cx^2$

where $a = -105.07$,     $b = 2812.6$,     $c = -7665.9$

For $x \geqslant 0.15$:     $T_R = a + bx + cx^2 + dx^3 + ex^4$

where $a = 5.5465$,     $b = 2388.8$,     $c = -13864.$,          (8)

$d = 32282.$,     $e = -32675.$

In fitting the data with $x \geq 0.15$ an additional data point was added at the PZT 50/50 composition at a temperature of $-273°C$. This was required to keep the high to low temperature rhombohedral boundary from crossing the morphotropic boundary at low temperatures. The fit of the experimental data using these equations is shown in Reference 4 in Figure 2.

Glazer et al.[5] determined the spontaneous tilt angle for the PZT 90/10 composition at 25 and 60°C. The values of the tilt angle reported represent the rotation about the cubic [111] direction. In the three-dimensional energy function used in this theory components ($\theta_3$) of the resultant tilt were included. Thus the component tilts were first calculated from the resultant tilts that were reported in the literature. The following relation was derived to relate the component tilts ($\theta_3$) about each orthogonal axis to the resultant tilt ($\theta_S$) about the body diagonal:

$$\cos \theta_3 = \tfrac{1}{2}(2 - \cos \theta_S) \qquad (9)$$

Another relation was also found to give similar results as Equation (9) for small angles:

$$3^{1/3} \theta_3 = \theta_S \qquad (10)$$

Equation (10) was used to calculate the component tilt ($\theta_3$) from Glazer et al.'s data.

This data was then used to determine the $P_L$ and $\theta_L$ constants for the PZT 90/10 composition that gave the best least-squares fit using Equation (4) combined with Equations (5)–(8). The resulting values of $P_L$ and $\theta_L$ are listed in Table I.

TABLE I

Values of $P_L$ and $\theta_L$

| Zr/Ti | $P_L$ (C m$^{-2}$) | $\theta_L$ (deg ) |
|---|---|---|
| 90/10 | 0 275 | 1 82 |
| 80/20 | 0 271 | 1 99 |
| 70/30 | 0 280 | 1 49 |
| 60/40 | — | 0 392 |
| 50/50 | 0 380 | — |

The experimental data and the fit using these constants is shown in Figure 5 in Reference 4.

The rotostrictive $R_{44}$ constant was used to fit the low-temperature rhomoohedral spontaneous strain $x_4$ data (from Reference 6) for the PZT 90/10 composition using Equation (24) from Reference 1, and the values of $P_L$ and $\theta_L$ determined above. Using the value of the electrostrictive constant $Q_{44}$ of 0.049 $m^4/C^2$ from Reference 7, resulted in a poor fit of the experimental data. However, a good fit was obtained by varying both the $Q_{44}$ and $R_{44}$ constants. The best least-squares fit resulted in $Q_{44}$ and $R_{44}$ values of 0.0433 $m^4/C^2$ and $-1.93 \times 10^{-4}$ deg$^{-2}$, respectively. The experimental strain data and the fit using these values is shown in Figure 1(a).

The change in the $Q_{44}$ constant from high to low temperature rhombohedral phases may indicate that the tilting of the oxygen octahedra influences the electrostriction, resulting in different electrostrictive constants in these two phases. Another possible cause of this could be that the tilt angle coefficients are temperature dependent and/or that a higher order tilt angle coefficient is needed ($\theta^6$ term). However, to not complicate matters any more than they already are, the $Q_{44}$ and $R_{44}$ constants of the low-temperature rhombohedral state were assumed to have the values given above independent of temperature and composition. The values of the electrostrictive constants of the high temperature rhombohedral state were still kept the same as given in Reference 7.

Using the same values of the $Q_{44}$ and $R_{44}$ constants given above for the PZT 90/ 10 composition, values of $P_L$ and $\theta_L$ were found that gave the best least-squares fit of the experimental spontaneous strain data for the PZT 80/20 composition. The values are listed in Table I. The experimental data and fit using these values are plotted in Figure 1(b).

The spontaneous strain $x_4$ was measured at two temperatures in the low-temperature rhombohedral state for the PZT 70/30 composition. Since there were only two experimental data points, a procedure was used to combine these data with a single tilt angle value at 9K that was measured by Amin *et al.*[3] for the PZT 60/40 composition.

The first step was to make an initial guess at a value of $P_L$ for the PZT 70/30 composition. This value of $P_L$ was used with the $P_L$ values listed in Table I for the PZT 90/10 and 80/20 composition to solve for a quadratic compositional dependence of $P_L$ (three unknown constants and three data points). This equation was used to extrapolate a value of $P_L$ to the PZT 60/40 composition, which allowed a value of $\theta_L$ to be found that fit the tilt angle data at 9K. This value of $\theta_L$ was used with the $\theta_L$ values listed in Table I for the PZT 90/10 and 80/20 compositions to solve for

TABLE II

Values of the Tilt Angle Related Coefficients at 25°C

| | Mole Fraction PbTiO₃ in PZT | | | |
|---|---|---|---|---|
| | 0 1 | 0 2 | 0 3 | 0 4 |
| $\beta_1$ ($10^5$ J/m³ Deg²) | 5 618 | 3 395 | 4 343 | 29 79 |
| $\beta_{11}$ ($10^4$ J/m³ Deg⁴) | 2.506 | 1 674 | 1 682 | 4 174 |
| $\phi$ ($10^9$ m/F Deg²) | −9.626 | −6 423 | −6.502 | −31 82 |
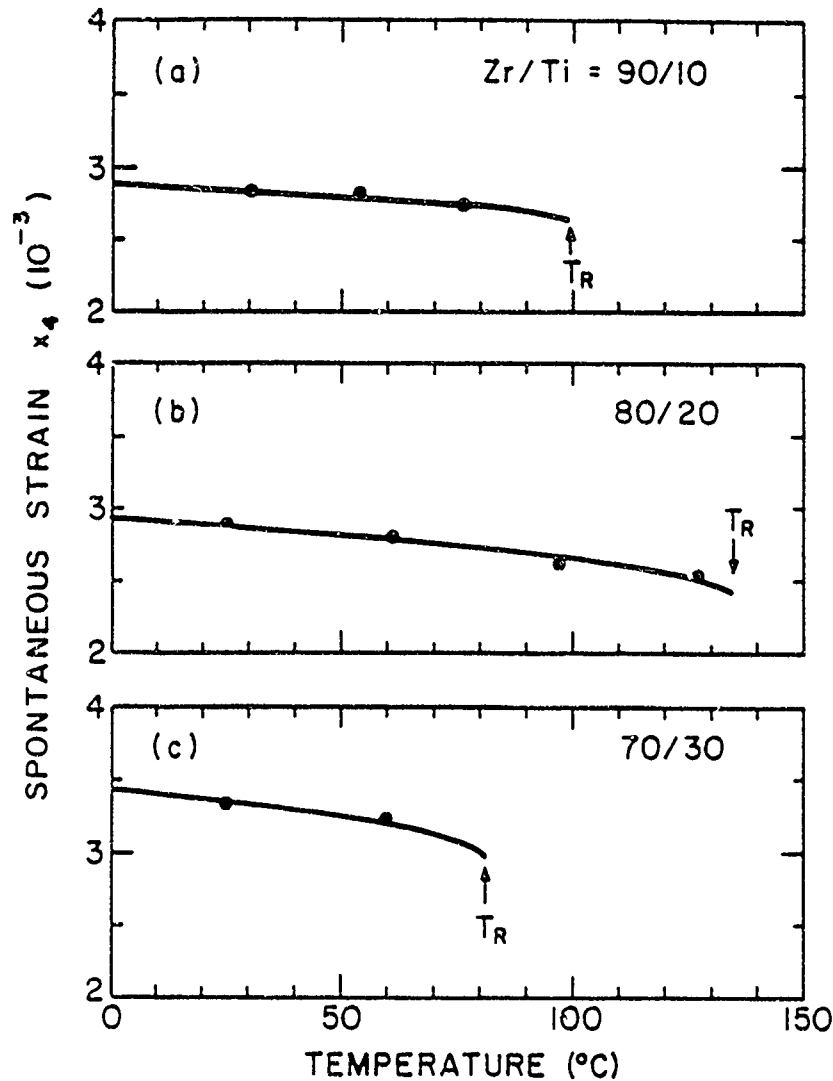
FIGURE 1  The spontaneous strain $x_4$ in the low-temperature rhombohedral state plotted versus temperature for the PZT 90/10, 80/20, and 70/30 compositions. The data points are from Reference 6 The solid curves are the theoretical fits of the data.

a quadratic compositional dependence of $\theta_L$. This equation was then used to calculate a value of $\theta_L$ back at the PZT 70/30 composition. This value was used with the initial guess of $P_L$ to determine the spontaneous strain $x_4$, and to calculate the least-squares error with the two data points. Another guess of $P_L$ for the PZT 70/ 30 composition was then made, and the entire procedure was repeated until the values that gave the best least-squares error were found.

A problem developed from the procedure described above: $P_L$ became less than $P_H$ for compositions near PZT 60/40. The difference in the values between $P_L$ and $P_H$ decreased from around PZT 80/20 to PZT 60/40, which seems to be in agreement with pyroelectric measurements.[9] However, it was felt that $P_L$ should probably not become less than $P_H$ (the polarization should increase when going to the low-temperature rhombohedral phase). Thus an additional manipulation was used to

keep $P_L$ from becoming less than $P_H$. To allow the difference between $P_L$ and $P_H$ to decrease as the titanium content increased, but to keep this difference from going to zero within the stability region of the low-temperature rhombohedral phase, an additional $P_L$ data point was included in determining the compositional dependence of $P_L$. This value was arbitrarily chosen by letting $P_L$ become equal to $P_H$ at the PZT 50/50 composition. This effectively moved the composition where $P_L$ became equal to $P$ into a metastable region.

This value of $P_L$ at PZT 50/50 (listed in Table I) was then used with the previous values of $P_L$ for the PZT 90/10, 80/20, and 70/30 compositions to determine the compositional dependence of $P_L$ by fitting the data with a cubic polynomial equation (four unknowns and four data points). This equation was used to calculate a $P_L$ value back at the PZT 60/40 compositions. Using this value a new $\theta_L$ value for PZT 60/40 was found by refitting the experimental tilt angle data point at 9 K. This value of $\theta_L$ for PZT 60/40 was then used with the previous values of $\theta_L$ for the PZT 90/10, 80/20, and 70/30 compositions to determine the compositional dependence of $\theta_L$ from a cubic polynomial fit.

The final values of $P_L$ and $\theta_L$ used in the fitting are listed in Table I, and plotted in Figure 2. The cubic compositional fits, also plotted in Figure 2, of these data are:

$$P_L \text{ and } \theta_L = a + bx + cx^2 + dx^3.$$

where for $P_L$: $a = 0.28079$

$$b = -0.030117$$

$$c = -0.46150$$

$$d = 1.8367 \tag{11}$$

and for $\theta_L$: $a = 0.91540$

$$b = 12.967$$

$$c = -40.255$$

$$d = 11.417 \tag{12}$$

The experimental spontaneous strain data and final fit for the PZT 70/30 composition are plotted in Figures 1(c). The experimental tilt angle data point and final fit for the PZT 60/40 composition is plotted in Figure 5 in Reference 4.

With the compositional dependences of $T_R$, $P_L$, and $\theta_L$ determined from Equations (8), (11), and (12), the tilt angle related constants $\beta_1 C$, $\beta_{11} C$, and $\phi C$ can be calculated from Equations (5)–(7).


## III.  SUMMARY

The tilt angle related coefficients, $\beta_1 C$, $\beta_{11} C$, and $\phi C$, were related to three new constants, $T_R$, $P_L$ and $\theta_L$, at the transition between the high and low temperature
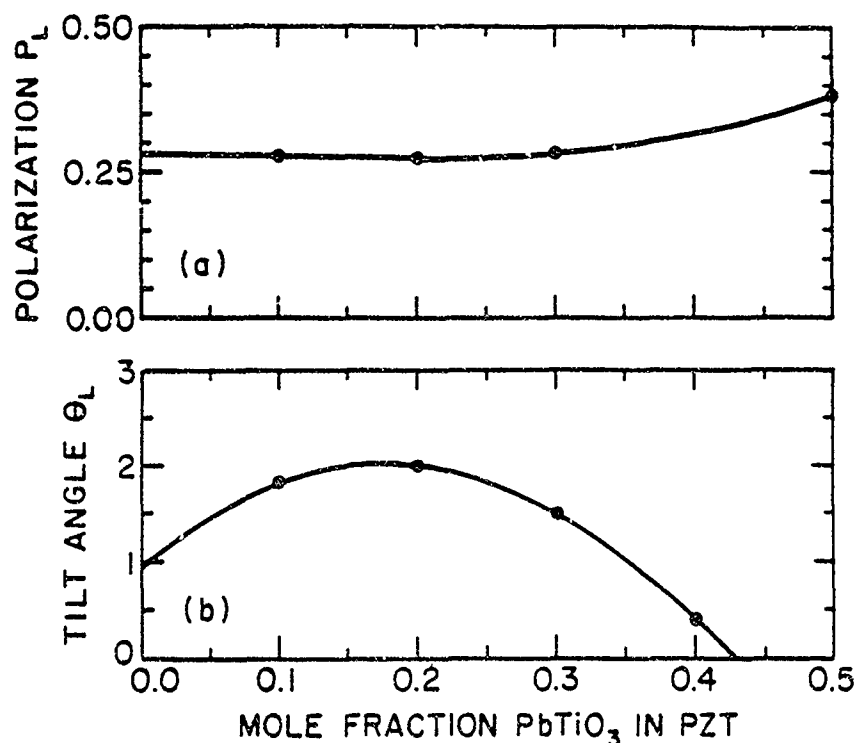
FIGURE 2   The spontaneous polarization ($P_L$) and tilt angle ($\theta_L$) of the low-temperature rhombohedral state at $T_R$ plotted versus composition   The data points are from Table I   The solid curves are fits of the data using Equations (11) and (12)

rhombohedral phases. The transition temperature between these phases, $T_R$, was determined from the phase diagram. Values of the spontaneous polarization and tilt angle of the low-temperature rhombohedral phase at $T_R$, $P_L$ and $\theta_L$, were determined from experimental spontaneous strain and tilt angle data. These values were then fit with equations to determine the compositional dependence of $P_L$ and $\theta_L$. These equations will be used in the last paper in this series to calculate the values of $\beta_1$, $\beta_{11}$, and $\phi$ for theoretical calculations of the phase stability and properties of the low-temperature rhombohedral phase. As a summary of this paper Table II gives values of these constants at four PZT compositions.

REFERENCES

1   M. J Haun, E. Furman, S. J Jang and L. E. Cross.  "Thermodynamic Theory of the Lead Zirconate-Titanate Solid Solution System, Part I. Phenomenology."  Ferroelectrics to be published with this paper.

2   M. J Haun, E Furman, H. A. McKinstry and L. E. Cross. "Thermodynamic Theory of the Lead Zirconate-Titanate Solid Solution System, Part II Tricritical Behavior." Ferroelectrics to be published with this paper

3   M. J Haun, Z. Q Zhuang, E. Furman, S J Jang and L. E. Cross. "Thermodynamic Theory of the Lead Zirconate-Titanate Solid Solution System, Part III. Curie Constant and Sixth-order Polarization Interaction Dielectric Stiffness Coefficients." Ferroelectrics to be published with this paper.

4   M. J Haun, E. Furman, S. J Jang and L. E. Cross. "Thermodynamic Theory of the Lead Zirconate-Titanate Solid Solution System, Part V Theoretical Calculations." Ferroelectrics to be published with this paper.

5. A. M. Glazer, S. A Mabud and R. Clarke. *Acta Cryst* . B34, 1060 (1978).

6  M. J  Haun, Y  H. Lee, H. A. McKinstry and L  E  Cross. *Advances in X-ray Analysis* Vol 30, edited by C  S. Barrett, J  V  Gilfrich, R  Jenkins. D  E  Leyden, J  C  Russ. and P  K  Predecki (Plenum Press, New York, 1987) pp  473–481

7  M  J  Haun, Z. Q  Zhuang, E. Furman, S  J  Jang and L  E  Cross. *J  Am  Ceram  Soc* . 72, 1140 (1989).

8  A. Amin, R. E. Newnham, L. E. Cross and D. E  Cox. *J  Solid State Chemistry* 37, 248 (1981)

9  Z. Q  Zhuang, M. J  Haun, A. Bhalla, S. J. Jang and L  E  Cross. unpublished data.

APPENDIX 28

# THERMODYNAMIC THEORY OF THE LEAD ZIRCONATE-TITANATE SOLID SOLUTION SYSTEM, PART V: THEORETICAL CALCULATIONS

M. J. HAUN,† E. FURMAN,‡ S. J. JANG and L. E. CROSS

*Materials Research Laboratory, The Pennsylvania State University,
University Park, PA 16802, USA*

In this final paper of a sequence of five papers presenting details of a thermodynamic phenomenology for the whole $PbZrO_3$ $PbTiO_3$ solid solution family, the constants derived in the earlier papers are used to calculate the temperature and composition dependence of the Elastic Gibbs Free Energy $\Delta G_1$ at zero stress, the spontaneous electric polarization and spontaneous tilt of the oxygen octahedra in a single domain, the anisotropic weak field dielectric permittivity and the piezoelectric constants for compositions all across the phase diagram.

These data can be used to determine the intrinsic component of the behavior of any pure lead zirconate lead titanate in any part of the phase field and at any temperature, and thus can form a first step in the separation of the experimentally observed properties into their intrinsic (single domain) component and their extrinsic domain and defect related responses

The function proposed is certainly not the final word for PZT, and will clearly be subjected to continuous modification and improvement as new and better experimental data becomes available. The purpose of the exercise has been to correlate a very wide panoply of experimental data with a single function, and to extract from it the constants which would be directly accessible if single domain single crystals could be grown at the interesting $PbZrO_3$ $PbTiO_3$ compositions

## I INTRODUCTION

This paper is the final paper in a series of five papers[1–4] describing the development of a thermodynamic theory for the entire lead zirconate-titanate (PZT) solid solution system. In this paper theoretical calculations will be made using the equations that were derived in the first paper[1] of the series, and the values of the coefficients determined in the second, third, and fourth papers.[2–4] The antiferroelectric calculations will be made using the coefficients that were determined in Reference 5.

The free energies of each phase will be calculated in the next section and used to determine the phase diagram. In Section III the spontaneous polarization and tilt angle will be calculated. The dielectric and piezoelectric properties will then be calculated in Sections IV and V, followed by a summary and discussion of the future applications of this theory.

†Now at E. I. du Pont de Nemours & Co, Electronics Dept., Experimental Station. P O Box 80334. Wilmington. DE, 19880-0334
‡Now at Allied-Signal Inc., Metals and Ceramics Laboratory. P O Box 1021R. Morristown. NJ, 07960.

## II.  PHASE DIAGRAM

In the second paper of the series. products of the dielectric stiffness coefficients $(\alpha_{ij})$ and the Curie constant $(C)$ were shown to be independent of $C$. These new constants $(\alpha_{ij}C)$ can be used to calculate products of the free energies and the Curie constant $(\Delta GC)$, which are also independent of $C$. Since the Curie constant is the same in all of the solutions of the energy function. the $\Delta GC$ products can be used to determine the phase stability independently of the effect of the compositional dependence of $C$.

In Figure 1 the product of the energies and Curie constant $(C)$ are plotted versus composition at three temperatures. The solution with the lowest $\Delta GC$ product corresponds to the stable phase. and a phase transition occurs when the curves cross. At 25°C [Figure 1(c)] the tetragonal solution has the lowest $\Delta GC$ on the lead titanate side of the figure. and is thus the stable phase Moving across the
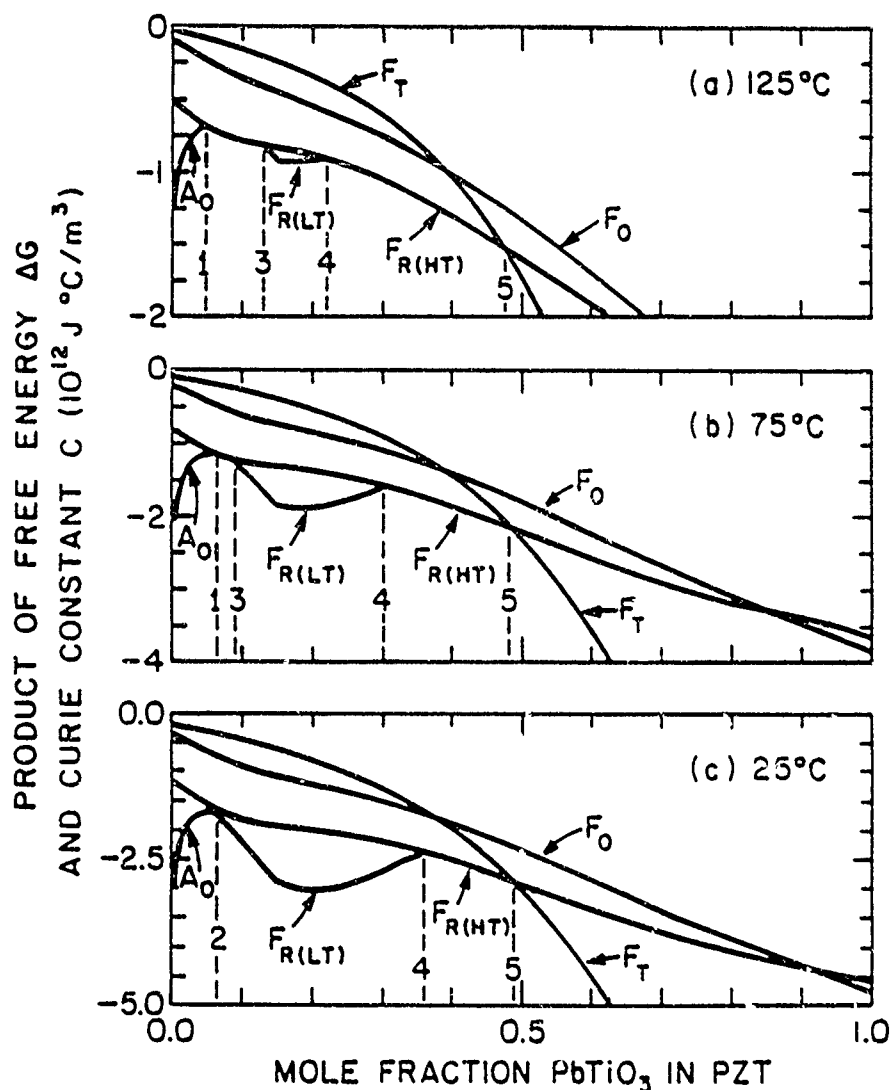


FIGURE 1    The product of the free energy $\Delta G$ and Curie constant plotted versus composition for the different solutions of the energy function.

figure towards lead zirconate the tetragonal phase remains stable to the dashed line labeled 5. At this point the $\Delta GC$ of the high-temperature rhombohedral solution becomes less than that of the tetragonal phase, and a phase transition occurs between these phases (the morphotropic phase boundary).

Continuing across the figure, the high-temperature rhombohedral phase remains stable to the dashed line labeled 4, where a transition to the low-temperature rhombohedral phase occurs. This phase is then stable until the dashed line labeled 2 is reached, and a transition to the antiferroelectric orthorhombic phase occurs. At higher temperatures an additional region of high-temperature rhombohedral phase develops between the low-temperature rhombohedral and antiferroelectric orthorhombic phase fields. The low-temperature rhombohedral phase field also becomes narrower as the temperature is increased.

The $\Delta GC$ curves for the low-temperature rhombohedral and antiferroelectric orthorhombic phases shown in Figure 1 were only drawn over the regions where these phases were stable. The compositional dependence of the antiferroelectric orthorhombic phase was determined by equating the energies of this phase with the high-temperature rhombohedral phase at the transition between these states (described in Reference 5). Since this transition only extends over a narrow compositional region, the above method will only apply over this region. Thus the energy of the antiferroelectric orthorhombic phase should only be calculated within this region.

In the case of the low-temperature rhombohedral phase the $\Delta GC$ can be calculated over a very small region into the adjacent phase fields, at which point either the spontaneous polarization becomes imaginary, or the low-temperature rhombohedral phase undergoes a metastable phase transition to the cubic state. At this point additional work needs to be conducted to more completely understand what is actually happening. This is particularly important in gaining a better understanding of the change in the spontaneous polarization from the high to low temperature rhombohedral phases, as will be discussed in more detail in the next section.

Calculating the $\Delta GC$ product of the ferroelectric orthorhombic phase provided an independent check on the values of the coefficients of the energy function. As shown in Figure 1 this phase was found to be metastable across the phase diagram, indicating that the ratios of the coefficients are at least in the right range.

By plotting the composition versus temperature where the $\Delta GC$ products of the solutions cross, the phase diagram is obtained as shown in Figure 2. The data points are from the experimental phase diagram,[6] and the solid curves are from the theoretical calculations. The excellent agreement between the experimental data and theoretical calculations is to be expected, because the data was used to determine values of the coefficients in such a way as to cause the energies of the adjacent phases to be equal at the transition. However, this agreement shows that the energy function and values of the coefficients that have been determined will quantitatively model all of the known phase transitions of the PZT solid solution system.

The inflection point in the transition temperature $T_C$ between the cubic and high-temperature rhombohedral phases near the PZT 90/10 composition (see Figure 2) appears to be due to the tricritical behavior. The Curie-Weiss temperature $T_0$ should
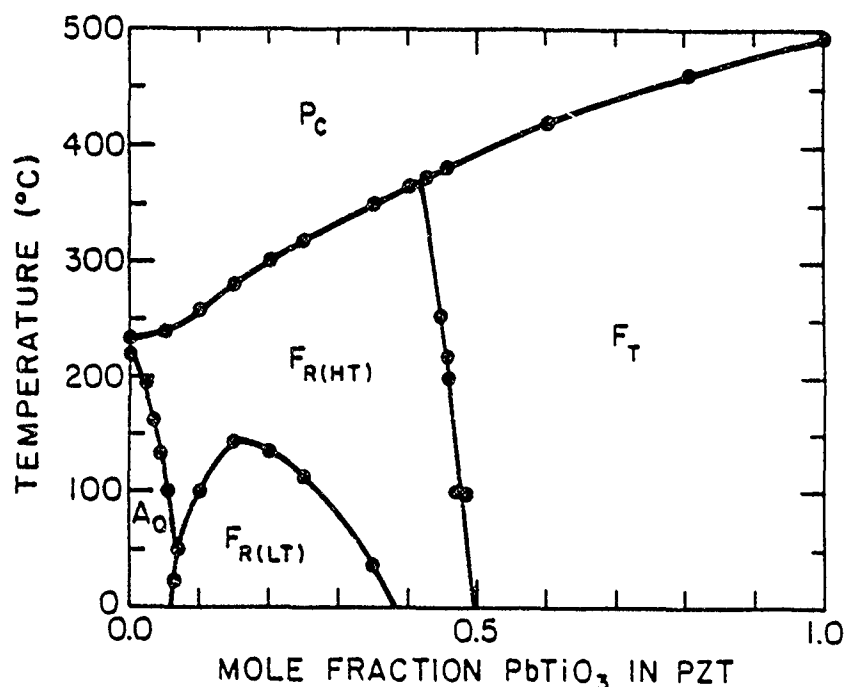
FIGURE 2  Superposition of the theoretical and experimental phase diagrams  The data points are from the experimental phase diagram.[3] The solid curves are the theoretical calculations

form a continuous function with a continuous slope across the phase diagram. because it is determined from the cubic phase. In the second-order region $T_C$ is equal to $T_0$. but in the first-order regions $T_0$ becomes less than $T_C$. The $T_C - T_0$ difference increases rapidly over a narrow compositional region. from zero at the tricritical point at 42°C for lead zirconate (see Figure 9 in Reference 2).

A question now arises as to why a similar change in $T_C$ is not seen at the second tricritical point near the PZT 28/72 composition. This may be because the $T_C - T_0$ difference only changes from zero at the tricritical point to 13.4°C for lead titanate, and this smaller change occurs over a much wider compositional range. In addition there is not enough $T_C$ data on the phase diagram in this region to really be able to notice this type of change in $T_C$. Additional high-temperature x-ray diffraction work is needed to more precisely locate the second tricritical point. In the process of this work it would be interesting to try and see if $T_C$ does change in a similar (but smaller) way as occurs on the lead zirconate side.

## III.  SPONTANEOUS POLARIZATION AND TILT ANGLE

Figure 3 shows the calculated spontaneous polarization plotted versus temperature for five tetragonal PZT compositions. The first order transitions of the $PbTiO_3$ and PZT 20/80 compositions can be seen by the discontinuous changes in the polarization at $T_C$. The other three compositions have second order transitions causing the polarization to change continuously at $T_C$. The dielectric stiffness coefficient
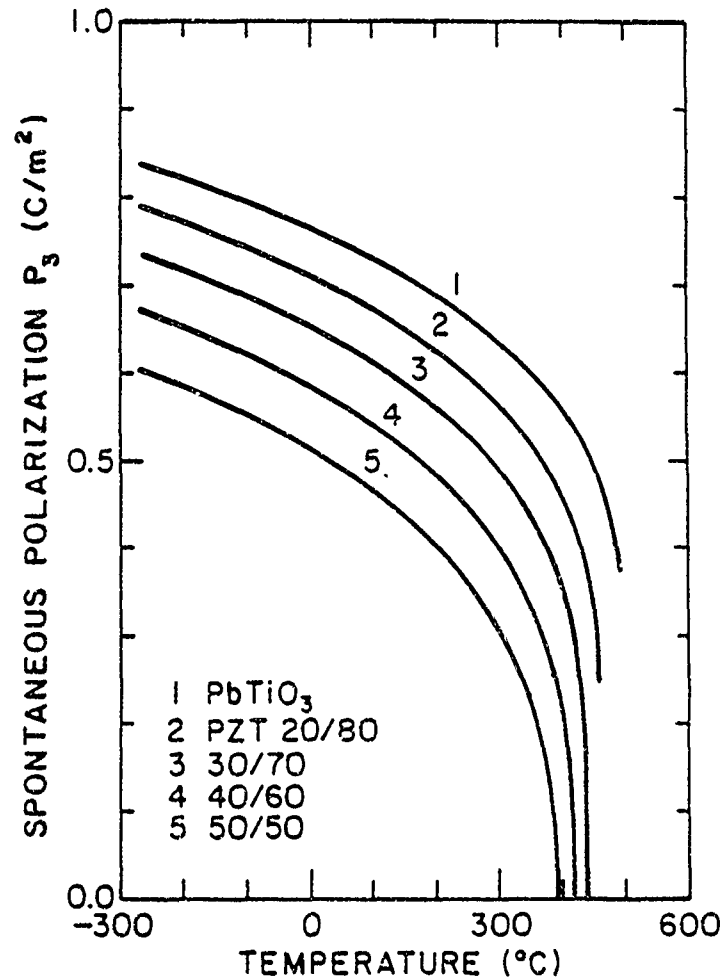
FIGURE 3    The theoretical spontaneous polarization $P$, plotted versus temperature for five tetragonal compositions.

$\alpha_{11}$ changes sign at a tricritical point between the PZT 20/80 and 30/70 compositions causing the transition to change from first to second order. This tricritical point was estimated to occur at the PZT 28/72 composition from an extrapolation of $\alpha_{11}$ presented in Reference 2.

The calculated spontaneous polarization data shown in Figure 3 are in good agreement with the available experimental data. The value of 0.75 C/m$^2$ at 25°C for lead titanate is equal to Gavrilyachenko et al.'s[7] experimental single-crystal measurement. The polarization values for the PZT 40/60 composition are slightly larger than the single-crystal measurements from 25 to 200°C of Tsuzuki et al.[8] They commented that the polarization was not completely saturated in their hysteresis loops, which would result in lower values of the polarization. The close agreement between the calculated polarization and experimental measurements indicates that the proper values of the electrostrictive constants were used.

The spontaneous polarization of four rhombohedral compositions with the high to low temperature rhombohedral phase transition is plotted versus temperature in Figure 4. The resultant polarization ($= 3^{1/2}P_3$) along the [111] direction was plotted in this figure. The small first order change in the polarization of the PZT
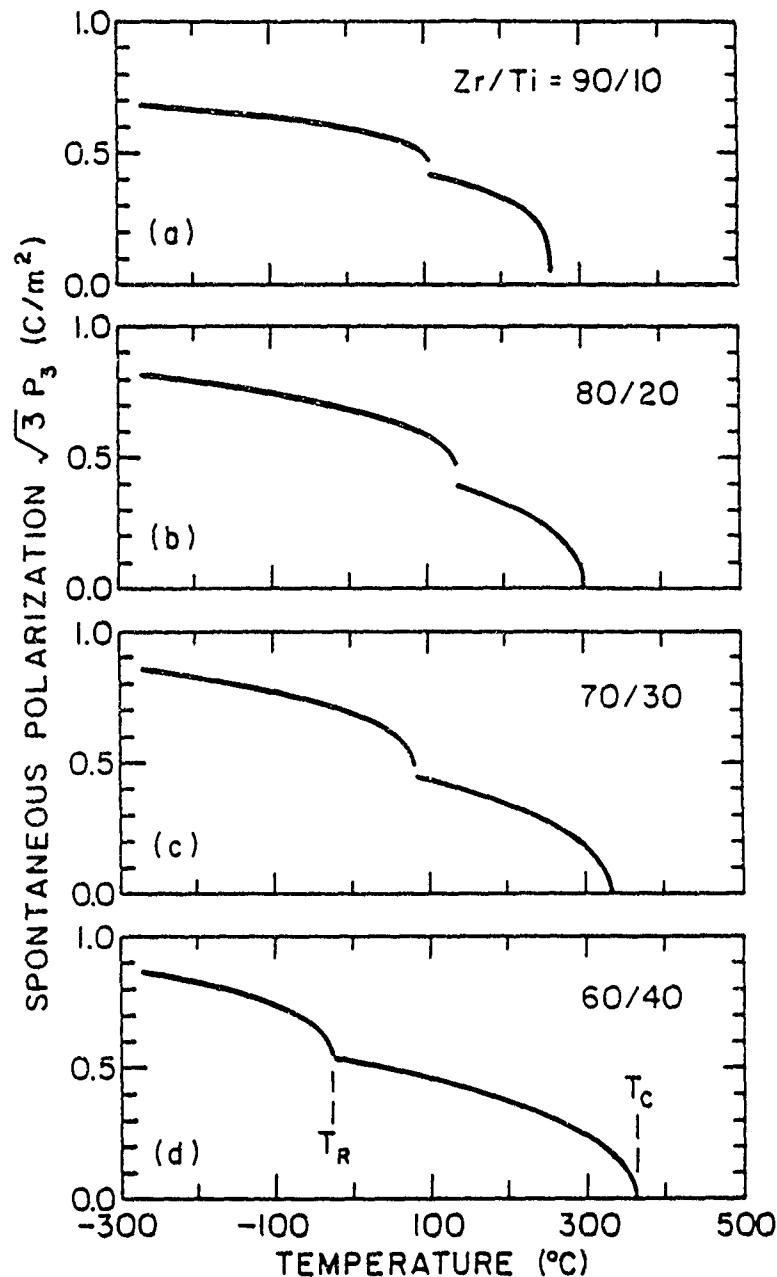
FIGURE 4   The theoretical resultant spontaneous polarization $P_\lambda$ $(3^{1:}P)$ plotted versus temperature for four compositions with the high to low temperature rhombohedral phase transition

90/10 composition at the high-temperature rhombohedral to cubic transition $(T_C)$ can be seen in Figure 4(a). The other three compositions [Figures 4(b)–(d)] all have a second order transition at $T_C$ This is because the fourth order rhombohedral dielectric stiffness $(\alpha_{11} - \alpha_{12})$ is slightly negative for the PZT 90/10 composition. and then changes sign at a tricritical point (close to PZT 90/10) and becomes positive for the other three compositions.

The high to low temperature rhombohedral phase transition is first order for all compositions, as can be seen in Figure 4 by the discontinuous change in the polarization at this transition. This discontinuous change in the polarization increases

from PZT 90/10 to 80/20. but then decreases as the titanium content is increased further. and becomes very small for the PZT 60/40 composition. This may explain why Zhuang et al.[9] found from pyroelectric measurements that the polarization only slightly changes through the high to low temperature rhombohedral transition for the PZT 70/30 and 60/40 compositions. but a large change occurs for the PZT 90/10 and 94/6 compositions.

The spontaneous polarization data for the PZT 90/10 composition [Figure 4(a)] is in fairly good agreement with the single-crystal measurements by Clarke and Glazer.[10] Some of their experimental data in the high-temperature rhombohedral region was used to determine the electrostrictive $Q_{44}$ constant for this composition. and thus good agreement occurs in this region. However. their data showed a decrease in the polarization on cooling in the high-temperature rhombohedral state close to the transition to the low-temperature phase. possibly due to a leakage of charge during their measurements. In this region the theoretically calculated polarization continues to increase as the temperature is decreased.

The spontaneous tilt angle was also calculated versus temperature for several compositions as shown in Figure 5. The resultant tilt angle about the cubic [111] direction ( = $3^{1/2}\theta_3$) was plotted. The data points are the only available experimental values of the tilt angle. and were determined from neutron diffraction by Glazer et al.[11] and Amin et al.[12] These data were used in determining values for two of the coefficients (see Reference 4). and thus the theory and experimental data should agree. The theoretical calculations can be used to determine values of the tilt angle at other compositions and temperatures. as shown in this figure.

The spontaneous tilt angle was also plotted in Figure 6 versus composition at several different temperatures. The curve labeled $\theta_L$ represents the tilt angle at the high to low temperature rhombohedral transition ($T_R$). The discontinuity in the slope of the curves at the PZT 85/15 composition occurs due to the relations that was used to fit $T_R$ [Equation (8) in Reference 4].

Figures 4 and 5 show that the spontaneous polarization and tilt angle increase very rapidly after transforming to the low-temperature rhombohedral phase. especially the compositions with greater titanium content. This may indicate a limitation of the present theory. For the PZT 70/30 and 60/40 compositions the discontinuous change in the polarization at the high to low temperature rhombohedral transition is very small compared to the sudden increase in polarization that occurs just below the transition. The increase in polarization in the low-temperature rhombohedral phase is even more noticeable when the polarization is plotted versus composition at different temperatures as shown in Figure 7. If the spontaneous polarization as a function composition does actually increase in the low-temperature rhombohedral phase as much as is shown in this figure. then it seems that the previous experimental measurements of the polarization on ceramic samples would have found a similar effect.

The polarization should increase going to the low-temperature rhombohedral phase. but the increase calculated from this theory seems to be too large. Two possible explanations of this large increase in polarization in the low-temperature rhombohedral phase will now be described.

The first possibility is that this large increase may actually occur. and that the previous measurements on ceramic samples missed this effect. because not enough
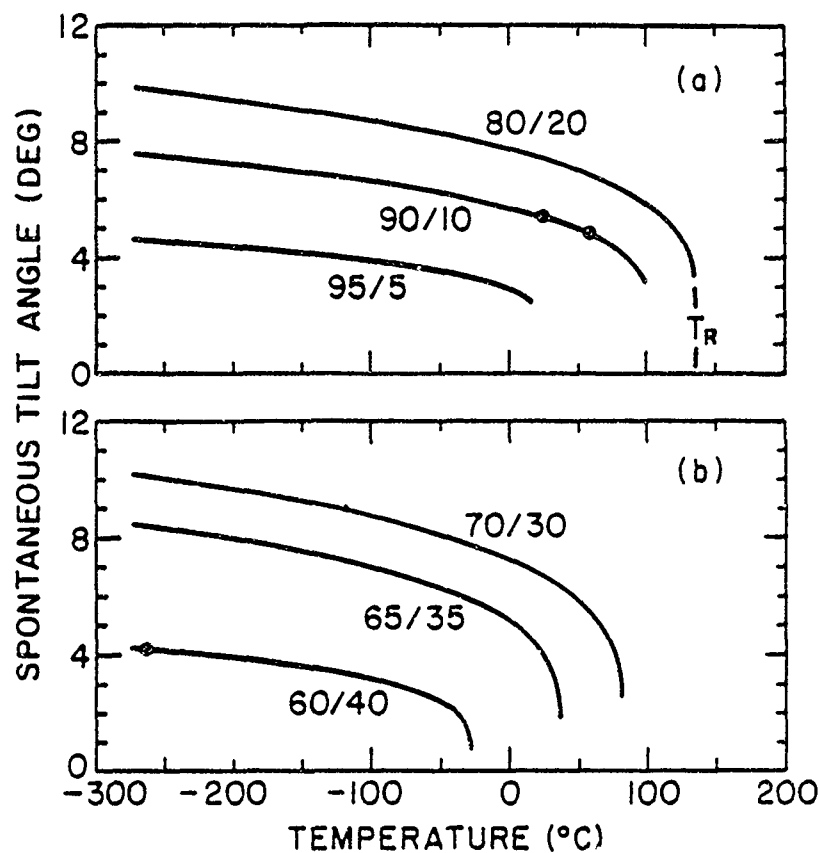
FIGURE 5    The resultant spontaneous tilt angle $\theta_s$ $(3^1\,^2\theta_3)$ plotted versus temperature  The data points are from References 11 and 12. The solid curves are the theoretical calculations.
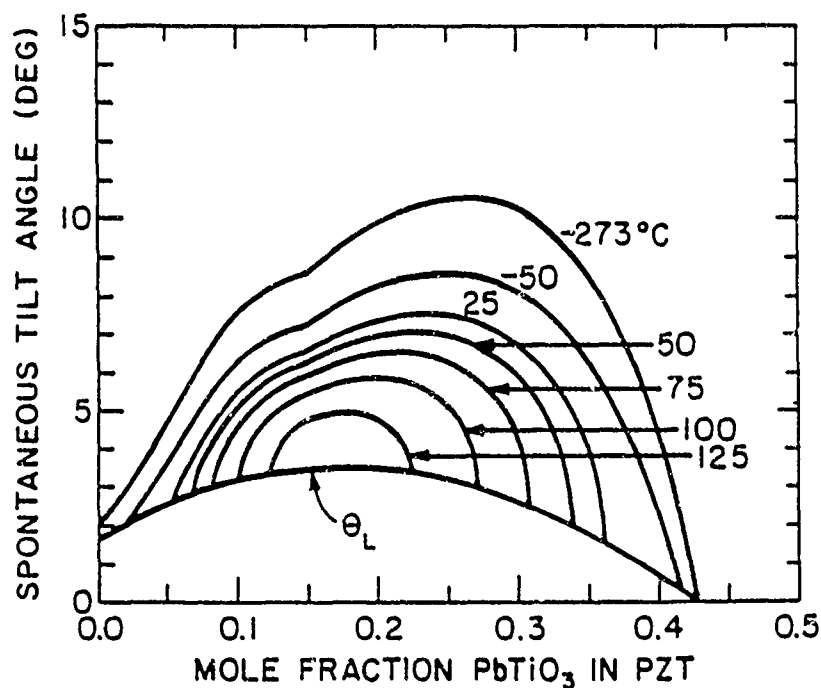


FIGURE 6    The theoretical resultant spontaneous tilt angle $\theta_s$ $(3^1\,^2\theta_3)$ plotted versus composition.
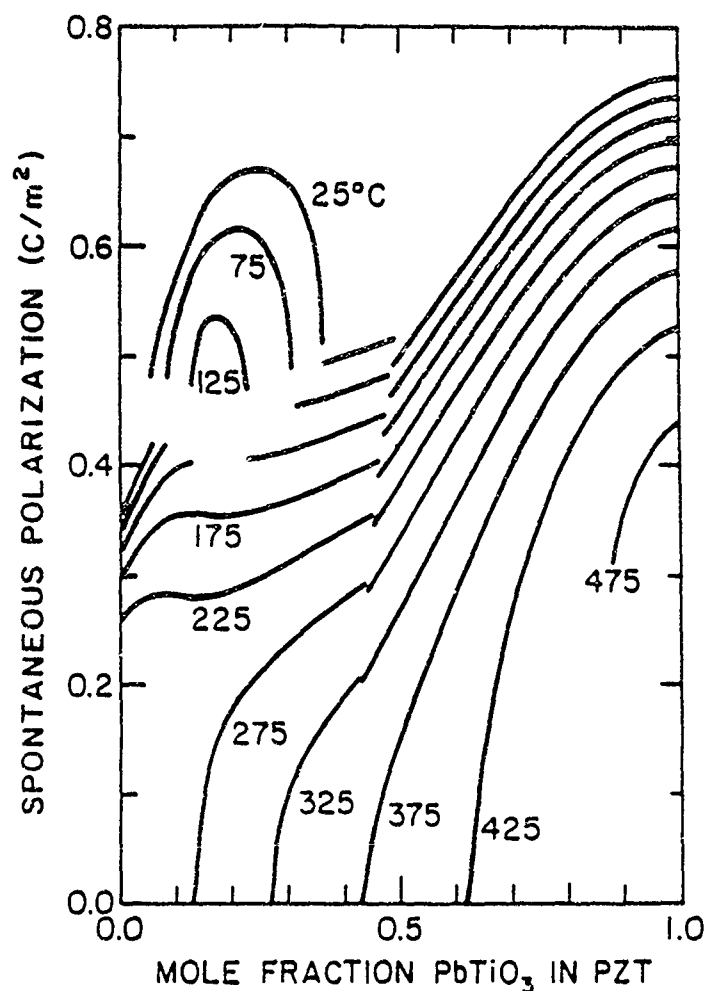
FIGURE 7    The theoretical spontaneous polarization plotted versus composition. The curves on the rhombohedral side of the figure represent the resultant spontaneous polarization $P_s$ $(3^{1/2}P_1)$

measurements were made. The effect of the morphotropic boundary on the ceramic data, where a coexistence of tetragonal and rhombohedral phases occurs, may have also made it more difficult to measure the polarization in the narrow region where the high-temperature rhombohedral phase is stable. Additional polarization measurements on homogeneous ceramic samples would be useful in trying to determine polarization changes in this region.

The second possibility, which seems more likely, is that the present theory does not adequately model the spontaneous polarization in the low-temperature rhombohedral phase for the compositions with greater titanium content. This could be due to the assumptions made in determining the coefficients. For example, the $Q_{44}$ and $R_{44}$ constants were assumed to be independent of composition and temperature in the low-temperature rhombohedral phase. The values of these constants were determined at the PZT 90/10 composition, and then used for the other compositions. The calculated polarization in the low-temperature rhombohedral phase of the PZT 90/10 composition does not have the large increase that occurs in the PZT 70/30 and 60/40 compositions. Therefore, it seems likely that the $Q_{44}$ and $R_{44}$ constants are dependent on composition, and if this was accounted for the large increase in

polarization in the PZT 70/30 and 60/40 compositions would be smaller. However, at this time there is not enough experimental data available in the literature to determine these compositional dependences. Additional tilt angle data obtained from neutron diffraction would possibly solve this problem.

Another significant change could be made to the present theory by adding a temperature dependence to the second-order tilt angle related coefficient ($\beta_1$), and/ or a sixth-order tilt angle term. Again the problem with this is that there is not enough data to properly determine all of these coefficients. The addition of a sixth-order tilt angle term will also greatly complicate the theory, because the equations for the spontaneous polarization and tilt angle in the low-temperature rhombo-hedral phase will change from quadratic to quartic.

The above discussion has shown that there may be some limitation to how well the present theory can quantitatively calculate the spontaneous polarization of the low-temperature rhombohedral phase for the compositions with greater titanium content. Due to the lack of tilt angle data and in order to avoid complicating the theory significantly more than it already is, the present theory is probably the best that it can be at this time, and is probably adequate for most applications.


## IV.  DIELECTRIC PROPERTIES

The calculated dielectric susceptibility coefficients of PZT 50/50 were plotted versus temperature in Figure 8. In comparison to the properties of PbTiO$_3$ (see Figure 8 in Reference 13), the dielectric susceptibilities and anisotropy have become much larger. The transition at $T_C$ is second order for PZT 50/50, while PbTiO$_3$ is first order. The LGD phenomenological theory of a second-order transition predicts that the dielectric susceptibility becomes infinite at $T_C$.

The compositional dependence of the dielectric susceptibility coefficients at 25°C is plotted in Figure 9. A peak occurs in these coefficients at the PZT 50/50 composition due to the peak that formed in the Curie constant (see Figure 2 in Reference 3). The increase in dielectric anisotropy ($\eta_{11}/\eta_{33}$) that occurs from PbTiO$_3$ to the PZT 50/50 composition is due to the change in the ratios of the dielectric stiffness coefficients ($\alpha_{12}/\alpha_{11}$, $\alpha_{112}/\alpha_{111}$, and $\alpha_{123}/\alpha_{111}$) as a function of composition.

On the rhombohedral side of the peak the anisotropy decreases and $\eta'_{11}$ eventually even becomes less than $\eta'_{33}$. This effect is at least partially due to compositional dependence of the ratios of the dielectric stiffness coefficients, but may also be due to an internal pressure that may develop within the perovskite structure when a larger zirconium ion is replaced by the smaller titanium ion. Amin et al.[14] showed that for the PZT 50/50 composition the application of hydrostatic stress would cause the anisotropy to decrease, and thus this effect might partially account for the small dielectric anisotropy on the PbZrO$_3$ side on the PZT system. Using the present theory of PZT the effect of mechanical boundary conditions on the properties and phase stability should now be investigated in more detail across the entire PZT system.

The dielectric susceptibility coefficients of two rhombohedral compositions, PZT 60/40 and 90/10, were plotted versus temperature in Figures 10 and 11. A similar change in the behavior of the dielectric anisotropy occurs from PZT 60/40 to 90/
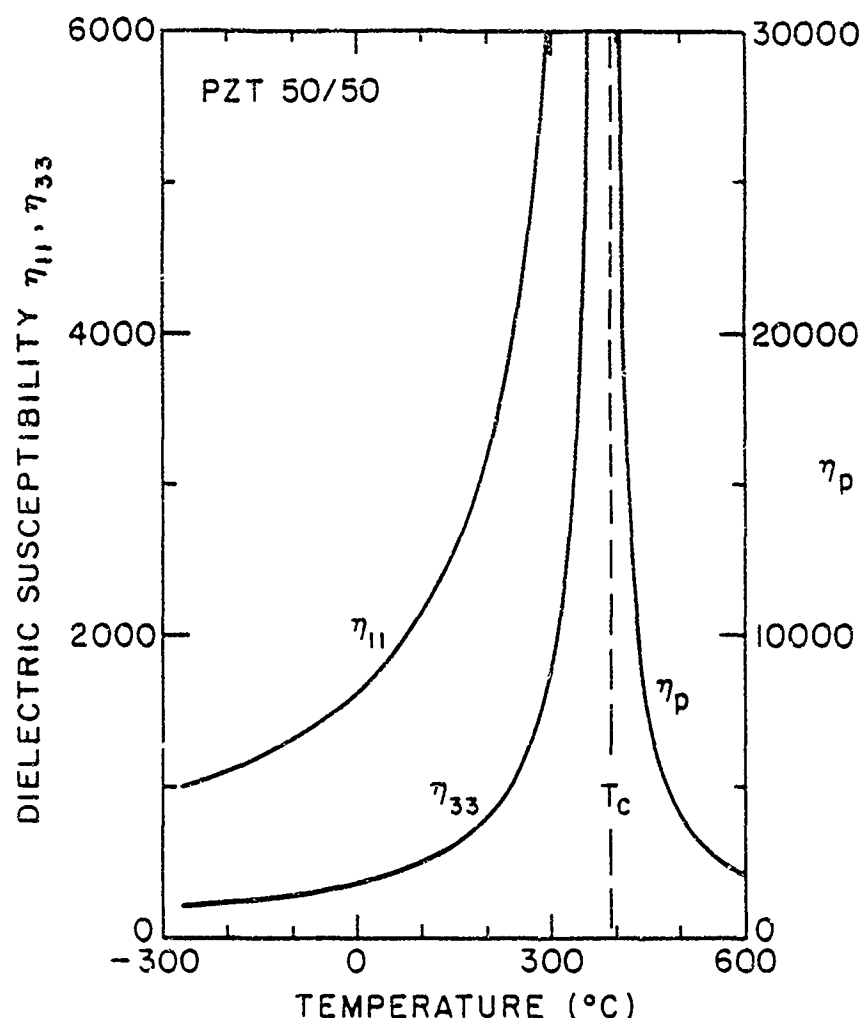
FIGURE 8  The theoretical dielectric susceptibility coefficients of PZT 50 50 plotted versus temperature

10 as occurred from PZT 50/50 to $PbTiO_3$. For PZT 90/10 and $PbTiO_3$ (see Figure 8 in Reference 13) the dielectric susceptibility parallel to the polar axis ($\eta_{33}$ or $\eta'_{33}$) is larger than the perpendicular susceptibility ($\eta_{11}$ or $\eta'_{11}$) at high temperatures, but smaller at low temperatures.

At high temperatures close to $T_C$ for rhombohedral compositions close to the morphotropic boundary (Ti content > 0.45) a problem develops when calculating the dielectric susceptibility coefficient $\eta'_{11}$ using the coefficients from References 2 and 3. At a temperature below $T_C$ the $\eta'_{11}$ coefficient will increase to infinity, and then becomes negative between this temperature and $T_C$. This is simply due to the values of the coefficients used, and indicates that in this region these values are not quite right. Because of this problem, care should be taken in calculating the rhombohedral dielectric susceptibilities at high temperatures for compositions near the morphotropic boundary. Considering that all of the coefficients were assumed to be independent of temperature, except $\alpha_1$, and that some of the coefficients were determined at $T_C$ (232–492°C) and others at 4.2 K, it is amazing that everything works as well as it does, and that more problems have not occurred.
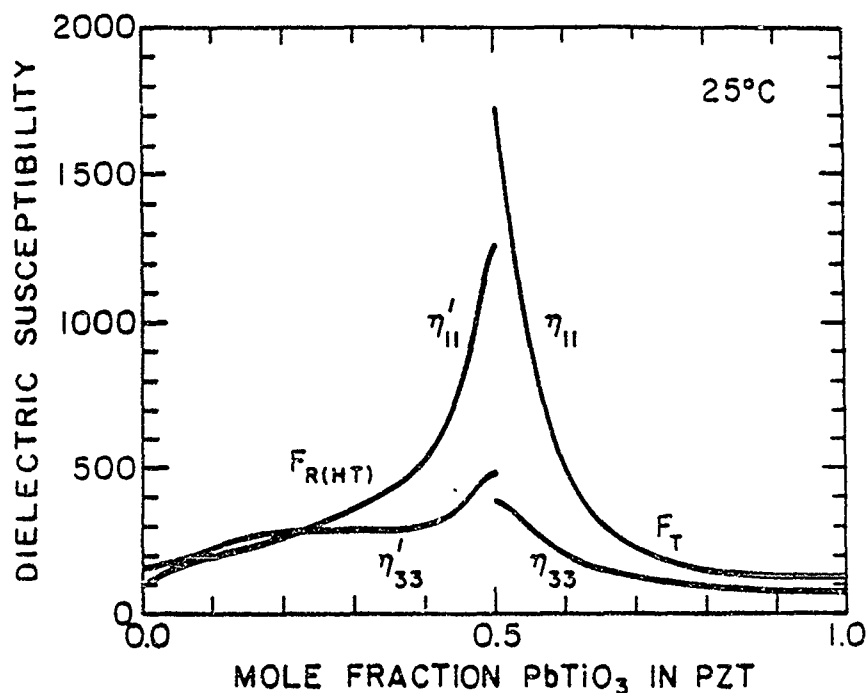
FIGURE 9    The theoretical dielectric susceptibility coefficients plotted versus composition at 25°C

Away from this region the calculated dielectric properties are in fairly good agreement with the available experimental data. Haun *et al.*[13] showed that the calculated dielectric susceptibility coefficients and anisotropy of $PbTiO_3$ were in good agreement with Fesenko *et al.*'s[15] experimental single-crystal data at low temperatures, where the defect contributions to the experimental measurements had "frozen out". The theoretically calculated dielectric properties near the morphotropic boundary have similar values as the experimental measurements on single crystals by Tsuzuki *et al.*[3] Good agreement was also found between the calculated dielectric properties and Clarke and Whatmore's[16] PZT 90/10 single-crystal measurements.

## V. PIEZOELECTRIC PROPERTIES

The calculated piezoelectric voltage coefficients $g_{ij}$ (assumed to be equal to the $b_{ij}$ coefficients) for the PZT 50/50, 60/40, and 90/10 compositions were plotted versus temperature in Figures (12)–(14). The $g_{ij}$ coefficients plotted in these figures are based on the cubic axes. Thus the $x_3$ axis is along the polar axis for the tetragonal coefficients, but not for the rhombohedral coefficients.

Since the electrostrictive constants were assumed to be independent of temperature, the negative temperature dependence of the $g_{ij}$ coefficients was caused by the temperature dependence of the spontaneous polarization. The PZT 90/10 composition has a first-order change in the spontaneous polarization, which causes discontinuities in the $g_{ij}$ coefficients at $T_C$. The PZT 50/50 and 60/40 compositions
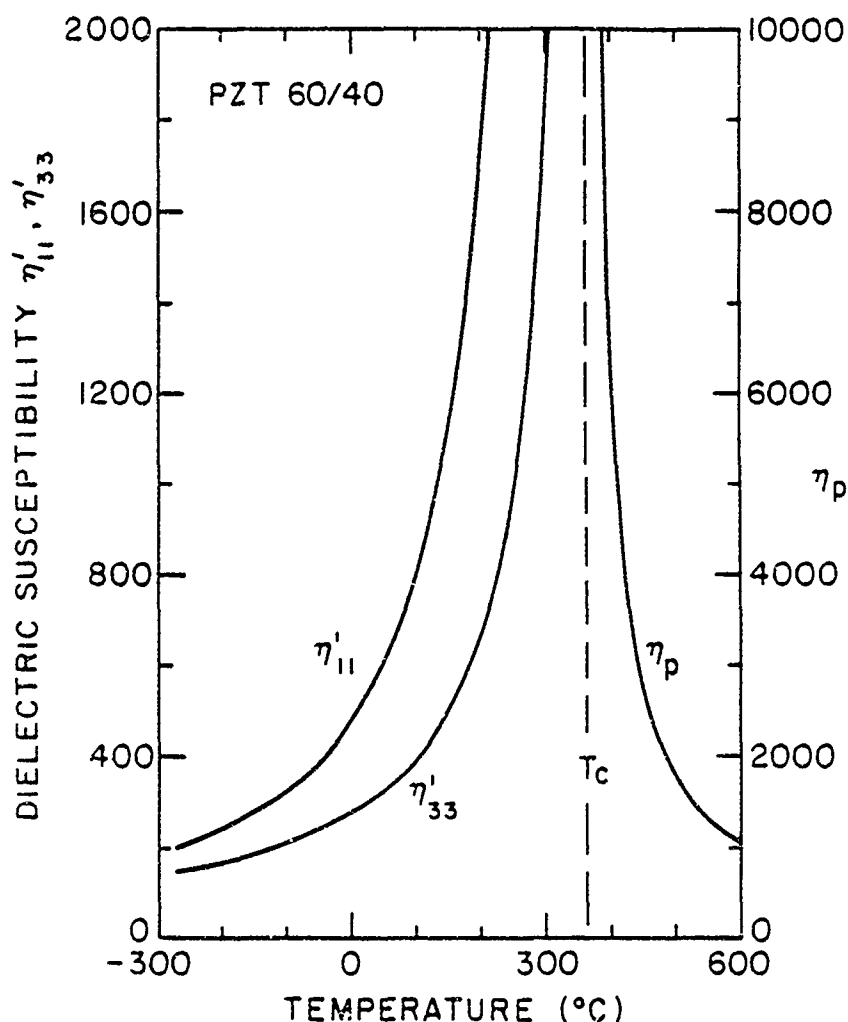
FIGURE 10 The theoretical dielectric susceptibility coefficients of PZT 60/40 plotted versus temperature

undergo second order transitions, and thus the $g_{ij}$ coefficients change continuously from a value of zero at $T_C$.

The compositional dependence of the $g_{ij}$ coefficients at 25°C is plotted in Figure 15. Since the electrostrictive constants were given a compositional dependence (see Figure 2 in Reference 17), the compositional dependence of the $g_{ij}$ coefficients depends on the electrostrictive constants and the spontaneous polarization (see Figure 7). The result is that the $g_{ij}$ coefficients change with composition as shown in Figure 15. The compositional dependences of the $g_{ij}$ coefficients are much smaller than that of the $d_{ij}$ coefficients, which will be presented next.

The piezoelectric charge coefficients $d_{ij}$ of the PZT 50/50 composition were plotted versus temperature in Figure 16. The positive temperature dependence of the $d_{ij}$ coefficients was caused by the strong temperature dependence of the dielectric susceptibility coefficients. In Figure 17 the $d_{ij}$ coefficients are plotted versus composition at 25°C, showing the large peak in these coefficients near the morphotropic boundary. The large increase of the $\eta_{11}$ coefficient near the morphotropic boundary (see Figure 9) caused a large increase to also occur in the $d_{15}$ coefficient.
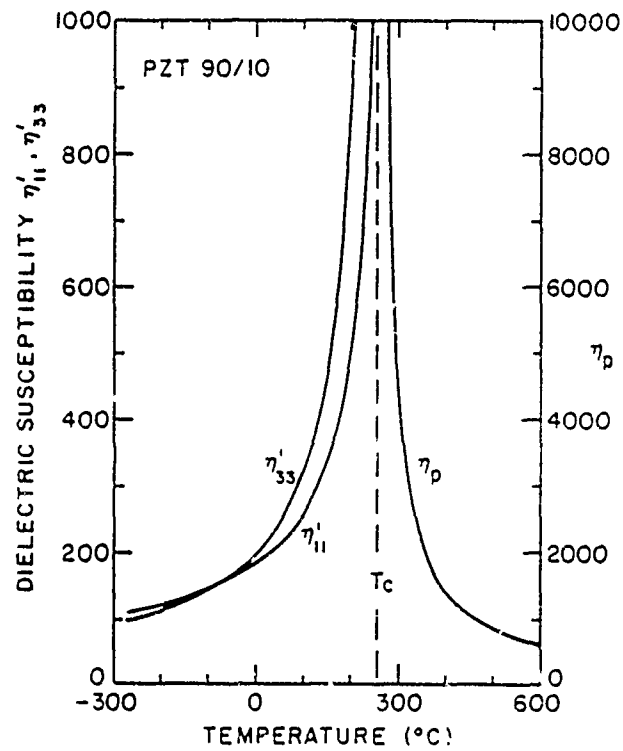
FIGURE 11  The theoretical dielectric susceptibility coefficients of PZT 90 10 plotted versus temperature
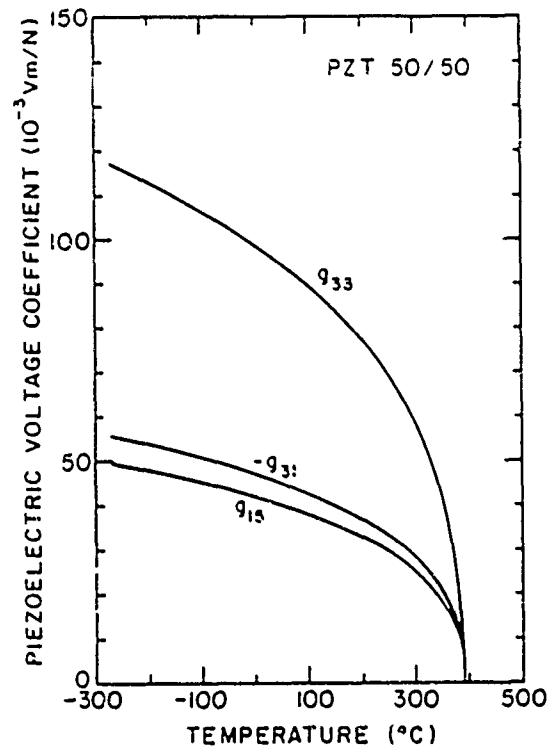


FIGURE 12  The theoretical piezoelectric voltage coefficients $g_{ij}$ of PZT 50 50 plotted versus temperature
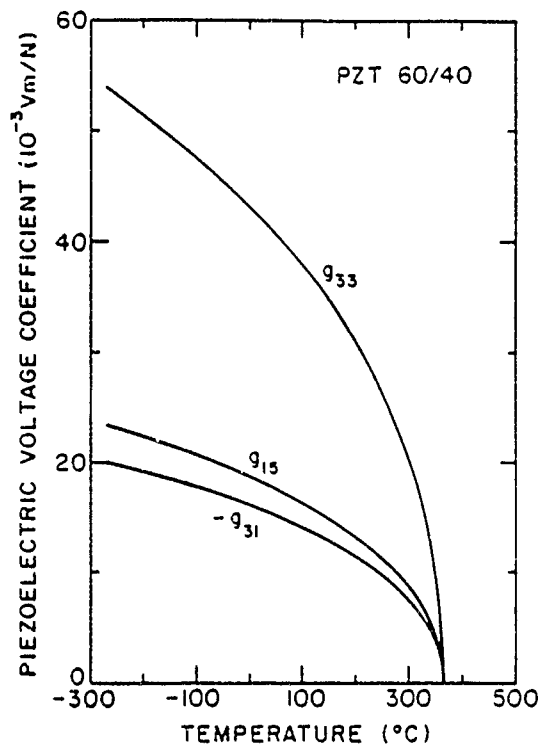
FIGURE 13   The theoretical piezoelectric voltage coefficients $g_{ij}$ of PZT 60/40 plotted versus temperature
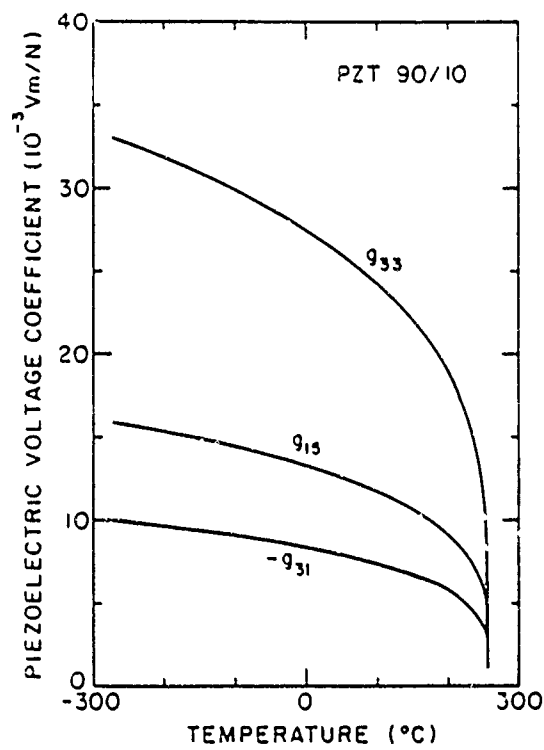


FIGURE 14   The theoretical piezoelectric voltage coefficients $g_{ij}$ of PZT 90/10 plotted versus temperature
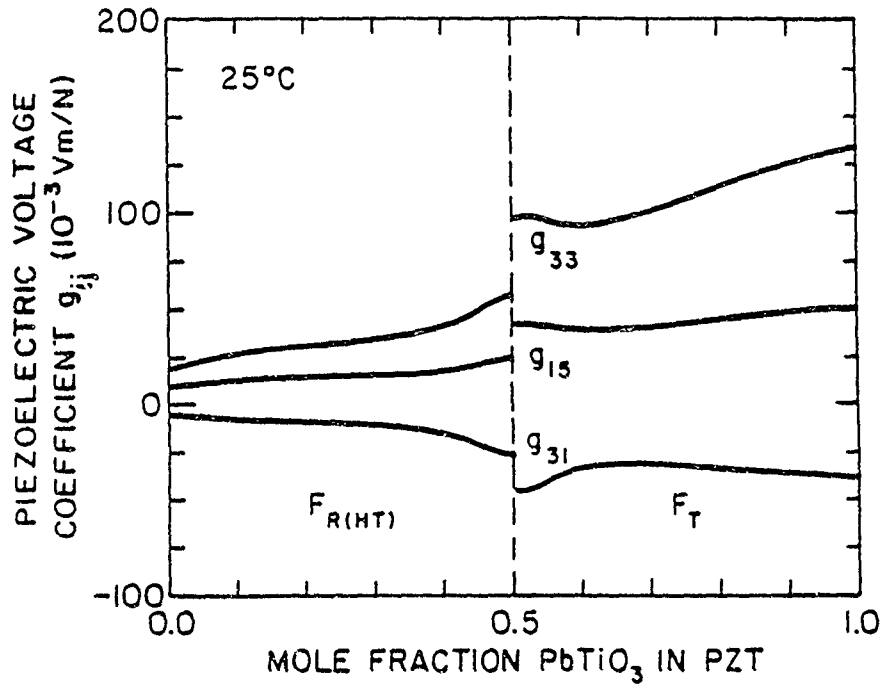
FIGURE 15   The theoretical piezoelectric voltage coefficients $g_{ij}$ plotted versus composition at 25°C

For the rhombohedral compositions the $d_{ij}$ coefficients were calculated based on the original cubic axes, resulting in four independent nonzero coefficients. The relations for the rhombohedral coefficients are more complicated than those for the tetragonal coefficients, because two terms are involved in three of the four
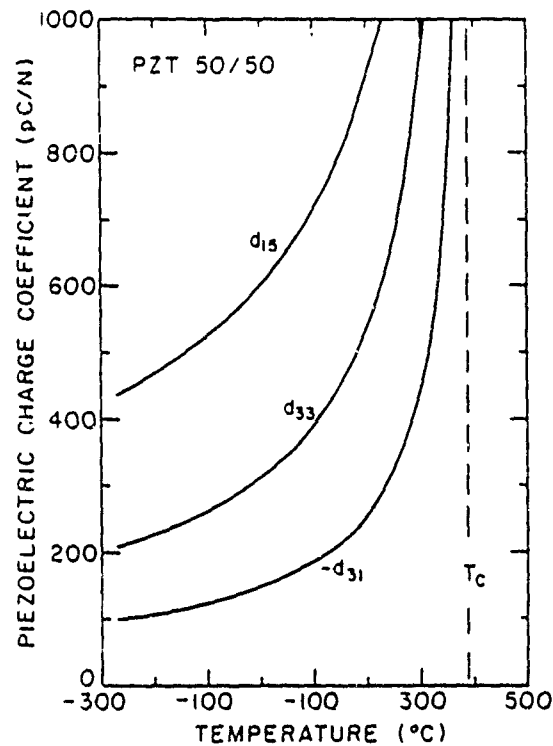


FIGURE 16   The theoretical piezoelectric charge coefficients $d_{ij}$ of PZT 50/50 plotted versus temperature.
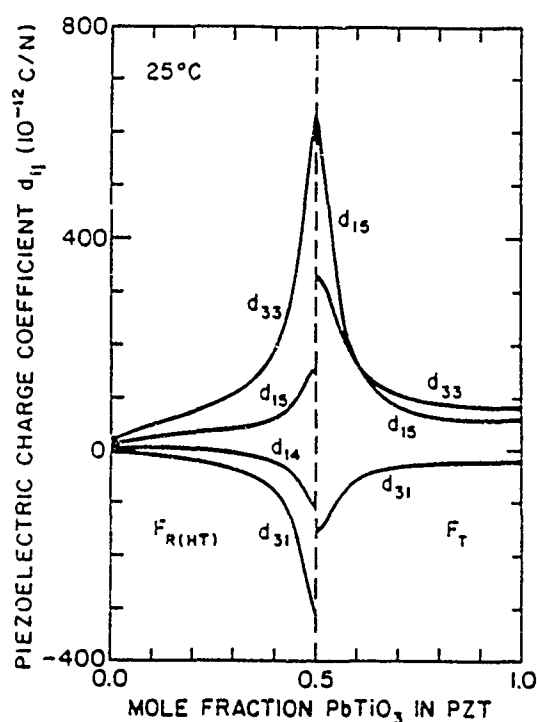
FIGURE 17   The theoretical piezoelectric charge coefficients $d$, plotted versus composition at 25°C

relations [see Equations (44) and (45) in Reference 1]. These two terms are often competing: one term being positive, while the other is negative. In addition the $\eta_{12}$ coefficient can be positive or negative depending on the composition and temperature.

The $d_{ij}$ coefficients are plotted versus temperature for two rhombohedral compositions, PZT 60/40 and 90/10, in Figures 18 and 19. The $d_{33}$ and $d_{15}$ coefficients form similar shaped curves for both compositions, but the $d_{31}$ and $d_{14}$ coefficients have definite differences.

For the PZT 60/40 composition the $d_{14}$ coefficient is negative at all temperatures, and becomes more negative with increasing temperature. The $d_{14}$ coefficient of the PZT 90/10 composition is slightly negative at low tempratures, and then becomes positive at about $-100°C$, and continues to increase with increasing temperature. These diffeences are due to the $\eta_{12}$ coefficient, which is negative for the PZT 60/40 composition, and positive for the PZT 90/10 composition (except at low temperatures where it changes sign and becomes negative).

The $d_{31}$ coefficient of the 60/40 composition is negative, and becomes more negative with increasing temperature. For the PZT 90/10 composition the $d_{31}$ coefficient is negative at low temperatures, becomes more negative with increasing temperature, and then suddenly increases and becomes positive just below $T_C$. This behavior is due to the changes that occur in the value of the $\eta_{12}$ coefficient, and also due to the two terms in the $d_{31}$ relation, which are of opposite sign with one dominating at low temperatures and the other at high temperatures.

The rhombohedral $d_{ij}$ coefficients described above are based on the original cubic axes. What needs to be done in the future is to rotate the axes, so that the new $x_3$
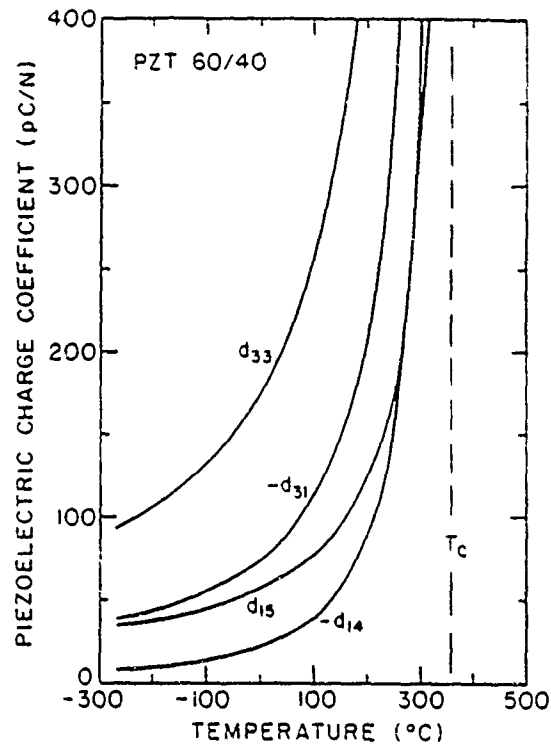
FIGURE 18   The theoretical piezoelectric charge coefficients $d_i$ of PZT 60/40 plotted versus temperature
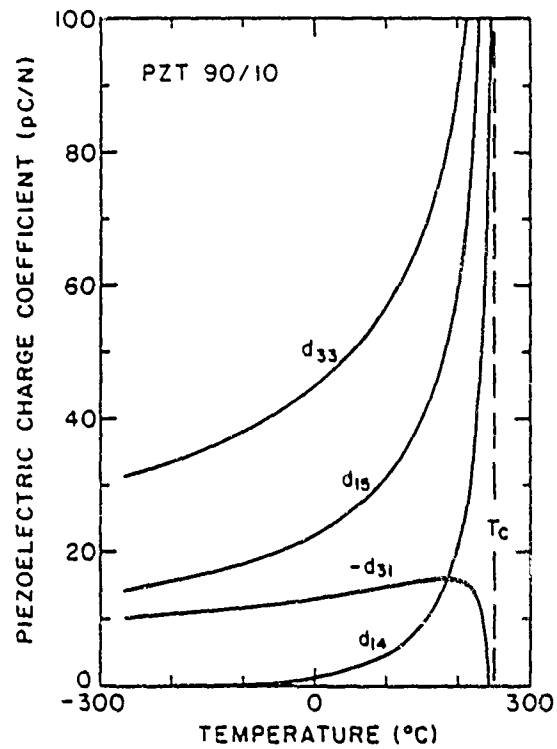


FIGURE 19   The theoretical piezoelectric charge coefficients $d_{ij}$ of PZT 90/10 plotted versus temperature.

axis is along the rhombohedral polar direction. This would reduce the number of independent nonzero coefficients to three ($d_{33}$, $d_{31}$, and $d_{15}$), similar to the tetragonal $d_{ij}$ matrix, and thus simplify the analysis of these coefficients.

The calculated $d_{ij}$ coefficients have similar values as the experimental ceramic data near the morphotropic boundary. The only available single-crystal data was measured by Gavrilyachenko and Fesenko[18] on lead titanate. Their data were compared with the theoretical lead titanate calculations in Reference 13. Fairly good agreement was found, especially for the $d_{31}$ coefficient.

## VI.  SUMMARY AND FUTURE APPLICATIONS OF THE THEORY OF PZT

The applications of compositions of the PZT solid solution system as piezoelectric transducers, pyroelectric detectors, electro-optic devices, and explosively induced charge storage devices were described in the first paper of this series to demonstrate the technological importance of PZT. In these applications PZT is used in polycrystalline ceramic form, and thus the properties of these ceramics are well established in the literature. However, the mechanisms contributing to these outstanding ceramic properties of PZT are not well understood, because of the number of contributing factors and complexity of the interactions within the ceramic.

A first step in the analysis of a ferroelectric ceramic material is to separate the intrinsic and extrinsic contributions to the properties. The intrinsic contributions result from the averaging of the single-domain single-crystal properties, while the extrinsic contributions arise from the interactions at grain or phase boundaries and from the domain wall or thermally induced defect motions. Unfortunately, due to the difficulty of growing good quality single crystals of PZT, very little reliable single-crystal data is available. Thus the goal of this project was to use a thermodynamic phenomenological theory to calculate the single-domain properties of PZT. The results of this theory could then be used to separate the intrinsic and extrinsic contributions to the ceramic properties. In addition there are several other applications of this theory, which will be described later in this summary.

In the first paper of this series a modified elastic Gibbs free energy function was expanded in powers of the ferroelectric and antiferroelectric order parameters. An additional order parameter was also included to account for the tilting of the oxygen octahedra in the low-temperature rhombohedral phase. The resulting energy function can be used to model the phase transitions and single-domain properties of the entire PZT system. Solutions to this energy function were used to derive relations for the energies; spontaneous polarizations, strains, and tilt angles; and dielectric and piezoelectric properties corresponding to the different phases in the PZT system.

All of the coefficients of the energy function were assumed to be independent of temperature, except the ferroelectric and antiferroelectric dielectric stiffness coefficients $\alpha_1$ and $\sigma_1$, which were given linear temperature dependences based on the Curie-Weiss law. The experimental phase diagram was extensively used in the evaluation of the coefficients, by requiring that the energies of the adjacent phases of a phase transition must be equal at the transition. The first partial derivative

stability conditions were also used as additional relations in the evaluation procedure.

Without single-crystal data, the development of this theory was complicated and involved indirect methods of determining the coefficients of the energy function. Additional experimental data were needed to determine the compositional dependence of the coefficients. A sol-gel procedure was used to prepare pure homogeneous PZT powders across the phase diagram to be used in collecting additional PZT data. The lattice constants versus temperature were determined from these powders from high-temperature x-ray diffraction, and used to calculate the spontaneous strain.[2][13][19] The sol-gel derived powders were also used to fabricate ceramic samples for dielectric, piezoelectric, elastic, pyroelectric, and electrostrictive measurements.[3][17][20][21][22] These data were very important in completing the evaluation of the coefficients of the energy function.

The compositional dependence of the cubic electrostrictive constants across the PZT system were determined from a combination of single crystal and ceramic data using series and parallel averaging relations (analogous to the Reuss and Voigt methods of averaging the elastic constants).[17] An interesting result of this work was that the electrostrictive constants form a peak at the PZT 50/50 composition. In addition, the ratios of the electrostrictive constants change with composition in such a way as to explain the compositional dependence of the electromechanical anisotropy found in PZT ceramics.[23] The electromechanical anisotropy is very large in compositions near the end members $PbTiO_3$ and $PbZrO_3$, but becomes very small for compositions in the center of the phase diagram near the morphotropic phase boundary.

In the second paper of this series the electrostrictive data were used with the spontaneous strain data to calculate the spontaneous polarization, which was used to determine values of the higher-order dielectric stiffness coefficients. In the third paper of this series low-temperature ceramic dielectric data were particularly important in determining the compositional dependence of the Curie constant, and in separating the sixth-order polarization interaction coefficients ($\alpha_{112}$ and $\alpha_{123}$). The tilt angle related coefficients were determined in the fourth paper of the series from spontaneous strain and tilt angle data. The compositional dependence of the antiferroelectric orthorhombic free energy was determined by combining data from a separate theory developed for $PbZrO_3$ with the requirement that the energies of the high-temperature rhombohedral and antiferroelectric orthorhombic phases must be equal at the transition between these phases.[5]

After determining values of the coefficients at several different compositions as described above, the compositional dependence of the coefficients was determined by fitting an equation to these values. A set of equations was then established that can be used to calculate values of the coefficients at any composition.

Using these equations the phase stability, spontaneous polarization, tilt angle, and dielectric and piezoelectric poperties were calculated. The theoretically calculated phase diagram was shown to quantitatively model the experimental phase diagram. An independent check of the coefficients was also made by calculating the free energy of the ferroelectric orthorhombic state, which showed that this phase was metastable across the phase diagram in agreement with the experimental diagram. The spontaneous polarization and tilt angle were calculated for several

compositions across the phase diagram. These calculations were in good agreement with the available experimental single-crystal data. The dielectric and piezoelectric properties were also calculated and found to be in good agreement with the experimental data. As a summary of these calculations, the theoretical properties of PZT at 25°C are listed in Table I.

Some limitations of the present theory were found. Due to the lack of experimental data for the low-temperature rhombohedral phase, especially tilt angle data, some assumptions were necessary in determining the compositional dependence of the tilt angle related coefficients. In addition these coefficients were assumed to be independent of temperature, and only tilt angle terms up to the fourth power were included. With these assumptions, the calculations of the spontaneous polarization, tilt angle, and dielectric properties were still in fairly good agreement with the experimental single-crystal data at the PZT 90/10 composition.

The problems developed in the calculations for compositions with greater titanium content. The spontaneous polarization calculated in the low-temperature rhombohedral phase for the PZT 70/30 and 60/40 compositions increased more than would be expected. Another problem was found when calculating the dielectric susceptibility (negative values resulted) in the high-temperature rhombohedral phase at temperatures near $T_C$ and at compositions close to the morphotropic boundary. However, away from this small region the dielectric properties could be calculated in good agreement with the available experimental data.

The present theory could be improved as additional experimental data becomes available. In particular, additional spontaneous strain data on very homogeneous powders are needed to more precisely locate the tricritical point on the lead titanate side of the phase diagram. Strain data for compositions close to lead zirconate are also needed to determine the compositional dependence of the antiferroelectric coefficients. Finally, additional tilt angle data are needed to more accurately determine the tilt angle related coefficients.

In this series of papers a single energy function and set of coefficients was presented that can be used to model all of the known phase transitions in the PZT solid solution system. This theory can also be used to calculate the single domain properties of PZT. In addition to the properties already calculated,the theory can be used to calculate the elastic compliances at constant electric field, the dielectric susceptibilities at constant strain (the dielectric susceptibilities calculated in this paper were at constant stress), and thermal properties such as the entropy change and latent heat at a transition.[26,27] This theory can now be used for several different applications.

One application that this theory has already been used for was to help explain the large electromechanical anisotropy that occurs in PbTiO$_3$ ceramics, but not in single crystals. By averaging the single-crystal constants obtained from this theory, a large electromechanical anisotropy was found to occur due to the particular values of the single-crystal electrostrictive ratios of PbTiO$_3$.[23] Other compositions in ceramic form, such as PZT 50/50, have small electromechanical anisotropy, because the values of the single crystal electrostrictive ratios have changed.

The intrinsic and extrinsic contributions to the properties of polycrystalline PZT ceramics can now be separated with the results of this theory. By using simple averaging relations the intrinsic contributions to the ceramic properties can be

TABLE 1

The theoretical properties of PZT at 25°C

| | Mole Fraction PbTiO₃ in PZT* | | | | | | | | | |
|---|---|---|---|---|---|---|---|---|---|---|
| | 0 1 | 0 2 | 0 3 | 0 4 | 0 5 | 0 6 | 0 7 | 0 8 | 0 9 | 1 0 |
| $P_s$ (C/m²) | 0 57 | 0 66 | 0 65 | 0 50 | 0 50 | 0 57 | 0 64 | 0 70 | 0 74 | 0 76 |
| $\theta_s$ (Deg.) | 5 42 | 7 36 | 6 64 | | | | | | | |
| $\eta_{11}$ or $\eta_{33}$ | 219 | 277 | 280 | 295 | 382 | 197 | 116 | 86.4 | 72 9 | 66 6 |
| $\eta_{33}$ or $\eta_{11}$ | 195 | 262 | 360 | 529 | 1721 | 498 | 218 | 143 | 121 | 124 |
| $g_{33}$ (10⁻³ Vm/N) | 26 8 | 30 9 | 34 6 | 41 9 | 96 6 | 92 9 | 101 | 114 | 124 | 134 |
| $g_{31}$ (10⁻³ Vm/N) | 8 13 | 9 53 | 11 2 | 15 6 | 46 0 | 33 8 | 31 8 | 34 2 | 37 1 | 39 2 |
| $g_{15}$ (10⁻³ Vm/N) | 12 9 | 14 3 | 15 5 | 18 1 | 41 0 | 38 6 | 40 8 | 44 9 | 48 6 | 50 9 |
| $d_{33}$ (10⁻¹² C/N) | 47 2 | 72 1 | 107 | 189 | 327 | 162 | 104 | 87 2 | 81 2 | 79 2 |
| $d_{31}$ (10⁻¹² C/N) | 13 3 | 21 6 | 38 5 | 80 5 | 156 | 58 9 | 32 6 | 26.2 | 23 9 | 23 1 |
| $d_{15}$ (10⁻¹² C/N) | 1 81 | 1 27 | 7 26 | 25 1 | | | | | | |
| $d_{15}$ (10⁻¹² C/N) | 21 2 | 34 5 | 42 0 | 60 0 | 624 | 169 | 78 6 | 57 0 | 52 1 | 56 1 |

* The values listed from 0 1 to 0 4 were calculated from the high-temperature rhombohedral equations, except for $P_s$ and $\theta_s$ from 0 1 to 0 3 which were calculated from the low-temperature rhombohedral equations. The values listed from 0 5 to 1 0 were calculated from the tetragonal equations. $P_s$, $P_s$, in the tetragonal state, but $P_s = 3^{1/2} P_s$ in the rhombohedral state. $\theta_s$, $\eta_{11}$, and $\eta_{33}$ were used in the tetragonal state, and $\eta_{11}$, and $\eta_{33}$ (see Section IV) were used in the rhombohedral state. The piezoelectric coefficients are all based on the cube axes.

calculated from the theoretical single-domain properties. By then comparing these properties with the experimental measurements on ceramic samples, the extrinsic contributions can be determined. Comparisons with low-temperature and high-frequency measurements on ceramics will be particularly useful in determining the conditions necessary for these extrinsic contributions to "freeze out" as temperature decreases and "relax out" as frequency increases. After separating the extrinsic contributions, comparisons of these results should be made with the calculations from other theories, such as that by Arlt and Peusens,[28] where the domain wall contributions to the dielectric constant of $BaTiO_3$ ceramics were calculated.

This theory can also be used to study the effects of electrical and mechanical boundary conditions on the properties and phase stability, which should also lead to a better understanding of ferroelectric polycrystalline materials where the boundary conditions may vary from grain to grain. Amin et al.[14,29] studied these effects using the earlier phenomenological theory that was developed for the morphotropic phase boundary region.[30] They found that the application of an electric field would easily transform the rhombohedral state to the tetragonal state, but that by applying a field to the tetragonal state would not transform it to the rhombohedral state. They concluded "that this may be part of the reason there is a rapid escalation of coercivity against poling in the tetragonal phase compositions." Amin et al.[14] also studied the effect of hydrostatic pressure on the properties and phase stability, and found that for morphotropic boundary compositions the rhombohedral phase can easily be transformed to the tetragonal phase from applied hydrostatic pressure. Additional studies of the effects of electrical and mechanical boundary conditions should now be continued using the more complete theory of PZT that has been presented here.

The energy function developed for PZT was based on the elastic Gibbs free energy, which resulted in dielectric stiffness coefficients under constant stress conditions. If the Helmholtz free energy had been used, then the dielectric stiffness coefficients would be under constant strain conditions. The fourth-order dielectric stiffness coefficients from these two energy functions can be related through terms involving the electrostrictive and elastic constants.[26,31] Since the fourth-order dielectric stiffness coefficients changed signs with composition and caused the tricritical behavior to occur, it would now be useful to compare these coefficients with the coefficients from the Helmholtz function to determine if the tricritical behavior is due to the electrostrictive coupling, or due to the intrinsic behavior of the material. By comparing the coefficients of the energy functions additional understanding of the phase stability may be gained.

With the phenomenological theory developed for the PZT system, extensions into more complex systems, such as lanthanum modified PZT (PLZT), can now be attempted. This should be important, because for most technological applications PZT is modified with other ions. Extending the PZT theory into the PLZT system should also be useful in furthering the understanding of relaxor type ferroelectric materials.

In addition to the applications described above, the phenomenological theory of PZT will provide a method of collecting all of the dielectric, piezoelectric, elastic, and thermal data into an organized and easily tractable form. The methodology outlined in this series of papers can be used similarly for any solid solution system

which has the same order parameters as PZT. Hypothetical phase diagrams with desired properties can be constructed, and then compared with existing systems to find candidates for further study.

REFERENCES

1. M. J. Haun, E. Furman, S. J. Jang and L. E. Cross, "Thermodynamic Theory of the Lead Zirconate-Titanate Solid Solution System, Part I. Phenomenology," *Ferroelectrics* to be published with this paper.
2. M. J. Haun, E. Furman, H. A. McKinstry and L. E. Cross, "Thermodynamic Theory of the Lead Zirconate-Titanate Solid Solution System, Part II: Tricritical Behavior," *Ferroelectrics* to be published with this paper.
3 M. J. Haun, Z. Q Zhuang, E. Furman, S. J. Jang and L. E. Cross, "Thermodynamic Theory of the Lead Zirconate-Titanate Solid Solution System, Part III. Curie Constant and Sixth-Order Polarization Interaction Dielectric Stiffness Coefficients," *Ferroelectrics* to be published with this paper
4 M. J Haun, E. Furman, T R. Halemane and L. E. Cross, "Thermodynamic Theory of the Lead Zirconate-Titanate Solid Solution System, Part IV Tilting of the Oxygen Octahedra," *Ferroelectrics* to be published with this paper.
5 M. J. Haun, T J. Harvin, M. T. Lanagan, Z. Q. Zhuang, S. J. Jang and L. E Cross, "Thermodynamic Theory of PbZrO₃," *J. Appl. Phys.* **65**, 3173 (1989).
6. B. Jaffe, W J. Cook and H. Jaffe, *Piezoelectric Ceramics* (Academic Press, London, 1971)
7 V G. Gavrilyachenko, R. I. Spinko, M. A. Martynenko and E. G Fesenko, *Fiz Tid. Tela,* **12**, 1532 (1970) [*Sov. Phys.-Solid State* **12**, 1203 (1970)].
8 H. Tsuzuki, K. Sakata and M Wada, *Ferroelectrics,* **8**, 501 (1974)
9 Z Q Zhuang, M. J. Haun, A. Bhalla, S J Jang and L. E. Cross, unpublished data.
10 R. Clarke and A. M. Glazer, *Ferroelectrics,* **12**, 207 (1976)
11 A. M. Glazer, S. A Mabud and R. Clarke, *Acta Cryst,* **B34**, 1060 (1978)
12. A. Amin, R. E. Newham, L. E. Cross and D E. Cox, *J Solid State Chemistry,* **37**, 248 (1981)
13. M. J Haun, E. Furman, S J Jang, H. A. McKinstry and L. E. Cross, *J Appl Phys,* **62**, 333 (1987)
14 A Amin, R. E Newham and L E Cross, *Phys Rev,* **B34**, 1595 (1986)
15 E. G. Fesenko, V G Gavrilyachenko, E. V Zarochentsev, *Izv Akad. Nauk SSR Ser Fiz,* **34**, 2541 (1970) [*Bull. Acad. Sci USSR,* **34**, 2262 (1970)].
16 R. Clarke and R. W Whatmore, *J of Crystal Growth,* **33**, 29 (1976)
17 M. J Haun, Z. Q Zhuang, E. Furman, S. J Jang and L. E Cross, *J Am Ceram Soc* **72**, 1140 (1989)
18. V G. Gavrilyachenko and E. G. Fesenko, *Kristallografiya,* **16**, 640 (1971) [*Sov Phys -Crystallogr,* **16**, 549 (1971).]
19 M. J Haun, Y. H. Lee, H. A. McKinstry, and L. E. Cross, *Advances in X-ray Analysis, Vol 30,* edited by C. S. Barrett, J V Gilfrich, R. Jenkins, D. E. Leyden, J C Russ, and P K. Predecki, (Plenum Press, New York, 1987) pp. 473-481.
20 Z. Q. Zhuang, M. J. Haun, S. J. Jang and L. E. Cross, *Proceedings of the 6th IEEE International Symposium on the Applications of Ferroelectrics,* Lehigh, PA, edited by Van Wood (IEEE, New York, 1986) pp. 394-397
21 Z. Q Zhuang, M. J. Haun, S. J Jang and L. E. Cross, *Advanced Ceram Mat.,* **3**, 485 (1988)
22. Z. Q Zhuang, M. J Haun, A. Bhalla, S. J Jang and L. E. Cross, unpublished data
23 M J Haun, E. Furman, S. J Jang and L. E. Cross, *Trans. IEEE Ultrasonics, Ferroelectrics and Frequency Control Soc.,* **36**, 393 (1989).
24 R. W. Whatmore, R. Clarke and A. M. Glazer, *J Phys C. Solid State Phys.,* **11**, 3089 (1978)
25 M. J Haun, Z. Q Zhuang, S. J. Jang, H. A. McKinstry and L. E Cross, *Proceedings of the 6th IEEE International Symposium on the Applications of Ferroelectrics,* Lehigh, PA, edited by Van Wood (IEEE, New York, 1986) pp. 398-401
26 A. F Devonshire, *Phil. Mag,* **42**, 1065 (1951).
27 E. Fatuzzo and W J Merz, *Ferroelectricity* (Wiley, New York, 1967).
28. G Arlt and H. Peusens, *Ferroelectrics,* **48**, 213 (1983)
29 A. Amin and L. E. Cross, *Jpn. J Appl. Phys,* **24** (Suppl. 24-2), 229 (1985)
30. A. Amin, M. J. Haun, B. Badger, H. A. McKinstry and L. E. Cross, *Ferroelectrics,* **65**, 107 (1985)
31. A. F Devonshire, *Phil. Mag,* **40**, 1040 (1949).

APPENDIX 29

# Electrostrictive Properties of the Lead Zirconate Titanate Solid-Solution System

Michael J. Haun,[*,•] Z. Q. Zhuang,[†] E. Furman,[‡] Sei-Joo Jang,[*] and L. Eric Cross[*]

Materials Research Laboratory, The Pennsylvania State University, University Park, Pennsylvania 16802

Values of the electrostrictive constants for the lead zirconate titanate (PZT) solid-solution system were required to complete the development of a thermodynamic phenomenological theory of PZT. The electrostrictive $\bar{Q}_{12}$ constant was measured as a function of composition on polycrystalline ceramic PZT samples. These data were used with additional single-crystal and ceramic data from the literature to approximate the compositional dependence of the electrostrictive constants of the PZT system. Series and parallel equations, analogous to the Voigt and Reuss models for the elastic constants, were used to relate the ceramic and single-crystal data, and to predict the upper and lower bounds of the ceramic electrostrictive constants from the single-crystal constants. [Key words: lead zirconate titanate, electrical ceramics, polycrystalline materials, electronic properties, solid solutions.]

## I. Introduction

COMPOSITIONS in the lead zirconate titanate (PZT) solid-solution system have been widely used in piezoelectric transducer applications in polycrystalline ceramic form.[1] However, considerable difficulty has been encountered when attempting to grow single crystals of PZT.[2] Without single-crystal data indirect methods have been required to determine the coefficients of a thermodynamic energy function for the PZT system.[3,4]

In one particularly important indirect method, spontaneous strain and electrostrictive data were used to calculate the spontaneous polarization.[3,4] Because of the lack of experimental electrostrictive data on PZT, the electrostrictive constants were assumed to be independent of composition and temperature. Zorn et al.[5] used an X-ray technique to measure the composition and temperature dependence of the electrostrictive constants of crystallites in PZT (modified with strontium, barium, and niobium) ceramic samples with compositions near the tetragonal–rhombohedral morphotropic phase boundary. They found that the electrostrictive constants were independent of temperature, but dependent on composition.

The purpose of this study was to further investigate the composition and temperature dependence of the electrostrictive constants in the PZT system. In the next section calculations of the temperature dependence of the electrostrictive constants for three PZT compositions will be presented. In Section III the results of experimental measurements of the compositional dependence of the ceramic electrostrictive $\bar{Q}_{12}$ constant will be described (throughout the paper a bar over a symbol will be used to refer to polycrystalline ceramic constants, and a symbol without a bar will refer to single-crystal constants). In Section IV series and

parallel averaging relations, analogous to the Voigt and Reuss methods of averaging the elastic constants,[6] will be used to calculate the single-crystal electrostrictive constants of two PZT compositions from a combination of single-crystal and ceramic data. The data from Sections III and IV will then be used in Section V with additional data from the literature to approximate the compositional dependence of the electrostrictive constants of PZT. Finally, a summary of this study will be presented in Section VI.

## II. Temperature Dependence of the Electrostrictive Constants of PZT

The temperature dependences of the electrostrictive constants of perovskite ferroelectrics were previously studied. Jang[7] and Uchino et al.[8] found that the single-crystal electrostrictive constants $Q_{11}$ and $Q_{12}$ of $Pb(Mg_{1/3}Nb_{2/3})O_3$ are independent of temperature, within the limits of their experimental error. Zorn et al.[5] found that from 150° to 200°C the electrostrictive constants $Q_{11}$, $Q_{12}$, and $Q_{44}$ of crystallites in $Pb_{0.83}Sr_{0.12}Ba_{0.05}[Zr_{0.6}Ti_{0.38}Nb_{0.02}]O_3$ ceramic were independent of temperature, again within the limits of the experimental error. In addition, Meng et al.[9] found that the $\bar{Q}_{11}$ and $\bar{Q}_{12}$ constants of ceramic PLZT were virtually independent of temperature. From these measurements the electrostrictive constants of perovskite ferroelectrics appear to be fairly independent of temperature. In this section additional calculations from published data will be presented to further demonstrate that the electrostrictive constants of PZT compositions are only slightly temperature dependent.

The temperature dependence of the spontaneous polarization and strain will be used to calculate the electrostrictive constants for $PbTiO_3$, PZT 40/60 (40% $PbZrO_3$ and 60% $PbTiO_3$), and PZT 90/10 using the following tetragonal and rhombohedral relations:[3]

Tetragonal

$$x_1 = x_2 = Q_{12}P_3^2 \tag{1a}$$

$$x_3 = Q_{11}P_3^2 \tag{1b}$$

$$x_4 = x_5 = x_6 = 0 \tag{1c}$$

Rhombohedral

$$x_1 = x_2 = x_3 = (Q_{11} + 2Q_{12})P_3^2 \tag{2a}$$

$$x_4 = x_5 = x_6 = Q_{44}P_3^2 \tag{2b}$$

The $x_i$ ($i = 1, 2, \ldots, 6$) are the spontaneous strains in reduced notation. $Q_{11}$, $Q_{12}$, and $Q_{44}$ are the cubic electrostrictive constants. $P_3$ is the component of the spontaneous polarization in the $x_3$ direction and is equal to the spontaneous polarization ($P_S$) in the tetragonal phase. In the rhombohedral phase $P_S = 3^{1/2}P_3$.

Equations (1) and (2) were derived from the Devonshire form of the elastic Gibbs free energy function under zero stress conditions[3] and can be used to calculate the electrostrictive constants from experimental spontaneous polarization and strain data. Equation (2) represents the spontaneous strain relations for the high-temperature rhombohedral phase in the PZT system. The low-temperature rhombohedral phase will not be dealt with in this paper (see Ref. 4 for strain relations for this phase). Equa-

tion (1) will be used for the PbTiO₃ and PZT 40/60 compositions, which have tetragonal structures in the ferroelectric state. Equation (2) will be used for the rhombohedral PZT 90/10 composition.

The only direct experimental data available on the temperature dependence of the spontaneous polarization of single-crystal PbTiO₃ was calculated by Remeika and Glass[10] from pyroelectric measurements. They found the room-temperature $P_s$ value to be 0.56 C/m² using liquid electrodes and a pulsed field technique. This value is smaller than Gavrilyachenko et al.'s[11] value of 0.75 C/m² For use in calculating the electrostrictive constants. Remeika and Glass's data were corrected to agree with Gavrilyachenko et al.'s value using the following relation:

$$P_s = (\Delta P + 0.17 \text{ C/m}^2)(0.75/0.56) \qquad (3)$$

$\Delta P$ was the change in polarization that Remeika and Glass calculated from their pyroelectric measurements, and 0.17 is their $P_s$ value at $T_C$.

Haun et al.[12] calculated the spontaneous strains $x_1$ and $x_3$ of the tetragonal structure of PbTiO₃ from high-temperature X-ray diffraction cell constant data by assuming that the electrostrictive constants were independent of temperature. The following procedure was used to recalculate the spontaneous strains independently of the electrostrictive constants. Using the data from Ref. 12 the first step was to use a linear extrapolation of the cubic cell constant down in temperature to the first four sets of tetragonal cell constant data. The spontaneous strains $x_1$ and $x_3$ were then calculated at these four temperatures using the following equations from Ref. 12:

$$x_1 = \frac{a_T - a_C'}{a_C'} \qquad x_3 = \frac{c_T - a_C'}{a_C'} \qquad (4)$$

where $a_T$ and $c_T$ are the tetragonal cell constants, and $a_C'$ is the extrapolation of the cubic cell constant. These four sets of strain data were fitted with the following theoretical relations (Eqs. (17) and (18) from Ref. 12).

$$x_1 = \psi x_{10} \qquad x_3 = \psi x_{30} \qquad (5)$$

where

$$\psi = \frac{2}{3}\left\{1 + \left[1 - \frac{3(T - \theta)}{4(T_C - \theta)}\right]^{1/2}\right\}$$

$T_C$ and $\theta$ are the Curie and Curie–Weiss temperatures, and $x_{10}$ and $x_{30}$ are the spontaneous strains of the tetragonal state at $T_C$. $T_C$ was set equal to 492.2°C (Ref. 12), and $\theta$, $x_{10}$, and $x_{30}$ were determined from the best least-squares fit of the data.

Using the constants obtained from this fitting the spontaneous strain was extrapolated down to lower temperatures and used with Remeika and Glass's corrected polarization data (described above) to calculate the temperature dependence of the electrostrictive $Q_{11}$ and $Q_{12}$ constants of PbTiO₃, as shown in Fig. 1(a). Only a slight temperature dependence was found up to about 300°C. The larger increase of the electrostrictive constants above 300°C was probably due to the larger error in polarization and strain data near $T_C$ where large changes occur in these quantities. The depolarization of the sample above 300°C is likely to cause an increase in calculated electrostrictive constants. The values of the percent change in $Q_{11}$, $Q_{12}$, $-Q_{11}/Q_{12}$, and $Q_h$ ($=Q_{11} + 2Q_{12}$) for PbTiO₃ from 0° to 100°C are listed in Table I. All three constants change less than 2%/100°C, and the ratio $-Q_{11}/Q_{12}$ changes only 0.37%/100°C.

Tsuzuki et al.[13] determined the spontaneous polarization versus temperature on a PZT 40/60 single crystal from ferroelectric hysteresis loop measurements. These data were used with spontaneous strain data from Amin et al.[3] to calculate the temperature dependence of the electrostrictive constants $Q_{11}$ and $Q_{12}$, as shown in Fig. 1(b). Since these strain data were calculated using the cubed root of the tetragonal volume as the extrapolation of the cubic cell constant (problems develop when using this procedure; see Ref. 12 for details), they were first corrected using the value of the $Q_{12}$ ratio that was determined in Section V of
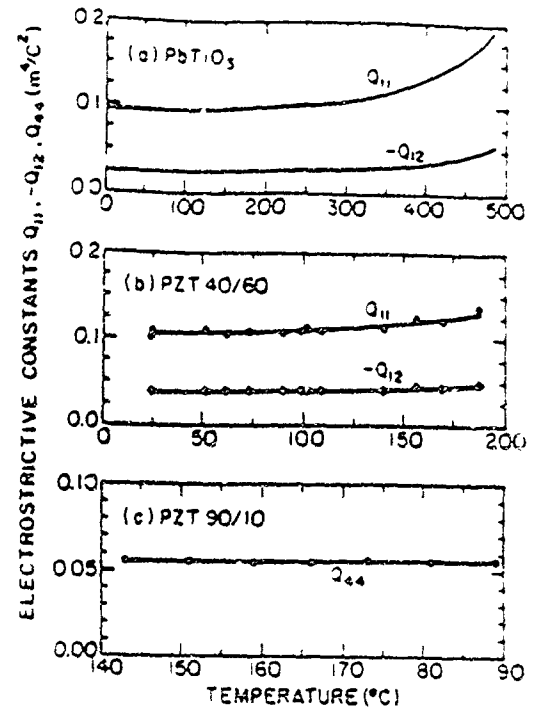


Fig. 1. Single-crystal electrostrictive constants plotted versus temperature for (a) PbTiO₃, (b) PZT 40/60. and (c) PZT 90/10.

this paper. As can be seen in Figure 4 1(b), the electrostrictive constants of PZT 40/60 are only slightly temperature dependent. This dependence again becomes stronger at temperatures approaching $T_C$, probably because of the larger error in this region. The % change/100°C is listed in Table I. The value is larger than that of PbTiO₃, but still should be considered small.

Clarke and Glazer[14] determined the temperature dependence of the spontaneous polarization of PZT 90/10 single crystals from hysteresis loop measurements. They also measured the rhombohedral cell constants using high-temperature X-ray diffraction. The spontaneous strain $x_4$ [$=(90 - \alpha_r)/90$] was calculated from their rhombohedral angle $(\alpha_r)$ data and used with the polarization data to calculate the electrostrictive $Q_{44}$ constant in the high-temperature rhombohedral state, as shown in Fig. 1(c). From 140° to 190°C the $Q_{44}$ constant was virtually independent of temperature with only a 0.47% change/100°C from a linear fit (listed in Table I). Above and below the plotted temperature range the $Q_{44}$ increased significantly as the temperature approached the transitions to the cubic phase at higher temperatures, and the low-temperature rhombohedral phase at lower temperatures. This is again believed to be due to the larger experimental error in the measurements at temperatures close to the transitions.

From the data in Fig. 1 and Table I, it can be concluded that the electrostrictive constants of PbTiO₃ and PZT compositions are only slightly temperature dependent in agreement with the data in the literature on perovskite ferroelectrics.

Table I. Temperature Dependence of the Electrostrictive Constants of PZT

| Composition | Constant | Temp. range (°C) | % change/100°C |
|---|---|---|---|
| PbTiO₃ | $Q_{11}$ | 0–100 | 1.4 |
| PbTiO₃ | $-Q_{12}$ | 0–100 | 1.8 |
| PbTiO₃ | $Q_h$ | 0–100 | 1.0 |
| PbTiO₃ | $-Q_{11}/Q_{12}$ | 0–100 | 0.37 |
| PZT 40/60 | $Q_{11}$, $-Q_{12}$ | 25–150 | 5.2 |
| PZT 90/10 | $Q_{44}$ | 140–190 | 0.47 |

**Table II. Experimental Values of the Ceramic PZT Electrostrictive $\overline{Q}_{12}$ Constant**

| Zr/Ti | $\overline{Q}_{12}$ m$^4$ C$^2$ |
|-------|--------|
| 90/10 | −0 0060 |
| 70/30 | −0 0075 |
| 60/40 | −0 0090 |
| 52/48 | −0 0158 |
| 50/50 | −0 0228 |

**Table III. Single-Crystal Electrostrictive Constants**

| Composition | $Q_{11}$ m$^4$ C$^2$ | $Q_{12}$ m$^4$ C$^2$ | $Q_{44}$ m$^4$ C$^2$ |
|-------------|-------|--------|--------|
| PbTiO$_3$ | 0.089* | −0 026* | 0 0675* |
| PZT 50/50 | 0 0966 | −0 0460 | 0 0819 |
| PZT 90/10 | 0 0508 | −0 0154 | 0 0490 |

*From Ref 12 †From Ref 22.

## III. Experimental Measurements of the Ceramic $\overline{Q}_{12}$ Constant

As described in Section I, the values of the single-crystal electrostrictive constants as a function of composition are required for the development of a thermodynamic theory of PZT. Because of the difficulty of growing single crystals of PZT, very few single-crystal electrostrictive data exist. Some electrostrictive data were measured on ceramic PZT samples,[5] but these data are conflicting and do not provide a complete picture of the electrostrictive properties of PZT. To provide additional data to determine the compositional dependence of the electrostrictive constants in the PZT system, the $\overline{Q}_{12}$ constant was measured on a series of ceramic samples. These measurements will be described in this section.

Pure homogeneous PZT ceramic samples were fabricated from sol–gel-derived powders as described in Ref. 16. Thin rectangular-shaped samples with dimensions of 10 by 4 by 0.3 mm were cut from sintered disks, and sputtered with gold electrodes. The electrostrictive strain and polarization were measured simultaneously under a cycling electric field at a frequency of 0.1 Hz. A variable frequency modified Sawyer–Tower circuit[17] was used to measure polarization–electric field hysteresis loops, which were then used to determine the polarization as a function of applied electric field. A polyimide-based foil strain gage[1] was carefully bonded to the samples with a polyester adhesive.[1] The gage resistance was measured using a dc bridge type dynamic strain amplifier.[**] The transverse strain level, $x_{12}$, was then recorded on a strip chart recorder as a function of electric field.

The electrostrictive $\overline{Q}_{12}$ constant was calculated from the slope of the transverse strain plotted versus the square of the polarization using the method described in Ref. 9. The resulting $\overline{Q}_{12}$ values for five PZT compositions are listed in Table II and plotted later in this paper in Fig. 3(b). The $\overline{Q}_{12}$ constant increased slightly from PZT 90/10 to 60/40, and then a large increase occurred near the PZT 50/50 composition. Zom et al.[5] found similar results for Pb$_{0.83}$Sr$_{0.12}$Ba$_{0.05}$[Zr$_x$Ti$_{0.98-x}$Nb$_{0.02}$]O$_3$ compositions with $x$ ranging from 0.45 to 0.65, where the $Q_{12}$ constant, as well as the $Q_{11}$ constant, increased with increasing titanium content.

## IV. Calculation of the Single-Crystal Electrostrictive Constants for PZT 50/50 and 90/10

The ceramic $\overline{Q}_{12}$ data presented in Section III were used with additional data from the literature to determine the single-crystal electrostrictive constants using series and parallel averaging relations PZT 50/50 and 90/10 were the only compositions where enough electrostrictive data were available to use this procedure. The methods used to calculate the constants for these compositions will be described in this section.

Series and parallel electrostrictive averaging relations, analogous to the Voigt and Reuss methods of averaging the elastic constants,[6] were presented in Ref 18 These equations relate the polycrystalline $\overline{Q}_{11}$, $\overline{Q}_{12}$, and $\overline{Q}_{44}$ constants to the single-crystal

constants. However, because a polycrystalline material is isotropic, the $\overline{Q}_{44}$ equation is related to the $\overline{Q}_{11}$ and $\overline{Q}_{12}$ relations, and thus only two independent equations exist for the series or parallel models. For this reason, if values of the polycrystalline $\overline{Q}_{11}$ and $\overline{Q}_{12}$ constants are known, then a single-crystal constant or some relation involving the single-crystal constants will also have to be determined to be able to use these averaging equations to solve for the single-crystal $Q_{11}$, $Q_{12}$, and $Q_{44}$ constants.

The following procedure was used to calculate the single-crystal constants of PZT 50/50 using the ceramic $\overline{Q}_{12}$ value of −0 0228 m$^4$/C$^2$ from Table II, and additional information from the literature. Zhuang et al.[19] measured the ceramic piezoelectric $\overline{d}_{33}$ and $\overline{d}_{31}$ charge coefficients and found that the $\overline{d}_{33}/\overline{d}_{31}$ ratio was −2.2 for the PZT 50/50 composition. The ceramic $\overline{Q}_{11}/\overline{Q}_{12}$ ratio has a value of −2.2, assuming that the boundary conditions are the same for the $\overline{d}_{33}$ and $\overline{d}_{31}$ coefficients (see Ref. 18 for more details concerning this assumption). If the ceramic $\overline{Q}_{11}/\overline{Q}_{12}$ ratio is close to −2, then the single-crystal $Q_{11}/Q_{12}$ ratio will also have a value close to −2 when using either the series or parallel models.[18] Zom et al.[5] experimentally found that the $Q_{11}/Q_{12}$ ratio was approximately −2 for PZT compositions (modified with strontium, barium, and niobium) close to the tetragonal–rhombohedral morphotropic boundary.

Using the ceramic $\overline{Q}_{12}$ value of −0 0228 m$^4$/C$^2$ and a ceramic $\overline{Q}_{11}/\overline{Q}_{12}$ ratio of −2.2, the single-crystal $Q_{11}/Q_{12}$ ratio was varied to obtain reasonable values of the single-crystal constants using the series and parallel models. This procedure resulted in a single-crystal $Q_{11}/Q_{12}$ ratio of −2.1, and the same single-crystal $Q_{11}$ and $Q_{12}$ constants when using either model, but different $Q_{44}$ values. The series model gave a $Q_{44}$ of 0.0532 m$^4$/C$^2$, while the parallel model resulted in a value of 0.1106 m$^4$/C$^2$. The average of the two models was taken as the $Q_{44}$ for this composition and is listed in Table III along with the resulting $Q_{11}$ and $Q_{12}$ values.

The series and parallel models were also used to determine the single-crystal constants for the PZT 90/10 composition using the ceramic $\overline{Q}_{12}$ value of −0.006 m$^4$/C$^2$ from Table II, and additional data from the literature. A single-crystal $Q_{44}$ constant of 0 049 m$^4$/C$^2$ was calculated in the high-temperature rhombohedral state from Clarke and Glazer's[14] spontaneous polarization data, and Haun et al.'s[20] spontaneous strain $x_4$ data. Ujma et al.[21] calculated the hydrostatic electrostrictive $\overline{Q}_h$ ($=\overline{Q}_{11} + 2\overline{Q}_{12}$) constant for ceramic PbZrO$_3$ as a function of temperature and defect concentration from measurements of the pressure Curie constant (linear slope of the inverse dielectric constant of the cubic phase versus pressure). They found that the $\overline{Q}_h$ decreased with increasing temperature above $T_C$. Assuming that this temperature dependence was due to their measurements close to $T_C$, a value of $\overline{Q}_h$ of 0.02 m$^4$/C$^2$ was chosen from their highest temperature measurement above $T_C$ on a defect-free sample. The PZT 90/10 composition was also assumed to have this value of $\overline{Q}_h$

Using the above values of the single-crystal $Q_{44}$ and ceramic $\overline{Q}_{12}$ and $\overline{Q}_h$ constants, the single-crystal electrostrictive constants of the PZT 90/10 composition were calculated from the series and parallel models. The ceramic $\overline{Q}_{12}$ constant and ceramic $\overline{Q}_{11}/\overline{Q}_{12}$ (calculated from $\overline{Q}_{12}$ and $\overline{Q}_h$) ratio were fixed, while the single-crystal $Q_{11}/Q_{12}$ ratio was varied until the average of the series and parallel $Q_{44}$'s was equal to the experimental value. Because the $Q_{11}/Q_{12}$ and $\overline{Q}_{11}/\overline{Q}_{12}$ ratios were used in the series and parallel

---

[1] Kyowa KFR-02-C1-11 Kyowa Electronic Instruments Co , Ltd., Tokyo, Japan.
[1] Kyowa PC-12.
[**] Kyowa DPM-612B.

models, the same values of $Q_{11}$ and $Q_{12}$ result with different $Q_{44}$'s. The series model gave a $Q_{44}$ value of 0.0385 m$^4$/C$^2$, while the parallel model gave a value of 0.0592 m$^4$/C$^2$. The average of these two values was used as the $Q_{44}$ for the PZT 90/10 composition and is listed in Table III along with the resulting $Q_{11}$ and $Q_{12}$ values.

## V.  Compositional Dependence of the Electrostrictive Constants of PZT

In this section the single-crystal electrostrictive constants determined in the last section for the PZT 50/50 and 90/10 compositions will be used with previously determined PbTiO$_3$ constants[12,22] to approximate the compositional dependence across the PZT solid-solution system. The values of the constants for these three compositions are listed in Table III. These data indicate that all three constants $Q_{11}$, $Q_{12}$, and $Q_{44}$ have larger values at the PZT 50/50 composition than at the PbTiO$_3$ or PZT 90/10 compositions.

The following Cauchy-type equation was used to fit the $Q_{11}$, $Q_{12}$, and $Q_{44}$ data:

$$ Q_{ij} = \frac{a}{1 + b(x - c)^2} + dx + e \qquad (6) $$

where $a$, $b$, $c$, $d$, and $e$ are constants, and $x$ is the mole fraction of PbTiO$_3$ in PZT. The constant $c$ was set equal to 0.5 to cause the peaks to form at the PZT 50/50 composition. Values of the $a$, $d$, and $e$ constants were found by fitting the data listed in Table III. The $b$ constant was used to control the shape (width) of the peaks. A value of 200 was found to give fairly good upper and lower bounds (series and parallel models) around the ceramic $Q_{12}$ data listed in Table II (see Fig. 3(b)).

The resulting values of the five constants for $Q_{11}$, $Q_{12}$, and $Q_{44}$ are listed in Table IV. These values were used to calculate the compositional dependence of the electrostrictive constants using Eq. (6), as shown in Fig. 2(a). At this time the cause of the increase of the electrostrictive constants in the center of the phase diagram is not understood. However, this behavior gives fairly good agreement with other experimental data. The anomalous behavior may be related to the tetragonal–rhombohedral morphotropic boundary, or possibly due to some type of ordering that occurs in the PZT structure at the PZT 50/50 composition. In addition to the peaks in the electrostrictive constants, and the well-established peaks in the dielectric and piezoelectric properties near the morphotropic boundary, the Curie constant has also been found to form a peak in this region.[23] Studying these properties in other solid-solution systems, such as the Pb(Mg$_{1/3}$Nb$_{2/3}$)O$_3$–PbTiO$_3$ system where the morphotropic boundary occurs well away from the 50/50 composition, may lead to a better understanding of this behavior.

The $Q_h$ constant and $-Q_{12}/Q_{11}$ ratio were also calculated and plotted versus composition in Figs. 2(b) and (c). The $-Q_{12}/Q_{11}$ ratio also forms a peak at the PZT 50/50 composition with the peak value approaching 0.5. The $-Q_{12}/Q_{11}$ ratio is analogous to Poisson's ratio, which is equal to $-s_{12}/s_{11}$, where the $s_{ij}$ are the elastic compliance coefficients. When the value of Poisson's ratio approaches 0.5, the material becomes mechanically incompressible. In a similar way, when the $-Q_{12}/Q_{11}$ ratio approaches 0.5, the hydrostatic electrostrictive constant becomes very small (see Fig. 2(b)), and it is difficult to produce a volumetric electrostrictive strain in the material.
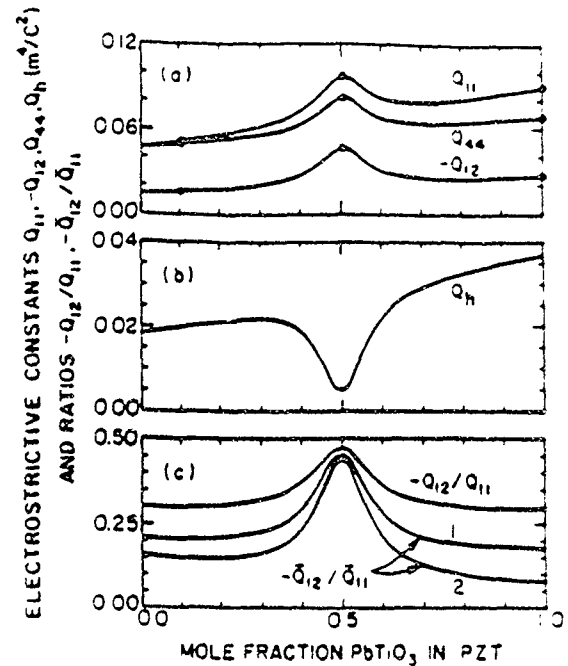


Fig. 2. Electrostrictive constants and ratios plotted versus composition. The single-crystal constants $Q_{11}$, $-Q_{12}$, $Q_{44}$, and $Q_h$ are plotted in (a) and (b). The single-crystal $-Q_{11}/Q_{12}$ and ceramic $-\overline{Q}_{11}/\overline{Q}_{12}$ ratios (upper and lower limits labeled 1 and 2) are plotted in (c). The data points in (a) are from Table III

Haun et al.[18] showed that as the single-crystal $-Q_{12}/Q_{11}$ ratio increases, the ceramic $-\overline{Q}_{12}/\overline{Q}_{11}$ ratio will also increase, when using either the series or parallel models. This effect is shown in Fig. 2(c), where the ceramic $-\overline{Q}_{12}/\overline{Q}_{11}$ ratio is plotted versus composition for the series and parallel models. The single-crystal $-Q_{12}/Q_{44}$ ratio also influences the ceramic $-\overline{Q}_{12}/\overline{Q}_{11}$ ratio, but has little effect when the single-crystal $-Q_{12}/Q_{11}$ ratio approaches 0.5.

The piezoelectric anisotropy $(-\overline{d}_{33}/\overline{d}_{33})$ in PZT ceramics is of considerable importance in hydrophone and medical ultrasonic imaging applications, where a large piezoelectric anisotropy is desired for increased hydrostatic sensitivity.[24] The piezoelectric anisotropy in PZT ceramics is much larger for compositions near the end members PbTiO$_3$ and PbZrO$_3$ than for compositions in the center of the phase diagram near the morphotropic phase boundary.

The values of the single-crystal electrostrictive ratios $-Q_{12}/Q_{11}$ and $-Q_{12}/Q_{44}$ have been shown to be related to the large piezoelectric anisotropy that occurs in ceramic PbTiO$_3$.[18] This same type of analysis can now be extended across the PZT system using the electrostrictive data plotted in Fig. 2. The change in the single-crystal electrostrictive ratios across the PZT system contributes to the change in piezoelectric anisotropy that occurs. The dielectric anisotropy and degree of polarization have also been shown to be related to the ceramic piezoelectric anisotropy.[1,25]

The single-crystal electrostrictive constants were also used to calculate the compositional dependence of the upper and lower limits of the ceramic constants using the series and parallel models, as shown in Fig. 3. The ceramic $\overline{Q}_{12}$ data points shown in Fig. 3(b) are from Table II and were used to determine the

Table IV.  Values of the Constants Used in Eq. (6) to Calculate the Compositional Dependence of the Electrostrictive Constants of PZT

| Constant | $a$ | $b$ | $c$ | $d$ | $e$ |
|---|---|---|---|---|---|
| $Q_{11}$ | 0.029 578 | 200 | 0.5 | 0.042 796 | 0 045 624 |
| $Q_{12}$ | −0.026 568 | 200 | 0 5 | −0.012 093 | −0.013 386 |
| $Q_{44}$ | 0.025 325 | 200 | 0 5 | 0 020 857 | 0 046 147 |
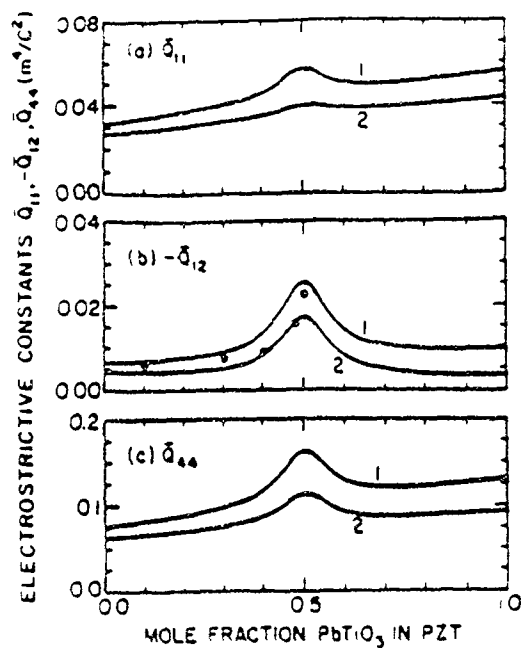
Fig. 3. Upper and lower limits of the polycrystalline ceramic electrostrictive constants plotted versus composition. Series and parallel models were used to calculate the curves labeled 1 and 2, respectively. The data points shown in (b) are from the ceramic measurements listed in Table II.

value of the $b$ constant (listed in Table IV) that caused the series and parallel models to give upper and lower bounds around the data, as described earlier in this section. Larger peaks occurred in the limits of the ceramic $\bar{Q}_{12}$ constant compared to that of the $\bar{Q}_{11}$ and $\bar{Q}_{44}$ constants. The upper and lower limits of the $\bar{Q}_{11}$ constant for PbZrO$_3$ are in good agreement with experimental ceramic measurements by Roleder.[35]

## VI. Summary

The electrostrictive constants of PZT were shown to be only slightly temperature dependent. The electrostrictive $\bar{Q}_{12}$ constant was measured as a function of composition on pure homogeneous PZT ceramic samples fabricated from sol-gel powders. These data were used with additional single-crystal and ceramic data from the literature to approximate values of the single-crystal electrostrictive constants using series and parallel models, analogous to the Voigt and Reuss models for the elastic constants.

Equations were then used to fit the compositional dependence of the single-crystal and ceramic $\bar{Q}_{12}$ data. These equations were used to approximate the single-crystal electrostrictive constants as a function of composition. A peak was found to occur in the electrostrictive constants in the center of the phase diagram. Additional research is needed to understand the cause of this anomalous behavior.

The change in the ratios of the single-crystal electrostrictive constants as a function of composition can be used to explain the large electromechanical anisotropy that occurs in ceramic samples with compositions near the end members PbTiO$_3$ and PbZrO$_3$, but does not occur in ceramic samples with compositions in the center of the phase diagram near the morphotropic phase boundary.

A thermodynamic theory for the entire PZT system has re-

cently been completed using the values of the electrostrictive constants that have been presented in this paper.[17]

## References

[1] B Jaffe, W J Cook, and H Jaffe, Piezoelectric Ceramics Academic Press, London, England, 1971

[2] R Clarke and R W Whatmore, "The Growth and Characterization of PbZr$_x$Ti$_{1-x}$O$_3$ Single Crystals," J Cryst Growth, 33, 29–38 (1976)

[3] A Amin, M J Haun, B Badger, H A McKinstry, and L E Cross, "A Phenomenological Gibbs Function for the Single Cell Region of the PbZrO$_3$ PbTiO$_3$ Solid Solution System," Ferroelectrics, 65, 107–30 (1985)

[4] M J Haun, Z Q Zhuang, S J Jang, H A McKinstry, and L E Cross, "A Phenomenological Theory for the Second Order Transition Region of the PZT Solid Solution System" pp 398–401 in Proceedings of the 6th IEEE International Symposium on the Applications of Ferroelectrics. Lehigh, PA Edited by V Wood. Institute of Electrical and Electronics Engineers, New York, 1986.

[5] G Zorn, W Wersing, and H Gobel, "Electrostrictive Tensor Components of PZT-Ceramics Measured by X-Ray Diffraction," Jpn J Appl Phys Supplement 24-2, 24, 721–23 (1985).

[6] R F S Hearmon, An Introduction to Applied Anisotropic Elasticity, pp. 41–44 Oxford University Press, Oxford, England, 1961

[7] S J Jang, "Electrostrictive Ceramics for Transducer Applications", Ph D Thesis, Pennsylvania State University, University Park, PA, 1979

[8] K Uchino, S Nomura, L E Cross, S J Jang, and R E Newnham, "Electrostrictive Effect in Lead Magnesium Niobate Single Crystals," J Appl Phys, 51 [2] 1142–45 (1980)

[9] Z Y Meng, U Kumar, and L E Cross, "Electrostriction in Lead Lanthanum Zirconate-Titanate Ceramics," J Am Ceram Soc, 68 [8] 459–62 (1985)

[10] J P Remeika and A M Glass, "The Growth and Ferroelectric Properties of High Resistivity Single Crystals of Lead Titanate," Mater Res Bull, 5, 37–46 (1970)

[11] V G Gavrilyachenko, R I Spinko, M A Martynenko, and E G Fesenko, "Spontaneous Polarization and Coercive Field of Lead Titanate," Fiz Tverd Tela (Leningrad), 12 [5] 1532–34 (1970), Sov Phys. — Solid State (Engl. Transl.), 12 [5] 1203–204 (1970).

[12] M J Haun, E Furman, S J Jang, H A McKinstry, and L E Cross, "Thermodynamic Theory of PbTiO$_3$," J Appl. Phys., 62 [8] 3331–38 (1987)

[13] K Tsuzuki, K Saketa, and M Wada, "Dielectric Properties of Single Crystals of Pb(Zr$_x$Ti$_{1-x}$)O$_3$ Solid Solutions (x = 0.5) " Ferroelectrics, 8, 501–503 (1974)

[14] R Clarke and A M Glazer, "The Ferroelectric-Ferroelectric Transition in Rhombohedral Lead Zirconate-Titanate," Ferroelectrics, 12, 207–209 (1976)

[15] Landolt-Bornstein Numerical Data and Functional Relationships in Science and Technology New Series, Group III. Crystal and Solid State Physics, Vol 16 Supplement to Volume III/11. Elastic, Piezoelectric, Pyroelectric, Piezooptic, Electrooptic Constants, and Nonlinear Dielectric Susceptibilities of Crystals. p 274 Edited by K H. Hellwege and O. Madelung. Springer-Verlag, New York, 1984

[16] Z Q Zhuang, M J Haun, S J Jang, and L E Cross, "Fabrication and Characterization of Pure Homogeneous PZT Ceramics from Sol-Gel Derived Powders," Adv Ceram. Mater, 3 [5] 485–90 (1988)

[17] J K Sinha, "Modified Sawyer and Tower Circuit for Investigation of Ferroelectric Samples," J Phys. E, 42, 696–701 (1965)

[18] M J Haun, E. Furman, S J Jang, and L E Cross, "Modeling of the Electrostrictive, Dielectric and Piezoelectric Properties of Ceramic PbTiO$_3$," to be published in IEEE Trans. Ultrason., Ferroelectr, Frequency Control.

[19] Z Q Zhuang, M J. Haun, S.J. Jang, and L E Cross, "Low Temperature Dielectric Piezoelectric, and Elastic Properties of Pure (Undoped) PZT Ceramics" pp 394–97 in Proceedings of the 6th IEEE International Symposium on the Applications of Ferroelectrics, Lehigh, PA. Edited by V Wood. Institute of Electrical and Electronics Engineers, New York, 1986.

[20] M J Haun, Y H. Lee, H. A. McKinstry, and L E Cross, High Temperature X ray Diffraction Study of Sol-Gel Derived Pb(Zr$_x$Ti$_{1-x}$)O$_3$ Powders", in Proceedings of the 35th Annual Conference on Applications of X-ray Analysis. Denver, CO, Aug. 4–8, 1986, Adv X-ray Anal., 30, 473–81 (1987)

[21] Z. Ujma, J Handerek, and M Pisarski, "Changes in Phase Transition Temperatures in PbZrO$_3$ with Pb and O Vacancies under the Influence of Hydrostatic Pressure," Ferroelectrics, 64, 237–45 (1985)

[22] A V Turik, E G Fesenko, V G Gavrilyachenko, and G I Khasabova, "Anisotropy of the Dielectric and Piezoelectric Properties of Lead Titanate," Kristallografiya, 19. 1095–97 (1974); Sov Phys. — Crystallogr (Engl Transl), 19 677–78 (1974)

[23] A Amin, L E Cross, and R E Newnham, "Calorimetric and Phenomenological Studies of the PbZrO$_3$ PbTiO$_3$ System," Ferroelectrics, 37, 647–50

[24] H Takeuchi, S Jyomura, and C Nakaya, "New Piezoelectric Material for Ultrasonic Transducers," Proc IMF-6, Jpn J Appl. Phys. Suppl 24-2, 24, 36–40 (1985).

[25] W Wersing, K Lubitz, and J Mohaupt, "Anisotropic Piezoelectric Effect in Modified PbTiO$_3$ Ceramics" presented at the 6th IEEE International Symposium on the Applications of Ferroelectrics, Lehigh, PA. 1986.

[26] K Roleder, "Measurement of the High-Temperature Electrostrictive Properties of Ferroelectrics," J Phys. E. 16. 1157–59 (1983).

[27] M J Haun, E. Furman, Z.Q Zhuang, S J Jang, T R Halemane H A McKinstry and L E Cross, "Thermodynamic Theory of the Lead Zirconate-Titanate Solid Solution System, Parts I–V", unpublished work.

APPENDIX  30

# Modeling of the Electrostrictive, Dielectric, and Piezoelectric Properties of Ceramic PbTiO₃

MICHAEL J. HAUN, EUGENE FURMAN, SEI JOO JANG, AND LESLIE E. CROSS, FELLOW, IEEE

*Abstract*—The upper and lower limits of the electrostictive constants, dielectric permittivities, spontaneous polarization, and piezoelectric coefficients were calculated for ceramic PbTiO₃ from theoretical single-crystal constants. Experimental ceramic data falls between these upper and lower limits. The large piezoelectric anisotropy $\bar{d}_{33}/\bar{d}_{31}$ of ceramic PbTiO₃ was shown to be related to the single-crystal PbTiO₃ electrostrictive anisotropies $Q_{11}/Q_{12}$ and $Q_{44}/Q_{12}$. The possibility of a change in sign of the ceramic $\bar{d}_{31}$ coefficient due to a slight variation in the single-crystal electrostrictive anisotropies was discussed. The single-crystal and predicted ceramic hydrostatic electrostrictive constants were found to be equal. Using this result the ceramic hydrostatic $\bar{g}_h$ coefficient is always smaller than the single-crystal $g_h$, but the ceramic hydrostatic $\bar{d}_h$ coefficient can be either larger or smaller than the single-crystal $d_h$, depending on the dielectric anisotropy $(\epsilon_{11}/\epsilon_{33})$ of the single-crystal.

## I. INTRODUCTION

LEAD TITANATE has been extensively used as an end member of ceramic solid solution systems with important piezoelectric properties [1]. One particularly interesting property is the large piezoelectric anisotropy $(d_{33}, d_{31})$ that has been achieved in modified lead titanate ceramics. but not present in the single crystal. These materials are of interest in high-frequency ultrasonic transducers applications [2]

Turk *et al* [3] showed that this large ceramic piezoelectric anisotropy could be obtained by averaging the single-crystal piezoelectric coefficients. They concluded that the small single-crystal dielectric and piezoelectric anisotropies of PbTiO₃ lead to large ceramic piezoelectric anisotropy Wersing *et al.* [4], [5] combined Luchaninov's [6] averaging equations with Devonshire's [7] single crystal relations to calculate the ceramic piezoelectric coefficients from the single-crystal dielectric permittivities, electrostrictive constants and spontaneous polarization. The ceramic $d_{31}$ coefficient was found to disappear for a particular ratio of the electrostrictive coefficients and a certain degree of polarization [5].

The purpose of this study is to further understand the

behavior of PbTiO₃ by calculating the ceramic electrostrictive constants, dielectric permittivities, spontaneous polarization, and piezoelectric coefficients from the single-crystal constants that were recently determined from a Devonshire type phenomonological theory [8]. The upper and lower limits of the properties will be calculated using simple averaging relations. These calculations will then be compared with experimental data.

## II. ELECTROSTRICTIVE CONSTANTS

The upper and lower limits of the ceramic elastic constants can be calculated from single-crystal values using the Voigt and Reuss methods of averaging [9]. Voigt determined the stiffness of the ceramic from the space average of the stiffnesses of the crystallites, while Reuss found the ceramic compliance from the space averages of the compliances of the crystallites. Hill [9] showed that both of these models are only approximate and that the true values should fall between these bounds. In most cases, the experimental values do fall between the Voigt and Reuss limits. Electrostriction is also a fourth rank tensor with similar matrix to tensor conversion as the elastic constants, and thus the same equations can be used to predict the upper and lower limits of the electrostrictive constants.

The electrostrictive $(Q_{ijkl})$ and inverse electrostrictive $(q_{ijkl})$ constants relate the strain $(x_{ij})$ to the polarization components $(P_k P)$ by the following relations:

$$x_{ij} = Q_{ijkl} P_k P_l \tag{1}$$

$$P_i P_j = q_{ijkl} x_{kl}. \tag{2}$$

The tensor to matrix conversions of the electrostrictive and inverse electrostrictive constants are the same as that of the elastic compliances and stiffnesses, respectively

$$Q_{ijkl} = Q_{mn}, \quad \text{when } m \text{ and } n = 1, 2, \text{ or } 3$$

$$2Q_{ijkl} = Q_{mn}, \quad \text{when } m \text{ or } n = 4, 5, \text{ or } 6$$

$$4Q_{ijkl} = Q_{mn}, \quad \text{when } m \text{ and } n = 4, 5, \text{ or } 6 \tag{3}$$

$$q_{ijkl} = q_{mn}, \quad \text{for all } m \text{ and } n. \tag{4}$$

Using a similar procedure as that of Voigt and Reuss for the elastic constants, the electrostrictive and inverse electrostrictive constants of a polycrystalline ceramic can be calculated from the space averages of the single crystal values by assuming that the ceramic is composed of a large

number of small signal crystals with all possible orientations. By also assuming that the single crystals have a cubic structure the following relations result:

$$\overline{Q}_{11} = 3/5Q_{11} + 2/5Q_{12} + 1/5Q_{44}$$

$$\overline{Q}_{12} = 1/5Q_{11} + 4/5Q_{12} - 1/10Q_{44}$$

$$\overline{Q}_{44} = 4/5Q_{11} - 4/5Q_{12} + 3/5Q_{44} \qquad (5)$$

$$\overline{q}_{11} = 3/5q_{11} + 2/5q_{12} + 4/5q_{44}$$

$$\overline{q}_{12} = 1/5q_{11} + 4/5q_{12} - 2/5q_{44}$$

$$\overline{q}_{44} = 1/5q_{11} - 1/5q_{12} + 3/5q_{44}. \qquad (6)$$

Equations (5) and (6) are analogous to the equations used by Reuss and Voigt for the elastic compliances and stiffnesses, respectively [9]. Since the ceramic is assumed to be isotropic:

$$\overline{Q}_{44} = 2(\overline{Q}_{11} - \overline{Q}_{12}) \qquad (7)$$

$$\overline{q}_{44} = 1/2(\overline{q}_{11} - \overline{q}_{12}). \qquad (8)$$

To use (6) to calculate one of the limits of the ceramic electrostrictive constants, the single crystal inverse electrostrictive constants were first determined by inverting the cubic electrostrictive matrix. These constants were used in (6) to determine the ceramic inverse electrostrictive ($\overline{q}_{mn}$) constants, which were then inverted back to obtain the electrostrictive constants using the following relations:

$$\overline{Q}_{11} = \frac{\overline{q}_{11} + \overline{q}_{12}}{(\overline{q}_{11} - \overline{q}_{12})(\overline{q}_{11} + 2\overline{q}_{12})}$$

$$\overline{Q}_{12} = \frac{-\overline{q}_{12}}{(\overline{q}_{11} - \overline{q}_{12})(\overline{q}_{11} + 2\overline{q}_{12})}.$$

$$\overline{Q}_{44} = \frac{1}{\overline{q}_{44}} = \frac{2}{\overline{q}_{11} - \overline{q}_{12}}. \qquad (9)$$

Equations (5) and (9) give ceramic electrostrictive constants corresponding to the series and parallel models, respectively, and will be used to calculate the upper and lower bounds of the ceramic electrostrictive constants from the single-crystal values. Devonshire [7], [10] calculated the ceramic electrostrictive constants of BaTiO₃ using (5). However at that time the single-crystal electrostrictive constants had been overestimated due to the low values of the spontaneous polarization that were used in the calculations. Thus the agreement with experimental ceramic electrostrictive constants was not very good. When a more realistic value of the polarization (0.26 C/m² at room temperature) was later measured [11], Jona and Shirane [12] recalculated the single-crystal electrostrictive constants and used (5) to determine the ceramic $\overline{Q}_{11}$ and $\overline{Q}_{12}$ values. These calculations were in good agreement with the experimental measurements.

The ceramic electrostrictive constants of BaTiO₃ were calculated from the single-crystal values using (5) and (9) as shown in Table I. The values of the experimental ce-

ramic electrostrictive constants, also listed in this table, fall between these upper and lower bounds. Thus the Voigt and Reuss type methods of averaging appear to work well in predicting the limits of the electrostrictive constants in addition to the elastic constants.

Two sets of calculated upper and lower bounds of the electrostrictive constants of ceramic PbTiO₃ are listed in Table I. The same values of the single crystal $Q_{11}$ and $Q_{12}$ constants were used in both sets of calculations, but different $Q_{44}$ values were used. In the first set of PbTiO₃ calculations a $Q_{44}$ of $6.75(10^{-2}$ m⁴/C²) was used. This value was calculated in (3) from experimental values of $\epsilon_{11}$, $d_{15}$, and $P_s$ from PbTiO₃ single crystals. In the second set of calculations a $Q_{44}$ of $2.0(10^{-2}$ m⁴/C²) was used. This value was calculated in (15) from spontaneous polarization and strain data for the rhombohedral Pb(Zr₀.₉Ti₀.₁)O₃ composition. In all three sets of data shown in Table I the magnitudes of the ceramic $\overline{Q}_{11}$ and $\overline{Q}_{12}$ constants are less than the corresponding single-crystal values, but the ceramic $\overline{Q}_{44}$ constants are larger.

The electrostrictive anisotropies $-\overline{Q}_{11}/\overline{Q}_{12}$ and $-\overline{Q}_{44}/\overline{Q}_{12}$ increase in BaTiO₃ and PbTiO₃ ceramics compared to the corresponding single crystal anisotropies as shown in Table I. The $-\overline{Q}_{11}/\overline{Q}_{12}$ anisotropy increases, even though the $\overline{Q}_{11}$ constant decreases, because of the greater decrease in the $-\overline{Q}_{12}$ constant. The $-\overline{Q}_{44}/\overline{Q}_{12}$ anisotropy increases because of both the decrease in $-\overline{Q}_{12}$ and increase in $\overline{Q}_{44}$.

The electrostrictive anisotropies of ceramic PbTiO₃ are larger than those in BaTiO₃, because of the differences in single crystal anisotropies. In the second set of PbTiO₃ data the ceramic anisotropies calculated from the parallel model changed sign because $\overline{Q}_{12}$ became positive. To bet-

TABLE I
ELECTROSTRICTIVE CONSTANTS AND ANISOTROPIES OF BaTiO₃ AND PbTiO₃

| | $10^{-2}$ m⁴/C² | | | $-Q_{11}$ | $-Q_{44}$ |
|---|---|---|---|---|---|
| | $Q$ | $Q_{12}$ | $Q_{44}$ | $Q_{12}$ | $Q_{12}$ |
| **BaTiO₃** | | | | | |
| Single-Crystal | 11.17 | -4.42ᵈ | 5.85ᵈ | 2.5 | 1.3 |
| Ceramic | | | | | |
| Series (5) | 5.06 | -1.90 | 15.9 | 3.2 | 8.4 |
| Parallel (9) | 3.64 | -0.690 | 8.66 | 5.3 | 2.6 |
| Experimental | 5.76ᵇ | -1.24ᵇ | 14.0ᶜ | 4.6 | 11.3 |
| **PbTiO₃** | | | | | |
| Single-Crystal | 8.9ᵈ | -2.6ᵈ | 6.75ᶜ | 3.4 | 2.6 |
| Ceramic | | | | | |
| Series (5) | 5.65 | -0.975 | 13.25 | 5.8 | 13.6 |
| Parallel (9) | 4.37 | -0.335 | 9.41 | 13.0 | 28.1 |
| Single-Crystal | 8.9ᵈ | -2.6ᵈ | 2.0 | 3.4 | 0.77 |
| Ceramic | | | | | |
| Series (5) | 4.70 | -0.500 | 10.4 | 9.4 | 20.8 |
| Parallel (9) | 2.28 | 0.708 | 3.5 | -3.2 | -4.4 |

ᵃCalculated from the spontaneous polarization (0.26 C/m²) and piezoelectric $g_{ij}$ data from [13]
ᵇFrom [14]
Calculated from (7)
ᵈFrom [8]
ᶜFrom [3]
From [15]

ter understand the effect of the single-crystal anisotropies on the ceramic anisotropy (5) and (9) can be rearranged as

$$\bar{\sigma}_{series} = \frac{-1 \ \sigma - 1/(2\mu) + 4}{3 \ \sigma - 1 \ \mu - 2},\qquad (10)$$

and

$$\bar{\sigma}_{parallel} =$$
$$\left[1 + \frac{2 + 3(1/\sigma - 1) - 4\mu(1/\sigma + 1)(1/\sigma - 2)}{4 + (1/\sigma - 1) - 2\mu(1/\sigma + 1)(1/\sigma - 2)}\right]^{-1},$$
$$(11)$$

where

$$\bar{\sigma} = -\bar{Q}_{12}/\bar{Q}_{11}, \ \sigma = -Q_{12}/Q_{11}, \text{ and } \mu = -Q_{12}/Q_{44}.$$
$$(12)$$

The ratio $\sigma$ is the electrostrictive analogue to Poisson's ratio ( $= -s_{12}/s_{11}$ ) The electrostrictive ratios defined by (12) are the inverse of the electrostrictive anisotropies listed in Table I.

In Fig. 1 the ceramic ratio $\bar{\sigma}$ was plotted versus the single-crystal $\sigma$ ratio for different values of the single-crystal $\mu$ ratio using (10) and (11). Using either the series of parallel models, the ceramic $\bar{\sigma}$ ratio decreases (anisotropy increases) as the single-crystal $\sigma$ and $\mu$ ratios decrease and increase, respectively The value of the $\mu$ ratio has less effect on the ceramic $\bar{\sigma}$ when using the series model compared to the parallel model. The ceramic $\bar{\sigma}$ can be either positive or negative depending on the values of the single-crystal ratios. A negative value of the ceramic $\bar{\sigma}$ would be due to a positive $\bar{Q}_{12}$, assuming that $\bar{Q}_{11}$ is also positive. If the ceramic $\bar{\sigma}$ changes sign because the $-\bar{Q}_{12}$ constant decreased to zero and changed sign, then the ceramic anisotropy ( $-\bar{Q}_{11}/\bar{Q}_{12}$ ) would increase and go to infinity

The square-shaped data points in Fig. 1 represent BaTiO₃, and the circular and triangular shaped data points represent the first and second sets of PbTiO₃ data in Table I, respectively As shown in Fig. 1 the single-crystal ratios of BaTiO₃ cause the ceramic $\bar{\sigma}$ ratio to be larger than that of PbTiO₃ resulting in less anisotropy. When using the smaller value of the $Q_{44}$ constant, the upper and lower limits of the PbTiO₃ ceramic $\bar{\sigma}$ ratio range from positive to negative values, illustrating the possibility of having very large anisotropy and a positive ceramic $\bar{Q}_{12}$ constant.

The larger value of the $Q_{44}$ constant shown in Table I should better represent the actual $Q_{44}$ of PbTiO₃, since this value was determined from measurements on PbTiO₃ This value will be used in calculating the piezoelectric coefficients later in the paper. When using this value, large ceramic anisotropy still resulted as shown in Table I The electrostrictive constants of perovskite ferroelectrics have been experimentally shown to be only slightly temperature dependent, [11], [16] and thus were assumed to be independent of temperature throughout this paper However, since the magnitude of the $\bar{Q}_{12}$ constant of ceramic PbTiO₃ is small, a slight temperature depen-
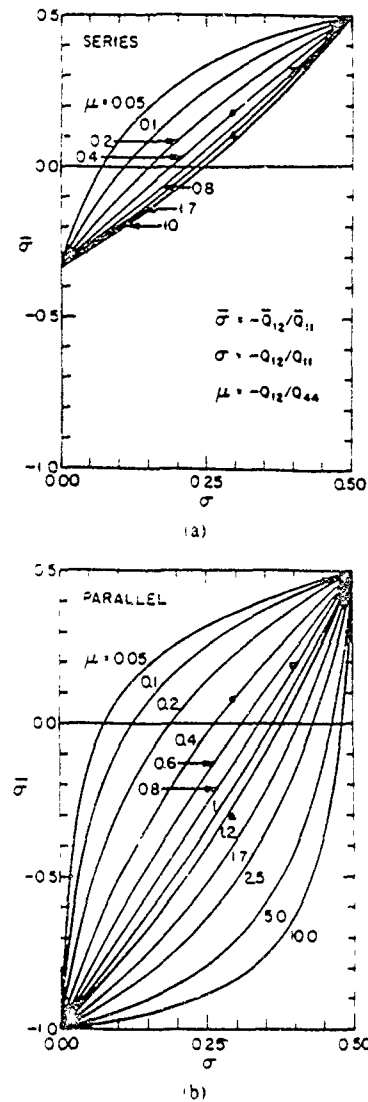


Fig 1   Ceramic $\bar{\sigma}$ ratio plotted versus single-crystal $\sigma$ ratio for different values of single-crystal $\mu$ ratio calculated from a) Series model using (10) and b) Parallel model using (11)  Square shaped data points correspond to BaTiO₃, circular shaped to first set of PbTiO₃ data in Table I and triangular shaped to second set of PbTiO₃ data.

dence of the single-crystal electrostrictive constants could cause the ceramic $\bar{Q}_{12}$ to go to zero and change signs as a function of temperature. This will be further discussed later in the paper when the electrostrictive anisotropy is related to the piezoelectric anisotropy.

An interesting result of this averaging procedure is that the ceramic hydrostatic electrostrictive constant ( $\bar{Q}_h = \bar{Q}_{11} + 2\bar{Q}_{12}$ ) is equal to the single-crystal $Q_h$ when using either (5) or (9), even though the magnitudes of the ceramic $\bar{Q}_{11}$ and $\bar{Q}_{12}$ coefficients are considerably lower than the single-crystal values. The experimental ceramic $\bar{Q}_h$ of BaTiO₃ is 3.3( $10^{-2}$ m⁴/C²) from the data in Table I, which is in fairly good agreement with the single-crystal and predicted ceramic values of 2.3. However, even better agreement is found with ceramic $\bar{Q}_h$'s of 2.1 and 2.8( $10^{-2}$ m⁴/C²), which can be calculated from data in [18] using the relation $Q_h = -(d\theta/dP)/(2\varepsilon_0 C)$, where $C$ is the Curie-Weiss constant and $d\theta/dP$ is the slope of

the pressure dependence of the Curie temperature ($\theta$). A similar result also occurs when using these series and parallel models for the elastic constants. The ceramic volume compressibility is equal to that of the single crystal

## III. DIELECTRIC PERMITTIVITY

Parallel and series models were also used to calculate the upper and lower limits of the ceramic dielectric permittivity from the single-crystal values:

$$\text{parallel } \bar{\epsilon} = (2/3)\epsilon_{11} + (1/3)\epsilon_{33} \qquad (13)$$

$$\text{series } 1/\bar{\epsilon} = (2/3)/\epsilon_{11} + (1/3)/\epsilon_{33} \qquad (14)$$

where $\bar{\epsilon}$ is the ceramic permittivity, and $\epsilon_{11}$ and $\epsilon_{33}$ are the single-crystal permittivities perpendicular and parallel to the polar axis, respectively (assumed to be equal to the dielectric susceptibilities).

The upper and lower limits of the ceramic permittivity were plotted versus temperature in Fig. 2 using (13) and (14) and the phenomenological calculations of the single crystal permittivities from [8]. Only a slight difference in the upper an lower limits was found, because of the small dielectric anisotropy of single-crystal PbTiO$_3$ The experimental data (cicular data points) plotted in this figure were calculated from the piezoelectric $d_{33}$ and $g_{33}$ data given in [19] (and plotted later in this paper) for a ceramic PbTiO$_3$ sample doped with 1.0-mole percent MnO$_2$. This experimental data is in good agreement with the predicted upper and lower bounds. Another experimental data point is plotted in this figure. This value was listed in a table in [19] for the same composition measured at room temperature. The predicted upper and lower limits of the ceramic dielectric permittivity at 25°C are 105 and 96 5. These values were calculated from the single-crystal $\epsilon_{11}$ and $\epsilon_{33}$ values of 124.4 and 66.6 from [8].

## IV SPONTANEOUS POLARIZATION

There are six possible directions for the polar axis in a tetragonal structure such as that of PbTiO$_3$. If an applied electric field causes all of the domains in a ceramic to align along the closest of these directions to the field, then the polarization of the ceramic ($\bar{P}$) will be: $\bar{P} = 0.831 P$, where $P$ is the single-crystal polarization [20]. This gives the upper limit of the ceramic polarization by assuming that 1 6 of the domains did not require switching, 1 6 switched through 180°, and 2/3 through 90° [21]. However, Carl [22] found that, in dense PbTiO$_3$ ceramics doped with small amounts of lanthanum and manganese, the 180° domain alignment was virtually perfect, but only about ten percent of the domains switched by 90° By assuming that no 90° domain switching occurs and that only 1/6 of the domains realign through 180°, $\bar{P} = (1/3)(0.831)P = 0.277 P$ This will be assumed to be the lower limit of the ceramic polarization. If 90° domain alignment does not occur, then the 2/3 of the domains that would ideally switch through 90° will instead possibly switch through 180° If all of these domains switch
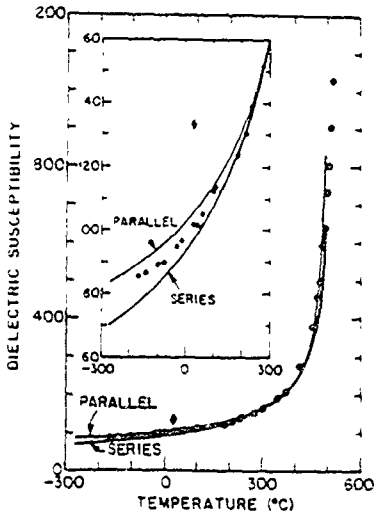


Fig 2 Dielectric susceptibility plotted versus temperature for ceramic PbTiO$_3$ Data points are experimental measurements from [19]
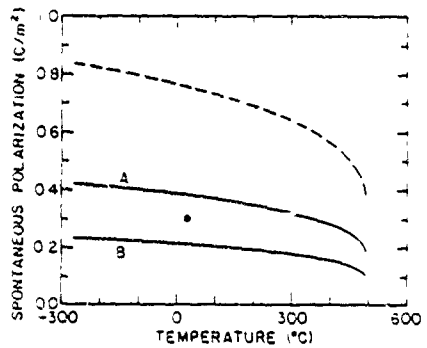


Fig 3 Spontaneous polarization of PbTiO$_3$ plotted versus temperature Dashed curve is single-crystal polarization calculated from phenomenological theory in [8] Solid curves represent approximations of upper ($= 0.5 P$) and lower ($= 0.277 P$) limits of ceramic polarization Data point is from [22]

through 180° then $\bar{P} = 0.5 P$ This result will be assumed to be the upper limit of ceramic polarization.

The upper and lower limits of the spontaneous polarization of ceramic PbTiO$_3$ are plotted in Fig. 3 along with the single-crystal polarization. Carl [22] found that the polarization of ceramic PbTiO$_3$ was approximately 0.3 C/m$^2$ at room temperature. This value falls between the calculated limits at 25°C of 0.21 and 0.38 C/m$^2$ as shown in Fig. 3.

## V PIEZOELECTRIC COEFFICIENTS

The piezoelectric voltage ($g_{ij}$) and charge ($d_{ij}$) coefficients of a single-crystal of PbTiO$_3$ are related to the electrostrictive constants, dielectric permittivities, and spontaneous polarization as follows:

$$g_{11} = 2Q_{11}P_3, \quad g_{31} = 2Q_{12}P_3, \quad g_{15} = Q_{44}P_3 \quad (15)$$

$$d_{33} = 2\epsilon_0\epsilon_{33}Q_{11}P_3, \quad d_{31} = 2\epsilon_0\epsilon_{33}Q_{12}P_3,$$

$$d_{15} = \epsilon_0\epsilon_{11}Q_{44}P_3. \qquad (16)$$

These equations are based on the approximation that the dielectric susceptibilities $\eta_{11}$ and $\eta_{33}$ are equal to the dielectric permittivities $\epsilon_{11}$ and $\epsilon_{33}$.

Equations (15) and (16) are single-crystal relations and should probably not be used for ceramics. However, these equations can be used to determine the upper and lower limits of the ceramic piezoelectric coefficients from the limits of the ceramic electrostrictive constants, dielectric permittivities, and spontaneous polarization. For example:

$$\bar{g}^{L}_{33} = 2\bar{Q}^{U}_{11}\bar{P}^{U}_{3}, \quad \bar{g}^{L}_{33} = 2\bar{Q}^{L}_{11}\bar{P}^{L}_{3}, \tag{17}$$

where $U$ and $L$ refer to the upper and lower limits as defined in the previous sections. Similar equations were used to calculate the ceramic limits for the other piezoelectric constants. Since there was very little difference between the upper and lower limits of the ceramic PbTiO₃ dielectric permittivity (see Fig. 2), the average of the series and parallel models were used in the calculations of the piezoelectric $d_{ij}$ constants. However, for a material such as BaTiO₃ with a large dielectric anisotropy, the limits of the dielectric permittivity should also be accounted for.

Using this procedure the upper and lower limits of the piezoelectric coefficients were calculated and plotted versus temperature in Fig. 4. The single-crystal coefficients are also plotted in this figure for comparison along with experimental ceramic data. The values of the piezoelectric coefficients at 25°C are listed in Table II. The circular data points shown in Figs. 4(a) and (d) were measured in [19] on ceramic PbTiO₃ doped with 1 0-mole-percent MnO₂. This data falls between the predicted upper and lower limits with similar temperature dependences as the calculated curves. The diamond shaped data points shown in Figs. 4(a), (b), (d), and (e) are also from [19] for the same composition. The corresponding experimental dielectric data was previously shown in Fig 2. The experimental $g_{31}$ and $d_{31}$ coefficients also fall between the upper and lower limits. The square shaped data points shown in Figs 4(c) and (f) are from [24] for ceramic PbTiO₃ doped with 1 0- and 2 5-mole-percent MnO₂ and LaO₃ ₂, respectively. The experimental $g_{15}$ coefficient of this composition falls between the limits, but the $d_{15}$ coefficient was greater than the upper limit because of a larger dielectric permittivity (170) than that predicted. The difference between the ceramic and single-crystal values of the $g_{15}$ and $d_{15}$ coefficients is smaller than that of the other coefficients, because the ceramic $\bar{Q}_{44}$ constant is larger than the single-crystal value.

From (15) and (16) the piezoelectric anisotropy of a single-crystal is found to be equal to the electrostrictive anisotropy as

$$g_{33}/g_{31} = d_{33}/d_{31} = Q_{11}/Q_{12} = -1 \sigma \tag{18}$$

This single-crystal relation can be used to approximate the upper and lower limits of the ceramic piezoelectric anisotropy from the ceramic electrostrictive anisotropy by assuming that

$$(\bar{g}_{33}/\bar{g}_{31})^{U} = \bar{g}^{U}_{33}/\bar{g}^{U}_{31}, (\bar{g}_{33}/\bar{g}_{31})^{L} = \bar{g}^{L}_{33}/\bar{g}^{L}_{31} \tag{19}$$

Equations (10) and (11) and Fig. 1 can then be used to predict the upper and lower bounds of the ceramic piezo-

electric anisotropy from the single-crystal electrostrictive anisotropies. From Table II, experimentally $-\bar{g}_{31}/\bar{g}_{33} = 0\ 11$ for ceramic PbTiO₃. This value falls between the predicted ceramic $-\bar{Q}_{12}/\bar{Q}_{11}$ bounds of 0.077 and 0 17 plotted in Fig. 1 (listed in Table I as $-Q_{11}/Q_{12}$). However, the experimental $-\bar{g}_{31}/\bar{g}_{33}$ of BaTiO₃ has a value of 0 41 [24], which does not fall between the predicted ceramic $-\bar{Q}_{12}/\bar{Q}_{11}$ bounds of 0.19 and 0 31 (see Table I)

Equation (19) was based on the assumption that the boundary conditions are the same for the $\bar{g}_{33}$ and $\bar{g}_{31}$ coefficients. However, the boundary conditions might not be the same, and thus the following relations should probably be used to calculate the bounds of the piezoelectric anisotropies:

$$(\bar{g}_{33}/\bar{g}_{31})^{U} = \bar{g}^{U}_{33}/\bar{g}^{L}_{31} = (\bar{d}_{33}/\bar{d}_{31})^{U} = \bar{d}^{U}_{33}/\bar{d}^{L}_{31}$$
$$= \bar{Q}^{U}_{11}/\bar{Q}^{L}_{12} \tag{20}$$

$$(\bar{g}_{33}/\bar{g}_{31})^{L} = \bar{g}^{L}_{33}/\bar{g}^{U}_{31} = (\bar{d}_{33}/\bar{d}_{31})^{L} = \bar{d}^{L}_{33}/\bar{d}^{U}_{31}$$
$$= \bar{Q}^{L}_{11}/\bar{Q}^{U}_{12}. \tag{21}$$

Since for a particular domain configuration in a ceramic the polarization $\bar{P}_3$ and dielectric permittivity $\bar{\epsilon}_{33}$ are the same in the $\bar{d}_{33}$ and $\bar{d}_{31}$ relations, they were assumed to cancel out of (20) and (21). The electrostrictive anisotropies $\bar{Q}^{U}_{11}/\bar{Q}^{L}_{12}$ and $\bar{Q}^{L}_{11}/\bar{Q}^{U}_{12}$ result in wider limits than those plotted in Fig. 1, and can be calculated from relations similar to (10) and (11). Using (20) and (21) the experimental value of $-\bar{g}_{31}/\bar{g}_{33}$ of BaTiO₃ (0 41) falls between the predicted $-\bar{Q}_{11}/\bar{Q}_{12}$ limits of 0 11 and 0 52 (calculated using the values from Table I)

From (20) and (21) the upper and lower limits of the ceramic piezoelectric anisotropy only depend on the electrostrictive anisotropy and are independent of the dielectric properties. However, from piezoelectric averaging equations Turik et al. [3] concluded that the low dielectric anisotropy of single-crystal PbTiO₃ contributed to the large ceramic piezoelectric anisotropy. Using Wersing's [4], [5] approach of combining Luchaninov's [6] averaging equations with single-crystal relations (16), and then solving for the anisotropy, results in the following relation.

$$\frac{\bar{d}_{33}}{\bar{d}_{31}} = \frac{\dfrac{2Q_{11}}{(1\ \delta - 1)Q_{12}} + \dfrac{\epsilon_{11}Q_{44}}{\epsilon_{33}Q_{12}} - 2}{\dfrac{Q_{11}}{Q_{12}} - \dfrac{\epsilon_{11}Q_{44}}{2\epsilon_{33}Q_{12}} + \dfrac{1 - \delta}{1 - \delta}}, \tag{22}$$

where $\delta = \langle \cos^4 \theta \rangle / \langle \cos \theta \rangle$, and $\theta$ is the angle between the direction of the spontaneous polarization of a crystallite and the direction of the poling field. Equation (22) indicates that if the single-crystal dielectric anisotropy $(\epsilon_{11}/\epsilon_{33})$ decreases, the ceramic piezoelectric anisotropy will increase. If $\delta = 3\ 5$ and $\epsilon_{11}/\epsilon_{33} = 1$, then the right side of (23) reduces to the electrostrictive series model (10) that gave the upper limit of the $\sigma$ ratio and the lower limit of the ceramic electrostrictive anisotropy. This indicates that Luchaninov's [6] averaging equations may
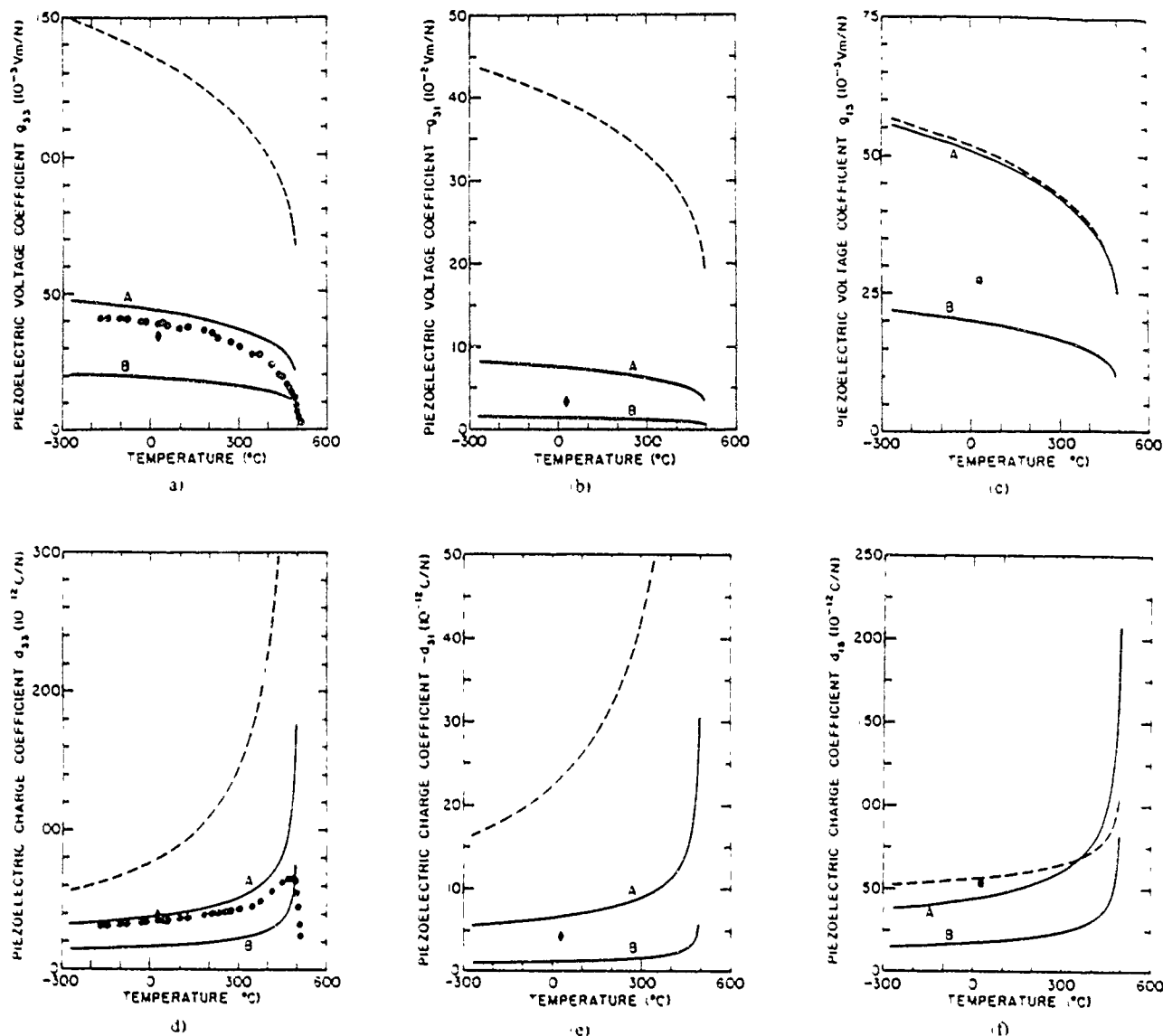
Fig 4 Piezoelectric voltage $(g_{ij})$ and charge $(d_{ij})$ coefficients plotted versus temperature for PbTiO. Dashed curves are theoretical single crystal coefficients calculated from phenomenological theory in [8] Solid curves A and B are upper and lower bounds of ceramic coefficients calculated using $(17)$ for $g_{33}$ and similar equations for remaining coefficients Data points are experimental measurements from [19] and [24]

TABLE II
THE PIEZOELECTRIC COEFFICIENTS OF CERAMIC PbTiO, AT 25°C

| Coefficient | Lower Limit | Experimental | Upper Limit |
|---|---|---|---|
| $g_{33} (10^{-3} Vm/N)$ | 18 3 | 33 - 38 | 42 6 |
| $g_{31} (10^{-3} Vm/N)$ | -1 40 | -3 5 | -7 36 |
| $g_{15} (10^{-3} Vm/N)$ | 19 7 | 27 | 50 0 |
| $d_{33} (10^{-12} C/N)$ | 6 3 | 39 - 34 | 18 0 |
| $d_{31} (10^{-12} C/N)$ | -1 25 | -4 2 | -6 57 |
| $d_{15} (10^{-12} C/N)$ | 17 6 | 53 | 44 6 |

Diamond shaped data points in Fig 4 (doped with 1 0 mole percent Mn. from [19])

'Circular shaped data points in Fig 4 (doped with 1 0 mole percent Mn. from [19])

Square shaped data points in Fig 4 (doped with 1 0 and 2 5 mole percent Mn and La, from [24])

represent the lower limit of the ceramic piezoelectric anisotropy that would result from the upper limits of the piezoelectric coefficients. Averaging equations for the lower limits of the piezoelectric coefficients may show that the ceramic piezoelectric anisotropy will increase when the single-crystal dielectric anisotropy increases, which is the opposite conclusion as that of the other limit Thus between these limits there may be little effect on the ceramic piezoelectric anisotropy from the single-crystal dielectric anisotropy.

Irrespective of the dielectric anisotropy and degree of polarization, the large ceramic piezoelectric anisotropy of PbTiO₃ can be explained by the large electrostrictive anisotropy that was shown in Section II to be due to the small magnitude of the ceramic $\bar{Q}_{12}$ constant. Since the

value of ceramic $\overline{Q}_{12}$ is close to zero, the sign of $\overline{Q}_{12}$ could easily change from a slight variation in the single-crystal anisotropies. This could also cause the $\overline{d}_{31}$ coefficient to change signs, and result in an infinite piezoelectric anisotropy when $\overline{d}_{31}$ goes to zero.

The single-crystal electrostrictive anisotropies of PbTiO$_3$ can be varied by changing the composition and/or temperature. When some of the titanium in PbTiO$_3$ is substituted with zirconium to form PZT, the single-crystal $-Q_{12}/Q_{11}$ ratio increases, while the $-Q_{12}/Q_{44}$ ratio decreases. This causes the ceramic $-\overline{Q}_{12}/\overline{Q}_{11}$ and $-\overline{d}_{31}/\overline{d}_{33}$ ratios to increase (see Fig. 1), which results in less anisotropy. Zorn *et al*. [17] experimentally found that $-\overline{Q}_{12}/\overline{Q}_{11} \approx 0.5$ and $-\overline{Q}_{12}/\overline{Q}_{44} \approx 0.3$ for the Pb$_{0.83}$Sr$_{0.12}$Ba$_{0.05}$(Zr$_{0.6}$Ti$_{0.38}$Nb$_{0.02}$)O$_3$ composition which is close to the morphotropic boundary. These values would result in a ceramic piezoelectric anisotropy $(-\overline{d}_{33}/\overline{d}_{31})$ of 2 using either the series or parallel models, which is in good agreement with the measured piezoelectric anisotropies [1].

Doping PbTiO$_3$ with other elements, such as samarium or calcium, was shown to increase the anisotropy [2], [26]. Large piezoelectric anisotropies have also been found for the Pb(Zr$_{0.95}$(Mn$_{1/3}$Nb$_{2/3}$)$_{0.05}$)O$_3$ composition [27]. This suggests that the single-crystal electrostrictive ratios in the PZT system change in such a way as to cause the anisotropy to increase when moving from the morphotropic boundary towards PbZrO$_3$, as occurs when going the other way to PbTiO$_3$.

From (15) and (16) the hydrostatic piezoelectric voltage $(g_h = g_{33} + 2g_{31})$ and strain $(d_h = d_{33} + 2d_{31})$ coefficients of a single-crystal can be calculated from

$$g_h = 2P_3 Q_h, \quad d_h = 2\epsilon_0\epsilon_{33}P_3 Q_h. \quad (23)$$

These single-crystal relations can also be used to predict the upper and lower bounds of the ceramic hydrostatic piezoelectric coefficients. By dividing the resulting equations for the ceramic bounds by the single-crystal equations, and again realizing that for a particular domain configuration in a ceramic the polarization $\overline{P}_3$ and dielectric permittivity $\overline{\epsilon}_{33}$ are the same in the $\overline{d}_{33}$ and $\overline{d}_{31}$ equations, the following relations are obtained:

$$\frac{\overline{g}_h^L}{g_h} = \frac{\overline{P}_3}{P_3}\frac{\overline{Q}_h^L}{Q_h}, \quad \frac{\overline{g}_h^U}{g_h} = \frac{\overline{P}_3}{P_3}\frac{\overline{Q}_h^U}{Q_h} \quad (24)$$

$$\frac{\overline{d}_h^L}{d_h} = \frac{\overline{\epsilon}_{33}}{\epsilon_{33}}\frac{\overline{P}_3}{P_3}\frac{\overline{Q}_h^L}{Q_h}, \quad \frac{\overline{d}_h^U}{d_h} = \frac{\overline{\epsilon}_{33}}{\epsilon_{33}}\frac{\overline{P}_3}{P_3}\frac{\overline{Q}_h^U}{Q_h} \quad (25)$$

Due to possibility of having different boundary conditions for the $\overline{Q}_{11}$ and $\overline{Q}_{12}$ constants, the limits of the hydrostatic electrostrictive constant should be calculated from

$$\overline{Q}_h^L = \overline{Q}_{11}^L + 2\overline{Q}_{12}^U, \quad \overline{Q}_h^U = \overline{Q}_{11}^U + 2\overline{Q}_{12}^L \quad (26)$$

However, if the boundary conditions of $\overline{Q}_{11}$ and $\overline{Q}_{12}$ are the same, then the upper and lower limits of $\overline{Q}_h$ would be equal to the single-crystal $Q_h$ (as described in Section II). These values of the single-crystal and ceramic $Q_h$'s of

BaTiO$_3$ are in fairly good agreement. Thus if the single-crystal and ceramic $Q_h$'s are assumed to be equal, then from (24) the ratio of the ceramic $g_h$ divided by the single-crystal $g_h$ only depends on the ratio of the ceramic polarization divided by the single-crystal polarization. Since the polarization of a ceramic is always lower than that of the single-crystal, the value of the ceramic $\overline{g}_h$ should be lower than the $g_h$ of the single-crystal. Experimentally, this is found in both PbTiO$_3$ and BaTiO$_3$.

The ratio of $\overline{d}_h$ coefficients would depend on the ratio of the ceramic $\overline{\epsilon}_{33}$ divided by the single-crystal $\epsilon_{33}$, in addition to the degree of poling. For a material such as PbTiO$_3$ with a small dielectric anisotropy, the value of the ceramic $\overline{d}_h$ should be lower than the $d_h$ of the single-crystal. Experimentally, PbTiO$_3$ has a $\overline{d}_h/d_h$ ratio of 0.46. However, (25) predicts that a material with a large dielectric anisotropy $(\overline{\epsilon}_{11}/\overline{\epsilon}_{33})$ such as BaTiO$_3$ could have a larger ceramic $\overline{d}_h$ than the corresponding single-crystal $d_h$. Experimentally, BaTiO$_3$ has a ceramic $\overline{d}_h$ value of approximately twice the single-crystal value [25]. These results may be important in the design of materials for hydrostatic transducer applications, such as when a piezoelectric powder is dispersed in a polymer [28]. The properties of this type of composite will depend on the composition of the powder used and whether the powder is composed of single-domain or multidomain particles.

## VI CONCLUSION

The upper and lower limits of the electrostrictive constants, dielectric permittivity, spontaneous polarization, and piezoelectric coefficients were calculated for ceramic PbTiO$_3$ from theoretical single-crystal constants. The ceramic was assumed to be composed of a large number of small single-crystals with all possible orientations. The ceramic properties were calculated from the space averages of the single crystal constants, assuming that only 180° domain switching occurs. The experimental ceramic data was shown to be within the predicted upper and lower limits. Additional comparisons have been made between the theoretical predictions and low-temperature dielectric and piezoelectric measurements on samarium-doped lead titanate ceramics [29].

The series and parallel equations used to calculate the upper and lower limits were used to derive relations that showed how the ceramic electrostrictive anisotropy $(\overline{Q}_{11}/\overline{Q}_{12})$ depends on the single-crystal electrostrictive anisotropies $(Q_{11}/Q_{12}$ and $Q_{44}/Q_{12})$. These relations can be used for any fourth-rank tensor with similar tensor to matrix conversion, such as the elastic constants. The ceramic piezoelectric anisotropy $(\overline{d}_{33}/\overline{d}_{31})$ was also shown to be related to the ceramic electrostrictive anisotropy. PbTiO$_3$ was shown to have a large piezoelectric anisotropy, because of the large electrostrictive anisotropy that was due to the small magnitude of the ceramic $\overline{Q}_{12}$ constant. Since the value the ceramic $\overline{Q}_{12}$ is close to zero, the sign of $\overline{Q}_{12}$ could easily change from a slight variation in the single-crystal anisotropies due to a temperature de-

pendence or modification of the composition. This would also cause the $\bar{d}_{31}$ coefficient to change signs, and result in an infinite piezoelectric anisotropy when $\bar{d}_{31}$ goes to zero.

Damjanovic et al. [30] found that in calcium or samarium modified PbTiO$_3$ ceramics the $\bar{d}_{31}$ coefficient changes sign from negative values at low temperatures to positive values at high temperatures. They showed that this change in sign was due to a positive extrinsic contribution to $\bar{d}_{31}$ that may dominate the negative intrinsic contribution. They also found that in samarium doped PbTiO$_3$ samples poled with low electric fields a positive $\bar{d}_{31}$ coefficient resulted over all of the temperature range tested (down to $-180°C$). If the $\bar{d}_{31}$ coefficient remains positive at low temperatures where the extrinsic contributions have "frozen out," then the intrinsic $\bar{d}_{31}$ may have increased to zero and become positive at low temperatures. They also found that as the poling field was increased, the $d_{31}$ versus temperature curves shifted to lower values (more negative). The amount of 90° domain switching increases as the poling field is increased causing the intrinsic ceramic anisotropy to decrease toward that of the single-crystal. This would cause the intrinsic $\bar{d}_{31}$ to shift to lower values approaching the single-crystal value as the poling field is increased and would possibly explain the poling dependence that Damjanovic et al. [30] found.

The single-crystal and ceramic hydrostatic electrostrictive constants were found to be equal when using either the series or parallel models. Using this result the ratio of the ceramic to single-crystal hydrostatic $g_h$ coefficients $(\bar{g}_n/g_h)$ was found to only depend on the degree of polarization $(\bar{P}/P)$. The $\bar{d}_h/d_h$ ratio was found to depend on the ceramic single-crystal dielectric ratio $\bar{\epsilon}_{33}/\epsilon_{33}$, in addition to the degree of poling. The ceramic $\bar{d}_h$ could be less than the single-crystal $d_h$ as is always true for the $\bar{g}_h$ coefficients, or could be larger depending on the dielectric anisotropy $(\epsilon_{11}/\epsilon_{33})$ of the single-crystal.

The averaging procedure described in this paper provides a simple method of predicting the upper and lower bounds of the intrinsic ceramic properties from the single-crystal constants. This procedure could also be used to determine single-crystal constants from the ceramic properties. Pan and Cross [31] have recently used the electrostrictive averaging equations to determine the single-crystal $Q_{44}$ constant of Pb(Mg$_{1/3}$Nb$_{2/3}$)O$_3$ from the measured single-crystal and ceramic $Q_{11}$ and $Q_{12}$ constants. These equations may also be useful in determining the compositional dependence of the single-crystal electrostrictive constants in the PZT system.

## ACKNOWLEDGMENT

## REFERENCES

[1] B. Jaffe, W. J. Cook, and H. Jaffe. Piezoelectric Ceramics. London Academic Press. 1971

[2] H. Takeuchi, S. Jyomura, E. Yamamoto, and Y. Ito. "Electromechanical properties of (Pb Ln)(Ti, Mn)O$_3$ ceramics (Ln = rare earths). J. Acoust. Soc. Am., vol. 72, no. 4, pp. 1114-1120, 1982

[3] A. V. Turik, E. G. Fesenko, V. G. Gavrilyachenko, and G. I. Khasabova. Anisotropy of the dielectric and piezoelectric properties of lead titanate. Kristallografiya, vol. 19, pp. 1095-1097, 1974 Sov. Phys.-Cryst., vol. 19, pp. 677-678, 1974

[4] W. Wersing, G. Zorn, K. Lubitz, and J. Mohaupt. "Comparison of piezoelectric constants of PZT ceramics with values calculated from electrostrictive coefficients." Jpn. J. App. Phys., vol. 24, suppl. 24-2, pp. 721-723, 1985

[5] W. Wersing, K. Lubitz, and J. Mohaupt. "Anisotropic piezoelectric effect in modified PbTiO$_3$ ceramics." presented at the 6th IEEE Int. Symp. Applic. Ferroelect., Lehigh, PA, 1986

[6] A. G. Luchaninov, A. V. Shil'nikov, and L. A. Shuvalov. "On the piezoelectric effect in acentric ferroelectrics ceramics with zero polarization." vol. 41, pp. 181-187, 1982.

[7] A. F. Devonshire. Theory of barium titanate-Part II. Phil. Mag. vol. 42, no. 333, pp. 1065-1079, 1951

[8] M. J. Haun, E. Furman, S. J. Jang, H. A. McKinstry, and L. E. Cross. Thermodynamic theory of PbTiO$_3$. J. Appl. Phys., vol. 62, no. 8, pp. 3331-3338, 1987

[9] R. F. S. Hearmon. An introduction to applied anisotropic elasticity. Oxford: Oxford Univ. Press 1961, pp. 41-44

[10] A. F. Devonshire. "Theory of ferroelectrics." Advances in Physics, vol. 3, no. 10, pp. 85-130, 1954

[11] W. J. Merz. "Double hysteresis loop of BaTiO$_3$ at the curie point" Phys. Rev. vol. 91, no. 3, pp. 513-517, 1953

[12] F. Jona and G. Shirane. Ferroelectric Crystals New York. Pergamon Press, Inc. 1962, pp. 145-147

[13] D. Berlincourt and J. Jaffe. "Elastic and piezoelectric coefficients of single-crystal barium titanate." Phys. Rev., vol. 111, no. 1, pp. 143-148, 1958

[14] G. Schmidt. Bestimmung der electrostriktionskonstanten $Q_i$ von barlumtitanatkeramik. Z. Physik. vol. 145, pp. 534-542, 1956

[15] M. J. Haun, Z. Q. Zhuang, S. J. Jang, H. A. McKinstry, and L. E. Cross. A phenomenological theory for the second order region of the PZT solid solution system. in Proc. 6th IEEE Int. Symp. Applic. Ferroelec. Lehigh, PA, 1986, pp. 398-401

[16] S. J. Jang. Electrostrictive Ceramics for Transducer Applications. Ph.D. Thesis. Pennsylvania State University, University Park, PA, 1979 and K. Uchino, S. Nomura, L. E. Cross, S. J. Jang, and R. E. Newnham. Electrostriction effect in magnesium niobate single crystals. J. Appl. Phys., vol. 51, no. 2, pp. 1142-1145, 1980

[17] G. Zorn, W. Wesing, and H. Gobel. Electrostrictive tensor components of PZT-ceramics measured by X-ray diffraction. Jpn J. App. Phys., vol. 24, suppl. 24-2, pp. 721-723, 1985

[18] G. A. Samara. "Pressure and temperature dependences of the dielectric properties of the perovskites BaTiO$_3$ and SrTiO$_3$." Phys. Rev., vol. 151, no. 2, pp. 378-386, 1966.

[19] I. Ueda. "Effects of additives on piezoelectric and related properties of PbTiO$_3$." Jpn. J. App. Phys., vol. 11, no. 4, pp. 450-462, 1972.

[20] H. G. Baerwald. "Thermodynamic theory of ferroelectric ceramics." Phys. Rev., vol. 105, no. 2, pp. 480-486, 1957

[21] D. Berlincourt and H. A. Krueger. Domain processes in lead titanate zirconate and barium titanate ceramics. J. Appl. Phys., vol. 30, no. 11, pp. 1804-1810, 1959

[22] K. Carl. Ferroelectric properties and fatiguing effects of modified PbTiO$_3$ ceramics. Ferroelec., vol. 9, pp. 23-32, 1975

[23] A. Amin, M. J. Haun, B. Badger, H. A. McKinstry, and L. E. Cross. "A phenomenological Gibbs function for the single cell region of the PbZrO$_3$ PbTiO$_3$ solid solution system." Ferroelec., vol. 65, pp. 107-130, 1985

[24] S. Ikegami, I. Ueda, and T. Nagata. "Electromechanical properties of PbTiO$_3$ ceramics containing La and Mn." J. Acoust. Soc. Amer., vol. 50, no. 4, pp. 1060-1066, 1971

[25] K. H. Hellwege. Landolt-Bornstein. Numerical Data and Functional Relationships in Science and Technology. New Series, Group III. Crystal and Solid Physics. vol. 16, Ferroelectrics and Related Substances. subvolume a, Oxide. New York: Springer-Verlag, 1981, p. 73

[26] D. Damjanovic, T R. Gururaja, S. J. Jang, and L. E. Cross, "Temperature behavior of the complex piezoelectric $d_{31}$ coefficient in modified lead titanate ceramics," *Mater Lett.*, vol. 4, pp 414–419, 1986.

[27] H Takeuchi, S Jyomura, and C. Nakaya, "New piezoelectric materials for ultrasonic transducers," *Jpn. J Appl. Phys*, vol. 24, suppl. 24-2, pp 36–40, 1985

[28] Y H Lee, M J Haun, A Safari, and R E. Newnham, "Preparation of PbTiO₃ powder for a flexible 0-3 piezoelectric composite," in *Proc 6th IEEE Int. Symp. Appic. Ferroelectr*, Lehigh, PA, pp. 318–321, 1986.

[29] J. N Kim, M. J Haun, S. J. Jang, L. E. Cross, and W. R. Xue, "Temperature behavior of dielectric and piezoelectric properties of samarium-doped lead titanate ceramics," *IEEE Trans. Ultrason. Ferroelect. Freq. Contr*, vol. 36, no. 4, pp. 389–392, 1989.

[30] D. Damjanovic, T. R. Gururaja, S. J. Jang, and L. E. Cross, "Possible mechanisms for the electromechanical anisotropy in modified lead titanate ceramics," in *Proc. IEEE Ultrason. Symp.*, Williamsburg, VA, Nov. 17-19, 1986.

[31] W Pan and L. E. Cross, "Direct and converse electrostrictive effects in Pb(Mg₁/₃Nb₂/₃)O₃ ceramics," to be published.

Michael J. Haun, for a photograph and biography please see page 392 of this TRANSACTIONS

**Eugene Furman** was born on May 25, 1959 in Kiev, U S S.R. He received the B S degree in computer engineering at Lehigh University, Bethlehem, PA, in 1980 and then started his graduate studies at Pennsylvania State University, University Park, PA. He obtained the M S degree in electrical engineering in 1986 and at the present time, is studying towards the Ph D in solid state science.

In the past, his major areas of research have been electrical properties of PLZT, dielectric breakdown phenomena, and phenomenology of ferroelectrics.

Mr. Furman is a member of the American Ceramic Society and Materials Research Society.

**Sei Joo Jang**, for a photograph and biography please see page 392 of this TRANSACTIONS.

**Leslie E. Cross**, (SM'79-F'84) for a photograph and biography please see page 392 of this TRANSACTIONS

APPENDIX 31

# Ferroelectric Properties of Tungsten Bronze Morphotropic Phase Boundary Systems

John R. Oliver* and Ratnakar R. Neurgaonkar*

Rockwell International Science Center, Thousand Oaks, California 91360

L. Eric Cross*

Materials Research Laboratory, The Pennsylvania State University,
University Park, Pennsylvania 16802

Tungsten bronze ferroelectrics which have a morphotropic phase boundary (MPB) can have a number of enhanced dielectric, piezoelectric, and electrooptic properties compared to more conventional ferroelectric materials. The structural and ferroelectric properties of several MPB bronze systems are presented, including data from sintered and hot-pressed ceramics, epitaxial thin films, and bulk single crystals. Included among these are three systems which had not been previously identified as morphotropic. The potential advantages and limitations of these MPB systems are discussed, along with considerations of the appropriate growth methods for their possible utilization in optical, piezoelectric, or pyroelectric device applications. [Key words: ferroelectrics, tungsten bronze, phases, electronic properties, phase boundary.]

## I. Introduction

THE search for increased electrooptic, pyroelectric, and piezoelectric effects in the tungsten bronze ferroelectric crystal family has stimulated interest in a number of potential mor-

phototropic phase boundary (MPB) systems. On a binary phase diagram, an MPB appears as a nearly vertical line separating two distinct ferroelectric phases. This phase boundary generally occurs at a nearly constant composition over a wide temperature range up to the ferroelectric phase transition temperature, $T_c$, an example is shown in Fig. 1 for the bronze MPB system, $Pb_{1-x}Ba_xNb_2O_6$ (PBN), which possesses both orthorhombic and tetragonal structures near $x = 0.37$.[1-4] Poled ceramics or single crystals of such MPB ferroelectrics can show an enhancement of numerous physical properties because of the proximity in free energy of an alternate ferroelectric structure, detailed descriptions of MPB behavior can be found in the work by Jaffe *et al.*[5]

Crystal compositions in other ferroelectric families can also possess MPB regions, with perhaps the best known of these being perovskite PZT and PLZT.[6] However, compositions in the tungsten bronze family have a number of potential advantages over the perovskites, particularly for optical device applications. These include a larger ensemble of nonzero quadratic electrooptic $g$ coefficients ($g_{11}$, $g_{12}$, $g_{13}$, $g_{33}$, $g_{44}$, $g_{66}$ compared to $g_{11}$, $g_{12}$, $g_{44}$ in perovskites) arising from a lower prototype symmetry (tetragonal $4/mmm$) in the high-temperature paraelectric phase, a unique 4-fold symmetry axis (no tetragonal twinning), and an open structure which can accommodate a wide range of ions in several crystallographic sites.

Figure 2 shows the tetragonal tungsten bronze prototype structure projected onto the (001) plane.[7] Ferroelectric compositions of the tungsten bronze type can be represented by the chemical formulas $(A_1)_4(A_2)_2C_4B_{10}O_{30}$ and $(A_1)_4(A_2)_2B_{10}O_{30}$ in which $A_1$, $A_2$, C, and B are the 15-, 12-, 9-, and 6-fold coordinated oxygen octahedra sites in the crystal structure, with the A sites occupied by Ba, Sr, Ca, Pb, K, or Na, and the B sites occupied by either Nb or Ta. The first formula represents the so-called "stuffed" bronze structure, in that all of the A, B, and C sites are occupied (e.g., $K_3Li_2Nb_5O_{15}$) The second formula represents bronzes which are either "filled" (all A sites occupied) or "partially filled" (⅚ of the A sites occupied), the latter being characteristic of ferroelectric bronze niobates such as $Sr_{1-x}Ba_xNb_2O_6$ (SBN).[13] The tungsten bronze structure is found over a wide range of the partially filled niobates, although the end compositions for A = Sr, Ba, or Ca are not of the tungsten bronze type. The introduction of K and Na on the A sites results in a filled bronze structure (e.g., lead potassium niobate (PKN)) and thereby enhances the structural stability.

Tungsten bronze solid solutions can be obtained with either tetragonal ($4mm$) symmetry in the ferroelectric phase or orthorhombic ($mm2$) symmetry, which can be both ferroelectric and ferroelastic. Tetragonal bronzes such as $Sr_{0.6}Ba_{0.4}Nb_2O_6$ (SBN 60) have spontaneous polarization only along the c axis (001) and generally have large transverse properties at room temperature, including the c-axis dielectric constant, $\epsilon_{33}$, the linear electrooptic coefficient, $r_{13}$, the piezoelectric coefficient, $d_{13}$, and the electromechanical coupling, $k_{33}$.[8-11] Such is not always the case, however, as has been shown by tetragonal $Ba_{2-x}Sr_xK_{1-x}Na_xNb_5O_{15}$

- CHEMICAL FORMULAE

$(A_1)_4(A_2)_2C_4B_{10}O_{30}$

$(A_1)_4(A_2)_2B_{10}O_{30}$

$A_1$ = 15-FOLD COORDINATED SITE
$A_2$ = 12 FOLD COORDINATED SITE
$C$ = 9-FOLD COORDINATED SITE
$B$ = 6-FOLD COORDINATED SITE (TWO SITES)

- CRYSTAL STRUCTURE

4/mmm TO 4mm (TETRAGONAL-TETRAGONAL)
TO mm2 (TETRAGONAL-ORTHORHOMBIC)

- KNOWN SYSTEMS

150 COMPOUNDS OR
SOLID SOLUTIONS BETWEEN END MEMBERS
SEVERAL MORPHOTROPIC PHASE BOUNDARY
SYSTEMS

Fig 2. Tetragonal prototypic structure of the tungsten bronze lattice projected into the (001) plane

BSKNN), [2,13] which can show large longitudinal properties such as $\epsilon_{33}$, $r_{51}$, $d_{15}$, etc.

Bronze compositions having an orthorhombic symmetry in the ferroelectric phase can have spontaneous polarization along the c axis, with generally very weak orthorhombic distortion of a and b (e g., $Sr_2NaNb_5O_{15}$), or else have spontaneous polarization along either of the orthorhombic a or b axes which are rotated 45° relative to the high-temperature prototypic axes (e g., $PbNb_2O_6$) [1] The better-known orthorhombic bronzes such as $Pb_{1-x}Ba_xNb_2O_6$ [3,4] generally show stronger longitudinal properties although again some exceptions may be found.

The availability of bronze structures with either orthorhombic or tetragonal point group symmetry in the ferroelectric phase, coupled with the possibility for several space group symmetries, naturally suggests the potential for binary, ternary, or quaternary solid solutions containing MPB regions. However, although numerous bronze solid solutions have been investigated during the past several decades, only a few MPB systems have been discovered. In this paper, we will discuss the properties for several MPB bronze ferroelectrics that we have examined, and additionally look at other tungsten bronze systems which may possess MPB regions which hitherto have not been identified.

## II. Lead-Containing Morphotropic Bronzes

### (1) The PBN System

The lead barium niobate (PBN) solid solution is arguably the most studied and developed MPB system in the tungsten bronze family. In addition to sintered ceramics, PBN has also been developed in the form of hot-pressed, grain-oriented ceramics [14–16] and as bulk single crystals using the Czochralski growth method. [14] The latter have been especially useful for determining the directionally dependent ferroelectric properties in this system, revealing the unusual behavior which can occur for compositions near the morphotropic boundary

The PBN solid solution is based on the binary system $(1 - x)$ $PbNb_2O_6$–$xBaNb_2O_6$, as shown in Fig 1 The MPB between orthorhombic (mm2) and tetragonal (4mm) symmetries occurs at $x = 0.37$ with a minimum Curie point of approximately 270°C for bulk single crystals, discussion of the crystal growth procedure may be found in the work by Shrout et al. [14] The crossover between the Curie temperatures $\theta_1$ and $\theta_3$ as one moves the composition through the MPB region leads to very large dielectric and piezoelectric constants at room temperature, in spite of the high ferroelectric transition temperature. [1,7] For example, near-morphotropic tetragonal $Pb_{0.6}Ba_{0.4}Nb_2O_6$ (PBN.60) has single-crystal dielectric constants of $\epsilon_{11}$ = 1900 along the a axis and $\epsilon_{33}$ = 500 along the c axis. [8] Spontaneous polarization in poled

crystals is also large, in the range of 70 $\mu C/cm^2$ at room temperature based on recent measurements

The large spontaneous polarization and large dielectric constants available in morphotropic PBN are especially significant for optical applications. From the phenomenology for oxide ferroelectrics, [19] the linear electrooptic effect may be considered a quadratic effect biased by the nonzero spontaneous polarization in the ferroelectric phase. In the case of tetragonal tungsten bronzes, the linear electrooptic coefficients, $r_{ij}$, are given by relations of the form [18]

$$r_{13} = 2g_{13}P_3\epsilon_{33}\epsilon_0$$

$$r_{33} = 2g_{33}P_3\epsilon_{33}\epsilon_0$$

$$r_{51} = r_{42} = 2g_{44}P_3\epsilon_{11}\epsilon_0 \tag{1}$$

where $P_3$ is the c-axis polarization and the $g_{ij}$ are the quadratic electrooptic coefficients, the latter being taken as largely independent of temperature with values roughly the same as those in the high-temperature paraelectric phase [19] Similar relations also apply for the piezoelectric $d_{ij}$ coefficients, with the quadratic $g$ coefficients being replaced by $Q_{ij}$ electrostriction constants

The relation for $r_{51}$ in Eq. (1) is of particular interest in that for tetragonal compositions near the MPB, but far from the ferroelectric transition temperature, both $P_3$ and $\epsilon_{11}$ can be large and nearly independent of temperature. In the case of single-crystal PBN 60, $r_{51}$ is now estimated at greater than 2000 × 10⁻¹² m/V at room temperature, many times greater than the values for the best non-morphotropic tetragonal bronzes such as SBN.60 [18] Similarly, the piezoelectric $d_{15}$ coefficient is also enhanced by the proximity of the MPB in PBN 60, with a value of roughly 260 × 10⁻¹² C/N [1]

For orthorhombic (mm2) compositions near an MPB with the polar axis along a (or b), the equivalent relations are given by

$$r_{11} = 2g_{11}P_1\epsilon_{11}\epsilon_0$$

$$r_{12} = 2g_{12}P_1\epsilon_{11}\epsilon_0$$

$$r_{13} = 2g_{13}P_1\epsilon_{11}\epsilon_0$$

$$r_{41} = 2g_{44}P_1\epsilon_{11}\epsilon_0 \tag{2}$$

In this case, $P_1$ and $\epsilon_{11}$ can be large so that large and nearly temperature-independent values of $r_1$ and $r_{41}$ may be anticipated

A limiting factor in the development of PBN single crystals is the high volatility of PbO at the temperatures required for crystal growth (1340° to 1400°C) Although it has been possible to grow PBN bulk single crystals of up to several millimeters cross section using the Czochralski method, the rapid loss of PbO from the melt leads to a considerable loss of stoichiometry and homogeneity with resulting crystal fracture problems. Hence, the present
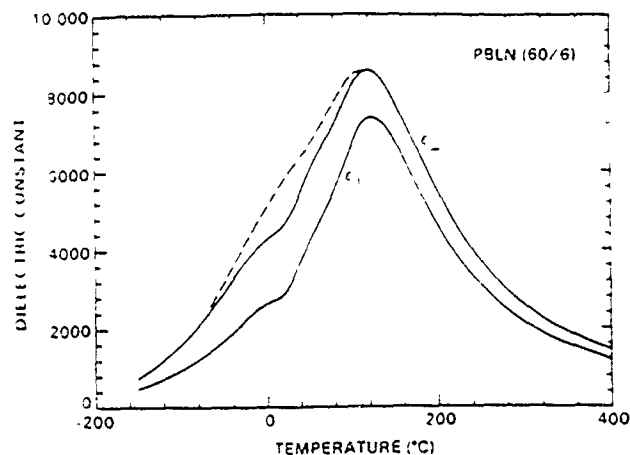
Fig. 3. Dielectric constant at 10 kHz versus temperature for hot-pressed ceramic PBLN(60/6) for directions parallel and perpendicular to the pressing direction after poling at 15 kV/cm. The dashed line indicates a normally depoled condition

crystals are considered to be of limited utility for many device applications, particularly optical.

An alternative to the bulk crystal growth of PBN is hot-pressed ceramic densification, with the advantages of lower growth temperatures, shorter exposures to elevated temperatures, and better control of the surrounding environment. Pioneering work on hot-pressed PBN ceramics was performed by Yokosuka[14] and Nagata *et al*[15,16] on lanthanum-modified PBN compositions to permit the development of transparent ceramics in much the same fashion as lanthanum-modified perovskite PZT (PLZT). These La$^{3+}$ modifications take the form $(Pb_{1-x}Ba_x)_{1-3v/2}La_vNb_2O_6$ (PBLN(1 − r/v)), with the advantages of good optical transparency resulting from
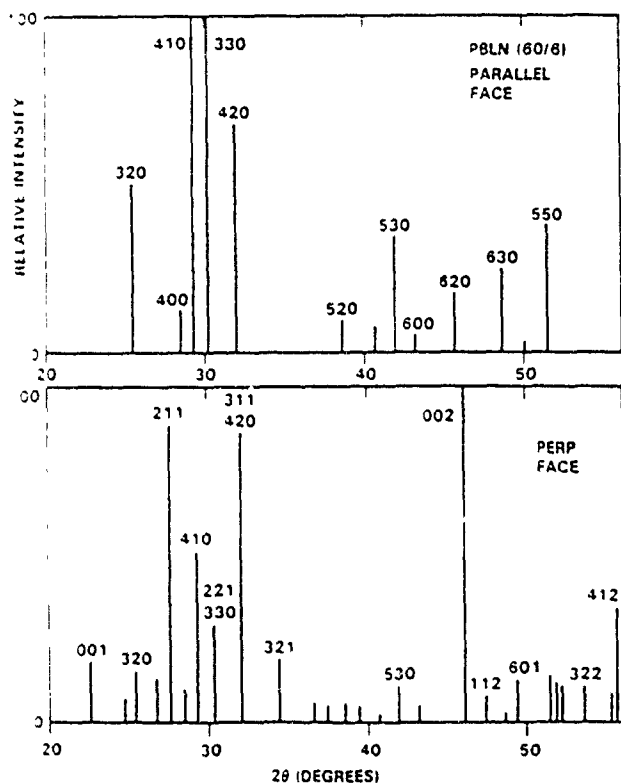
improved grain boundaries and the potential for very large dielectric constants as a consequence of the substantial decrease in the phase transition temperature.

An example of the dielectric properties for hot-pressed PBLN ceramics developed in our own work is shown in Fig. 3 for the PBLN(60/6) composition. Ceramic preparation involved calcining the proportioned oxide powders at 780° to 800°C for 10 to 12 h, ball-milling in acetone for 12 to 20 h, and then cold-pressing the dried mixture into pellets prior to uniaxial hot-pressing in an oxygen atmosphere. Since PBLN is densified by liquid-phase sintering due to the presence of PbO, an excess of PbO powder is required in the starting mixture to effect optimum densification and to minimize Pb$^{2+}$ deficiency in the ceramic. Whereas our initial work on unmodified PBN 60 and PBN 70 ceramics showed an optimum PbO excess of 6 mol% for typical growth temperatures of 1240° to 1280°C, this reduced to roughly 2 mol% in La-modified material. This result is consistent with our earlier observations of reduced PbO losses during sintering for tungsten bronze $Pb_{1-x}K_xLa_xNb_2O_6$ ceramics compared to other Pb-containing materials.[20]

The dielectric data for PBLN(60/6) shown in Fig. 3 were obtained on ceramic material hot-pressed at 1260°C for 3 h at a pressure of 3000 psi. The Curie point, $T_c$, declines to 120°C as a result of La modification, accompanied by a considerable broadening of the phase transition region compared to unmodified PBN 60. As a result, the room-temperature dielectric constant for a measuring field perpendicular to the pressing axis is 4400 after poling, the latter being accomplished by cooling from $T_c$ with a dc field of 15 kV/cm applied to the sample.

The dielectric anisotropy between the directions perpendicular and parallel to the pressing axis arises from the preferential orientation of the needle-shaped c-axis grains in the plane normal to the pressure axis.[15,16] The degree of grain orientation, which appears to be only slight in Fig. 3 because of the proximity of the MPB, is in fact nearly complete based on microscopic and X-ray evaluations. Figure 4 shows the relative strengths of the X-ray diffraction lines taken from ceramic PBLN(60/6) samples with face normals parallel and perpendicular to the pressing axis, with the former showing the virtual absence of hk1 and hk2 reflections. The calculated lattice constants are $a, b = 1.2543$ nm, $c = 0.3924$ nm compared to $a, b = 1.2576$ nm, $c = 0.3978$ nm for unmodified PBN 60. The transparency of these hot-pressed ceramics is generally very good, although polished samples show a mild yellow coloration due to a gradual transmission roll-off for wavelengths below 600 nm. However, in the near-IR region, Nagata and Okazaki[15,16] have reported bulk optical transmission approaching 97% in hot-pressed PBLN.



Fig. 4. Relative X-ray diffraction line strengths for hot-pressed PBLN(60/6) with face normals parallel and perpendicular to the pressing direction. Note the absence of hk1 and hk2 reflections in the upper figure, indicating preferential grain orientation.
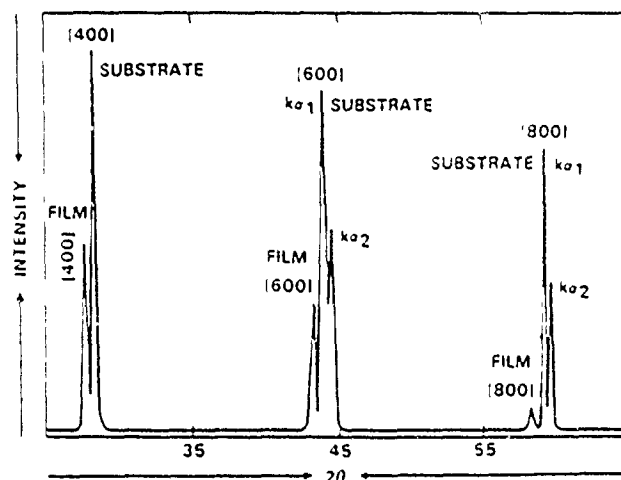


Fig. 5. X-ray pattern for a sputtered PBN 60 film on a (100)-oriented SBN 60 substrate. Growth was performed in a 50/50 Ar/O₂ atmosphere at 600°C, postgrowth annealing was not necessary. Pattern shows dominant substrate lines due to the relatively thin film thickness (2000 nm)
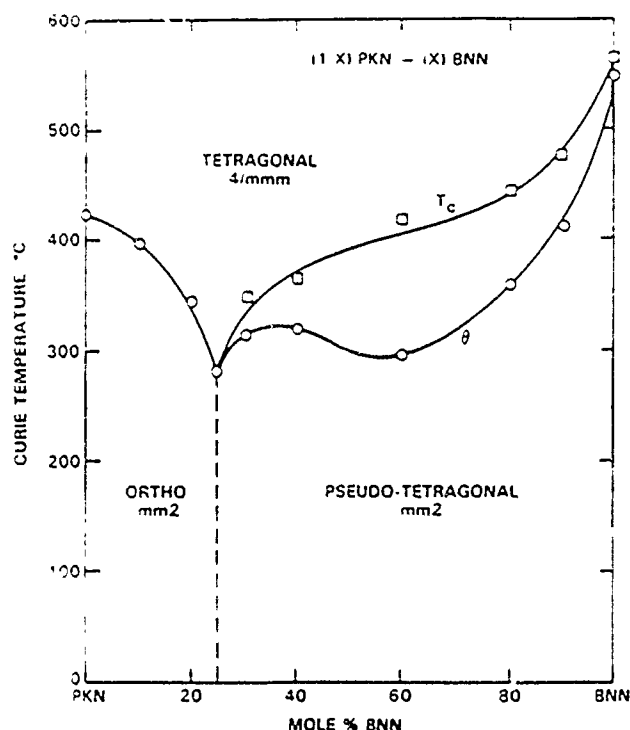
Fig. 6. Ferroelectric phase transition temperature (Curie point). $T_c$, and Curie temperature, $\theta$, as a function of composition for ceramic $(1 - x)$ Pb$_2$KNb$_5$O$_{15}$-$x$Ba$_2$NaNb$_5$O$_{15}$



Fig. 7. Dielectric constant of ceramic $(1 - x)$PKN-$x$BNN at $T_c$ and at room temperature. $F = 10$ kHz. Note the dramatic change in the properties near the MPB at $x = 0.25$

The difficulties encountered in the Czochralski growth of single-crystal PBN have also led to the exploration of epitaxial thin films. Liquid-phase epitaxial growth of PBN has been frustrated thus far by the lack of a suitable flux (solvent) permitting single-phase growths below 1100°C to minimize PbO volatilization. However, the rapid emergence of ferroelectric oxide films grown by rf magnetron sputtering[21,22] has led to encouraging initial results for PBN. Figure 5 shows the X-ray pattern for a sputtered PBN 60 thin film grown on a (100)-oriented SBN:60 substrate at 600°C.[23] The film crystallinity and orientation are excellent. in part because of the good lattice match to the underlying SBN·60 substrate $(a, b = 1.2467$ nm. $c = 0.3937$ nm). Compositional control is also very good, based on the close agreement between the film lattice constants and those of the ceramic PBN target. We have also performed sputtered growths on glass and quartz substrates. although in these cases the films have been polycrystalline with no preferred orientation.

It appears that sputtered thin film growth may be a highly viable method for growing stoichiometric, homogeneous PBN and PBLN films of up to several micrometers thickness for optical, surface acoustic wave (SAW), and pyroelectric applications, particularly when grown on closely lattice matched substrates. PBN thin films grown on SBN 60 substrates could ultimately prove valuable in several optical device concepts since (1) PBN 60 has a substantially larger linear electrooptic coefficient than SBN 60, and (2) there is a large difference in their refractive indices (2.44 for PBN 60 vs 2.29 for SBN 60) making such structures attractive for optical waveguides. This growth method would appear to be appropriate for other volatile Pb-containing or non-Pb bronze ferroelectrics as well.

### (2) The PKN–BNN System

The diversity of ferroelectric solid solutions available within the tungsten bronze structural family presents the possibility for other morphotropic systems based on the binary combination of end members such as PbNb$_2$O$_6$ (PN). Pb$_2$KNb$_5$O$_{15}$ (PKN), Sr$_2$NaNb$_5$O$_{15}$ (SNN). Ba$_2$NaNb$_5$O$_{15}$ (BNN), etc Solid solutions based on Pb$_2$KNb$_5$O$_{15}$ are particularly attractive because of the
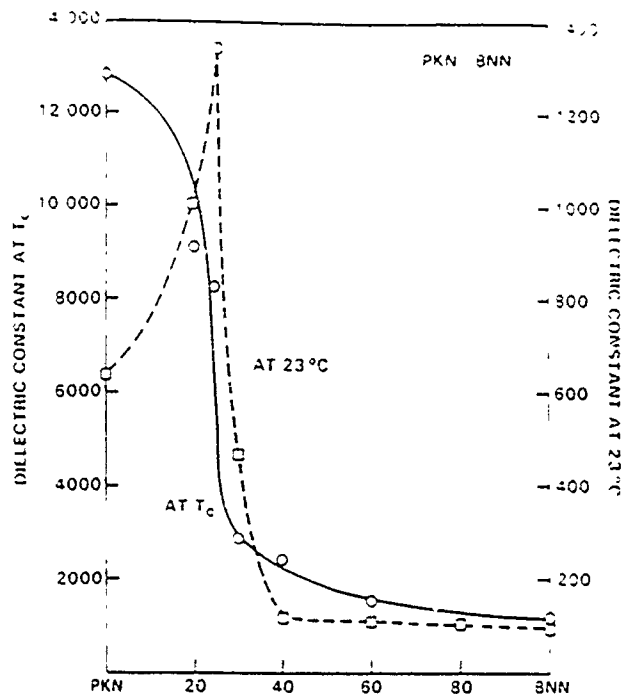
potentially large dielectric and piezoelectric constants and large spontaneous polarization available in this material.[24,25] The orthorhombic structure of PKN $(a = 1.7835$ nm. $b = 1.7944$ nm. and $c = 0.3938$ nm) makes it particularly suitable for combination with tetragonal or pseudotetragonal bronzes such as Ba$_2$NaNb$_5$O$_{15}$[26,27] to attempt an MPB condition.

We have investigated the binary join $(1 - x)$PKN–$x$BNN using ceramic compositions sintered at 1200° to 1380°C.[23] Figure 6 shows the behavior of the ferroelectric phase transition temperature. $T_c$, and the Curie temperature. $\theta$, as a function of composition. with $\theta$ determined from the Curie-Weiss dielectric behavior in the paraelectric phase given by

$$\epsilon = C_c (T - \theta) \tag{3}$$

Both $T_c$ and $\theta$ attain a sharp minimum of 280°C at a 25 mol% BNN composition, similar to the behavior found in PBN (Fig. 1) The PKN side of the phase diagram shows a virtually second-order phase transition $(T_c = \theta)$, changing to first-order $(T_c > \theta)$ for $x > 0.25$ As a result, the value of the dielectric constant at $T_c$, shown in Fig. 7, rapidly declines for compositions beyond $x = 0.25$ On the other hand, the dielectric constant at room temperature peaks sharply at the MPB due to the decline of $T_c$, followed by the change to a first-order transition with a decreasing Curie constant, $C_c$, as shown in Fig. 8 It should be cautioned that these dielectric data necessarily average over all crystallographic directions because of the random orientation of the ceramic grains. However, as a consequence, they also indicate the profound effect of the MPB on both the polar and nonpolar properties

The morphotropic boundary between the orthorhombic and pseudotetragonal phases in PKN–BNN is indicated by the abrupt change in the $b$ and $c$ lattice constants determined by powder X-ray diffraction analysis, as shown in Fig 9 Particularly interesting is the fact that although both end members are orthorhombic, an abrupt phase boundary occurs because of the differing orientations of the polar vector (orthogonal to $c$ for PKN, parallel to $c$ for BNN)

### (3) The PKN–SNN System

We have also investigated sintered ceramics in the binary system $(1 - x)$PKN–$x$SNN.[28] Figure 10 shows the behavior of $T_c$ and $\theta$
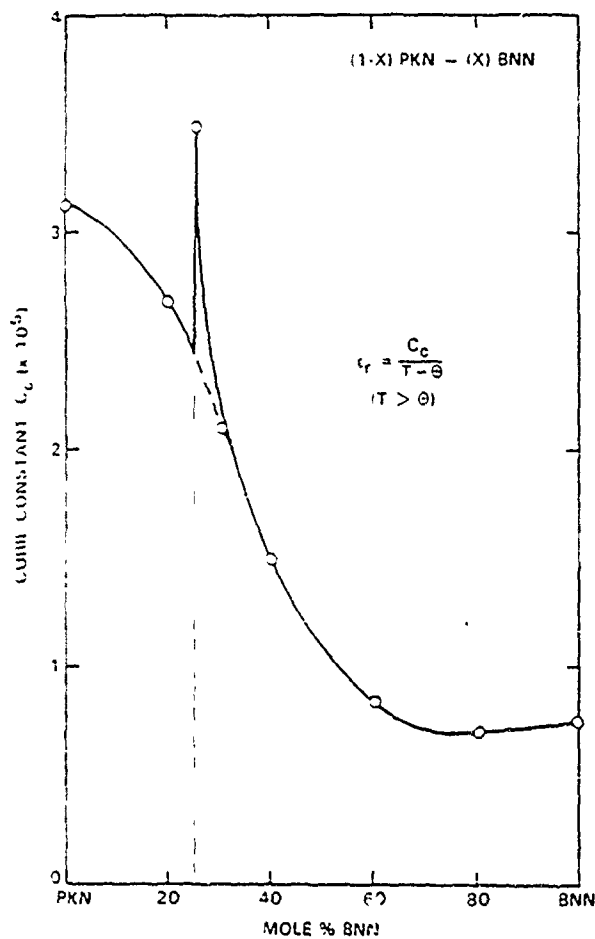
**Fig. 8.** Curie–Weiss constant for the system $(1 - x)$PKN–$x$BNN. The anomalous behavior near the MPB at $x = 0.25$ has also been found in other ceramic MPB systems (Ref 28)
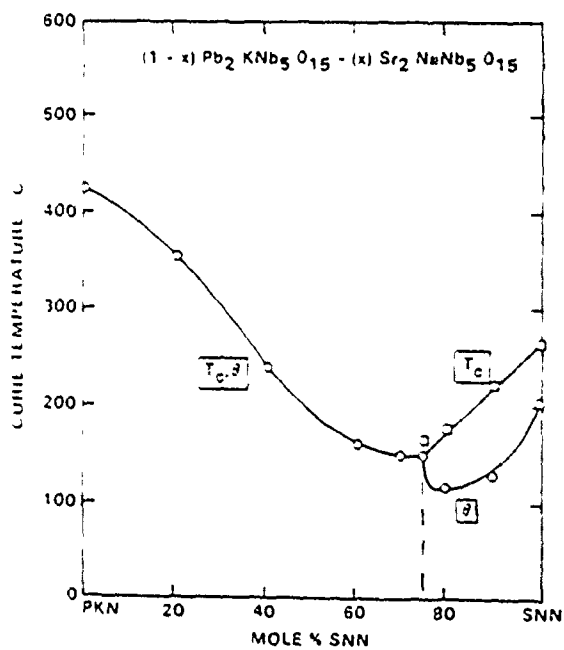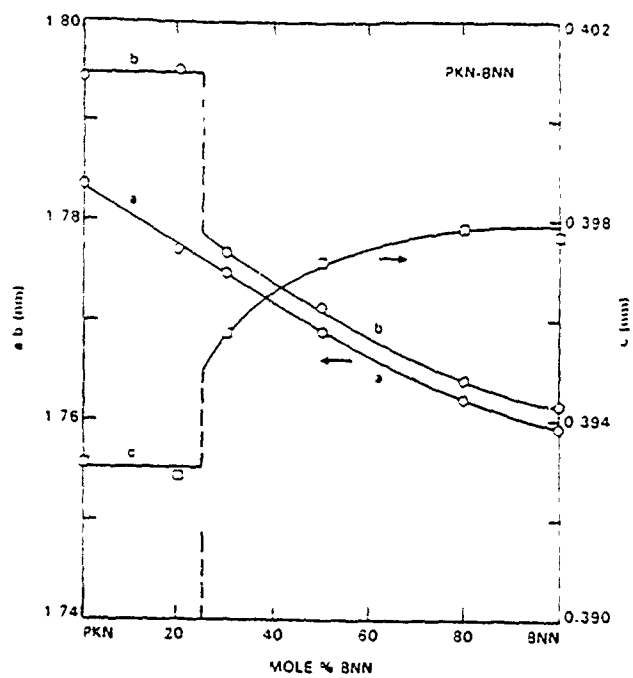


**Fig. 9.** Lattice parameters for the PKN–BNN system. Note the apparent discontinuity in the $b$ and $c$ parameters at the 0 75PKN–0 25BNN morphotropic composition.

in this system, with a broad minimum in $T$, (155°C) occurring for $0.70 \le x \le 0.75$. However, the lattice parameters (Fig. 11) do not show any abrupt change near $x = 0.75$, but instead a broad region where the $a$ and $b$ constants become nearly indistinguishable. It may be that the MPB region, if any, is quite broad in this case. making lattice parameter evaluation more difficult. In all other



**Fig. 10.** $T$, $\theta$ as a function of composition for ceramic $(1 - x)$Pb$_2$KNb$_5$O$_{15}$–$(x)$Sr$_2$NaNb$_5$O$_{15}$.
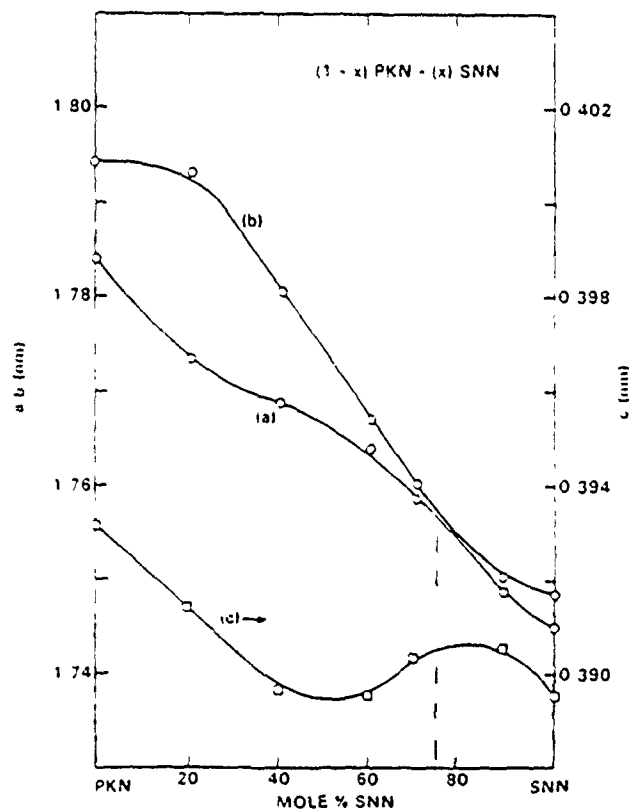


**Fig. 11.** Lattice parameters for the PKN–SNN system
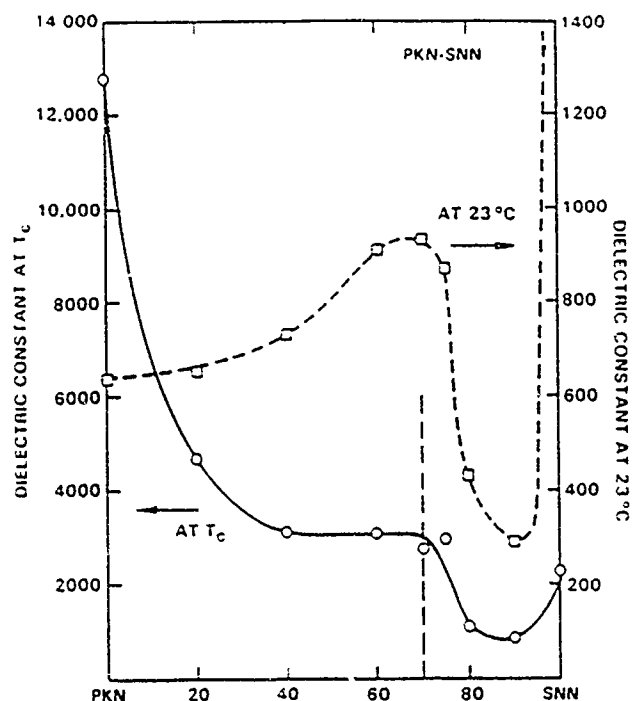
Fig. 12.  Dielectric constant at $T_c$ and at room temperature for ceramic PKN–SNN. $F = 10$ kHz.



Fig. 13.  $T_c$, $\theta$ as a function of composition for ceramic $(1 - x)$Ba$_2$NaNb$_5$O$_{15}$–$x$Sr$_2$NaNb$_5$O$_{15}$.

respects, however, this system displays the behavior expected for an MPB system, including abrupt changes in the dielectric properties near $x = 0.75$, as shown in Fig. 12. The growth of bulk single crystals would be particularly helpful in clarifying the presence or absence of an MPB region in PKN–SNN, although this is a difficult system for crystal growth because of the growth difficulties inherent in both end members.[14,27]

### III.  Lead-Free Morphotropic Bronzes

#### (1)  The BNN–SNN System

The bronze system $(1 - x)$BNN–$x$SNN is attractive from the standpoint of bulk single-crystal growth because it does not contain lead, and it was initially studied by Bell Laboratories as a part of the original work on BNN.[27] Although both end members are weakly orthorhombic, they possess different space group symmetries ($Ccm2_1$ for BNN, $Bbm2$ for SNN)[29,30] and therefore the potential for MPB behavior in a binary system. To this end, we investigated the structural and dielectric properties of BNN–SNN using sintered ceramics, with particular care given to obtaining optimum sintering conditions for each composition; these ranged from 1380°C for pure BNN to 1280°C for SNN with sintering times of 2 to 4 h.

Figure 13 shows the variation of $T_c$ and $\theta$ with composition as determined from dielectric measurements on these ceramics. An interesting feature is that the phase transition remains first-order ($T_c > \theta$) over the entire compositional range. A sharp minimum occurs for $T_c$ at $x = 0.60$ ($T_c = 170$°C), whereas $\theta$ varies only slightly in this same region. The Curie constant also increases abruptly at this point, as shown in Fig. 14, this change, coupled with the decrease between $T_c$ and $\theta$ for $x > 0.60$, leads to a dramatic increase in the dielectric constant at the phase transition temperature, as shown in Fig. 15.

The dielectric constant at room temperature for ceramic BNN–SNN compositions, also shown in Fig. 15, rises monotonically from a value of 100 for BNN ($x = 0$) largely as a consequence of the decreasing phase transition temperature. However, near $x = 0.6$, there is an abrupt jump in the room-temperature constant due, in part, to the discontinuity in the Curie constant. Less obvious, though, is the cause for the rapid decline of the room-

temperature constant in the range $0.6 < x < 0.7$. Beyond this range up to pure SNN, the room-temperature dielectric constant then rises to nearly 2000 as a result of a broad, low-level peak centered at roughly $-50$°C in ceramic SNN. This same peak has also been observed in SNN c-axis crystals,[26] although its origin has not been identified.
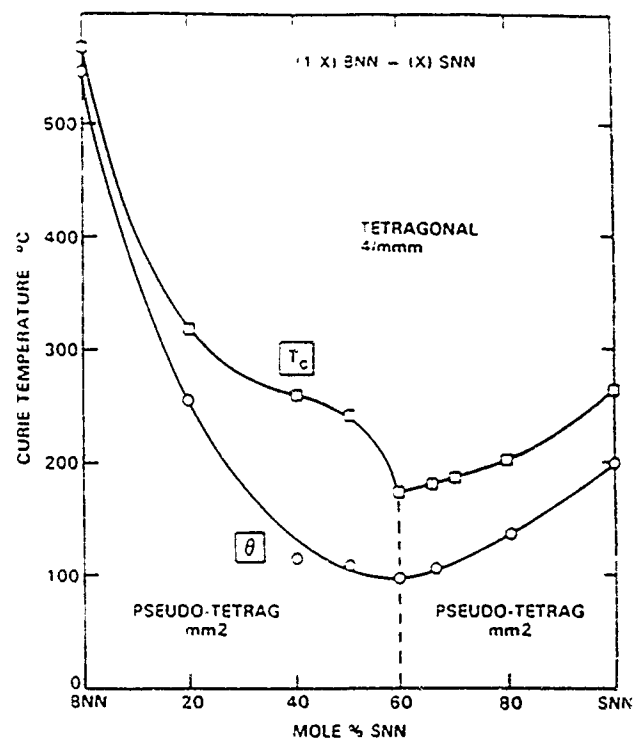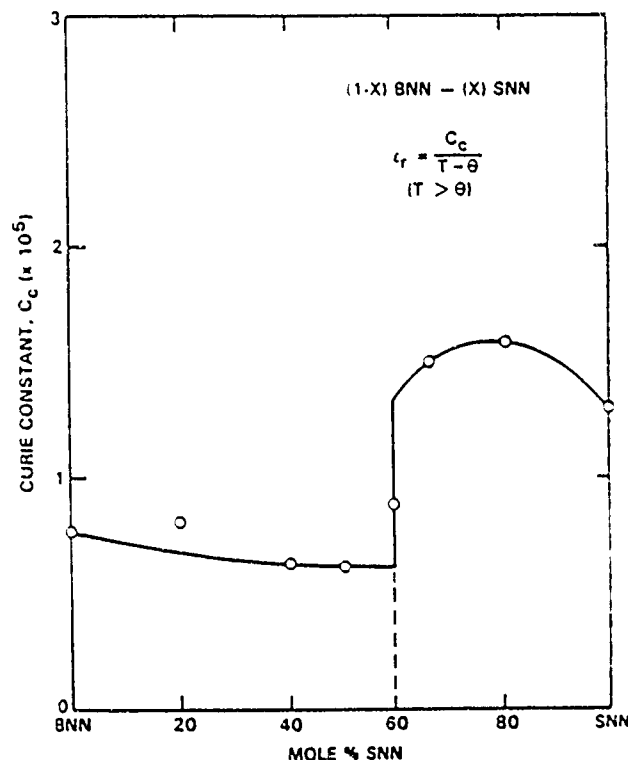


Fig. 14.  Curie constant, $C_c$, as a function of composition for ceramic $(1 - x)$BNN–$x$SNN.
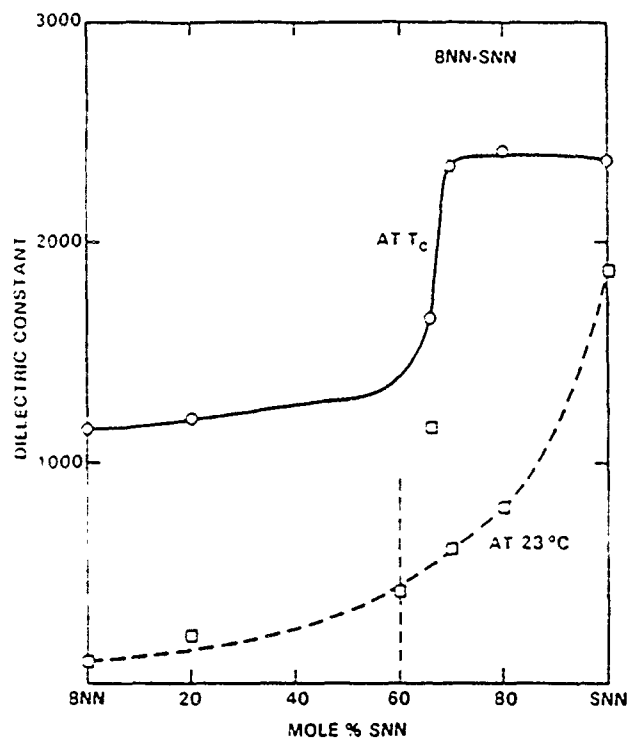
Fig. 15. Dielectric constant at $T_c$ and at room temperature for ceramic BNN-SNN $F = 10$ kHz

The lattice parameters for the BNN–SNN system are shown in Fig 16 Two independent pseudotetragonal phases appear on either side of the $x = 0.6$ region, a feature reflected by the abrupt discontinuity of the Curie constant (Fig. 14). Hence, from these data it appears that the BNN–SNN system may have an MPB near the composition $Ba_{0.8}Sr_{1.2}NaNb_5O_{15}$, something which had not been previously suggested.

### (2) The BSKNN System

Another important non-Pb-containing bronze ferroelectric is $Ba_{1-x}Sr_xK_{1-x}Na_xNb_5O_{15}$ (BSKNN), which exists in the quaternary
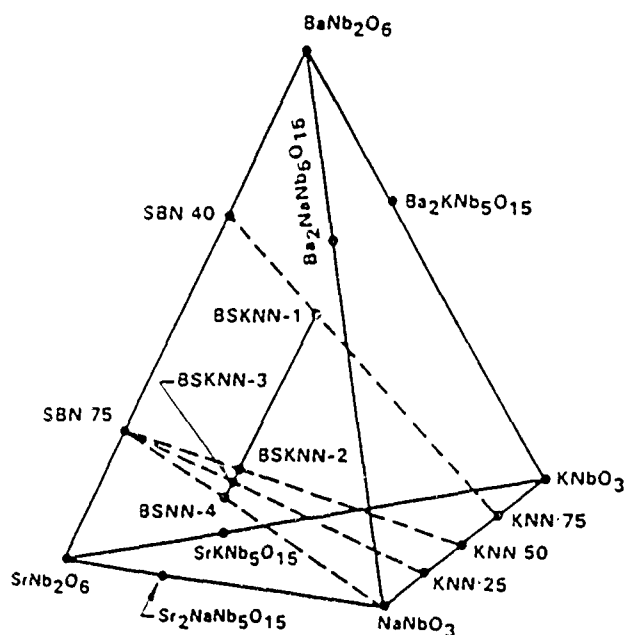


Fig 17 Quaternary phase diagram for the system $BaNb_2O_6$–$SrNb_2O_6$–$KNbO_3$–$NaNbO_3$ Tungsten bronze BSKNN ceramics and single crystals discussed here exist on the join BSKNN-1–BSNN-4
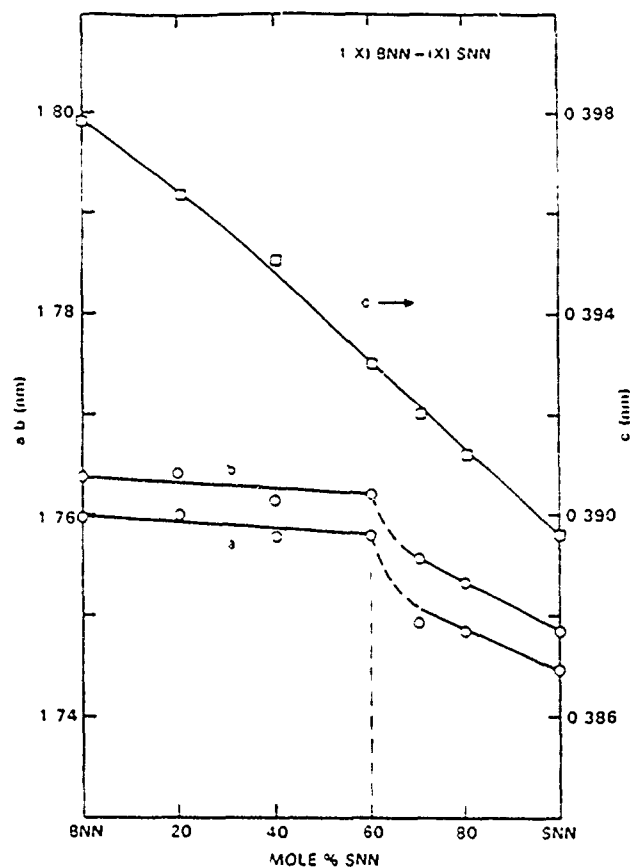


Fig. 16. Lattice parameters for the BNN–SNN system

system $BaNb_2O_6$–$SrNb_2O_6$–$KNbO_3$–$NaNbO_3$ shown in Fig. 17. Our work on BSKNN was spurred by the initial research of Yuhuan and Cross[31] and has focused on the join between BSKNN-1 ($Ba_{1.2}Sr_{0.8}K_{0.75}Na_{0.25}Nb_5O_{15}$) and BSNN-4, the latter occurring on the Sr-rich end of the orthorhombic BNN–SNN binary system.

BSKNN-1 is a "filled" tetragonal ($4mm$) tungsten bronze which exists on the pseudobinary join SBN:40–KNN:75 (Fig. 17) with lattice constants $a, b = 1.2506$ nm, $c = 0.3982$ nm, and a phase transition temperature of 203° to 208°C. This composition was the first in the BSKNN system to be successfully grown as good-quality, moderate-size c-axis crystals of up to 1-cm cross section; details on crystal growth may be found in previous papers.[11-13,32]
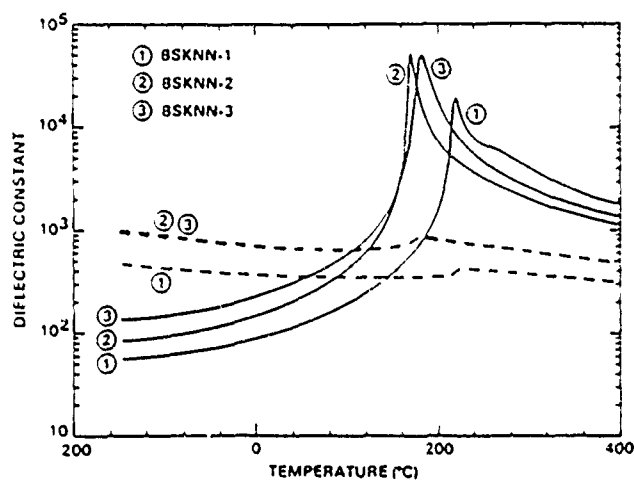


Fig. 18. Temperature dependencies of the dielectric constants for BSKNN crystal compositions Solid line c axis, poled at 3 kV/cm, dashed line: b axis (Ref. 18)

We have investigated other BSKNN compositions on the join between BSKNN-1 and BSNN-4 using sintered ceramic material, and these revealed a drop in the transition temperature for BSKNN-2 ($Ba_{0.5}Sr_{1.5}K_{0.5}Na_{0.5}Nb_5O_{15}$) and then a moderate increase for BSKNN-3 and beyond. However, these ceramics showed only a monotonic increase of the room-temperature dielectric constant with composition and little in the way of conclusive evidence for an MPB region based on lattice parameter determinations, although the $a$ and $c$ parameters show a substantial decline at BSKNN-2 ($a, b = 1.2437$ nm, $c = 0.3935$ nm)

The Czochralski c-axis crystal growths of BSKNN-2 and BSKNN-3 have proved substantially easier than the growth of BSKNN-1, in part, we believe, because the former lie closer to a true congruent melting region. BSKNN-2 and BSKNN-3 also have a more circular cross section compared to the nearly square growth habit of BSKNN-1.[13] Figure 18 shows the dielectric properties as a function of temperature for the nonpolar a-axis ($\epsilon_{11}$) and polar c-axis ($\epsilon_{33}$) directions in these crystal compositions. Like other tungsten bronze crystals such as SBN, $\epsilon_{33}$ follows a Curie–Weiss law (Eq. (3)) both above and *below* $T_c$ with essentially a second-order phase transition character. There is little frequency dependence of the dielectric constant (100 Hz to 100 kHz) except within a few degrees of $T_c$ where a characteristic rise in the loss tangent is also observed. This is due to fluctuations of the site preference distribution for Sr and Ba in the lattice, resulting in a narrow distribution of phase transition temperatures in the crystal bulk and a corresponding frequency dependence for the dielectric properties.[13]

The c-axis Curie constant in the ferroelectric phase increases for compositions beyond BSKNN-1, resulting in room-temperature $\epsilon_{33}$ values for BSKNN-2 (170) and BSKNN-3 (270) which are considerably greater than for BSKNN-1 (120) in spite of the only moderate differences in $T_c$. Furthermore, BSKNN-2 and BSKNN-3 show nearly identical a-axis dielectric behavior (Fig. 18) which differs considerably from that of BSKNN-1. These results suggest the possibility of an MPB region in the vicinity of BSKNN-2, with a pseudotetragonal orthorhombic phase for compositions at and beyond BSKNN-2. Furthermore, recent optical measurements on BSKNN-2[13] show values for the linear electrooptic coefficient $r_{13}$ ($160 \times 10^{-12}$ to $180 \times 10^{-12}$ m/V) which are a factor of 2 greater than anticipated from the phenomenology given in Eq. (1). This may be due to a ferroelastic contribution to $r_{33}$ which is not accounted for in the phenomenology for a simple proper bronze ferroelectric.[29,33] Measurements of the change in $\epsilon_{13}$ with applied dc field for BSKNN-2 in the ferroelectric phase also indicate anomalous behavior[34,35] and suggest the onset of an improper ferroelastic transition about 90°C below $T_c$.

Figure 19 shows the room-temperature dielectric constants and the ferroelectric phase transition temperature, $T_c$, for BSKNN single crystals as a function of the tetragonal or pseudotetragonal a-axis lattice constant. Also shown in Fig. 19 are data for two other ferroelectric bronzes, $K_3Li_2Nb_5O_{15}$ (KLN)[26,36,37] and $K_{3-x}Li_2Na_xNb_5O_{15}$ ($x = 0.3$, KLNN),[36] which also have filled A and $A_2$ lattice sites. These data illustrate why larger-unit-cell bronzes such as KLN have not been generally favorable for optical applications, since their comparatively low dielectric constants necessarily reflect low electrooptic constants. In contrast, Ce-doped BSKNN-2 and BSKNN-3 have proved especially useful for photorefractive applications[12,13,16,38] as a result of their large dielectric and electrooptic properties, these being similar, in many ways, to those found in perovskite $BaTiO_3$. However, BSKNN compositions are substantially easier to grow as large, optical-quality crystals of 1.5-cm diameter. Furthermore, unlike $BaTiO_3$, BSKNN crystals retain their ferroelectric properties when cooled below room temperature and therefore do not require careful environmental control. Hence, these crystals may prove particularly advantageous in a number of present and future optical device concepts.

### IV. Other Potentially Morphotropic Systems

Table I lists three additional tungsten bronze solid solutions
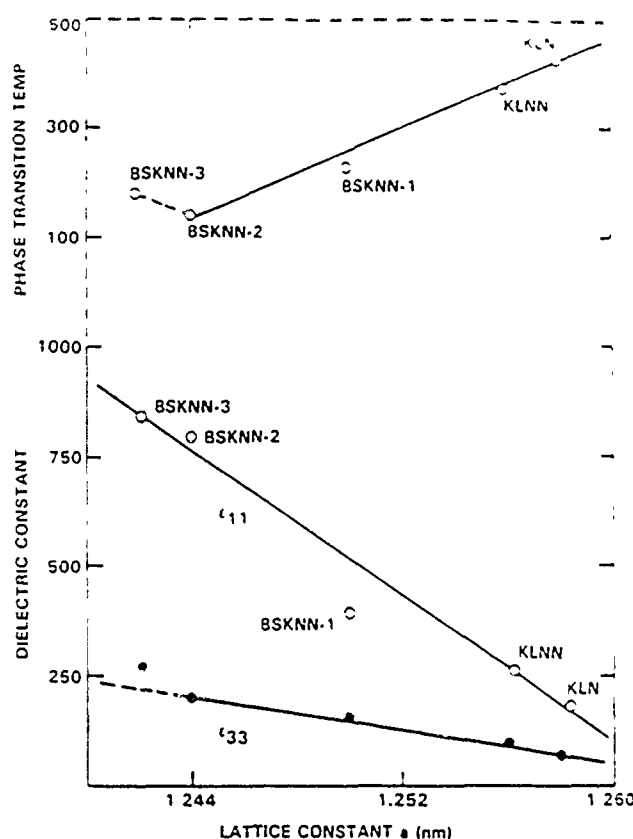


Fig. 19. Ferroelectric phase transition temperature and dielectric constants $\epsilon_{11}$ and $\epsilon_{33}$ as a function of the a-axis lattice constant for "filled" tungsten bronze BSKNN, KLN, and KLNN single crystals

which have been reported in the literature.[30,39] These binary systems were initially studied to determine the stability of the bronze structure and to establish the basic roles of each cation in the partially filled and filled lattice formulations. Each of these systems possesses a local minimum for the phase transition temperature behavior suggestive of an MPB.

Two examples of the variation of $T_c$ with composition are shown in Fig. 20 for the systems SKN–PKN and BNN–PNN from the work by Ravez, Perron-Simon, and Hagenmuller.[30] In both instances, the observed $T_c$ minima were found to occur at boundaries between tetragonal (or pseudotetragonal) and orthorhombic phases. Typical of MPB materials having orthogonal orientations of the polar vector in the two phases, these MPB regions are also accompanied by abrupt changes in the c-axis lattice constant as well.

Although the binary systems in Table I all show MPB-type behavior, they were not identified as morphotropic systems in their original investigation. It appears likely that all of these systems have true MPB regions, and thus the potential for very large dielectric, piezoelectric, and electrooptic properties. Certainly it would be worthwhile to continue their investigation in more detail, particularly in the form of grain-oriented ceramics, epitaxial thin films, or bulk single crystals to establish the directional dependencies of the ferroelectric properties.

Table I. Potentially Morphotropic Bronze Systems

| System | $T_c$ minimum (°C) | $\epsilon$ |
|---|---|---|
| $(1 - x)Sr_2KNb_5O_{15}-xPb_2KNb_5O_{15}$[a] | 110 | 0.17 |
| $(1 - x)Ba_2NaNb_5O_{15}-xPb_2NaNb_5O_{15}$[a] | 280 | 0.05 |
| $(1 - x)Pb_{2.5}Ta_5O_{15}-xPb_2NaNb_5O_{15}$ | 40 | 0.85 |

[a]Ravez et al[30] [b]Ikeda et al[39]
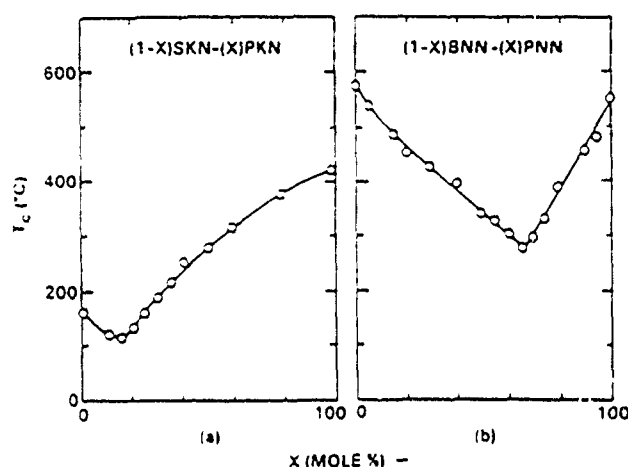
Fig. 20. Phase transition temperature versus ceramic composition for (a) (1 − x)SKN–xPKN and (b) (1 − x)PNN–xBNN. From the work by Ravez et al. (Ref 30)

## V. Summary

Table II summarizes the properties of the major MPB bronze systems that we have examined in our work. Included in the table is the system PN–SNN, details of which may be found in an earlier paper.[3] The last system in the table. PN–KLN, is one we have just begun to investigate based on the orthorhombic and tetragonal structures of its end members. This system has relatively high phase transition temperatures for both end members (in excess of 400°C), presenting the possibility for a moderately high $T_c$ value at the MPB. This can be of particular value in optical applications because of the possibility for large, nearly temperature-independent dielectric and electrooptic constants at normal device operating temperatures.

We are also investigating a variant of the BNN–SNN bronze system involving the partial substitution of Ca for both Ba and Sr. This work initially focused on the $Sr_{2-x}Ca_xNaNb_5O_{15}$ (SCNN) solid solution because of an observed enhancement of the room-temperature dielectric constant of ceramic SNN with Ca modification. Czochralski crystal growths for the $x = 0.10$ composition $Sr_{1.9}Ca_{0.1}NaNb_5O_{15}$ have shown large room-temperature dielectric constants (≥1700) for both polar and nonpolar directions, a unique property of importance in photorefractive and electrooptic device applications such as three-dimensional memories and optical displays. However, bulk single-crystal growths of SCNN with diameters greater than 0.5 cm have proved difficult, so we are now investigating growths along the pseudobinary join SCNN–BNN. These have been very encouraging, with fracture-free crystal boules in excess of 1.0-cm diameter being grown in some instances. Details of this work are beyond the intended scope of this paper and instead will be published in a forthcoming paper.

It is evident that there are numerous possibilities for morphotropic systems within the tungsten bronze ferroelectric family, although in no way should the present paper be considered a comprehensive review of all such possibilities. The wealth of available MPB systems reflects the inherent flexibility of the bronze crystal structure in contrast to the more limited flexibility found in other crystal systems. This same structural flexibility has also proved advantageous for the development of optical-quality Ce- and Cr-doped crystals for photorefractive applications.[3] Although the Pb-containing MPB bronzes, such as PBN, have very large spontaneous polarization and large dielectric and piezoelectric properties, their most serious drawback is the high volatility of PbO at crystal growth temperatures. Hence, lower-temperature growth methods such as hot-pressed, grain-oriented ceramics or epitaxial thin films may prove more useful for practical applications of these materials. For example, epitaxial thin films are particularly suited to SAW and pyroelectric detector applications which may benefit from the enhanced ferroelectric properties available in these materials. However, many of the non-Pb-containing MPB bronzes, and perhaps some systems which contain only a small fraction of Pb at the MPB composition (e.g., PN–SNN, SKN–PKN), are still potential candidates for bulk single-crystal development.

## VI. Conclusions

Ceramic and single-crystal investigations of niobates and tantalates having the tungsten bronze structure have shown the existence of MPB regions in several systems with PN, PNN, PKN, BN, BNN, SNN, SKN, PT, etc., as constituent end members. In some cases, MPB behavior had been previously observed without mentioning the possible existence of a morphotropic boundary. Because of the wide variety of MPB systems available in the tungsten bronze family, the selection criteria for continuing materials development necessarily rest upon the ferroelectric properties available within each system (e.g., polarization, dielectric constants, pyroelectric coefficient, piezoelectric constants) as applied to the specific needs of a given device application. However, the ultimate applicability of these MPB ferroelectrics will be determined by the ability to grow these materials in the appropriate densified ceramic, thin film, or bulk single-crystal form with material quality (homogeneity, transparency, minimal defects and striations, low dielectric losses, etc.) sufficient for these applications. The highly successful work to date on the development of morphotropic PBN and other bronze systems should therefore prove invaluable for the continued growth and application of these and other new MPB bronze ferroelectrics in the future.

### References

[1] E. C. Subbarao, G. Shirane, and F. Jona, "X-Ray, Piezoelectric and Optical Studies of PbNb₂O₆ and Related Compounds," *Acta Crystallogr* 13. 226-11 (1960)

[2] M. H. Francombe, "The Relation between Structure and Ferroelectricity in Lead Barium and Barium Strontium Niobate," *Acta Crystallogr* 13. 131-40 (1960)

[3] T. R. Shrout, H. Chen, and L. E. Cross. Dielectric and Piezoelectric Properties of $Pb_{1-x}Ba_xNb_2O_6$ Ferroelectric Tungsten Bronze Crystals." *Ferroelectrics* 36 45-48 (1983).

[4] T. R. Shrout, L. E. Cross, and H. A. Dukin. Ferroelectric Properties of Tungsten Bronze Lead Barium Niobate (PBN) Single Crystals," *Ferroelectrics Lett* 44 325-30 (1983)

[5] B. Jaffe, W. R. Cook, and H. Jaffe, Piezoelectric Ceramics Academic Press New York, 1971

[6] G. H. Haertling and C. E. Land. Hot-Pressed (Pb La)(Zr Ti)O₃ Ferroelectric Ceramics for Electrooptic Applications." *J Am Ceram Soc* 54 (1) 1-11 (1971)

Table II. Summary of Present MPB Tungsten Bronze Systems

| System | Space group | x at MPB | T (°C) | ε at 23°C |
|---|---|---|---|---|
| (1 − x)PbNb₂O₆–xBaNb₂O₆ | Bb2₁m-P4bm | 0.37 | 280 | 1000 |
| (1 − x)PbKNb₅O₁₅–xBa₂NaNb₅O₁₅ | -Ccm2₁ | 0.25 | 280 | 1350 |
| (1 − x)Pb₂KNb₅O₁₅–xSr₂NaNb₅O₁₅ | -Bbm2 | 0.70 | 155 | 950 |
| (1 − x)Pb₂.₅Nb₅O₁₅–xSr₂NaNb₅O₁₅ | Bb2₁m-Bbm2 | 0.75 | 135 | 3400 |
| (1 − x)Ba₂NaNb₅O₁₅–xSr₂NaNb₅O₁₅ | Ccm2₁-Bbm2 | 0.60 | 180 | 450 |
| Ba₂₋ₓSrₓK₁₋ₓNaₓNb₅O₁₅ | | ∼1.5 | 170 | 190 |
| (1 − x)Pb Nb₂O₆–xK₁₋ₓNb₅O₁₅ | Bb2₁m-P4bm | | | |

A Magneli  Crystal Structure of Tetragonal Potassium Tungsten Bronze  *Ark Kemi* 1 [24] 213–21 (1949)

[1]P B Jamieson S C Abrahams, and J L Bernstein. Ferroelectric Tungsten Bronze-Type Crystal Structures I Barium Strontium Niobate $Ba_{0.75}Sr_{0.25}Nb_2O_{6}$. *J Chem Phys.*, 48 [11] 5048–57 (1968)

[2]A M Glass. "Investigation of the Electrical Properties of $Sr_{1-x}Ba_xNb_2O_6$ with Special Reference to Pyroelectric Detection. *J Appl. Phys.*, 40 [12] 4699–713 (1969)

[3]T R Shrout, L E Cross, P Moses, H A McKinstry, and R R Neurgaonkar. A Phenomenological Theory for Predicting the Temperature Dependence of Elastic, Dielectric and Piezoelectric Properties in Simple Proper Ferroelectric Crystals. *Proc IEEE Ultrasonics Symp.*, 414–19 (1980)

[4]R R. Neurgaonkar, J R Oliver, and L E. Cross, "Ferroelectric Properties of Tetragonal Tungsten Bronze Single Crystals. *Ferroelectrics*, 56, 31–36 (1984)

[5]R R Neurgaonkar, W K. Cory, and J R Oliver, Ferroelectric Tungsten Bronze BSKNN Crystals for Photorefractive Applications, *SPIE Proc.*, 739 91–96 (1987)

[6]R R. Neurgaonkar, W K Cory, J R Oliver, W. W Clark III, G. L. Wood, M J Miller, and E J Sharp, "Growth and Ferroelectric Properties of Tungsten Bronze $Ba_{2-x}Sr_xK_{1-y}Na_yNb_5O_{15}$ (BSKNN) Single Crystals," *J. Cryst. Growth*, 84, 629–37 (1987)

[7]M Yokosuka, "A New Transparent Ferroelectric Ceramic. Lanthanum Modified Lead-Barium Metaniobate (PBLN)," *Jpn. J. Appl Phys.*, 16 [2] 379–80 (1977)

[8]K. Nagata and K. Okazaki, "Properties of Hot-Pressed Tungsten Bronze Transparent Ceramics", presented at the Japan–U.S. Study Seminar on Dielectric and Piezoelectric Ceramics, No W-11, Tokyo. Japan. 1982.

[9]K Nagata, Y Kawatani, and K Okazaki, "Anisotropies of Hot-Pressed Transparent $(Pb, Ba, La)Nb_2O_6$ Ceramics, *Jpn. J Appl Phys.*, 22 [9] 1353–56 (1983)

[10]R R Neurgaonkar and L E Cross, "Temperature Compensated Piezoelectric Materials. DARPA Final Rept., Contract No F49620–78–C–0093 Defense Advanced Research Projects Agency, Arlington, VA. 1982.

[11]R R Neurgaonkar, J R Oliver, M D Ewbank, and W F Hall Development and Modification of Photorefractive Properties in the Tungsten Bronze Family Crystals." *Opt Eng.*, 26 [5] 392–395 (1987)

[12]M DiDomenico and S. H. Wemple, "Oxygen Octahedra Ferroelectrics. I Theory of Electro-Optical and Nonlinear Optical Effects." *J. Appl. Phys.*, 40 [2] 720–34. II. Electro-Optical and Nonlinear Optical Device Applications," *ibid.*, 735–52 (1969)

[13]R.R. Neurgaonkar, J R. Oliver, W K. Cory, and L. E. Cross, "Structural and Dielectric Properties of the Phase $Pb_{1-x}K_xM_1^{3+}Nb_5O_{15}$, M = La or Bi," *Mater. Res. Bull.*, 18, 735–41 (1983).

[14]M Ishida, S. Tsugi, K. Kimura, H Matsunami, and T. Tanaka, "Epitaxial Growth of Ferroelectric PLZT Thin Films," *J. Cryst. Growth*, 45, 393–98 (1978)

[15]K Iijima, Y Tomita, R. Takayama, and I. Ueda, "Preparation of c-Axis Oriented $PbTiO_3$ Thin Films and Their Crystallographic, Dielectric, and Pyroelectric Properties," *J Appl. Phys.*, 60 [11] 361–67 (1986).

R R Neurgaonkar and J R Oliver  Research on Sputtering of Ferroelectric Thin Films  DARPA Annual Rept  Contract No F49620–86–C–0052 Defense Advanced Research Projects Agency, Arlington VA 1987

[4]J Nakano and T Yamada  Ferroelectric and Optical Properties of Lead Potassium Niobate. *J Appl Phys* 46 [6] 2361–65 (1975)

[5]K Nagata, T Yamazaki, and K Okazaki, Dielectric and Piezoelectric Properties of Hot-Pressed Lead Potassium Niobate  presented at the 2nd Meeting on Ferroelectric Materials and Their Applications, No F-10, Tokyo, Japan, 1979

[26]L. G Van Uitert, H J Levenstein, J J Rubin, C. D Capio, E. F Dearborn and W A Bonner  Some Characteristics of Niobates Having Filled Tungsten Bronze-Like Structures, *Mater Res Bull.*, 3, 47–58 (1968).

[7]L. G Van Uitert, J J Rubin, W K Grodkiewicz, and W A. Bonner, "Some Characteristics of Ba, Sr, Na Niobates." *Mater Res Bull.*, 4, 63–74 (1969).

[8]J R Oliver, R R Neurgaonkar, and G L Shoop, "Structural and Ferroelectric Properties of Morphotropic Phase Boundary Systems in the Tungsten Bronze Family  pp 485–89 in Proceedings of the Sixth IEEE International Symposium in Applications of Ferroelectrics (ISAF) IEEE, New York. 1986

[9]J C Toledano, Theory of the Ferroelastic Transition in Barium Sodium Niobate." *Phys Rev B.*, 12 [3] 943–50 (1975)

[10]J Ravez, A Perron-Simon, and P Hagenmuller, "The Tetragonal Tungsten Bronze Phases. Crystallochemical Rules. Relations between Ferroelectric Properties and Structural Distortions  (in Fr), *Ann Chim. (Paris)*, 1, 251–68 (1976)

[11]X. Yuhuan, H Chen, and L E Cross, "Single Crystal Growth and Determination of Physical Properties for $(K_{1-x}Na_x)_{0.4}(Sr_{1-x}Ba_x)_{0.8}Nb_2O_6$," *Ferroelectrics* 54 123–26 (1984)

[12]R R Neurgaonkar, W K Cory and J R Oliver, "Growth and Applications of Ferroelectric Tungsten Bronze Crystals. *Ferroelectrics*, 51, 3–8 (1983)

[13]T Ikeda, A Phenomenological Theory of the Phase Transition in $Ba_2NaNb_5O_{15}$. *Jpn J Appl Phys*, 13 [7] 1065–71 (1974)

[14]J R Oliver, R R Neurgaonkar, and L E. Cross, "A Thermodynamic Phenomenology for Ferroelectric Tungsten Bronze $Sr_{0.6}Ba_{0.4}Nb_2O_6$ (SBN 60) *J Appl Phys*, 64 [1] 37–47 (1988)

[15]J R Oliver and R R Neurgaonkar, Preliminary Results on the Thermodynamic Phenomenology for Ferroelectric Tungsten Bronze $Ba_{0.3}Sr_{1.5}K_{0.5}Na_{0.5}Nb_5O_{15}$ (BSKNN-2)  in ONR Final Technical Rept., Contract No N00014–81–C–0463 Office of Naval Research, Arlington, VA. 1988

[16]M Adachi, "Growth and Properties of Tungsten-Bronze Ferroelectric Crystals and Films". Ph.D. Thesis, Kyoto University, Kyoto, Japan. 1982.

[17]M Adachi and A Kawabata, "Elastic and Piezoelectric Properties of Potassium Lithium Niobate (KLN) Crystals," *Jpn J. Appl Phys.*, 17 [11] 1969–73 (1978)

[18]J. Rodriguez, A. Siahmakoun, G. Salamo, M. J. Miller, W. W. Clark III, G L Wood, E. J Sharp, and R R. Neurgaonkar, "BSKNN as a Self-Pumped Phase Conjugator," *Appl Opt.*, 26 [9] 1732–36 (1987)

[19]T Ikeda, K. Uno, K. Oyamada, A Sagara, J Kato, S. Takano, and H Sato Some Solid Solutions of the $A_2B_{10}O_{30}$ and $A_6B_{10}O_{30}$ Tungsten Bronze Ferroelectrics *Jpn J Appl Phys*, 17 [2] 341–48 (1978).                                       □

APPENDIX 32

# A thermodynamic phenomenology for ferroelectric tungsten bronze Sr$_{0.6}$Ba$_{0.4}$Nb$_2$O$_6$ (SBN:60)

J. R. Oliver and R. R. Neurgaonkar

*Rockwell International Science Center, Thousand Oaks, California 91360*

L. E. Cross

*Materials Research Laboratory, The Pennsylvania State University, University Park, Pennsylvania 16802*

The tetragonal tungsten bronze ferroelectrics in the strontium barium niobate system have been extensively studied over many years. As for many of the bronzes, a crude interpretation of the experimental data has been attempted in the past using the simple Landau-Ginsburg-Devonshire expansion of the Gibbs free energy as a Taylor series in powers of the polarization, lumping all the temperature dependence into the lowest order term. In this paper new measurements are presented for the temperature dependence of dielectric polarization, permittivity, and the $E$-field dependence of the permittivity. It is shown that for a realistic fitting of the data, the Taylor expansion must be taken to at least the eighth power term, and that the coefficients of terms up to the sixth power must be taken as functions of temperature. Since the phenomenology describes equilibrium behavior, it is the total static polarizability that is being explored in this treatment. The nature of this temperature dependence strongly suggests that the phase transition from a macropolar to a macrononpolar state is tetracritical.

## I. INTRODUCTION

Tungsten bronze ferroelectric oxides have received considerable attention for many years, with perhaps the best known of these being compositions in the $Sr_{1-x}Ba_xNb_2O_6$ (SBN) solid solution system. Numerous applications have been realized for SBN, particularly in the areas of pyroelectric infrared detection,[1] piezoelectrics,[2,3] electro-optics,[4-5] and photorefractive optics,[6-14] the latter resulting from the evolution of techniques for the growth of high-quality single crystals in the congruently melting $Sr_{0.6}Ba_{0.4}Nb_2O_6$ (SBN:60) composition.[15] As in the case for other ferroelectric materials, much of the experimental data for SBN have been interpreted on the basis of the Landau-Ginsburg-Devonshire (LGD) phenomenology, as in the extensive work by Shrout *et al.*[16] on the elastic, dielectric, and piezoelectric properties of SBN:60.

With some important exceptions, nearly all of these interpretations of ferroelectric behavior have involved simple LGD expansions of the Gibbs free energy as a Taylor series in even powers of the polarization, truncated at the sixth power, with all temperature dependence carried only in the lowest order coefficient.[17] This approach has proven successful for SBN:60,[3,16] although in some instances only rough approximations of the experimental data can be obtained, as in the case of the dielectric properties.

The development of optical quality SBN:60 crystals has made it possible to accumulate very reproducible dielectric and polarization data as a function of temperature. In this paper, we present new measurements of these properties along with measurements of the electric field dependence of the permittivity as a function of temperature. It is shown, that for an accurate fitting to these data in the ferroelectric phase the Taylor expansion of the Gibbs free energy must be taken out to at least the eighth power of the polarization, and that the coefficients of terms up to the sixth power must be taken as strong functions of temperature. Since the phenomenology describes equilibrium behavior, it is the total static polarizability, summing all possible contributions, which is being explored in this treatment.

## II. THERMODYNAMIC PHENOMENOLOGY

The free-energy function of interest for a polarizable insulator is the elastic Gibbs function, given by

$$G_1 = U - TS - Xx, \qquad (1)$$

where $U$ is the internal energy, $T$ the temperature, $S$ the entropy, $X$ the elastic stress, and $x$ the strain. Under the symmetry constraints of bronze ferroelectrics with a high-temperature tetragonal prototype symmetry 4/$mmm$, the change in free energy, $\Delta G_1$, due to nonzero polarization $P$, may be written as a power series expansion in the $P_i$'s along the three principal crystallographic axes. Under isothermal conditions and zero stress, the LGD phenomenological elastic Gibbs function in the shortened matrix notation[18] becomes

$$\Delta G_1 = 1/\epsilon_0 [\alpha_1(P_1^2 + P_2^2) + \alpha_3 P_3^2 + \alpha_{11}(P_1^4 + P_2^4) + \alpha_{12}P_1^2 P_2^2 + \alpha_{13}(P_1^2 + P_2^2)P_3^2 + \alpha_{33}P_3^4 + \alpha_{111}(P_1^6 + P_2^6)$$

$$+ \alpha_{112}(P_1^4 P_2^2 + P_1^2 P_2^4) + \alpha_{113}(P_1^4 + P_2^4)P_3^2 + \alpha_{133}(P_1^2 + P_2^2)P_3^4 + \alpha_{123}P_1^2 P_2^2 P_3^2 + \alpha_{333}P_3^6$$

$$+ \alpha_{1111}(P_1^8 + P_2^8) + \alpha_{1112}P_1^4 P_2^4 + \alpha_{1133}(P_1^4 + P_2^4)P_3^4 + \alpha_{3333}P_3^8]. \qquad (2)$$

where the $a$ s have been normalized by the free-space permittivity, $\epsilon_0$, for later convenience. Equation (2) principally differs from earlier treatments[3,16] by the inclusion of terms out to the eighth power of the polarization for reasons which will become evident later.

For nonzero electric fields, $E_i$, we must examine the complete Gibbs function $\Delta G = \Delta G_1 - (E_1 P_1 + E_2 P_2 + E_3 P_3)$. Setting the first partial derivatives of $\Delta G$ with respect to polarization equal to zero then gives the electric field relations along the principal axes:

$$E_1 = 1/\epsilon_0 [ 2a_1 P_1 + 4a_{11} P_1^3 + 2a_{12} P_1 P_2^2 + 2a_{13} P_1 P_3^2$$
$$- 6a_{111} P_1^5 + a_{112}(2P_1 P_2^4 + 4P_1^3 P_2^2) - 4a_{113} P_1^3 P_3^2$$
$$+ 2a_{133} P_1 P_3^4 + 2a_{123} P_1 P_2^2 P_3^2 + 8a_{1111} P_1^7$$
$$- 4a_{1122} P_1^3 P_2^4 - 4a_{1133} P_1^3 P_3^4 ], \quad (3)$$

$$E_3 = 1/\epsilon_0 [ 2a_3 P_3 + 2a_{13}(P_1^2 + P_2^2) P_3 + 4a_{33} P_3^3$$
$$+ 2a_{113}(P_1^4 + P_2^4) P_3 + 4a_{133}(P_1^2 + P_2^2) P_3^3$$
$$+ 2a_{123} P_1^2 P_2^2 P_3 + 6a_{333} P_3^5$$
$$+ 4a_{1133}(P_1^4 + P_2^4) P_3^3 + 8a_{3333} P_3^7 ]. \quad (4)$$

The electric field expression for $E_2$ has been omitted since it is formally equivalent to Eq. (3) for the tetragonal symmetry assumed here.[16] The solutions of these equations with $E_i = 0$ determine the normal ferroelectric states; in the case of tetragonal bronze ferroelectrics, the 3 (or $c$) axis is the only spontaneously polarizable axis, so that Eqs. (3) and (4) reduce to

$$E_1 = 1/\epsilon_0 [ 2a_1 P_1 + 4a_{11} P_1^3 + 2a_{13} P_1 P_3^2 - 6a_{111} P_1^5$$
$$+ 4a_{113} P_1^3 P_3^2 + 2a_{133} P_1 P_3^4$$
$$+ 8a_{1111} P_1^7 + 4a_{1133} P_1^3 P_3^4 ]$$
$$(P_2 = 0), \quad (5)$$

$$E_3 = 1/\epsilon_0 [ 2a_3 P_3 + 4a_{33} P_3^3 + 6a_{333} P_3^5 + 8a_{3333} P_3^7 ]$$
$$(P_1 = P_2 = 0). \quad (6)$$

The dielectric stiffnesses, $\chi_{ii} = \epsilon_{ii}^{-1}$, are then given by

$$\chi_{11} = \epsilon_0 \frac{\partial E_1}{\partial P_1} = 2a_1 + 12a_{11} P_1^2 + 2a_{13} P_3^2 + 30a_{111} P_1^4$$
$$+ 12a_{113} P_1^2 P_3^2 + 2a_{133} P_3^4$$
$$+ 56a_{1111} P_1^6 + 12a_{1133} P_1^2 P_3^4$$
$$(P_2 = 0), \quad (7)$$

or

$$\chi_{11} = 2a_1 + 2a_{13} P_3^2 + 2a_{133} P_3^4 \quad (P_1 = P_2 = 0), \quad (7a)$$

and

$$\chi_{33} = \epsilon_0 \frac{\partial E_3}{\partial P_3} = 2a_3 + 12a_{33} P_3^2$$
$$+ 30a_{333} P_3^4 + 56a_{3333} P_3^6$$
$$(P_1 = P_2 = 0) \quad (8)$$

At temperatures well above the ferroelectric Curie point, $T_c$, $P_3 = 0$ under zero bias conditions and the paraelectric stiffnesses generally follow a linear Curie–Weiss behavior of the form

$$\chi_{11} = 2a_1 = (T - \theta_1)/C_1 \quad (T > T_c) \quad (9)$$

$$\chi_{33} = 2a_3 = (T - \theta_3)/C_3 \quad (T > T_c). \quad (10)$$

with $\theta_1 \ll \theta_3$. For a first-order phase transition $\theta_3 < T_c$, whereas for a second-order transition $\theta_3 = T_c$ under ideal conditions.[17,19]

Generally, there are no restrictions on the temperature dependence of the higher order Devonshire coefficients $a_{11}$, $a_{33}$, $a_{111}$, etc., and indeed for cases such as BaTiO$_3$ some temperature dependence has been found.[20] However, in most treatments of ferroelectric materials, the higher order coefficients are assumed to be temperature invariant, at least over a limited range below $T_c$, and reasonably good fits to dielectric and spontaneous polarization data can be obtained. Nevertheless, the uniqueness of the Devonshire coefficients is necessarily determined by physically measurable parameters such as the low-frequency dielectric constant, the spontaneous polarization, and the electric field which must rigorously satisfy the dielectric stiffness and electric field equations as well as other derived phenomenological relations. These we shall now examine on the basis of macroscopic experimental data for tungsten bronze SBN 60.

## III. TUNGSTEN BRONZE SBN:60

The congruently melting SBN 60 composition is a smaller unit cell bronze with a tetragonal 4-mm crystal structure at room temperature and lattice constants $a,b = 12.465$ Å and $c = 3.935$ Å as determined by x-ray diffraction measurements. The SBN solid solution system is represented by the formula $(A_1)_4 (A_2)_2 B_{10} O_{30}$ in which both the Sr$^{2+}$ and Ba$^{2+}$ ions occupy the fifteenfold ($A_1$) and twofold ($A_2$) coordinated oxygen octahedra sites.[21,22] Since only $\frac{5}{6}$ of these sites are occupied, SBN is referred to as an unfilled bronze. The high-temperature prototype symmetry is tetragonal $4/mmm$, placing SBN in the Shuvalov ferroelectric species $4/mmm(1)D4F4m$.[23]

The SBN·60 solid solution crystals examined were grown by the Czochralski technique[15,24,25] using an automatic-diameter control system to facilitate tight compositional control and high optical quality during bulk crystal growth. Further details may be found in previous papers.[5,8,12] Over 100 growths have now been performed in the SBN system, including undoped and doped crystals (Ce, La, Fe, etc.), and crystal quality has evolved to the point where $c$-axis boules up to 4 cm diam are now routinely grown, free of detectable imperfections and major optical striations. These crystals have been of sufficiently high optical quality to permit extensive optical measurements such as two- and four-wave mixing and self-pumped phase conjugation.[8–14]

A photograph of a typical SBN 60 crystal boule is shown in Fig. 1. A general characteristic of tungsten bronze crystals is the presence of major facets parallel to the growth axis, in the particular case of SBN 60 $c$-axis growths there are 24 facets, including (100), (010), (110), etc, a feature which significantly eases the task of crystal orientation and cutting.

## IV. EXPERIMENTAL METHOD

The two principal crystallographic axes of interest in SBN 60 are the $a$ or $b$ axes ((100) or (010)) and the polar $c$
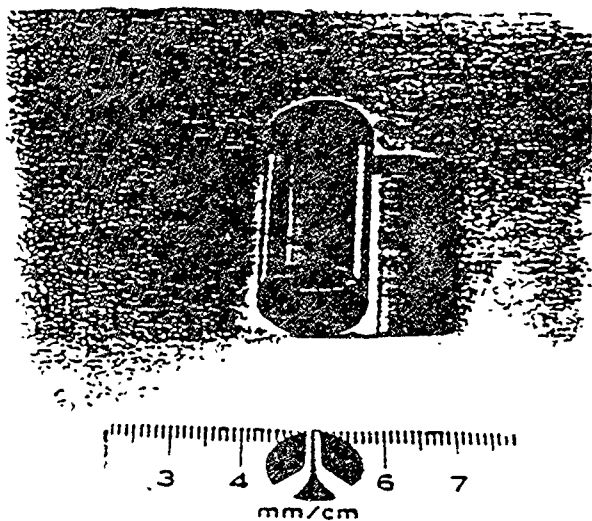
FIG 1 Czocnralski-grown SBN 60 bulk single crystals.

axis ((001)) Crystal wafers in these orientations were cut with a diamond saw and then mechanically lapped and, in some instances, additionally polished to an optical finish. However, the latter step was not found to be particularly necessary for electrical measurements, as long as the contacts were annealed. We have used sputtered Pt or Au full area contacts almost exclusively in our measurements, and although other materials (such as Al) and contact forming methods (such as fired pastes) are viable alternatives, sputtered noble metal contacts have been found more stable at elevated temperatures and yield highly reproducible electrical measurement data.

Contacted crystal samples were generally annealed in a dry oxygen atmosphere at 450–550 °C for 1–3 h prior to measurement. Although the crystal boules undergo a post-growth anneal at 1300–1400 °C, the second low-temperature anneal establishes a good interface between the contact metallization and the crystal surface, and helps to minimize surface conductivity along the unmetallized edges. Surface damage due to cutting, polishing, and metal deposition appears to be minimized at these relatively low temperatures, and residual internal stress is also probably reduced.

The measurement apparatus for dielectric, conductivity, and polarization measurements consisted of a fully shielded alumina sample mount enclosed in an environmentally sealed alumina chamber. Electrical contact with the test samples was established by small Pt pads which lightly pressed against a portion of the contact metallization using an adjustable spring-loaded alumina rod. Details of the design are given in the paper by Mohn, Oliver, and Housley;[26] the apparatus in its present configuration represents evolutionary refinements of the original design. Sample temperature control was facilitated by a Kanthal-wound tube furnace, with temperatures below room temperature achieved by spraying liquid nitrogen onto the sample chamber wall. $N_2$ gas was used in the chamber below 0 °C and $O_2$ above at a ~2 psi positive pressure to maintain a dry environment.

All dielectric measurements were made with a calibra-

ted HP4274A bridge covering the frequency range of 100 Hz–100 kHz. dc currents were measured with a Keithley 619 electrometer All data acquisition, process control, and data analysis were facilitated by a HP9816 desktop computer using an IEEE-488 interface bus.

## V. POLAR-AXIS PROPERTIES

The bronze solid solution system $Sr_{1-x}Ba_xNb_2O_6$, $0.25 < x < 0.75$, is characterized by a large dielectric anomaly along the polar $c$ axis at the paraelectric/ferroelectric phase transition temperature, $T_c$. An example is shown in Fig. 2 for the weak-field $c$-axis dielectric constant, $\epsilon_{33}$, as a function of temperature for an SBN:60 crystal poled to a single ferroelectric domain. A recurring feature of SBN is the significant dielectric dispersion which appears within a 10–15 °C range of $T_c$ (~75 °C) as shown in Fig. 2. This Debye-type relaxation behavior is why SBN solid solution crystals are generally referred to as relaxor ferroelectrics. This behavior is postulated to occur because of the distribution of phase transition temperatures in the bulk of the crystal arising from the site uncertainty of the $Sr^{2+}$ and $Ba^{2+}$ ions in the partially filled lattice. Further evidence for this postulate is provided by comparison with "filled" bronze ferroelectrics, such as $Ba_{2-x}Sr_xK_{1-y}Na_yNb_5O_{15}$(BSKNN),[14] where relaxor behavior is greatly diminished.

For temperatures approximately 20 °C or more on either side of $T_c$, the dielectric dispersion is small (typically < 2% from 100 Hz–100 kHz), as is the dielectric loss (tan $\delta$ typically 0.007 or less at 20 °C, and less than 0.001 at 120 °C). Room-temperature dark dc conductivity is also very small, typically $10^{-15} \Omega^{-1} cm^{-1}$ or less, and can only be measured under absolutely stable temperature conditions because of the large pyroelectric currents which can otherwise occur.

SBN 60 crystals which have been thermally depoled by a warming well above 100 °C show the same low dielectric dispersion and loss above $T_c$, but show a very large dispersion and loss (tan $\delta$ = 0.10–0.25 at 20 °C) which persist well
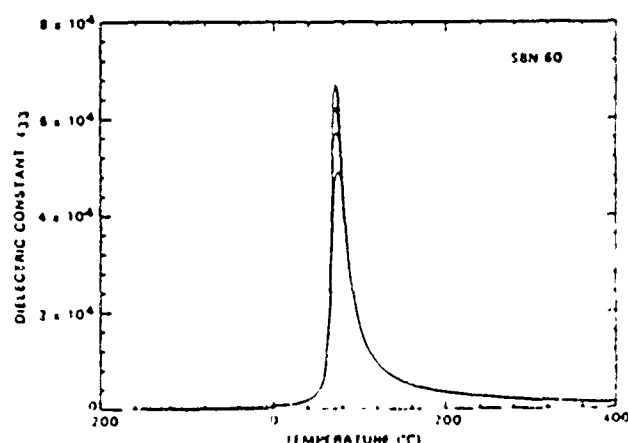


FIG 2 Polar axis dielectric constant for a poled SBN 60 crystal at 100 Hz (highest curve), 1 10 and 100 kHz (lowest curve) $T_c$ = 73–76 °C depending on frequency

Oliver Neurgaonkar and Cross
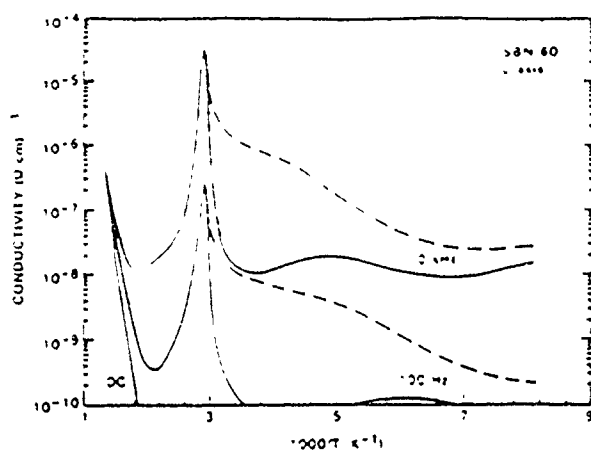
FIG. 3 Arrhenius plots of the polar axis conductivity of SBN 60 at dc, 100 Hz, and 10 kHz. The dashed lines are for a thermally depoled crystal, the solid lines are for the same crystal in a poled condition
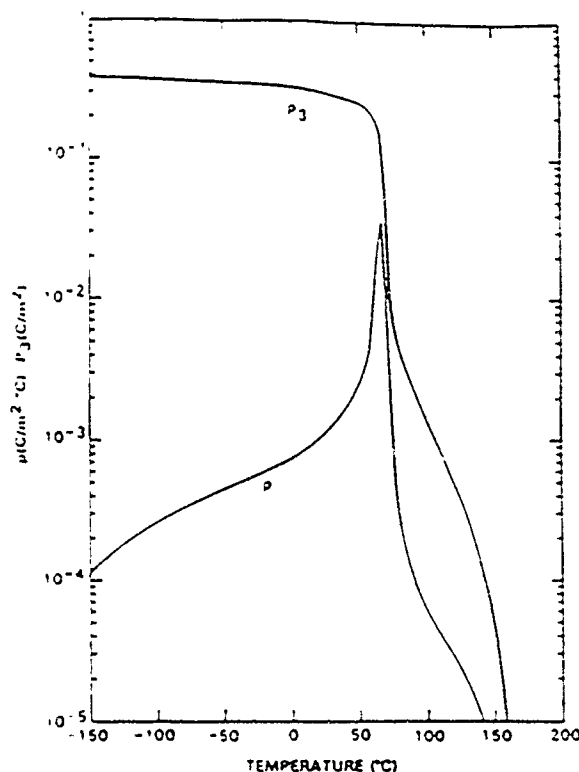


FIG 4 The polar-axis polarization, $P_3$, and the pyroelectric coefficient, $p$, for SBN 60 The high-temperature tail regions tend to vary somewhat with the poling conditions.

below 0 °C. The substantial differences between the poled and depoled ac conductivities are shown in the Arrhenius plots of Fig. 3 at 100 Hz and 10 kHz. The higher conductivities and large dielectric dispersion for depoled crystals are felt to primarily arise from antiparallel domain wall relaxation[27] which progressively freezes out at lower temperatures. A curiosity of SBN compositions is that at low temperatures, typically below −100 °C, the antiparallel ferroelectric domains of a depoled crystal effectively clamp the crystal, resulting in a nearly dispersionless dielectric constant which is less than that for a normally poled crystal.

SBN:60 may be poled to a single ferroelectric domain by applying a 5–10 kV/cm dc field along the polar c axis at room temperature. However, an initial thermally depoled condition is necessary since the inadvertent application of a reversed polarity field to a partially poled crystal can result in the formation of antipolar macrodomains which cannot be fully switched.[28–30] For this work, poling was accomplished by a field-cooling method with the dc field applied from just below $T_c$ down to room temperature or below. Although it would appear advantageous to apply a poling field well above $T_c$ and then cool because of the distributed nature of the phase transition temperature in the crystal bulk, in practice this was found to degrade the room-temperature dielectric losses by as much as a factor of 3 due to space-charge effects and did not result in any significant changes of the measured polarization.

Figure 4 shows the c-axis polarization, $P_3$, and the pyroelectric coefficient, $p$, for a poled SBN 60 crystal. These data were obtained during warming at a nominal 3 °C/min rate, with other rates giving substantially the same results The polarization was determined from the numerically integrated charge released during warming at zero bias. The pyroelectric coefficient was measured simultaneously with the polarization[19] using

$$p = -\frac{dP_3}{dT} = -\frac{J_p}{r_t}.\qquad(11)$$

where $r_t$ is the rate of temperature change and $J_p$ is the measured current density. Although either form of Eq. (11) may be used to determine $p$, numerical differentiation of the polarization data was found less noisy since it was less affected by small fluctuations in the thermal ramp rate.

The pyroelectric maximum for SBN:60 occurs at 67 °C (Fig. 4), roughly 8 °C below $T_c$, and the net polarization persists well above $T_c$ because of the distribution of phase transition temperatures; this distribution is estimated to have a Gaussian half-width of 8 °C. At room temperature, $P_3 = 0.28$ C/m² and $p = 9.7 \times 10^{-4}$ C/m² °C, values which are comparable to other published results.[1,28] Secondary pyroelectric contributions to these data due to thermal dilatation are expected to be small except very close to $T_c$.[31]

### A. Phenomenological fitting

From the standpoint of the thermodynamic phenomenology, it is preferable to examine the polar axis dielectric constant of SBN 60 in terms of the dielectric stiffness, $\chi_{11} = \epsilon_{11}'$, as shown in Fig. 5 The dielectric stiffness accurately follows a linear Curie–Weiss law both above and below $T_c$ over a wide temperature range, with

$$\epsilon_{11} = C_1/(T - \theta_1)\quad(T > \theta_1)$$

$$C_{1f}/(\theta_{1f} - T)\quad(T < \theta_{1f}).\qquad(12)$$

where in the paraelectric phase $C_1 = 4.1 \times 10^5$ °C and $\theta_1 = 75$ °C, and in the ferroelectric phase $C_{1f} = 4.5 \times 10^4$ °C and $\theta_{1f} = 69$ °C The general behavior of the dielectric stiff-

ness suggests a near-second order phase transition. The fact that $\theta_{3f} = \theta_3 \neq T_c$ is felt to be due to the finite distribution of phase transition temperatures in SBN crystals. Indeed for "filled" bronzes such as BSKNN this difference amounts to, at most, 1-2 °C.[?]

The linear behavior of the dielectric stiffness over such a wide temperature range below $T$ is unusual compared to other ferroelectric materials such as LiNbO$_3$ and BaTiO$_3$.[19,20] A quick inspection of the electric field and dielectric stiffness expressions in Eqs. (6), (8), and (10) shows that for a stiffness expansion truncated at the fourth power of $P_3$ and temperature invariant $\alpha_{33}$ and $\alpha_{333}$, only a ~4:1 ratio for $C_1.C_{3f}$ is predicted in the low-temperature limit ($P_3$ large), compared to the ~9:1 ratio measured. Adiabatic versus isothermal considerations can modify the predicted results,[17,19] but only weakly due to the slow variation of the spontaneous polarization well below $T_c$.

An examination of the spontaneous polarization (Fig. 4) shows a linear temperature dependence for $P_3^6$ over a very wide temperature range, as shown in Fig. 6. Deviations from linearity occur only very close to $T_c$ and at the low-temperature extreme. Formally,

$$P_3 = P_{30}(\theta_{3f} - T)^{1/6}. \tag{13}$$

with $\theta_{3f} = 69$ °C, as before, and $P_{30} = 0.150$ C/m$^2$ °C[1/6]. From Eq. (11), the pyroelectric coefficient is then

$$p = P_{30}/6(\theta_{3f} - T)^{5/6} = P_3/6(\theta_{3f} - T). \tag{14}$$

which is experimentally satisfied over an equally wide temperature range.

The temperature dependence of $p$ in Eq. (14) may be compared with the phenomenology by taking the derivative with respect to temperature of the electric field expression in Eq. (6) under zero field conditions. For temperature invariant higher order coefficients and $\alpha_3$ defined by Eq. (10), we have

$$0 = \frac{1}{C_3} P_3 + \left(\frac{T - \theta_3}{C_3} + 12\alpha_{33}P_3^2 \right.$$

$$\left. + 30\alpha_{333}P_3^4 + 56\alpha_{3333}P_3^6\right)\frac{dP_3}{dT} \tag{15}$$
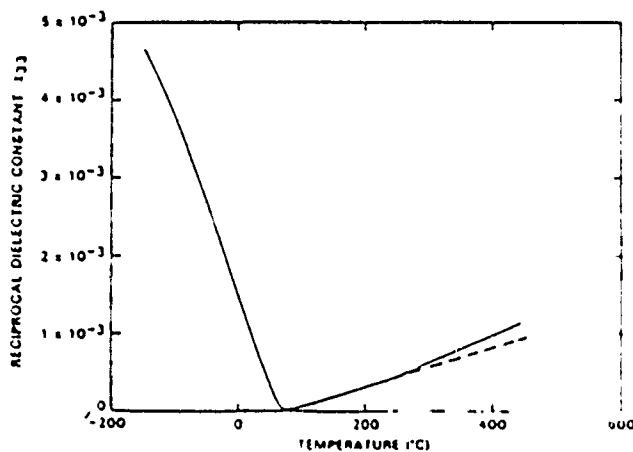
FIG. 5. The polar-axis reciprocal dielectric constant at 10 kHz for poled SBN-60.
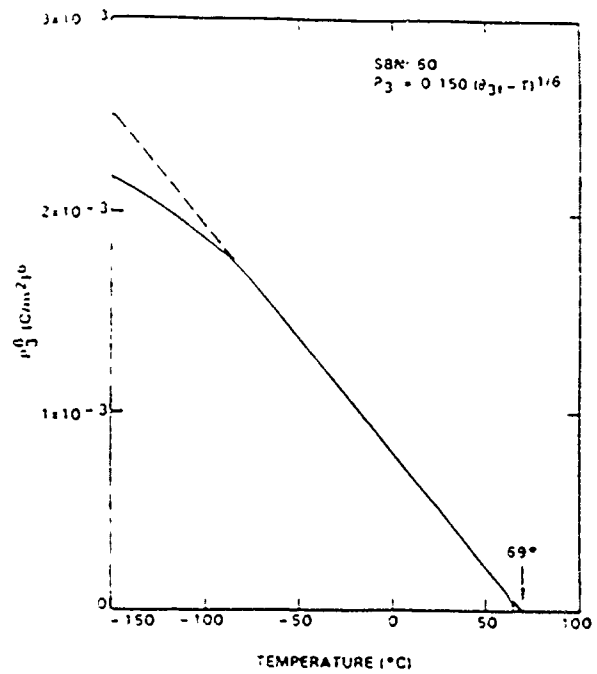
FIG. 6 Plot of the sixth power of $P_3$ vs temperature, showing a wide linear region below the zero intercept at 69 °C.

Comparing this with the dielectric stiffness expression in Eq. (8), Eq. (15) reduces to

$$p = -\frac{dP_3}{dT} = \frac{\epsilon_{33}P_3}{C_3}. \tag{16}$$

Using the empirical relation for $\epsilon_{33}$ given in Eq. (12) for $T < \theta_{3f}$, Eq. (16) becomes

$$p = C_{3f}P_3/C_3(\theta_{3f} - T) = P_3/9.11(\theta_{3f} - T), \tag{17}$$

a relationship which is in vast disagreement with the observed behavior of Eq. (14). Note that Eqs. (16) and (17) are correct for any number of higher order Devonshire coefficients, as long as they remain independent of temperature. In the particular case of SBN:60, this assumption is clearly not valid.

The dielectric, pyroelectric, and polarization behaviors described here for SBN:60 have been consistently found in a large number of crystal samples, with relatively minor variations in the physical constants being found from one crystal growth to another. Effects due to sample geometry are also not significant; excellent agreement in the properties has been found for samples from 0.35 mm up to several mm in thickness, indicating that contact layer effects do not play an important role.

It is evident from the polar-axis behavior of SBN:60 that the phenomenology for the Gibbs free energy must be taken out to at least the eighth power of $P$ (sixth power in dielectric stiffness) with temperature-dependent higher order coefficients. Ironically, a reasonable sixth-order least-squares fit to the dielectric data can still be achieved over a moderate temperature range using temperature-independent coefficients.[18] However, the pyroelectric data clearly show that the relationship between $p$ and $P_3$ [Eq. (14)] is *independent*

of the Curie–Weiss coefficient $C$ in violation of the phenomenology for temperature independent higher order coefficients [Eqs. (16) and (17)]. This situation is not unique to undoped SBN·60, we have found equivalent behavior in other SBN compositions (e.g., SBN·50) doped crystals (e.g., La[?]) and more importantly for other ferroelectric bronzes including compositions in the BSKNN system.[?]

The measured temperature dependencies of the spontaneous polarization and the polar-axis dielectric stiffness are highly suggestive of higher order thermodynamic coefficients of the form

$$\alpha_{11} = \alpha_{11}^0 (\theta_{1f} - T)^{2/3},$$
$$\alpha_{111} = \alpha_{111}^0 (\theta_{1f} - T)^{1/3},$$
$$\alpha_{1111} = \alpha_{1111}^0.$$

which qualitatively at least, will then satisfy the observed temperature dependence of $\epsilon_{33}$. The measured relationship between $p$ and $P_3$ [Eq. (14)] will also be satisfied, but unfortunately without yielding any information about the magnitudes of $\alpha_{33}^0$, etc. However, the postulated temperature dependencies may be unnecessarily strict since the dielectric stiffness and electric field relations involve the sum and difference of at least four (potentially large) terms in the ferroelectric phase. Hence, an additional experimental method is needed to determine the thermodynamic coefficients in an unequivocal manner.

## 8. The linear electro–dielectric effect in SBN:60

The extension of the LGD phenomenology out to the eighth power of $P_3$ in the Gibbs free-energy expansion necessarily leads to an underdetermined set of equations based on the physically measurable parameters $E_3$ and $\epsilon_{33}$, so that no unique values for the higher order coefficients can be established. One solution to this problem is to examine the behavior of the dielectric constant at several different applied fields, this will lead, for example, to upward shifts of the phase transition temperature for applied fields of the same polarity as the poling field.[17] This technique has been used by many authors to investigate ferroelectric materials, including the excellent work by Glass[1] on SBN compositions and the work by Burns et al.[32] to determine the values of the sixth-order Devonshire coefficients for La-modified $Sr_2KNb_5O_{15}$ crystals. Unfortunately, this type of analysis is necessarily limited to a small temperature range near $T_c$, and is further complicated by finite distributions of transition temperatures in materials such as SBN.

An alternative technique is to examine small changes in the dielectric constant with changes in the applied field at fixed temperatures, this method was successfully used by Drougard, Landauer, and Young[20] to establish the strong temperature dependence of the fourth power coefficient in $BaTiO_3$ using a dynamic low-frequency biasing technique above $T_c$. This method may also be applied below $T_c$ as long as instrument sensitivity and accuracy are sufficient to measure $\Delta\epsilon_{33}$. In the particular case of the eighth-order phenomenology presented here, the change in the dielectric stiffness with applied electric field along the $c$ axis may be calculated from Eq. (8):

$$\frac{\partial\gamma_{33}}{\partial E_3} = (24\alpha_{33}P_3 - 120\alpha_{333}P_3^3 - 336\alpha_{3333}P_3^5)\frac{\partial P_3}{\partial E_3} \tag{18}$$

For small changes in $E_3$, $\partial P_3/\partial E_3 = \epsilon_0\epsilon_{33}$, so that Eq. (18) may be written as

$$\frac{\partial\gamma_{33}}{\partial E_3} = \frac{\epsilon_0\epsilon_{33}}{P_3}(24\alpha_{33}P_3^2 - 120\alpha_{333}P_3^4 - 336\alpha_{3333}P_3^6) \tag{19}$$

This equation, combined with the relations for the electric field [Eq. (6)] and dielectric stiffness [Eq. (18)], completes the set of equations necessary to determine the higher order coefficients. Under the constraint of small linear changes of $\chi_{33}$ with applied field, the solutions are

$$\alpha_{33} = \frac{1}{32\epsilon_{33}P_3^2}\left(\frac{P_3}{\epsilon_0}\frac{\partial\chi_{33}}{\partial E_3} + 24\epsilon_{33}\frac{(\theta_3 - T)}{C_3} - 11\right),$$
$$\alpha_{333} = \frac{-1}{24\epsilon_{33}P_3^4}\left(\frac{P_3}{\epsilon_0}\frac{\partial\chi_{33}}{\partial E_3} + 12\epsilon_{33}\frac{(\theta_3 - T)}{C_3} - 9\right),$$
$$\alpha_{3333} = \frac{1}{64\epsilon_{33}P_3^6}\left(\frac{P_3}{\epsilon_0}\frac{\partial\chi_{33}}{\partial E_3} + 8\epsilon_{33}\frac{(\theta_3 - T)}{C_3} - 7\right) \tag{20}$$

To this point, we have made no assumptions regarding any specific temperature dependencies, except for the paraelectric dielectric stiffness, $(T - \theta_3)/C_3$. In the particular case of SBN·60, we may substitute for the temperature dependence of $P_3$ and $\epsilon_{33}$, and with the approximation $\theta \cong \theta_3 \cong \theta_{1f}$, the expressions in Eq. (20) become

$$\alpha_{3333} \cong \frac{1}{64C_{3f}/P_{10}}\left(\frac{P_3}{\epsilon_0}\frac{\partial\chi_{33}}{\partial E_3} + \frac{8C_{3f}}{C_3} - 7\right), \text{ etc.,}$$

where $C_{3f}$ and $P_{30}$ are as defined earlier. Hence, if $\partial\chi_{33}/\partial E_3$ varies with temperature as $P_3^{-1}$, $\alpha_{3333}$ is a constant. Similarly, $\alpha_{33}$ and $\alpha_{333}$ will vary, respectively, with temperature as $(\theta - T)^{2/3}$ and $(\theta - T)^{1/3}$, as suggested earlier. However, note that the higher order coefficients need not follow any specific simple functions of temperature, but need only satisfy the general expressions given in Eq. (20).

The linear electro–dielectric effect, $\partial\chi/\partial E$, is the low-frequency analog of the linear electro-optic effect in ferroelectric crystals, and it is a particularly powerful test for the validity of truncated free-energy power expansions. For example, rearrangement of the third expression in Eq. (20) gives

$$\frac{\partial\gamma_{33}}{\partial E_3} = \frac{\epsilon_0}{P_3}\left(64\epsilon_{33}\alpha_{3333}P_3^6 - 8\epsilon_{33}\frac{(\theta_3 - T)}{C_3} + 7\right). \tag{21}$$

so that by setting $\alpha_{3333} = 0$, the electro-dielectric response for a sixth-order Gibbs free-energy expansion may be calculated. In the particular case of SBN·60 at 20 °C, with $\epsilon_{33} = 920$ and $P_3 = 0.285$ C/m$^2$, the calculated sixth-order response is $190 \times 10^{-12}$ m/V. The measured value, constant for linear dielectric changes of up to several percent, is $118 \times 10^{-12}$ m/V, more than twice the calculated sixth-order value. This discrepancy cannot be accounted for by adiabatic or contrapiezoelectric corrections since these amount to, at most, a 3%–4% correction to the calculated value. This particular result is what finally confirmed our recent

suspicions that a sixth-order LGD phenomenology was inadequate to characterize SBN compositions, and perhaps the tungsten bronze crystal family in general.

A full series of electro-dielectric measurements were carried out from −140 C to $T_c$ on poled SBN 60 crystals from different growths. All measurements were made at fixed temperatures to insure equilibrium conditions. Although the response times for changes in applied field were short below 50 °C (on the order of the bridge-balancing time of ~1 s or less) these increased to tens of seconds near $T_c$, rendering methods such as low-frequency dynamic biasing to be of limited value. Nevertheless, the latter has appealing features and may be explored in future work. In the present work, all electro-dielectric measurements were performed using static electric fields of alternating polarity.

Representative electro-dielectric response data for SBN 60 are shown in Fig. 7. The higher order Devonshire coefficients were calculated from these data and from measured $\epsilon_{33}$ and $P_s$ values using Eq. (20), and are plotted on a log-log scale versus $(\theta_{3f} - T)$ in Fig. 3. These coefficients are well characterized by the postulated temperature dependencies, with

$$\alpha = -1.22 \times 10^{-8}(\theta_3 - T),$$

$$\alpha_3 = 1.54 \times 10^{-4}(\theta_{3f} - T)^{2.1} \quad (m^2/C)^2,$$

$$\alpha_{33} = -1.03 \times 10^{-2}(\theta_{3f} - T)^{1.3} \quad (m^2/C)^4,$$

$$\alpha_{333} = 2.20 \times 10^{-1} \quad (m^2/C)^6.$$

The solid curve in Fig. 7 is calculated from Eq. (21) using the value of $\alpha_{3333}$ given above.
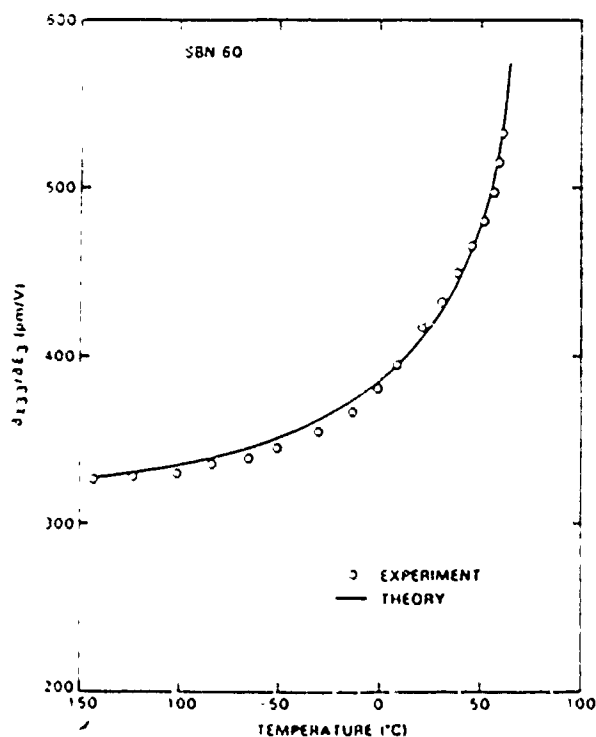


FIG. 7 The polar-axis linear electro-dielectric response of poled SBN 60. The solid line is the theoretical curve based on the derived phenomenological constant $\alpha_{3333}$.
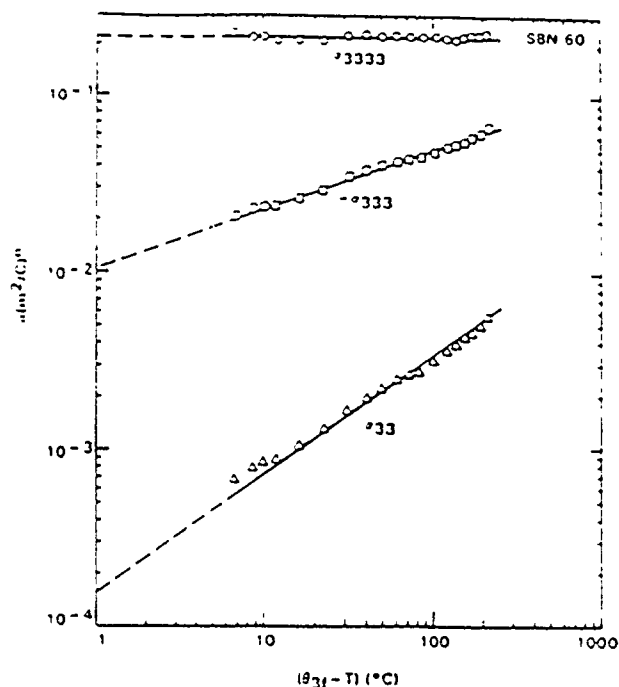


FIG. 8 Log-log plots of the higher order c-axis Devonshire coefficients vs $(\theta_{3f} - T)$. The coefficients follow a $(\theta_{3f} - T)^n$ temperature dependence, with $n = 0$, ½, and ¾

The electro-dielectric response was found to be independent of applied voltage, as expected, for dielectric changes up to 3%–4%; the maximum applied voltage was adjusted with temperature to maintain adequate sensitivity and linearity. However, close to $T_c$ no consistent data could be obtained due to long-term drifts. In spite of the long equilibration times necessary after temperature changes near $T_c$ (~1 h), the dielectric data were found to be highly reproducible on cooling, indicating that a fully poled, single ferroelectric domain condition can be maintained in SBN:60 even after long-term exposures to elevated temperatures near $T_c$.

Figure 9 shows the calculated crystal free energy, $\Delta G_1$, as a function of polarization. At room temperature, the depth of the potential well is only ~1 meV per unit cell, substantially below the thermal energy, $kT$, thus illustrating the cooperative coupling of microdomains necessary to maintain a uniform macrodomain state. The calculated free energy is absolutely stable over the entire temperature range; metastable states for $\Delta G = \Delta G_1 - E_3 P_3$ do exist for reverse polarity fields, but these are inaccessible since they lie at energies above those for the absolutely stable states. Calculated $P_3$ vs $E_3$ hysteresis loops for SBN:60 show a coercive switching field of approximately 20 kV/cm at room temperature, a factor of 8 larger than the ~2.5 kV/cm encountered experimentally. However, this result is not surprising since the phenomenological model does not attempt to account for the kinetics of microdomain reversal.[13,14]

The electro-dielectric character of SBN 60 crystals was also examined above the ferroelectric phase transition temperature. In this phase, $P_3$ is small or zero at zero bias, hence, using $P_3 = \Delta P_3 = \epsilon_0 \epsilon_{33} \Delta E$, in Eq. (8), and ignoring higher order terms.
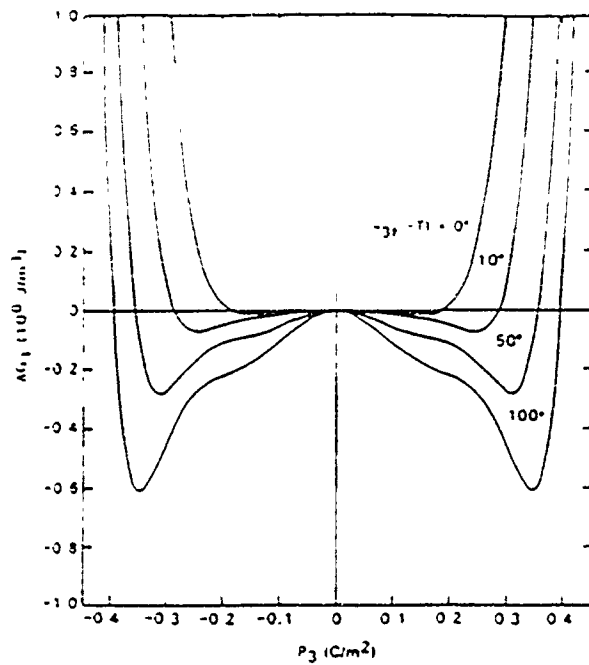
FIG. 9. Calculated curves for the Gibbs free energy of SBN 60 at four temperatures, showing absolute stability for the energy minima at $P_3 = \pm P_s$.



FIG. 10. The $a$-axis dielectric constant of SBN 60 at 10 kHz. Data at other frequencies are essentially identical. The dashed curve is calculated from the phenomenological model using temperature-independent higher order coefficients.

$$\Delta\chi_{33}/\Delta E_3 \cong 24\alpha_{33}\epsilon_0^2\epsilon_{33}^2\Delta E_3 \quad (T > T_c), \tag{22}$$

or

$$\Delta\epsilon_{33}/\epsilon_{33} \cong -24\alpha_{33}\epsilon_{33}^3 (\epsilon_0\Delta E_3)^2 \tag{23}$$

Therefore, $\Delta\epsilon_{33}/\epsilon_{33}$ is expected to vary quadratically with applied electric field and rapidly diminish above $T_c$ with the third power of $\epsilon_{33}$. This behavior was found in SBN:60, but some asymmetry with $\pm \Delta E_3$ was seen in poled crystals at temperatures as much as 40 °C above $T_c$. A more symmetric response was found after thermal depoling under shorted conditions, although measurements below 95 °C remained unreliable due to long-term drifts, presumably due to crystal repoling. From the measurements over the temperature range of 100–150 °C, the averaged value of $\alpha_{33}$ calculated from Eq. (23) is

$$\alpha_{33} \cong -1.4 \times 10^{-4}(m^2/C)^2 \quad (T > T_c),$$

a value opposite in sign to the $T < T_c$ value. Although it was difficult to establish any temperature dependence for $\alpha_{33}$ in the paraelectric phase, it seems reasonable to presume that $\alpha_{33}$ changes sign somewhere near $T_c$ with no abrupt discontinuities. Such a sign change may also occur for $\alpha_{333}$, but this could not be determined from these measurements.

## VI. NONPOLAR PROPERTIES

We now turn attention to the dielectric properties of SBN:60 along the nonpolar $a$ or $b$ axis. The weak-field dielectric stiffness at zero bias is given in Eq. (7a) and repeated here for convenience:

$$\chi_{11} = \chi_{22} = (T - \theta_1)/C_1 + 2\alpha_{11}P_3^2 + 2\alpha_{111}P_3^4$$

$$(P_1 = P_2 = 0). \tag{24}$$

A dielectric anomaly is therefore anticipated for polar directions as a result of the onset of the spontaneous polarization, $P_3$. A complicating factor in the measurement of the nonpolar dielectric properties is the large dielectric anisotropy of most tetragonal ferroelectric bronzes. Incomplete contact coverage or slight axial misalignment can cause erroneous results, particularly near $T_c$. However, we were able to obtain a nearly perfectly oriented crystal wafer (as evidenced by x-ray diffraction and conductivity measurements), and its dielectric behavior on an expanded scale in Fig. 10. Corresponding Arrhenius plots of the $a$-axis conductivity at 0.1, 1.0, and 10 kHz are plotted in Fig. 11, showing the virtual absence of major conductivity peaks near $T_c$.
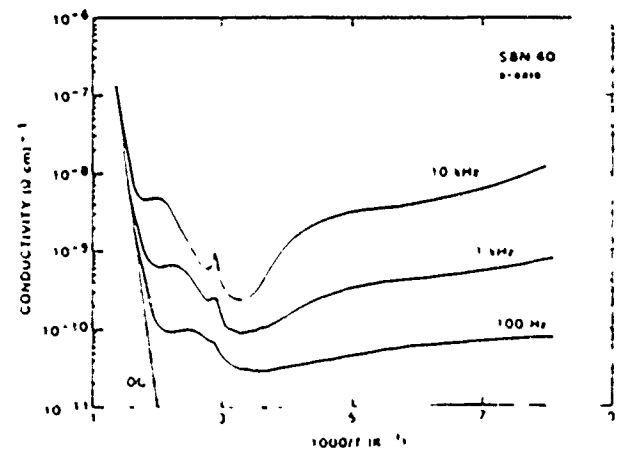


FIG. 11. Arrhenius plots of the $a$-axis conductivity for SBN (4) at dc, 100 Hz, 1 kHz, and 10 kHz, much of the 100-kHz conductivity was below instrument sensitivity. Note the virtual absence of a large conductivity peak at $T_c$.

The $a$-axis dielectric dispersion over 100 Hz–100 kHz was found to be minimal except at the temperature extremes where it increased to 2%–5%. Dielectric losses were similarly low, with $\tan \delta = 0.003$ or less over most of the temperature range, rising primarily above 300 °C due to the onset of significant dc conductivity. At room temperature, the dark dc conductivity was typically $5 \times 10^{-16}\ \Omega^{-1}\ cm^{-1}$ or less.

As expected, changes in $\epsilon_{11}$ with applied field were unmeasurable because of the small induced polarization $\Delta P_i = \epsilon_0 \epsilon_{11} \Delta E_i$, hence, the values of coefficients such as $\alpha_{11}$ and $\alpha_{111}$ in Eq. (7) ($P_i \neq 0$) could not be determined. This is of little consequence, since these coefficients do not contribute to the dielectric stiffness [Eq. (24)] or the Gibbs free energy [Eq. (2)] at zero bias ($P_1 = P_2 = 0$).

The dielectric stiffness expression in Eq. (24) could be fitted to the measured data under the assumption of temperature invariant $\alpha_{13}$ and $\alpha_{133}$. The calculated curve is shown as the dashed line in Fig. 10 based on the following constants:

$$C_1 = 2.04 \times 10^5,$$
$$\theta_1 = -245 \pm 20\ °C,$$
$$\alpha_{13} = 3.78 \times 10^{-3}\ (m^2/C)^2,$$
$$\alpha_{133} = 1.40 \times 10^{-2}\ (m^2/C)^3.$$

The calculated fit to the $a$-axis dielectric data is generally quite good (less than 3.5% error) except near $T_c$. Perhaps the most interesting discrepancy is the roughly 10 °C difference between the theoretical and measured dielectric maxima. The $a$-axis dielectric peak is also higher in temperature than the $c$-axis peak by 6–8 °C. The shift in temperature between the theoretical and experimental maxima of $\epsilon_{11}$ may be accounted for, at least in part, by fluctuations in $P_3$ such that $\langle P_3 \rangle \cong 0$, but $\langle P_3^2 \rangle \neq 0$, above $T_c$. This would also help to explain the small discrepancies in the theoretical and measured values for the paraelectric phase well above $T_c$.

## VII. DISCUSSION

The thermodynamic phenomenology developed for SBN:60 may be applied to the calculation of other important crystal properties such as the entropy, $S$, and the excess heat capacity. Using the crystal free-energy expression in Eq. (2) with $P_1 = P_2 = 0$ and the measured temperature dependencies of the coefficients, the entropy is given by

$$S = -\left(\frac{\partial \Delta G_1}{\partial T}\right)_{P_i}$$
$$= \frac{P_3^2}{\epsilon_0}\left(-\frac{1}{2C_3} + \frac{2}{3}\alpha_{33}^0(\theta_{3f} - T)^{-1/3}\right.$$
$$\left.\times P_3^2 + \frac{1}{3}\alpha_{333}^0(\theta_{3f} - T)^{-2/3}P_3^4\right) \quad (25)$$

Inserting the measured temperature dependence of $P_3$ into Eq. (25), we have

$$S = -0.14(\theta_{3f} - T)^{1/3}\ cal/mol\ °C, \quad (26)$$

and therefore the excess heat capacity due to nonzero polarization below $T_c$ is

$$c_\epsilon - c_P^0 = T\left(\frac{\partial S}{\partial T}\right)_\epsilon$$
$$= 0.047\ T(\theta_{3f} - T)^{-2/3}\ cal/mol\ °C. \quad (27)$$

The excess heat capacity is thus expected to peak sharply as the phase transition temperature is approached from below, in qualitative agreement with the experimental results by Glass[1] on early SBN crystals. However, very close to the transition, the calculated excess heat capacity represents a substantial fraction of the background lattice heat capacity of 30–40 cal/mol °C, whereas the measured values represent only a few percent of the total. Our own preliminary heat capacity results show similar behavior. However, this is not entirely unexpected since the phenomenological model does not account for a distribution of phase transition temperatures, but rather presents an average of the macroscopic crystal behavior for regions well above and below the transition region.

The Gibbs free-energy function for SBN:60 possesses continuous first derivatives with respect to $P,T$ and discontinuous second derivatives, making SBN:60 a second-order phase transition ferroelectric. However, it is interesting to note that the temperature behavior of the heat capacity is of the form expected for a classic first-order transition,[19] this being due to the strong temperature dependencies of the higher order Devonshire coefficients. Since these coefficients tend to zero as $T \to \theta$, the phenomenology suggests that the transition from macropolar to macrononpolar is tetracritical in SBN:60.

The highly regular temperature dependencies of the major physical properties for SBN:60 permit the straightforward evaluation of several parameters relevant to device applications. For example, the commonly accepted figure of merit for longitudinal pyroelectric infrared (IR) detectors is $p/\epsilon_{33}$. Using Eqs. (12) and (14),

$$p/\epsilon_{33} = P_{30}(\theta_{3f} - T)^{1/6}/6C_{3f}, \quad (28)$$

indicating that this figure of merit varies only weakly with the separation between the operating temperature, $T$, and the transition temperature. Equation (28) is also valid for other SBN compositions (e.g., SBN.50, SBN.75), with differences principally occurring in the value of $\theta_{3f}$ and, to a lesser extent, $P_{30}$.

Another parameter of interest for optical applications is the linear electro-optic coefficient, $r_{ij}$. The linear electro-optic effect in bronze ferroelectrics may be considered a prototypic quadratic effect biased by the nonzero spontaneous polarization in the ferroelectric phase.[35] Hence, along the polar $c$ axis,

$$r_{33} = 2g_{33}P_3\epsilon_0\epsilon_{33} = 2g_{33}P_{30}\epsilon_0 C_{3f}/(\theta_{3f} - T)^{5/6}, \quad (29)$$

where $g_{33}$ is the quadratic electro-optic coefficient. Measurements of $g_{33}$ on SBN crystals[36] have shown this to be essentially independent of temperature, with a value of ~0.10 $m^4/C^2$, so that at room temperature the calculated linear coefficient for SBN:60 is $r_{33} = 464 \times 10^{-12}$ m/V. This value is in excellent agreement with room-temperature measurements at optical wavelengths,[8,12,14] although data at other temperatures are presently lacking. However, considerable data for the temperature dependence of $r_{11}$ have been ob-

...ained for SBN·60 at millimeter-wave frequencies — 94 GHz].[] At room temperature the equivalent $r$ value is 1600-1700 × 10⁻¹² m/V with the spread in value due partly to complications arising from moderate dielectric losses. At 77 K, where the dielectric losses are considerably lower $r_{33} = 725 \times 10^{-12}$ m/V in general agreement with the temperature dependence predicted in Eq. (29). These large values indicate that $g_{33}$ is substantially higher at millimeter-wave frequencies, with a computed value of approximately 0.60 m⁴/C².

The linear electro-optic effect at optical and millimeter-wave frequencies is the high-frequency equivalent of the low-frequency linear electro-dielectric effect. However, it must be cautioned that although the room-temperature value for $r_{33}$ at optical frequencies is similar to the electro-dielectric value ($418 \times 10^{-12}$ m/V), their functional origins are vastly different. This is reflected in the temperature dependencies, with the linear electro-dielectric effect in SBN·60 following a $(\theta_{3f} - T)^{-1/6}$ dependence, as may be deduced from Eq. (21), whereas $r_{33}$ follows a much stronger $(\theta_{3f} - T)^{-3.4}$ power law. Nevertheless, these two effects do share a common strong dependence on the value of the low-frequency dielectric constant, $\epsilon_{33}$.

In the derivation of the phenomenological constants for SBN:60, we have made use of the measured $c$-axis dielectric properties in the paraelectric phase to determine the Curie-Weiss constants $C_3$ and $\theta_3$, as discussed in Sec. V. These constants were determined from the linear inverse susceptibility region which exists above $T_c$ up to approximately 250 °C (Fig. 4). However, above 250 °C there exists a second linear Curie-Weiss region, with constants $C_3' = 2.8 \times 10^5$ and $\theta_3' = 134$ °C, the latter being substantially above the phase transition temperature. It has been postulated in the work by Burns and Dacol[38,39] on bronze $Sr_2KNb_5O_{15}$ (SKN), and more recently in their work with Bhalla et al.[40] on SBN, that observed deviations of the optical refractive index from a linear temperature dependence above $T_c$ may arise from fluctuations in the polarization such that $\langle P_3 \rangle = 0$, but $\langle P_3^2 \rangle \neq 0$, over a large temperature range. This would necessarily affect the low-frequency dielectric properties as well, and may account for the change in slope of $\chi_{33}$ in the paraelectric region below 250 °C.

This, then, raises the question regarding which values of $C_3$ and $\theta_3$ to use in the development of the $c$-axis phenomenology for the ferroelectric phase. However, evaluation of the ferroelectric phenomenology using the alternative constants from the high-temperature paraelectric region shows a rapid divergence of all of the higher order $c$-axis Devonshire coefficients near the phase transition, leading to metastable energy states and anomalous calculated hysteresis loops. This is in sharp contrast to the well-behaved, predictable temperature dependencies shown in Sec. V. This result, combined with the phenomenological similarities determined for other tungsten bronzes such as BSKNN,[41] leads us to conclude that the lower temperature Curie-Weiss region provides a more valid description of the macroscopic paraelectric behavior of SBN·60 as it applies to the temperature dependence of $\alpha_3$ in the ferroelectric phase.

The presence of fluctuating polar microdomains in the paraelectric phase below 300 °C would also serve to explain the deviation of $\epsilon_{11}$ from the extrapolated high-temperature Curie-Weiss behavior, as shown in Fig. 10. An average rms polarization, $P_d = \langle P^2 \rangle^{1/2}$, may be calculated from a least-squares fit of Eq. (24) to the measured $a$-axis paraelectric data using the temperature-independent values for $\alpha_{13}$ and $\alpha_{111}$ calculated earlier. Such a fit shows a substantial nonzero $P_d$ which declines nearly linearly with temperature up to ~250-300 °C, in qualitative agreement with the results from optical index measurements.[40] However, the calculated magnitude of $P_d$ critically depends upon the chosen values for the Curie-Weiss parameters $C_1$ and $\theta_1$ in Eq. (24), and hence cannot be determined with particular confidence. This uncertainty also exists to some extent in the interpretation of the refractive index data, as it also depends upon the chosen extrapolation of a linear high-temperature region.[38-40]

While this analysis is adequate to qualitatively account for the deviation of $\epsilon_{11}$ from Curie-Weiss behavior in the paraelectric phase, the situation is more complicated along the $c$ axis. In this direction, any spatially fluctuating (and possibly dynamically inverting) polar microdomains would be perturbed by an ac measurement field, $E_3$, and thus would significantly contribute to the macroscopic dielectric polarizability.[40] At the lowest order this would qualitatively lead to an apparent change in the Curie-Weiss behavior of $\alpha_3$ [Eqs. (6) and (8)], with the higher order terms contributing to the measured dielectric behavior by a considerably smaller amount. By inference from the discussion of ferroelectric stability given above, this contribution from fluctuating microdomains would necessarily extrapolate well into the ferroelectric region below $T_c$. Further support for this hypothesis is provided by millimeter-wave measurements, which show anomalous $c$-axis dielectric losses at room temperature which diminish on further cooling to 77 K.[7,37]

## VIII. CONCLUSIONS

The experimental data for ferroelectric SBN 60 show that for a more realistic fitting of the data, the Taylor series expansion of the Gibbs free energy must be taken out to at least the eighth power of the polarization, and that the coefficients of terms up to the sixth power must be taken as functions of temperature. This phenomenological description should provide a foundation for future comparisons with other compositions in the bronze crystal family, and may also assist in uncovering potentially anomalous ferroelectric behavior in materials which otherwise may appear to have well-behaved dielectric and polarization properties. It is noteworthy, however, that a more classical sixth-order phenomenology with temperature invariant higher order coefficients still provides a useful, approximate description for many of the measured properties,[16] and has proven particularly effective for comparisons with other crystal families.[36]

The extended eighth-order phenomenology is that of a simple proper crystalline ferroelectric. The highly regular behavior of the phenomenology suggests that this description is perfectly adequate to account for the observed ferroelectric properties in SBN·60. However, there has been some suggestion that SBN may be an incommensurate phase tran-

sition ferroelectric.[4] Although the present phenomenology does not preclude such a possibility, neither does it suggest it since the computed energy states remain absolutely stable over the entire temperature range. In either case, the phenomenology should prove useful in developing a much clearer theoretical description for the ferroelectric behavior in SBN crystals, and perhaps for other bronze crystal systems as well.

## ACKNOWLEDGMENTS

[1] A. M. Glass, J. Appl. Phys. 40, 4699 (1969).

[2] R. R. Neurgaonkar, M. H. Kalisher, T. C. Lim, E. J. Staples, and K. L. Keester, Mater. Res. Bull. 15, 1235 (1980).

[3] R. R. Neurgaonkar, DARPA Final Report, Contract No. F49620-78-C-0093 (1982) (unpublished).

[4] G. Burns, IEEE Trans. Electron Devices ED-16, 506 (1969). Includes an extensive bibliography of early tungsten bronze papers.

[5] Y. Tada, T. Mizutani, Y. Aoki, K. Muto, and K. Awazu, Jpn. J. Appl. Phys. 21, 1622 (19   ).

[6] R. R. Neurgaonkar, W. K. Cory, and J. R. Oliver, Ferroelectrics 51, 3 (1983).

[7] W. F. Hall, W. W. Ho, R. R. Neurgaonkar, and W. K. Cory, in Proceedings of the 6th IEEE International Symposium on Applications of Ferroelectrics (ISAF), edited by V. Wood (IEEE, New York, 1986), p. 469.

[8] R. R. Neurgaonkar, J. R. Oliver, W. K. Cory, and L. E. Cross, in Advances in Materials for Active Optics, edited by S. Musikant (SPIE, Bellingham, WA, 1985), Vol. 567, p. 44.

[9] S. Fischer, M. Ingold, A. Goomb, J. O. White, A. Yariv, and R. R. Neurgaonkar, Appl. Phys. Lett. 40, 863 (1982).

[10] G. Salamo, M. J. Miller, W. W. Clark III, G. L. Wood, and E. J. Sharp, Opt. Commun.      (1986).

[11] E. J. Sharp, M. J. Miller, G. L. Wood, W. W. Clark III, G. J. Salamo, and R. R. Neurgaonkar, in Proceedings of the 6th IEEE International Symposium on Applications of Ferroelectrics (ISAF), edited by V. Wood (IEEE, New York, 1986), p. 51.

[12] R. R. Neurgaonkar and W. K. Cory, J. Opt. Soc. Am. B 3, 274 (1986).

Includes an extensive bibliography of early and more recent papers on tungsten bronze ferroelectrics.

[13] G. Rakuljic, A. Yariv, and R. R. Neurgaonkar, Opt. Eng. 25, 1212 (1986).

[14] R. R. Neurgaonkar, W. K. Cory, J. R. Oliver, M. D. Ewbank, and W. F. Hall, Opt. Eng. 26, 392 (1987).

[15] Y. Megumi, N. Nagatsuma, K. Kashiwada, and Y. Furunata, Mater. Sci. 11, 1583 (1976).

[16] T. R. Shrout, L. E. Cross, P. Moses, H. A. McKinstry, and R. R. Neurgaonkar, in Proceedings of the IEEE 1980 Ultrasonics Symposium (IEEE, New York, 1980), p. 414.

[17] A. F. Devonshire, Adv. Phys. 3, 35 (1954).

[18] See, for example, J. F. Nye, Physical Properties of Crystals (Clarendon, Oxford, 1969).

[19] M. E. Lines and A. M. Glass, Principals and Applications of Ferroelectrics and Related Materials (Clarendon, Oxford, 1977).

[20] M. E. Drougard, R. Landauer, and D. R. Young, Phys. Rev. 98, 1010 (1955).

[21] M. H. Francombe, Acta Cryst. 13, 131 (1960).

[22] P. B. Jamieson, S. C. Abrahams, and J. L. Bernstein, J. Chem. Phys. 48, 5048 (1968).

[23] L. A. Shuvalov, Proc. Second Int'l Meeting on Ferroelectricity, J. Phys. Soc. Jpn. 28, (Suppl.), 38 (1970).

[24] A. A. Ballman and H. Brown, J. Cryst. Growth 1, 311 (1967).

[25] R. B. Maciolek and S. T. Liu, J. Electron. Mater. 2, 191 (1973).

[26] F. J. Morin, J. R. Oliver, and R. M. Housley, Phys. Rev. B 6, 4434 (1977).

[27] R. Clarke and J. C. Burfoot, J. Phys. D 8, 1115 (1975).

[28] I. Camlibel, J. Appl. Phys. 40, 1690 (1969).

[29] T. W. Cline and L. E. Cross, J. Appl. Phys. 49, 4298 (1978).

[30] G. Borchardt, J. v. Cieminski, and G. Schmidt, Phys. Status Solidi A 76, K141 (1983).

[31] A. S. Bhalla and L. E. Cross, Ferroelectrics 38, 935 (1981).

[32] G. Burns, D. F. O'Kane, E. A. Giess, and B. A. Scott, Solid State Commun. 6, 223 (1968).

[33] M. Hayashi, J. Phys. Soc. Jpn. 33, 616 (1972).

[34] L. Godefroy, Ferroelectrics 35, 207 (1981).

[35] M. DiDomenico and S. H. Wemple, J. Appl. Phys. 40, 720 (1969).

[36] R. R. Neurgaonkar and L. E. Cross, DARPA Semi-Annual Technical Reports No. 1 (1983) and No. 5 (1985), Contract No. N00014-82-C-2466 (unpublished).

[37] R. R. Neurgaonkar, J. R. Oliver, L. E. Cross, and W. F. Hall, ONR Annual Report No. 5, Contract No. N00014-81-C-0463 (1985) (unpublished).

[38] G. Burns, Phys. Rev. B 13, 215 (1976).

[39] G. Burns and F. H. Dacol, Phys. Rev. B 30, 4012 (1984).

[40] A. S. Bhalla, R. Guo, L. E. Cross, G. Burns, F. H. Dacol, and R. R. Neurgaonkar, Phys. Rev. B 36, 2030 (1987).

[41] J. R. Oliver, R. R. Neurgaonkar, and L. E. Cross (unpublished).

[42] J. Schneck, J. C. Toledano, R. Whatmore, and F. W. Ainger, Ferroelectrics 36, 327 (1981).

APPENDIX 33

# Composition and Temperature Dependence of the Dielectric, Piezoelectric and Elastic Properties of Pure PZT Ceramics

Z. Q. ZHUANG, MICHAEL J. HAUN, SEI-JOO JANG, AND LESLIE E. CROSS, FELLOW IEEE

*Abstract*—Pure (undoped) piezoelectric lead zirconate titanate (PZT) ceramic samples at compositions across the ferroelectric region of the phase diagram have been prepared from sol-gel derived fine powders. Excess lead oxide was included in the PZT powders to obtain dense (95-96 percent of theoretical density) ceramics with large grain size ( > 7 μm), and to control the lead stoichiometry. The dielectric, piezoelectric, and elastic properties were measured from 4.2-300° K. At very low temperatures, the extrinsic domain wall and thermal defect motions "freeze out." The low temperature dielectric data will be used to determine coefficients in a phenomenological theory. The extrinsic contribution to the properties can then be separated from the single domain properties derived from the theory.

## I. INTRODUCTION

PIEZOELECTRIC lead zirconate titanate (PZT) ceramics have been used in a wide range of applications since the 1950's [1]. However, the growth of good quality single crystals of PZT for compositions across the entire phase diagram has not been accomplished. Clarke and Whatmore [2] have described the previous attempts at growing single crystals of $PbZr_xTi_{1-x}O_3$, and have found that crystals of reasonable quality can be grown within the ranges $1 > x > 0.84$ and $0.25 > x > 0$, but were unsuccessful for values of $x$ between these two ranges.

Due to the lack of PZT single-crystal data, the development of a phenomenological theory of PZT has been complicated and involved indirect methods of determining the coefficients of an energy function [3]-[5]. Additional experimental data is needed to separate the sixth order dielectric stiffness coefficients [5]. Dielectric constant measurements on ceramic samples at low temperatures, where the extrinsic domain wall and thermal defect motions "freeze out" [6], [7], may provide this data.

Pure homogeneous PZT ceramic samples at compositions across the phase diagram have been prepared from sol-gel derived fine powders. The low-temperature dielectric, piezoelectric, and elastic properties were measured from 4.2-300 K. The procedure used to prepare the sol-gel powders and ceramic samples, along with the low

temperature measurement apparatus, will be described in the next section. The results of the measurements will then be discussed.

## II. EXPERIMENTAL PROCEDURE

A sol-gel method similar to the procedure described in [8] was used to prepare PZT compositions with four to eight mole percent excess lead oxide, depending on the composition. The starting chemicals were lead acetate $[Pb(C_2H_3O_2)_2 \cdot 3H_2O]$, titanium isopropoxide $[Ti(OC_3H_7)_4]$, and zirconium $n$-propoxide $[Zr(OC_3H_7)_4]$.

The lead acetate was dissolved in methoxyethanol $(C_3H_8O_2)$ in a three neck reaction flask. To remove the adsorbed water, a reflux condenser was connected to the reaction flask, and the solution was heated until the temperature reached 125°C (the boiling point of methoxyethanol). After cooling the solution to 75°C, the titanium isopropoxide and zirconium $n$-propoxide were added, and again heated to 125°C to drive off excess methoxyethanol.

The solution was cooled to −25°C with a liquid nitrogen isopropanol bath. The water for hydrolysis (4 moles $H_2O$ per mole alkoxide) was first mixed with an equal amount of methoxyethanol, and then added to the cooled solution. By slowly heating the flask up to room temperature (or higher depending on composition), the solution gelled. The gel was then heated in a 100°C oven for one to two days until dry.

The dried gels were calcined at 800°C for one hour. The calcined powders were then ground, and pressed into pellets without binder under a pressure of 50 000 psi. The green pellets, with four to eight mole percent excess lead oxide, were sintered on platinum sheets in a set of alumina crucibles with a lead source powder. The samples were sintered from 1000°C to 1260°C for 20-60 h depending on the composition. The sintered ceramic samples had densities of 95 to 96 percent of theoretical density, and average grain sizes larger than 7 μm.

X-ray diffraction patterns of the calcined powders showed that both perovskite PZT and lead oxide were present. However, after sintering, no lead oxide diffraction peaks could be detected, indicating that the excess lead oxide was volatilized during sintering.

The ceramic samples were sputtered with gold electrodes, and poled with electric fields of 20-40 KV/cm

for 4–30 min. The piezoelectric strain coefficient $d_{33}$ was then measured using a Berlincourt Piezo-$d_{33}$ meter to determine the completeness of poling. The poled discs were cut into bars, cylinders. and discs according to the IRE Standards [9].

The apparatus used for the low temperature measurements was composed of an Air Products and Chemicals model LT-3-110 cyrogenics system, which can stabily control the temperature from 4.2° K to 300° K. The dielectric and resonance properties were measured on a Hewlett Packard 4270 A automatic digital capacitance bridge and 3585A Spectrum analyzer. The samples with thermal-resistance wire attached as leads, were shielded in a copper enclosure. The samples were first cooled down to 4 2° K, and then the measurements were made during heating to 300° K. The IRE standard method [9] for piezoelectric resonance measurements was used for the calculations.

## III. RESULTS AND DISCUSSION

The dielectric constant measured at room temperature and 1-kHZ was plotted versus composition for poled (measured parallel to the poling direction) and unpoled ceramic samples in Fig. 1. The peak in the dielectric constant occurs close to the morphotropic phase boundary between the tetragonal and rhombohedral phases at a composition of approximately $Pb(Zr_{0.52}Ti_{0.48})O_3$. By poling the samples the dielectric constant increased and decreased for the tetragonal and rhombohedral compositions, respectively.

The increase of the dielectric constant when poling the tetragonal samples was previously explained [10] as being due to the elimination of the effect of compression of the 180-degree domains. This occurs due to the virtually complete 180-degree domain reorientation along the poling direction, and dominates the decrease in dielectric constant from 90-degree domain reorientation.

For the rhombohedral compositions, the dielectric constant decreases when poling the samples. This net decrease occurs, because the decrease of the dielectric constant due to the 71 (109) degrees domain reorientation dominates the effect of the removal of compression [10].

The dielectric constant and dissipation factor for several PZT compositions measured at 1-kHZ are plotted versus temperature in Fig. 2. The dielectric constants of the compositions close to the morphotropic boundary showed a much stronger temperature dependence than the compositions away from the boundary.

Broad peaks in the dissipation factor versus temperature were found to occur at 225–250° K for the rhombohedral compositions and at 100–150° K for the tetragonal compositions. The different activation energies for domain wall motion in the tetragonal and rhombohedral samples would possibly account for these loss peaks, and is presently under further investigation. The PZT 52/48 composition, which showed coexistence of both tetragonal and rhombohedral phases, had loss peaks in both temperature ranges.
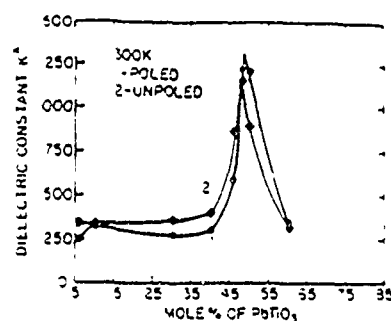


Fig. 1 Dielectric constant for poled and unpoled ceramic samples at room-temperature plotted versus composition
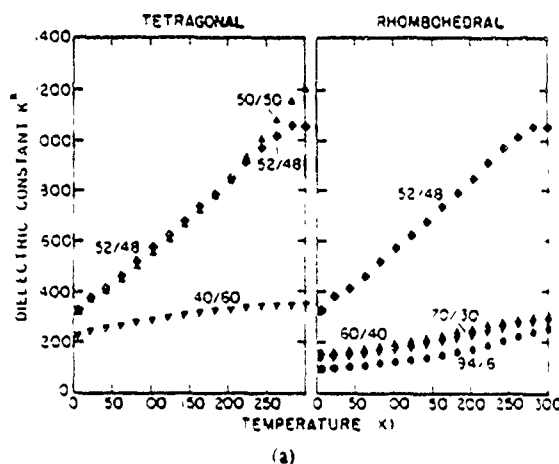


(a)
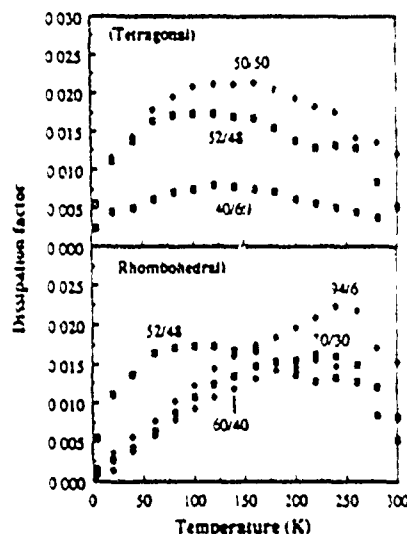


(b)

Fig. 2. PZT composition plotted versus temperature. a) Dielectric constant. (b) Dissipation factor.

Fig. 3 shows the temperature dependence of the coupling factors $k_{31}$ and $k_{33}$, piezoelectric strain coefficients $d_{31}$ and $d_{33}$, elastic compliance coefficient $s_{11}^E$, and frequently constant $N_b$. The compositions close to the morphotropic boundary again showed the largest temperature dependence.

The compositional dependence of the elastic compliance coefficient $s_{11}^E$, the frequency constant $N_b$, Poisson's ratio $\gamma$, and mechanical quality factor $Q_m$ at 4 2 and 300 K are shown in Fig. 4. The effect of the morphotropic
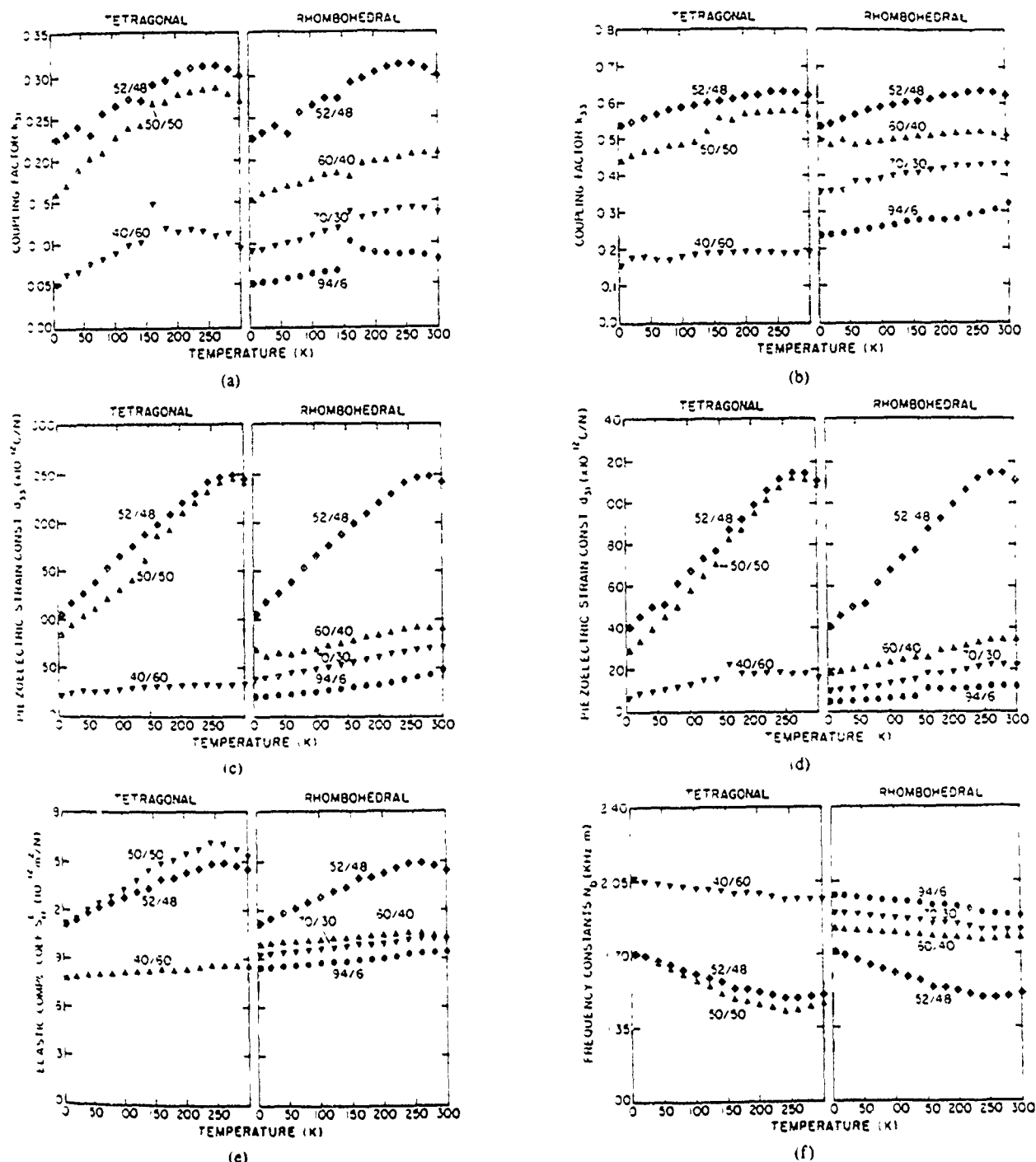
Fig 3 PZT composition plotted versus temperature. (a) Coupling factor $k_{31}$ (b) Coupling factor $k_{33}$ (c) PZT strain coefficient $d_{31}$ (d) PZT strain coefficient $d_{33}$ (e) Elastic compliance coefficient $s_{11}^E$ (f) Frequency constant $N_b$

boundary between the tetragonal and rhombohedral phases can be seen in this figure, along with the effect of the morphotropic boundary between the ferroelectric rhombohedral and antiferroelectric orthorhombic phases near the PZT 94/6 composition.

## IV CONCLUSION

A sol-gel method was used to prepare pure PZT powders across the ferroelectric region of the phase diagram. Excess PbO was included in the powders to obtain dense (95 to 96 percent of theoretical density) ceramics with large grain size ($>7$ μm), and to control the lead stoichiometry during sintering.

The dielectric, piezoelectric, and elastic properties were measured from 4.2° K to 300° K. At very low temperatures the domain wall and thermal defect motions "freeze out." The compositions near the morphotropic phase boundary had the largest temperature dependence. Dielectric loss peaks were found to occur from 225° K to 250° K for the rhombohedral compositions, and from 100° K to 150° K for the tetragonal compositions.

APPENDIX 34

# Temperature Behavior of Dielectric and Piezoelectric Properties of Samarium-Doped Lead Titanate Ceramics

J. N. KIM, MICHAEL J. HAUN, SEI JOO JANG, LESLIE E. CROSS, FELLOW, IEEE, AND X. R. XUE

*Abstract*—The dielectric and electromechanical coupling properties of Sm- and Mn-doped PbTiO$_3$ ceramics were investigated from 4.2 to 300° K. The upper and lower limits of the ceramic dielectric and piezoelectric properties were calculated by averaging the single-domain constants that were determined from a phenomenological theory. Comparisons of the measured and calculated properties were then made. The measured dielectric permittivity $\epsilon_{33}^T$ and piezoelectric strain coefficient $d_{33}$ appear to be mainly due to the averaging of the intrinsic single-domain response. The large piezoelectric and electromechanical anisotropies present in modified PbTiO$_3$ ceramics also appears to be an intrinsic property of the material. The piezoelectric coefficient $d_{31}$, as well as the planar coupling coefficient $k_p$, were found to have very small values over two temperature regions, from 120 to 170° K and from 240 to 270° K.

## INTRODUCTION

MODIFIED PbTiO$_3$ ceramics that show large anisotropic piezoelectric coupling at room temperature were recently reported [1]–[4]. The temperature behavior of the piezoelectric properties of Sm- and Mn-doped PbTiO$_3$ were also investigated [5]. It is interesting as well as important to understand why these modified PbTiO$_3$ ceramics have such a large anisotropic electromechanical coupling property.

In this study, the dielectric properties, $\epsilon_{33}^T$ and tan $\delta$, and electromechanical coupling properties, $d_{31}$, $d_{33}$, $k_p$, and $k_t$, of 10 mole percent Sm- and 2 mole percent Mn-doped PbTiO$_3$ ceramics were investigated from 4.2 to 300° K. At low temperatures, the thermally activated contributions to the dielectric and coupling properties "freeze out." These contributions will be referred to as extrinsic contributions. The observed temperature behavior of the material properties, $\epsilon_{33}^T$, $d_{33}$ and $d_{31}$, were compared with predicted upper and lower limits of the ceramic properties [6] that were calculated by averaging the single-domain

single crystal constants determined from a phenomenological theory of PbTiO$_3$ [7]. These predicted properties will be referred to as the intrinsic contribution to the ceramic properties. The unusually small values of piezoelectric coefficient $d_{31}$ were also explained according to the recent results of Damjanovic *et al.* [9], [10].

## EXPERIMENTAL PROCEDURE

The composition investigated in this study was (Pb$_{0.85}$Sm$_{0.10}$)(Ti$_{0.98}$Mn$_{0.02}$)O$_3$. Reagent grade oxides, PbO, Sm$_2$O$_3$, TiO$_2$, and MnO were mixed and milled for six hours using zirconia balls, then dried and calcined in a closed alumina crucible at 900°C for 1 h. The calcined powder was pressed in a die at 5000 psi to form green disks. These disks were fired at 1200°C for 1 h in a closed crucible with a lead source. The final density of the ceramic samples was better than 95 percent of the theoretical value. Disks were cut to several different shapes and dimensions to measure the dielectric and electromechanical coupling coefficients. Reshaped samples were electroded with sputtered gold and poled in silicone oil with a field of 60 kV/cm applied for 5 min at 150°C. All of the samples satisfied the dimensional requirements of the IRE standards on piezoelectric crystals [8]. The samples were carefully connected with very fine silver wire and suspended in a vacuum in an in-house made holder on an Air Products and Chemicals Model LT-3-110 cryogenics system. The dielectric properties were measured on a Hewlett Packard automatic capacitance bridge model 4270A. The electromechanical coupling properties were investigated by the resonance method using a Hewlett Packard spectrum analyzer model 3585A. The planar and thickness resonance frequencies were approximately 262 and 295 kHz, respectively, due to the sample geometries.

## RESULTS AND DISCUSSION

Two samples with the same composition and fabricated by the same procedure were studied. The relative dielectric permittivity $\epsilon_{33}^T$ and dissipation factor tan $\delta$ were measured at 1 kHz from 4.2 to 300° K. These measurements are plotted in Fig. 1(a) and 1(b).

The dielectric permittivity of ceramic PbTiO$_3$ was calculated using series and parallel models in [6]. These calculations were adjusted by shifting the Curie temperature

Fig 1 (a) Relative dielectric permittivities $\epsilon_{33}^T$ Solid curves are calculation of upper and lower limits of intrinsic ceramic permittivity (b) Dissipation factor tan δ at 1 kHz plotted versus temperature Data points are experimental measurements
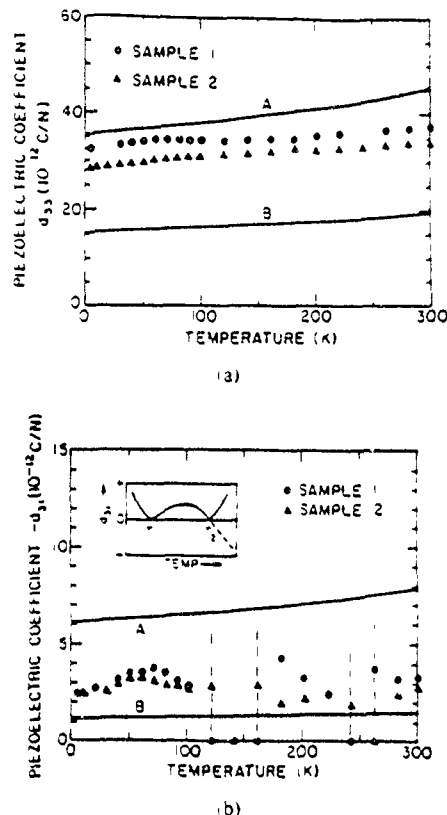


Fig 2 Piezoelectric strain coefficients (a) $d_{33}$ and (b) $d_{31}$ plotted versus temperature Data points are experimental measurements and solid curves are calculations of upper and lower limits of the intrinsic piezoelectric response Insert in (b) illustrates measured temperature dependence (solid curve) compared with results of Damjanovic, et al [9], [10] dashed curve)

$T_c$ to 300°C to match that of the samples fabricated in this study In Fig. 1(a), the experimental and theoretical permittivities are compared. At low temperatures where the extrinsic contributions, such as thermally activated domain wall and defect motions, have "frozen out," the agreement is fairly good As the temperature is increased, only a small difference develops between the experimental and theoretical permittivities, indicating that the polarizability is still largely due to the intrinsic averaging of the single-domain response.

The dielectric loss measurements are shown in Fig. 1(b) Below about 50° K the loss decreases very rapidly, which suggests that the thermally activated contributions to the dielectric properties freeze out quickly at low temperatures.

The measured piezoelectric coefficients, $d_{33}$ and $d_{31}$, are shown in Figs 2(a) and 2(b) along with the calculated upper and lower limits of the intrinsic ceramic piezoelectric coefficients These calculations were made by shifting the Curie temperature to 300°C, as was done with the dielectric data, using the results of [6]. The experimental $d_{33}$ data falls between the predicted upper and lower limits with a similar temperature dependence. This indicates that the measured $d_{33}$ is mostly due to the intrinsic single domain response.

The $d_{31}$ measurements also fall between the predicted upper lower limits, except over two temperature regions, from 120 to 170° K and from 240 to 270° K. Over these temperature regions, the resonance spectrum displaced

upon the HP 3585A analyzer was too weak to measure, as shown in Fig. 3, with the resonance at 300° K for comparison. This suggests that the IRE standard method may not be adequate near these two temperature regions.

The exceedingly small frequency differences between parallel ($f_p$) and series ($f_s$) resonances may not be close enough to the differences between the maximum ($f_n$) and minimum ($f_m$) impedance frequencies. The vector impedance method is more accurate in obtaining greater precision in the case of immeasurably small resonance regions like these.

Damjanovic et al. [9], [10] used this method to measure the complex values of the material constants ($d_{ij}^*$, $s_{ij}^*$, and $\epsilon_i^*$) They found that the real part of the $d_{31}$ coefficient changes sign and becomes positive at high temperatures. This result is illustrated in the insert in Fig. 2(b) by the dashed curve (note that the negative $d_{31}$ is plotted) The sign of $d_{31}$ could not be measured using the resonance method in this study, and therefore was not assumed to change sign at $T_2$ However, a change in sign would account for the immeasurably small resonance region at $T_2$ Damjanovic, et al. [10] also found that below $T_2$ the $d_{31}$ coefficient formed a peak (when plotting the negative $d_{31}$ as in Fig. 2(b), this would be a minimum with a value approaching zero) at about 125° K. This behavior probably accounts for the small resonance region at $T_1$.
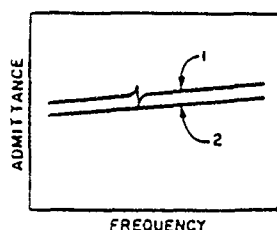
Fig 3 Admittance plotted versus frequency at 300° K (curve 1) and at temperature within temperature regions where resonance was too weak to measure (curve 2).

The change in sign of the $d_{31}$ coefficient at $T_2$ to positive values at high temperature was explained by Damjanovic et al. [10] as being due to the positive extrinsic contributions that dominate the negative intrinsic contribution. This appears to be possible, since the intrinsic $d_{31}$ is very small. In [6], the small values of the $d_{31}$ coefficient and thus large piezoelectric anisotropy ($d_{33}/d_{31}$) of PbTiO$_3$ ceramics were shown to be due to the intrinsic averaging of the single-crystal electrostrictive constants. The possibility of a change in sign of the intrinsic $d_{31}$ due to a slight variation in the single-crystal electrostrictive anisotropies ($Q_{11}/Q_{12}$ and $Q_{44}/Q_{12}$) was also demonstrated.

The planar coupling coefficient, $k_p$, is plotted as a function of temperature in Fig. 4(a). In two temperature regions, as discussed for $d_{31}$, $k_p$ becomes extremely small. The thickness coupling coefficient, $k_t$, is weakly dependent on temperature and has a value of about 46 percent. Fig. 4(b) shows the ratio $k_t/k_p$ plotted versus temperature. This ratio becomes very large in two temperature regions, 120 to 170° K and 240 to 270° K. These large electromechanical anisotropies indicate that this material would be useful in ultrasonic transducer applications.

## CONCLUSION

The relative dielectric permittivity, $\epsilon_{33}^T$, of the modified PbTiO$_3$ ceramics fabricated in this study appears to be largely due to the averaging of the intrinsic single-domain response. The calculated values of the upper and lower limits of the ceramic permittivity agree fairly well at low temperatures with the measured values, and only a small difference develops as the temperature increases. The piezoelectric $d_{33}$ and thickness coupling $k_t$ coefficients are weakly dependent on temperature and have values of about $30 \times 10^{-12}$ C/N and 46 percent, respectively. The planar coupling $k_p$ and piezoelectric $d_{31}$ coefficients exhibit very interesting temperature behaviors. In two temperature regions, from 120 to 170° K and from 240 to 270° K (or $T_1$ and $T_2$ in Fig. 2(b)), $|d_{31}|$ and $k_p$ become too small to measure using the resonance method.

Damjanovic et al. [9], [10] used a vector impedance method and found that the $d_{31}$ coefficient changes sign at $T_2$ to positive values at high temperatures. The low values of the $|d_{31}|$ at $T_1$ were found to be due to a minimum in the $|d_{31}|$ that occurs in this temperature region.

The values of the measured $d_{33}$ and $d_{31}$ coefficients were within the predicted upper and lower bounds that were calculated by averaging the intrinsic single-domain prop-
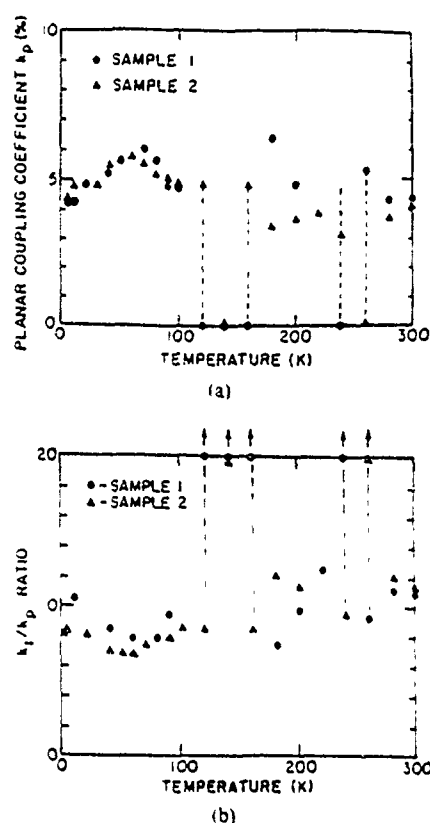


Fig 4 Planar coupling (a) coefficient $k_p$ and (b) ratio $k_t/k_p$ plotted versus temperature.

erties. The generally large piezoelectric and electromechanical anisotropies present in modified PbTiO$_3$ ceramics appear to be an intrinsic property of the material

## REFERENCES

[1] H Takeuchi, S. Jyomura, E. Yamamoto, and Y Ito, "Electromechanical properties of (Pb,Ln)(Ti,Mn)O$_3$ ceramics (Ln = rare earths)," J Acoust. Soc. Am., vol. 72, no. 4, pp. 114–120, 1982

[2] T Takahashi and Y Yamashita, "Anisotropic piezoelectric properties of modified Lead Titanate ceramics," Proc. Second U S. Japan Seminar on Dielectric and Piezoelectric Ceramics, Williamsburg, VA, vol. 1, 1984, pp. 20–25.

[3] H Takeuchi and S. Jyomura, "Piezoelectric ceramics with large electromechanical anisotropy," Proc. Second U S., Japan Seminar on Dielectric and Piezoelectric Ceramics, Williamsburg, VA, vol. 1, 1984, pp. 324–329

[4] H Takeuchi, S Jyomura, and C Nakaya, New piezoelectric materials for ultrasonic transducers, Jpn J Appl. Phys., vol. 24, suppl 24-2, pp. 35–40, 1985.

[5] X R Xue, J N Kim, S. J Jang, L. E. Cross, and R E. Newnham "Temperature behavior of dielectric and electromechanical coupling properties of samarium modified Lead Titanate ceramics, Jpn J Appl. Phys., vol 24, suppl. 24-2, pp. 718–720, 1985

[6] M J Haun, E. Furman, S. J Jang, and L. E. Cross, Modeling of the electrostrictive, dielectric and piezoelectric properties of ceramic PbTiO$_3$," IEEE Trans. Ultrason. Ferroelect. Freq. Contr, vol 36 no 4, pp. 393–401, July 1989

[7] M J Haun, E. Furman, S. J Jang, H. A. McKinstry, and L E Cross, 'Thermodynamic theory of PbTiO$_3$,' J Appl. Phys, vol 62, no 8, pp 3331–3338, 1987

[8] 'IRE standards on piezoelectric crystals: Measurements of piezoelectric ceramics, 1961, Proc. IRE, vol. 49, pp. 1161–1169, 1961

[9] D Damjanovic, T R Gururaja, S J Jang, and L. E Cross, "Temperature behavior of the complex piezoelectric $d_{31}$ coefficient in modified Lead Titanate ceramics," *Mater Lett.*, vol. 4, pp. 414–419, Sept. 1986.

[10] D Damjanovic, T R. Gururaja, S J Jang, and L. E. Cross, "Possible mechanisms for the electromechanical anisotropy in modified Lead Titanate ceramics," in *Proc IEEE Ultrason. Symp.*, Williamsburg, VA, Nov 1986 in press.

Sei Joo Jang received the B S degree in electrical engineering from Sogang University, Seoul, Korea, in 1973, the M.S. degree in physics from Boston College, Boston, MA, in 1976, and the Ph.D. degree in solid state science from the Pennsylvania State University, University Park, PA, in 1979

He was a member of the Technical Staff at AT&T Engineering Research Center, Princeton, NJ, from 1979 to 1983 Currently he is a Senior Research Associate with the Materials Research Laboratory at the Pennsylvania State University

Dr Jang is a member of the American Ceramic Society and the Optical Society of America.

J. N. Kim received the Ph.D degree in physics from the Pusan University, Pusan, Korea.

Leslie E. Cross (SM'79–F'84) was born on August 14, 1923 in Leeds, England. He received the B Sc. and Ph D degrees in physics from Leeds University, Leeds, England, in 1948 and 1952, respectively.

He is an Evan Pugh Professor of electrical engineering and Director of the Materials Research Laboratory at the Pennsylvania State University, University Park, PA. Prior to joining the Pennsylvania State University in 1961 he held positions with Leeds University as Lecturer (1948–1951) and as Research Associate (1954–1961). His research interests include ferroelectric materials and ferroic phenomena; dielectric, piezoelectric, and pyroelectric crystals, ceramics and composites; electronic ceramics and their applications, electrostriction and phase transitions.

Dr. Cross is a member of the National Academy of Engineering and a Fellow of the American Institute of Physics, the American Ceramic Society, and the American Optical Society.

Michael J. Haun was born on November 30, 1958 in Baltimore, MD He received the B.S degree in ceramic engineering from Clemson University, Clemson, SC, in 1980, the M.S. degree in ceramic science from the Pennsylvania State University, University Park, PA, in 1983, and currently is working towards the Ph.D degree in solid state science at the Pennsylvania State University

His research has involved the development of a phenomenological theory of perovskite ferroelectrics and antiferroelectrics accounting for oxygen octahedral tilting and critical behavior, lattice parameter determination using high temperature X-ray diffraction, sol-gel processing, low temperature sintering and dielectric property measurements of relaxor ferroelectrics for multilayer capacitors, and fabrication, evaluation, and theoretical modeling of piezoelectric composites for hydrophone applications.

Mr Haun is a member of the American Ceramic Society

W. R. Xue graduated from the Department of Silicate Engineering at Nanjing Institute of Chemical Technology in 1960. His research interests are in the area of the ferrites, ferroelectrics, and mechanical properties of oxides. He was a Visiting Scientist from 1982 to 1984 at the Materials Research Laboratory at Pennsylvania State University, University Park, PA He is currently an Associate Professor and leader of the Materials Science Group at the Nanjing Institute of Chemical Technology, People's Republic of China.

APPENDIX 35

# Sol–Gel Processing of Lead Titanate in 2-Methoxyethanol: Investigations into the Nature of the Prehydrolyzed Solutions

Thomas W. Dekleva,* James M. Hayes, Leslie E. Cross,* and Gregory L. Geoffroy

Materials Research Laboratory and Department of Chemistry, The Pennsylvania State University, University Park, Pennsylvania 16802

*A previously developed system for the sol–gel processing of lead titanate powders and films has been analyzed by a variety of spectroscopic, chromatographic, and wet-chemical means. The results indicate that refluxing $Pb(OAc)_2 \cdot 3H_2O$ in 2-methoxyethanol is accompanied by the volatilization of 0.5 equiv of organic acetate and results in solutions containing what is believed to be anhydrous basic lead acetate, $3Pb(OAc)_2 \cdot PbO$. This has been isolated as its monohydrate, which has been fully characterized by elemental (C, H, Pb), infrared, $^1H$ NMR, and XRD analyses. The anhydrous salt generated in situ reacts further with $Ti(OR)_4$ under reflux conditions to liberate more organic acetates. The final stoichiometries (one volatilized acetate per lead) tend to preclude the possibility that significant amounts of polymeric intermediates are generated. Analyses of the organic volatiles also indicate that, at least under our conditions, significant transalcoholysis of the precursor $Ti(OR)_4$ (R=Et, i-Pr, n-Pr) occurs (80% to 90% replacement). The conclusions and consequences of these and related observations are presented.*

SOL–GEL processing is one of several methods currently under investigation for the preparation of electronic and high-technology ceramic materials. Because of the intrinsic nature of the synthetic schemes available, this type of processing offers significant advantages such as higher purity, molecular homogeneity, reduced processing temperatures, and unique fabrication opportunities over conventional processing methods.[1,2]

The chemistry of the gelation step normally involves the controlled hydrolyses of single-component or multicomponent alkoxides to form a three-dimensional network of metal–oxygen linkages. Part of the versatility of this technique arises from the fact that the soluble inorganic salts can be incorporated into these networks, by either actual chemical reaction or simple entrapment in the gelled matrix. Several groups have recently taken advantage of the solvating ability of 2-methoxyethanol (2-MOE) to develop synthetic schemes for the preparations of a series of lead-containing perovskite materials in the lead lanthanum zirconate titanate system[3-8] using lead acetate, $Pb(OAc)_2 \cdot 3H_2O$, as the precursor.

Several points in these reports attracted our attention. For example, in the

lead titanate (PT) system, Gurkovich and Blum[4-6] reported that the reaction between $Pb(OAc)_2$ (which was dehydrated in situ by refluxing the hydrated salt in 2-MOE) and $Ti(O-i-Pr)_4$ in refluxing 2-MOE results in liberation of an unquantified amount of isopropyl acetate. On this basis, they proposed a condensation reaction between these components which, though not cited as such, was completely analogous to trans-esterification reactions involving bulky organic acetates,[9] for example

$$M(OR)_n + xCH_3COOR' \longrightarrow$$

$$M(OR)_{n-x}(OR')_x + xCH_3COOR \quad (1)$$
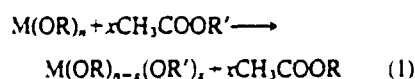
where M = Ti, Nb; $n = 4$, 5; R' = t-Bu, $Pb(OAc)$. They also speculated that the prehydrolyzed solutions contained either bi- or trimetallic structures, for example

OR
|
RO–Ti–O–Pb(OAc)
|
OR

**I**

OR      OR
|         |
RO–Ti–O–Pb–O–Ti–OR
|         |
OR      OR

**II**

OR
|
RO–Ti–O–Pb–OR'
|
OR

**III**
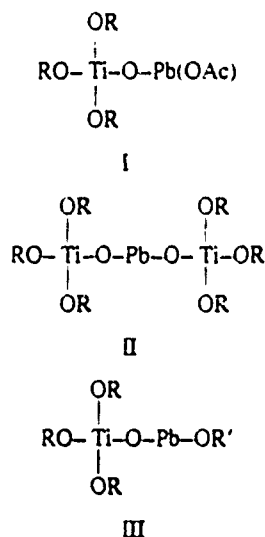
However, they favored structure II. Their rationale for this favored structure was based on the apparent low volatility and high viscosity of the sol. These same properties suggested, to us, the polymeric structure

OR
|
—Ti–O–Pb–O—
|
OR

          *n*

**IV**
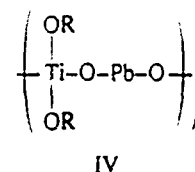
The subject of inorganic polymers is currently of great interest to the chemical community.[11] Therefore, we turned our attention toward attempting to differentiate these two possibilities. To do this, an analytical method was developed for the analyses of the volatile organic compounds released during the course of these preparations.

In doing this work, we have also had the opportunity to address a second question more related to processing of these types of compositions. Payne and co-workers[8] reported that DTA curves for PT-precursor powders derived from $Ti(O-i-Pr)_4$ differed from those derived from $Ti(O-n-Pr)_4$, the former exhibiting a single sharp exotherm of ≈300°C, whereas the latter exhibited additional exotherms at higher temperatures (430° and 500°C), depending on the extent of hydrolysis. Film morphologies reportedly also showed differences. The observations were interpreted as being due to the different organic groups present. However, $Ti(OR)_4$ complexes are known to undergo alcohol exchange reactions, and, in such systems, the established equilibria are driven to completion by removal of the more volatile alcohol (ROH)

$$Ti(OR)_4 + 4R'OH \rightleftharpoons Ti(OR')_4 + 4ROH$$

$$(2)$$
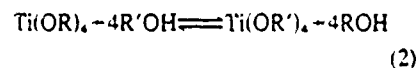
In this case, the boiling points of pure i-PrOH (82.4°C) and n-PrOH (97.4°C) are much lower than that of 2-MOE (124.6°C). Condensation of expected azeotropic mixtures should allow for efficient removal of the more volatile alcohol, and a priori expectations would predict that under the reaction conditions, complete or near-complete trans-alcoholysis would have transformed both $Ti(OR)_4$ precursors into the same species, namely $Ti(OR')_4$ (where R' is the alkyl group of the solvent alcohol). Because the differences in the reported DTA curves and film morphologies suggested that this was not the case, we considered it necessary to determine how efficiently the volatiles were removed in these reactions. Preliminary data are presented here.

## EXPERIMENTAL PROCEDURE

The chemicals $Pb(OAc)_2 \cdot 3H_2O$,* $Ti(OEt)_4$,* $Ti(O-i-Pr)_4$,* $Ti(O-n-Pr)_4$,* and 2-methoxyethanol‡ were used as supplied. Manipulations with the moisture-sensitive $Ti(OR)_4$ complexes were done under an-

Pb(OAc)₂·3H₂O
│ · in 2-MOE
↓ · heat to 123°C, fraction 1
gold solution
│ · 1 0 equiv Ti(OR)₄
↓ · to 123°C, fraction 2
yellow-gold solution
│ · dilute to 1M to 2M
│ · cool to −20° to −25°C
│ · hydrolyze (4 H₂O/Ti)
↓ · warm to room temperature, <30 min
transparent gel
│ · dry under high vacuum
│ · fraction 3
↓ · grind, sieve
PT-precursor powder

**Fig. 1.** Sol–gel preparation of PbTiO₃-precursor powder.

---

hydrous conditions; however, only the Ti(O-*i*-Pr)₄ was assayed gravimetrically.

Gas–liquid chromatographic analyses of the organic volatiles were made using a gas chromatograph[1] equipped with a flame intensity detector, using a 6 ft (1 8 m) by 0.125 in. (0 32 cm) column.[1]

The column temperature was programmed to increase from 70° to 220°C at 12°C/min. In the cases where EtOAc was liable to be present, partial overlap of the EtOAc and 2-MOE peaks necessitated that a slower temperature ramp be employed initially. In these cases, the column was heated at either 2° or 4°C/min for the first 12 to 13 min (until the 2-MOE peak was completely removed). Even so, partial overlap still existed, making quantification difficult. Samples for analyses were prepared using toluene or *m*-xylene as the internal standard. Errors in the reported values are estimated to be 5% to 8%

Infrared spectra were obtained on a Fourier transform spectrometer[**] (±4 cm⁻¹) using samples prepared as KBr pellets.

Solutions and gels leading to the formation of PT were prepared by a procedure which was a modification (Fig. 1) of that given by Gurkovich and Blum.[4] We made five modifications: (*a*) The reaction scale was reduced (Table I) so that the initial solvent volumes varied from 75 to 300 mL. (*b*) The extent of heating was governed by the temperature of the vapor condensing in the still head of a standard distillation assemblage and not only by the temperature of the solution. The reaction solutions were heated until the temperature of the condensing vapors reached that found for pure 2-MOE (under our conditions, this was found to be 122° to 123°C); under these conditions, solution temperatures rarely exceeded 135°C. (*c*) The final concentrations of lead and titanium in the prehydrolyzed solutions ranged arbitrarily from 2M to

4M, though these were diluted to 1M to 2M prior to hydrolysis. (*d*) Hydrolyses were accomplished by adding dropwise acid-free deionized water (4 H₂O/Ti) dissolved in 2-MOE to cold (−20° to −25°C) precursor solutions. On warming to room temperature, the homogeneous solutions set to yellow-gold transparent gels within 30 min. (*e*) Entrapped solvent was removed from the gels by room-temperature trap-to-trap distillation, using standard high-vacuum techniques. All distillate fractions (i.e., those obtained before and after addition of Ti(OR)₄ and from the gel desolvation) were analyzed quantitatively for the constituent alcohols and alkyl acetates, as described above.

To determine more directly the fate of the charged lead acetate in solution after the dehydration step, but before the addition of the Ti(OR)₄, the following experiment was conducted. The volume of a solution of Pb(OAc)₂·3H₂O (7 2 g, 19 0 mmol) in 2-MOE (initially 50 mL) was reduced by distillation until the solution temperature reached 150°C, at this time, the gold, water-sensitive solution was separated into two equal parts, each of these being reduced to an oily, yellow-gold wax at room temperature under high vacuum. Reagent-grade tetrahydrofuran (THF, 50 mL) was added to the first portion under N₂, producing a white slurry. This was washed with THF and anhydrous diethyl ether (Et₂O) and air-dried to yield a white powder (2.43 g), whose spectral parameters (IR, ¹H NMR) were identical with those given below. To the second portion, reagent-grade *i*-PrOH (50 to 80 mL) was added, again producing a white slurry, which was transferred under N₂ to a 750-mL Erlenmeyer flask. The mixture was heated to boiling with rapid stirring and concomitant additions of *i*-PrOH until the mixture cleared to a colorless solution. This solution was removed from the heat, sealed, and allowed to stand undisturbed overnight. The resulting mixture was filtered in air, the solid being washed with *i*-PrOH and Et₂O, and air-dried to yield 3Pb(OAc)₂·PbO·H₂O (2.35 g, 7.7 mmol) as white

leaflets. Anal. Calcd for C₁₂H₂₀O₁₄Pb₄: C, 11.84, H, 1 66; Pb, 68.1. Found. C, 11 ⁻9, H, 1.42; Pb, 67 6. ¹H NMR (200 MHz) δ_{dmso-d₆}, 2.495 (1 H), 2.485 (1 H), 1 715 (18 H). IR (cm⁻¹ ±4): ν_{OH}=3524 (m, sh), 3463 (br, vs); ν_{OAc}=1566 (vs), 1511 (vs), 1406 (vs), 1335 (m). The XRD patterns of samples prepared as either Colloidan smears or double-sided tape mounts were consistent with this formulation, but showed a time-dependent transformation to a yet unidentified species (vide infra).

## RESULTS AND DISCUSSION

The results of the study relating to the quantification of volatilized organic compounds (Table I) show that, irrespective of the reaction scale or nature of Ti(OR)₄, at least over this limited range of experiments, the formation of PT-precursor powders is accompanied by the loss of ≈1 equiv of acetate and >3 equiv of precursor alcohol per charged Pb or Ti compound. While Gurkovich and Blum[4-6] implied that the precursor alcohol and acetate were removed as precursor alcohol acetate, we determined that the amount of precursor alcohol acetate formed was very dependent upon the reaction concentration. Under dilute reaction conditions, most of the liberated acetate is removed as the solvent alcohol acetate, with little precursor alcohol acetate formed. Under concentrated reaction conditions, the amount of precursor alcohol acetate formed increases as the amount of solvent alcohol acetate formed decreases. This of course is the result of the different equilibrium concentrations present under dilute conditions as opposed to concentrated conditions.

The fact that only one acetate per lead is released during the reaction sequence tends to eliminate the possibility that structures III and IV (see Introduction) exist to any significant extent. Rather, structures I and/or II would be consistent with our results. It should be recognized that if structure II is present, the compositional stoichiometry requires the presence of an additional equivalent of Pb(OAc)₂. Infrared spectra of the PT-

---

**Table I.** Summary of the Quantification of the Volatile Organic Constituents Formed During the Syntheses of PT-Precursor Powders

| Experiment[*] | Concn (M) | Charged Pb(OAc)₂·3H₂O[†] (mmol) | Recovered[‡] (mmol) | | | Total Pb[§] (mmol/mmol) | |
|---|---|---|---|---|---|---|---|
| | | | ROH | ROAc | R'OAc | Alcohol | Acetate |
| PT (Et)[‡‡] | 0.13 | 17 34 | 53 25 | 0 | 14.62 | 3 07 | 0 84 |
| PT (Et)[‡‡] | 4.0 | 47.77 | 105 61 | 16.97 | 37 60 | 2 65 | 1 14 |
| PT (*i*-Pr) | 0.15 | 17.11 | 63 66 | 0 | 6 85 | 3 72 | 0 40 |
| PT (*i*-Pr) | 4 3 | 42.52 | 114 58 | 18.26 | 15 78 | 3 36 | 1 04 |
| PT (*n*-Pr) | 0 14 | 18 38 | 67 96 | 0 48 | 14 48 | 3 72 | 0 81 |
| PT (*n*-Pr) | 4.4 | 43.63 | 100.75 | 28.14 | 15.10 | 2.95 | 0 99 |
| PbO[¶] | | 25.9 | | | 13.5 | | 0.5 |
| PbO** | | 26.3 | | | 14 1 | | 0 5 |
| TiO₂ | | 18.4[††] | 65 | | | 3.5 | |

*Designations in parentheses give nature of R group in Ti(OR)₄ precursor 'Except for final three entries, reaction stoichiometry Pb(OAc)₂·3H₂O, Ti(OR)₄ = 1, 1, so that mmol of Pb(OAc)₂·3H₂O = mmol of Ti(OR)₄. R corresponds to organic moiety associated with Ti(OR)₄ precursor (given in parentheses in column 1). R' refers to alkyl group of solvent alcohol, CH₃OCH₂CH₂OH. ‡Ratios of total recovered alcohols (as ROH and ROAc) to charged Ti(OR)₄ and acetates (as ROAc and R'OAc) to charged Pb(OAc)₂·3H₂O give measure of overall stoichiometry, theoretical limits for alcohol and acetate are 4 0 and 2.0, respectively ¶Water added after dehydration step. **Solution taken to dryness without addition of water ††No lead involved, only Ti(O-*i*-Pr)₄ ‡‡The Ti(OEt)₄ used was contaminated by Ti(O-*i*-Pr)₄ (≈15%, determined by ¹H NMR)

---

[1]Aerograph Series, Varian Instrument Group, Palo Alto, CA.
Model 80/100 Carbopack C/0 1% SP 1000, Supelco, Inc., Bellefonte, PA.
**Model IR-32, IBM Instruments, Inc., Danbury, CT.

Table II.   XRD Pattern Data for $3Pb(OAc)_2 \cdot PbO \cdot H_2O$[*]

| Phase 1 | $3Pb(OAc)_2 \cdot PbO \cdot H_2O$[‡] | Phase 2 | Expansion[§] (%) |
|---|---|---|---|
| 5 926 (14) | 5 956 (32)* | 6 088 (43) | 2.73 |
| 4 575 (1) | 4 553 (31) | 4 848 (1) | 5 97 |
| 3 943 (22) | 3 959 (35)* | 4 058 (27) | 2.92 |
| 3 296 (1) | 3 303 (30) | 3.401 (1) | 3 19 |
| 2.954 (100) | 2.964 (100)* | 3 038 (96) | 2.84 |
| 2 633 (1) | 2 620 (13) | 2.706 (1) | 2.77 |
| 2 365 (76) | 2.368 (82)* | 2.433 (100) | 2.88 |
| 1 969 (15) | 1 972 (31)* | 2.027 (25) | 2.95 |
| 1 689 (<1) | 1 695 (6) | 1 740 (1) | 3 02 |
|  | 1 758 (11)* |  |  |
| 1.478 (1) | [¶] | 1.520 (1) | 2.84 |
| 1.313 (5) | [¶] | 1.352 (4) | 2.97 |

[*]Phases 1 and 2 are defined in the text. The *d* spacings are in Ångstroms (1×10⁻¹ nm) and values in parentheses give observed and reported relative peak intensities (*I/I₀*) [‡]Taken from Ref 13, but is not intended to represent the entire listing for this material by these authors Rather it is presented for comparative purposes only Asterisks (*) designate peaks previously associated with preferred orientation [§]Gives relative increase in *d* spacing for peak in phase 2 with respect to corresponding peak on phase 1 [¶]Outside range reported in Ref 13

precursor powders could not differentiate the two structures, showing absorbances attributable to acetate stretching modes identical to those of $Pb(OAc)_2 \cdot 3H_2O$ (1561 (s), 1401 (s), 1337 (m) cm⁻¹).

Perhaps the most unexpected finding in this study was that refluxing $Pb(OAc)_2 \cdot 3H_2O$ in 2-MOE liberates 0.5 equiv of organic acetate, even in the absence of added $Ti(OR)_4$. The resulting solutions were gold colored, exhibiting an almost metallic sheen. Also, these solutions were water sensitive, immediately decolorizing and eventually precipitating a white solid on its addition. This observation led us initially to believe that the dehydrated solutions contained lead alkoxide species, possibly formed by the incomplete perturbation of the equilibria given by

$$Pb(OAc)_2 + R'OH \rightleftharpoons Pb(OAc)(OR')$$
$$- HOAC \qquad (3)$$

$$HOAC + R'OH \rightleftharpoons R'OAC + H_2O \qquad (4)$$
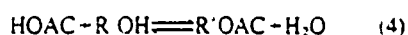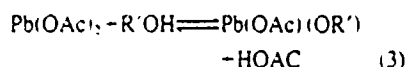
However, the gold color was inconsistent with previous reports that solutions of lead alkoxides are colorless [2] More direct evidence for the nature of these solutions came with the isolation, in high yield, of a compound with the stoichiometry of basic lead acetate, $3Pb(OAc)_2 \cdot PbO \cdot H_2O$ Although redissolving the isolated solid in a 2-MOE produced a colorless solution, suggesting that some reaction has occurred during the workup procedure, it is important to note that the stoichiometry of the solid is entirely consistent with the results of quantifying the organic byproducts.

$$4Pb(OAc)_2 + H_2O \longrightarrow 3Pb(OAc)_2 \cdot PbO$$
$$+ 2HOAc \qquad (5)$$

$$HOAC + R'OH \longrightarrow R'OAC + H_2O \qquad (6)$$
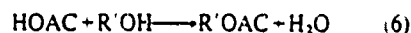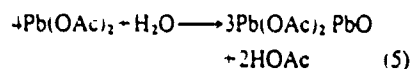
The yellow-gold color is likely due to the presence of the anhydrous PbO in the formulation.

The leaflet nature of the isolated basic lead acetate had significant effects on the XRD patterns. Kwestroo and Langereis[13] have reported that certain peaks in the XRD patterns of powdered basic lead acetate exhibited disproportionately large intensities due to preferred orientation. With the present leaflets, XRD patterns taken immediately after sample preparation (in fact, while the isoamyl acetate/Collodian binder was still wet) showed the presence of extremely strong peaks, the positions and relative intensities of which corresponded exactly to those indicated as being due to preferred orientation (Table II, phase 1). As time progressed (half-life on the order of 1 h), the intensity of this pattern decreased, being replaced peak for peak by that of a second phase of approximately equal intensity as the first. After 24 h, only the pattern of the second phase was present (Table II, phase 2). Interestingly, the position of virtually every peak in the second phase corresponds to a 3% increase in lattice spacing with respect to the first. This type of behavior is often observed in clay systems and probably represents the results of some intercalation of atmospheric gases.

Finally, it is now possible to comment on the work of Payne and co-workers regarding the differences involved when using $Ti(O\text{-}i\text{-}Pr)_4$ and $Ti(O\text{-}n\text{-}Pr)_4$. Whereas, in our experimental design, the total amount of recovered precursor alcohol was essentially independent of its nature, it must be recognized that our conditions were apparently more severe than those reported by Payne's group. Specifically, they report all reactions to be carried out at 120°C, though they do not indicate whether this temperature refers to solution or vapor. In either case, these conditions are marginally milder than ours (final vapor temperature of 123°C). This slight difference in absolute temperature, however, is expected to have a very significant effect on the final solution composition in the two cases. That

is, because the difference in boiling points of isopropyl alcohol (82.4°C) and n-propyl alcohol (97 4°C) is so large, the latter system will tend to retain relatively more of the precursor alcohol in the final mixes, unless the reactions are driven to completeness. Even under our more driving conditions, n-propyl alcohol was unique in that it was the only system in which some precursor alcohol was recovered in the hydrolysis step. Certainly, more detailed studies are required before any definite conclusion is made.

## SUMMARY

It was observed that the formation of $PbTiO_3$-precursor powders via sol–gel was accompanied by the loss of ≈1 equiv of acetate and >3 equiv of precursor alcohol per charged Pb or Ti. The relative proportions of precursor alcohol, precursor alcohol acetate, and solvent alcohol acetate formed as a result of the formation of such powders were determined to be dependent on the reaction concentration. It was interesting to observe that refluxing $Pb(OAc)_2 \cdot 3H_2O$ in a 2-MOE liberates 0.5 equiv of solvent alcohol acetate in the absence of $Ti(OR)_4$, and that basic lead acetate, $3Pb(OAc)_2 \cdot PbO \cdot H_2O$, was isolated as a result of such reaction.

## REFERENCES

[1]Better Ceramics Through Chemistry, Materials Research Society Symposia Proceedings, Vol 32 Edited by C J Brinker, D E Clark, and D R Ulrich Elsevier, New York, 1984

[2]Ultrastructure Processing of Ceramics, Glasses, and Composites Edited by L L Hench and D R Ulrich. Wiley-Interscience, New York, 1984

[3]Nippon Soda Co . Ltd , WO 8403003 A1, Aug. 2, 1984; *Chem Abstr Jpn* 101 [18] 162265 W (1984)

[4]S R Gurkovich and J B Blum, Preparation of Monolithic Lead Titanate by a Sol–Gel Process", Ch. 12 in Ultrastructure Processing of Ceramics, Glasses, and Composites. Edited by L L Hench and D R Ulrich. Wiley-Interscience, New York, 1984

[5]S R Gurkovich and J B. Blum, "Crystallization of Amorphous Lead Titanate Prepared by a Sol–Gel Process," *Ferroelectrics* 62, 189–94 (1985)

[6]J B Blum and S R Gurkovich, "Sol–Gel-Derived $PbTiO_3$," *J Mater Sci*. 20, 4479–83 (1985)

[7]K D Budd, S K Dey, and D A Payne, "Sol–Gel Processing of $PbTiO_3$, $PbZrO_3$, PZT, and PLZT Thin Films", pp 123–41 in Special Proceedings of British Ceramic Society on Electronic Ceramics, Stoke-on-Trent, England, Dec 17–18, 1984

[8]K D Budd, S K Dey, and D A Payne, Properties of Sol–Gel Derived Films in the PLZT System" Paper No 46-E-85 Presented at the 87th Annual Meeting of the American Ceramic Society, Cincinnati, OH, May 7, 1985

[9]D C Bradley, R C Mehrotra, and D P Gaur, Metal Alkoxides; Chs. 2.5 and 4 4 Academic Press, New York, 1978

[10]D C Bradley, R C Mehrotra, and D P Gaur, Metal Alkoxides; Chs. 2.4 and 4 3 Academic Press, New York, 1978

[11]H R Allcock, "Inorganic Macromolecules, Developments at the Interface of Inorganic, Organic, and Polymer Chemistry," *Chem Eng News*, 63 [11] 22–36 (1985)

[12]L M Brown and K S Mazdiyasni, "Cold-Pressing and Low-Temperature Sintering of Alkoxy-Derived PLZT," *J Am Ceram Soc* . 55 [11] 541–44 (1972).

[13]W Kwestroo and C Langereis, "Basic Lead Acetates," *J Inorg. Nucl. Chem.*, 27, 2533–36 (1965) □

APPENDIX 36

journal

# Field-Forced Antiferroelectric-to-Ferroelectric Switching in Modified Lead Zirconate Titanate Stannate Ceramics

Wuyi Pan, Qiming Zhang, Amar Bhalla,* and Leslie E. Cross*

Materials Research Laboratory, The Pennsylvania State University,
University Park, Pennsylvania  16802

Electric-field-forced antiferroelectric-to-ferroelectric phase transitions in several compositions of modified lead zirconate titanate stannate antiferroelectric ceramics are studied for ultra-high-field-induced strain actuator applications. A maximum field-induced longitudinal strain of 0.85% and volume expansion of 0.95% are observed in the ceramic composition $Pb_{0.97}La_{0.02}(Zr_{0.66}Ti_{0.09}Sn_{0.25})O_3$ at room temperature. Switching from the antiferroelectric form to the ferroelectric form is controlled by the nucleation of the ferroelectric phase from the antiferroelectric phase. A switching time of $<1$ $\mu s$ is observed under the applied field above 30 kV/cm. The polarization and strains associated with the field-forced phase transition decrease with increasing switching cycle, a so-called fatigue effect. Two types of fatigue effects are observed in these ceramic compositions. In one, the fatigue effects only proceed to a limited extent and the properties may be restored by annealing above the Curie temperature, while in the other, the fatigue effects proceed to a large extent and the properties cannot be restored completely by heat treatment. Hydrostatic pressure increases the transition field and the switching time. But when the applied electric field is larger than the transition field, the induced polarization and strain are not sensitive to increasing hydrostatic pressure until the transition field approaches the applied field. [Key words: ferroelectrics, stannates, titanates, zirconate, lead.]

## I.  Introduction

CERAMICS in lead zirconate titanate stannate and further modified forms have been studied extensively in the past 20 years for many potential applications in energy conversion.[1,2] The interest stems from the fact that, as is evident in Fig. 1, there are regions on the ternary phase diagrams at room temperature where antiferroelectric and ferroelectric phases abut and thus, for these compositions, must be of closely similar free energy. Since the different antiferroelectric and ferroelectric phases are all distinguished by small ($\sim0.2$ Å ($\sim0.02$ nm)) displacement of ions from a common high-temperature cubic prototypical form, switching between forms can be accomplished without breaking any energetic bonds. As the ferroelectric domains carry a large spontaneous electric polarization and the antiferroelectrics are centric, it is not surprising that antiferroelectric forms close to bonding compositions can be switched into ferroelectrics under high electric fields. Similarly, the atomic arrangement of an antiferroelectric is more compact than that of the ferroelectric counterpart. One may expect ferroelectric compositions close to the boundary to invert to antiferroelectric under suitable hydrostatic or uniaxial stress. Such pressure switching has been very extensively investigated. Upon inversion to the antiferroelectric form, a poled ferroelectric ceramic releases all polarization charges and therefore can supply very high instantaneous currents.[1] The electric-field-forced phase transitions were also studied for different applications. The first

systematic study in the 1960s was done at Clevite laboratories to explore the use of phase change compositions in capacitive energy storage.[3,4] Uchino *et al.* studied this effect for the shape memory application.[5]

For the same composition, an antiferroelectric form has a smaller lattice volume than the paraelectric form, while a ferroelectric form has a larger lattice volume than the paraelectric form.[5] Therefore, if the change directly from an antiferroelectric to the ferroelectric can be accomplished by an electric field, large shape change should take place  However, the field-forced phase change was not considered for actuator applications.

In an earlier paper,[7] we demonstrated the large field-induced strain in $BaTiO_3$ single crystal by the mechanisms of field-forced paraelectric-to-ferroelectric phase change and 90° domain reorientation, and in another paper[3] we demonstrated the large field-induced strain in PLZT ceramic compositions near the tetragonal-rhombohedral phase boundary by a mechanism of non-180° domain reorientation. In this paper, we present the field-induced strain

(A)



(B)
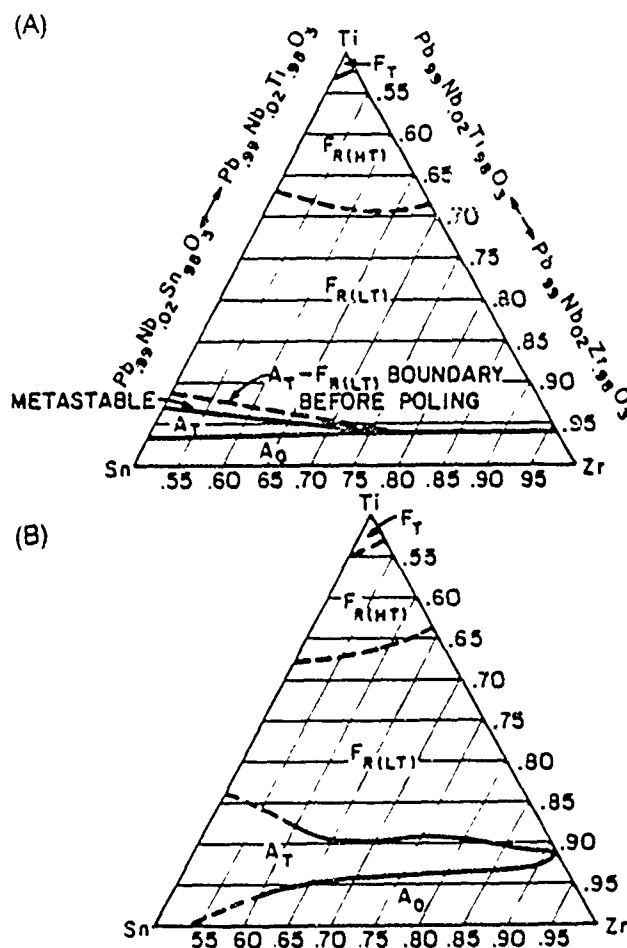


Fig. 1.  (a) Ternary phase diagram for the system $Pb_{0.99}Nb_{0.02^-}$ $(Zr,Sn,Ti)_{0.98}O_3$  at 25°C. (b) Ternary phase diagram for the system $Pb_{0.97}La_{0.02}(Zr,Sn,Ti)O_3$  at 25°C
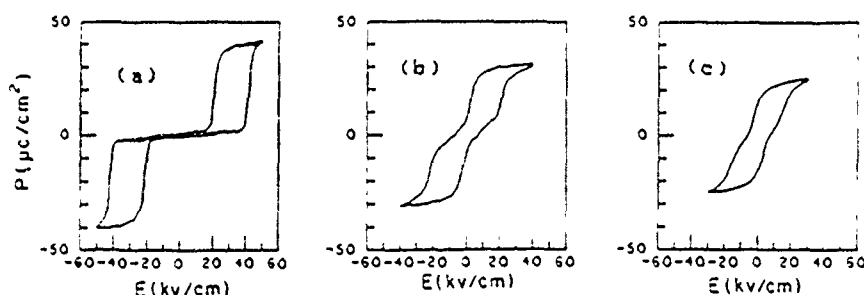
Fig. 2.  Polarization–electric field hysteresis loops for various compositions

and kinetics of the field-forced antiferroelectric-to-ferroelectric phase transition in modified lead zirconate titanate stannate switchable antiferroelectric ceramics and discuss the possibility of this family of ceramics for ultra-high-field-induced strain actuator applications.

## II. Experimental Procedure

### (1) Composition Selection and Sample Preparation

The compositions chosen for study were close to the compositions chosen at Clevite laboratory for the pressure switching experiments.[5] These compositions are all near the antiferroelectric–ferroelectric phase boundary: $Pb_{0.99}(Zr_{0.57}Ti_{0.05}Sn_{0.38})_{0.98}Nb_{0.02}O_3$ (1), $Pb_{0.92}Sr_{0.05}La_{0.02}(Zr_{0.44}Ti_{0.16}Sn_{0.30})O_3$ (2), $Pb_{0.92}Mg_{0.05}La_{0.02}$-$(Zr_{0.59}Ti_{0.11}Sn_{0.30})O_3$ (3), $Pb_{0.97}La_{0.02}(Zr_{0.66}Ti_{0.09}Sn_{0.25})O_3$ (4), and $Pb_{0.97}La_{0.02}(Zr_{0.53}Ti_{0.12}Sn_{0.35})O_3$ (5).

The positions in the phase diagram for compositions 4 and 5 are shown in Fig. 1(a). These two compositions are in the region of the antiferroelectric tetragonal close to the phase boundary between antiferroelectric tetragonal and ferroelectric rhombohedral (LT low-temperature phase) phases. The position of composition 1 in the phase diagram is shown in Fig. 1(b). It is observed that the position of composition 1 in the phase diagram is very close to the phase boundary between antiferroelectric tetragonal and metastable ferroelectric rhombohedral (LT). The phase diagrams for compositions 2 and 3 are not available.

The above compositions were made up from reagent-grade oxides using the conventional solid-state sintering technique. Calcining temperatures were in the range of 750° to 900°C. Disks were cold-pressed using a small amount of poly(vinyl alcohol) (PVA) binder and fired at 1350°C in a PbO atmosphere provided by excess $PbZrO_3$ in closed containers.

### (2) Measurements

*A) Field-Induced Polarization and Strain.*  The samples were cut with a string saw into dimensions $0.6 \times 0.4$ cm with thickness ranging from 0.15 to 0.3 mm depending on the transition field of the ceramic compositions. The major surfaces were fine ground and gold electroded. The longitudinal strains were measured with a laser interferometer as described in an earlier paper.[3] The polarization versus electric field was measured using a modified Sawyer and Tower circuit. The transverse strains were measured using the bonded strain gage technique. Temperature variation was accomplished using a hot stage immersed in a liquid-nitrogen container and the temperature was controlled by a transformer in series with a temperature controller.[4] Pressure variation was accomplished in a well-sealed oil container to which an air-driven intensifier pump supplied a high-pressure medium.[5] The value of pressure was monitored with a Heise gauge with an accuracy of $\pm 100$ bar ($\pm 10$ MPa).

*B) Switching-Current Measurements*  The samples were cut into thicknesses ranging from 0.2 to 0.25 mm. For these experiments, the areas of the samples were kept under 0.03 cm² to

ensure that the power supply could provide sufficient current. The shapes of the samples were made irregular to reduce the interference of a radical piezoelectric resonance mode. The major surfaces of the samples were sputtered twice with gold to ensure equal potential surfaces even under high current conditions.

The kinetics of the switching in these samples was studied by the conventional square pulse technique in which one measures the current which flows through a series resistor to the sample electrodes.[10] The rectangular pulse was generated with a pulse generator[*] and then input into a high-power pulse generator[†] for power amplification. The high-power pulse generator possesses 9-kW power, and 6-A current can be supplied by the machine under 1500 V and a pulse width of 50 μs. The rise times for both pulse generators were shorter than 20 ns. The resistance value of the series resistor was kept small in order to have the resistance–capacitance (RC) time constant of the high-frequency capacitance of the sample and the resistor less than 10 ns. The current flowing to the sample electrode during the switching was obtained by measuring the voltage across the series resistor. The voltage as a function of time was recorded with a digital oscilloscope.[‡] The scope has a 50-MHz bandwidth and up to 200-MHz sampling frequency. An invertor is used to change the polarity of the pulse to prepare the sample for further switching because remanent polarization is observed for the compositions studied, especially for composition 1.

The switching time was obtained by reading the time at which the switching current dropped to 20% of its maximum value. The switching-current values were obtained from the voltage across the series resistor and the resistance value of the resistor. The charges flowing through to the sample electrode were obtained by integrating the areas under the switching current–time curves. The RC peaks were extrapolated by hand to longer time and the areas under the peaks were subtracted from the total areas to find out the charges due to polarization switching only.

*C) Measurement of Fatigue Effect.*  The fatigue effect was studied by measuring the field-induced polarization and transverse strain as a function of switching cycles. A 10-Hz sine wave form was used to drive the ceramic samples continuously through the phase change. The fatigued samples were annealed at 300°C for 12 h.

## III. Results and Discussion

### (1) Field-Induced Polarization and Strains

*(A) Induced Polarization and Strains for Different Compositions.*  A maximum electric field up to 70 kV/cm was applied to achieve the field-forced antiferroelectric–ferroelectric phase switching in the five ceramic compositions. But compositions 2 and 3 could not be switched even under the maximum field level attempted.

The polarization–electric field hysteresis loops are shown in Fig. 2. Composition 4 shows a classic antiferroelectric hysteresis loop. In the low-field region, this ceramic composition shows characteristics of a linear dielectric with no hysteresis loops. The two hysteresis loops associated with positive and negative electric field are well separated by a straight line. Composition 1 shows a hysteresis loop quite similar to that of a ferroelectric, because the
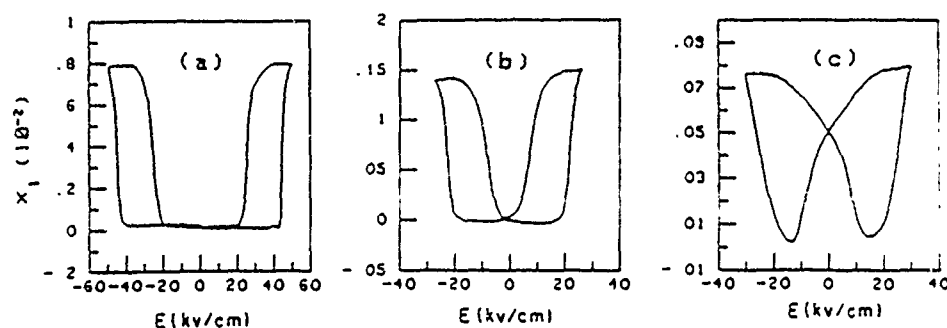
Fig. 3.   Longitudinal strain–electric field hysteresis loops for various compositions.



(a)

T = −93°C          T = −60°C          T = −40°C          T = 25°C
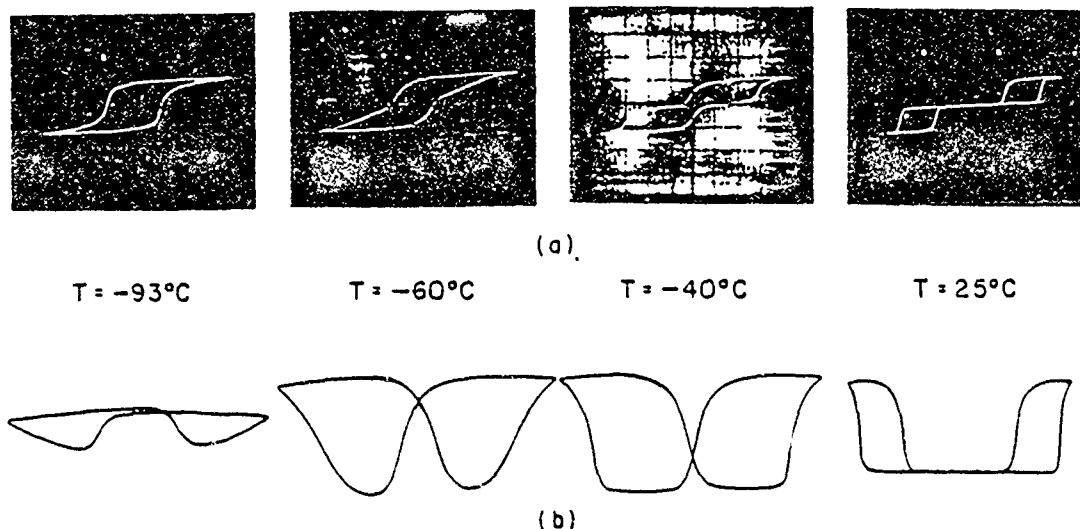


(b)

Fig. 4.   (a) Polarization–electric field and (b) transverse strain–electric field hysteresis loops as a function of temperature for composition 4

position of this composition in the phase diagram is very close to the phase boundary between antiferroelectric tetragonal and metastable ferroelectric rhombohedral (LT) after poling. However, the kinks in the middle of the hysteresis loop indicate that there is a recovery of the antiferroelectric form. Composition 5 shows a behavior in between those of compositions 1 and 4. For this composition, the antiferroelectric phase does recover under positive field, however, two hysteresis loops associated with positive and negative field appear slightly overlapped. The longitudinal strains accompanying the *P-E* hysteresis loops for the three compositions are shown in Fig 3 The transverse strain hysteresis loops are essentially the same in shape except that the strains are less than the longitudinal strains. The signs of the transverse strains are also positive, contrasting with those of the ferroelectrics. It must be mentioned that the hysteresis loops recorded are not for the first switching cycles When the antiferroelectric state in a virgin state is switched into ferroelectric, the transition field is much higher than that for the subsequent cycles, a phenomenon observed also by Berlincourt[5] and Pulvari[1] As the antiferroelectricity of the compositions increases from 1 to 5 to 4, the difference between the first cycle transition field and that for the subsequent switching becomes small.

The field-induced strains and the related switching data are summarized in Table I. It may be seen that the induced polarization seems to be proportional to the transition field. The transition field is a measure of the coupling between the two sublattices The stronger the coupling between the two sublattices, the smaller the lattice volume of the antiferroelectric form, hence the higher the transition field. When the antiferroelectric form becomes smaller in volume, the volume difference between the antiferroelectric form and the ferroelectric form becomes larger; therefore, the

field-induced strains increase It must be mentioned that for composition 4, when the virgin state is switched, a longitudinal strain can be larger than 0 9% But this magnitude cannot be observed repeatedly. The value listed in Table I is obtained after quite a few switching cycles. It may be seen from Table I that the field-induced volume expansion for these ceramic compositions is quite large because the transverse strain is positive while in ferroelectrics the transverse strain is negative and thus attenuating the volume expansion caused by the longitudinal strain. It may also be noted that the ratio of the longitudinal strain to the transverse strain is by no means a constant for all the compositions. It is 9 17 for composition 4, 2.63 for composition 5, and only 1 92 for composition 1.

(*B*) *Temperature Dependence of Field-Induced Polarization and Strain.*   The polarization and transverse strain were measured as a function of temperature for compositions 4 and 5. The polarization and strain hysteresis loops at some typical temperatures for composition 4 are shown in Fig. 4. It is observed that at low temperature the ceramic composition tends to show a ferroelectric-like hysteresis loop. It suggests that at very low temperature the ferroelectric phase is a thermodynamically stable phase.

Table I.   Summary of Switching and Strain Data for Modified Switchable Lead Zirconate Titanate Stannate Ceramics

| Comp | $E$, (kV/cm) | $P$ ($\mu$C/cm$^2$) | $t$, (%) | $z$, (%) | $\Delta v/v$ (%) | $t_{11}/t$ |
|------|------|------|------|------|------|------|
| 1 | 10 | 24 | 0.08 | 0.042 | 0.164 | 1.92 |
| 4 | 48 | 40 | 0.78 | 0.085 | 0 95 | 9.17 |
| 5 | 30 | 25 | 0.15 | 0.057 | 0.264 | 2.63 |
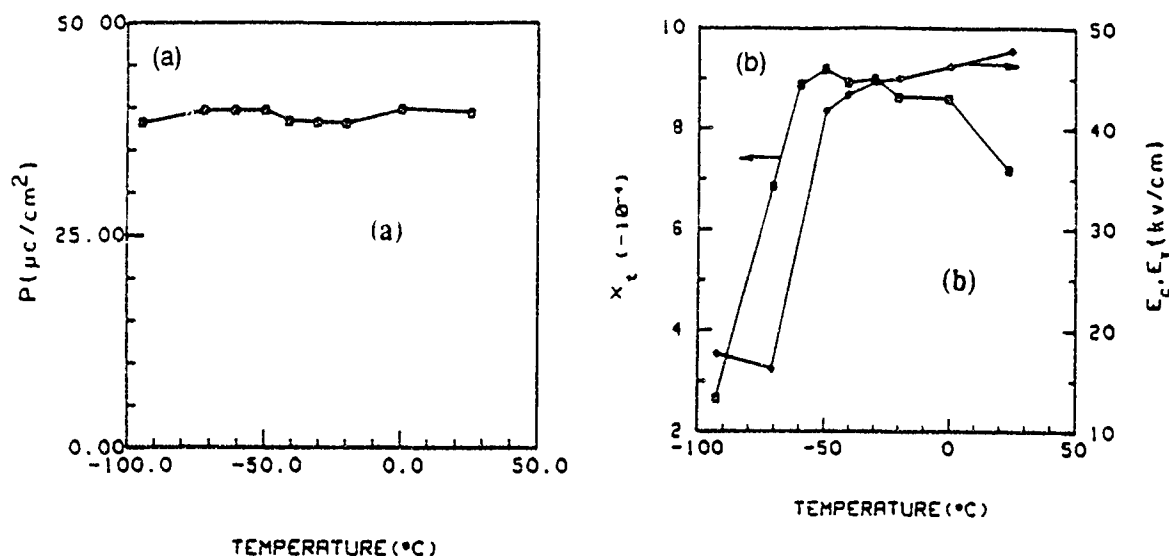
Fig. 5. (a) Field (52 kV/cm) induced polarization as a function of temperature and (b) the transition field (or coercive field) and the field (52 kV/cm) induced transverse strain as a function of temperature for composition 4
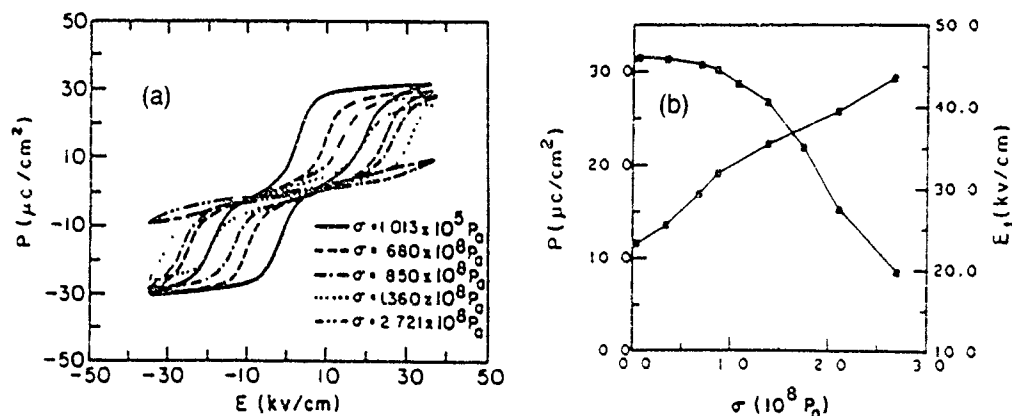


Fig. 6. (a) Polarization–electric field hysteresis loops under various hydrostatic pressures and (b) the field (36 kV/cm) induced polarization and transition field as a function of hydrostatic pressure at room temperature for composition 5

Figure 5(a) shows the induced polarization at a field level of 52 kV/cm as a function of temperature and Fig. 5(b) shows the transverse strain induced at a field level of 52 kV/cm and the transition field (or coercive field) as a function of temperature. The induced polarization is shown to vary very little with temperature. However, the transition field and the field-induced strain vary with temperature differently. The transition field (or coercive field) decreases as temperature decreases. The sudden decrease occurs at −60°C. The transverse strain increases as the temperature decreases to −50°C and then decreases as the temperature is decreased. The sudden decrease in strain also occurs at −60°C. It is believed that the dominant mechanism for the field-induced strain is the phase change between the antiferroelectric and ferroelectric forms. When the temperature approaches −60°C from a higher temperature, the energy difference between the two forms decreases and, therefore, the field-forced transition is facilitated. The increased field-induced strain may be due to this effect. When the temperature decreases further below −60°C, the ceramic gains ferroelectricity and the field-induced strain associated with the phase change decreases drastically.

(C) *Pressure Dependence of the Field-Forced Phase Transitions* The field-forced phase transition from antiferroelectric to ferroelectric under hydrostatic pressure was also investigated. The polarization–electric field hysteresis loops as a function of hydrostatic pressure for composition 5 are shown in Fig. 6(a)

It is observed that the transition field increases with increasing hydrostatic pressure. If the applied field level is kept constant, the field-induced phase transition will be eventually suppressed by the hydrostatic pressure. This evidence further confirms that the antiferroelectric form is more compact than the ferroelectric counterpart. Hydrostatic pressure favors the smaller-volume antiferroelectric form and therefore increases the transition field.

The polarization induced under peak electric field (36 kV/cm) and the average transition field as a function of hydrostatic pressure are shown in Fig. 6(b). It may be seen that the transition field increases with hydrostatic pressure in a reasonably uniform manner, but the polarization decreases nonuniformly with increasing hydrostatic pressure. At a low hydrostatic pressure level, the induced polarization is almost maintained at a constant level because the applied field is larger than the transition field. At about 1000 atm (about 100 MPa), the induced polarization begins to decrease more quickly because the transition field approaches the applied field. This behavior shows an advantage of the antiferroelectric over ferroelectric for the "on/off" type of switching. As long as there is enough field for the phase transition to take place, the induced strain may not be very sensitive to the hydrostatic load over a substantial range of hydrostatic load.

(2) *Kinetics of Field-Forced Phase Transition*

Figure 7 shows the polarization–electric field hysteresis loops

of ceramic compositions 1 and 5 used for the kinetics study Composition 5 shows an explicit double hysteresis loop with a well-defined transition field. This loop is slightly different from those of the samples used for strain study probably because of the variation in preparation parameters. The remanent polarization at zero electric field is very small, indicating that the composition recovers to an antiferroelectric form under the absence of the electric field. Composition 1 shows a ferroelectric-like hysteresis loop The transition field is diffused, but kinks are observed in the middle of the $P$-$E$ hysteresis loop, indicating that the recovery to an antiferroelectric occurs in a negative field.

*(A)  Composition 5*     Figure 8(a) shows the switching current–time curves under different applied field levels for composition 5. It is observed that the shapes of the switching current–time curves are similar to those observed in the ferroelectric crystals.[10] An RC peak is followed by the switching current. The $I_{max}$ increases with increasing electric field and the switching time decreases with increasing electric field The switching can be completed within 1 $\mu$s above a field level of 30 kV/cm The switching time is much shorter than 0 1 s reported by Uchino *et al*[1] It is believed that the power level used for the measurement is very important for accurate measurement of switching time An antiferroelectric has a high transition field and a sharp increase in polarization at the transition field. Large current has to be supplied under a high voltage level to ensure a nondelayed phase change. Therefore, a high power level is required for the measurement We speculate that the large difference between the switching times reported by Uchino *et al* and our data is due to the different power levels used for the measurements

Figure 8(b) shows the induced polarization integrated from the switching current–time curves It is observed during the experiment that under a field level of 30 kV/cm, not much polarization can be induced by the pulses Above the field level of 30 kV/cm, the induced polarization does not vary too much with the applied electric field. The field level of 30 kV/cm is slightly larger than the transition field of the ceramic composition. This indicates that the induced polarization is contributed mainly by the phase change If the field is high enough, the extra field will not induce too much polarization because the polarization induced because of the dielectric constant of the ferroelectric phase is much less than the polarization change due to the occurrence of the phase transition If the field is not enough to induce the phase change, the induced polarization is very small. It seems that a threshold field exists for composition 5 which has a sharp phase change at the transition field.

Figure 9(a) shows $1/t_s$ vs $E$ and ln $(1/t_s)$ vs $1/E$ and Fig. 9(b) shows $I_{max}$ vs $E$ and ln $(I_{max})$ vs $1/E$ It may be noted that the plots are not the same as those for the polarization reversal in ferroelectric crystals.[10]

For the polarization reversal in ferroelectric crystals, the switching time under a low field level is controlled by the nucleation of new domains. The switching time and the maximum switching current can be expressed by the following relations under the low applied electric field:

$$I_{max} \sim e^{-\alpha E} \qquad t_s \sim e^{\alpha E}$$

where $\alpha$ is the so-called activation field Under a high electric field, the switching is controlled by domain wall motion. The switching time and $I_{max}$ can be expressed by the following relations with the applied field:

$$I_{max} \sim KE \qquad 1/t_s \sim KE$$

where $K$ is a constant which is a measure of the ease with which the domain walls move.[9] When $I_{max}$ or $1/t_s$ is plotted against $E$, an exponential relation holds in the low-field region within which nucleation of new domains controls the switching and a linear relation holds in the high-field region within which the domain wall motion controls the switching. On the other hand, when ln $(I_{max})$ or ln $(1/t_s)$ is plotted against $1/E$, a linear relation should hold in the low-field region, within which nucleation of the new domain
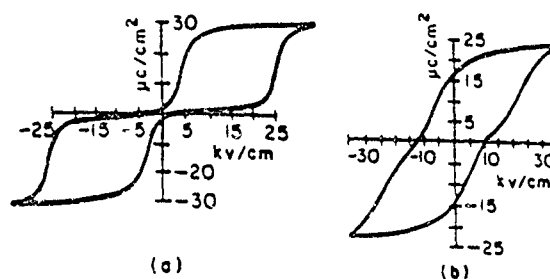
controls the switching, but not in the high-field region, within which the domain wall growth controls the switching.

In Fig. 9, nucleation-controlled switching and domain-wall-controlled switching seem to be separated at about 36 kV cm from either the $1/t_s$ vs $E$ or $I_{max}$ vs $E$ plots. Above this field level, the points seem to follow a linear relation. However, this is not true for either ln $(1/t_s)$ vs $1/E$ or ln $(I_{max})$ vs $1/E$ plots because the points for the field above 36 kV/cm still seem to follow the linear relation, indicating the nucleation may be still controlling
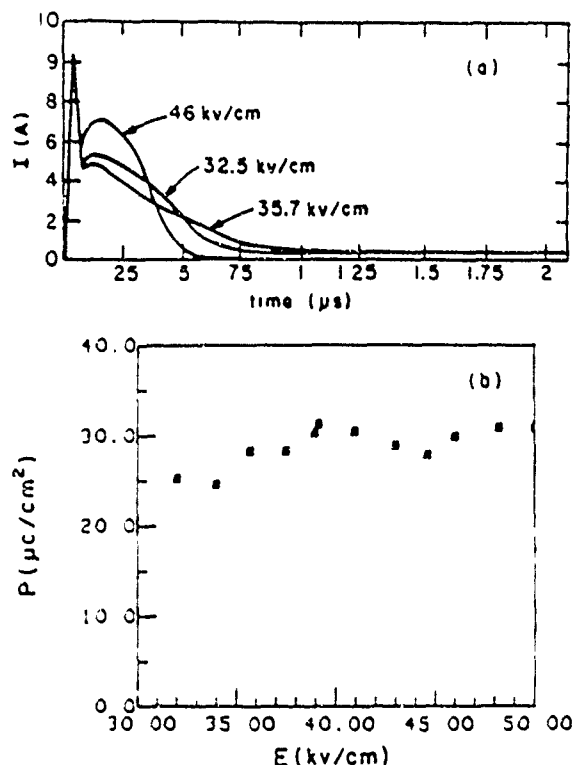
Fig. 9. (a) 1/t, vs E and in (1/t,) vs 1/E and (b) $I_{max}$ vs E and ln $I_{max}$ vs 1/E for composition 5
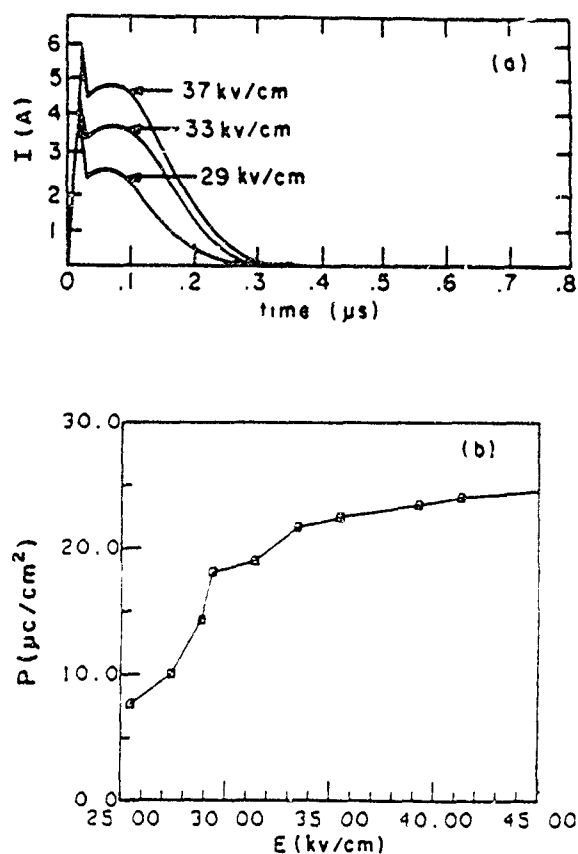


Fig. 10. (a) Switching current–time curves under different applied field and (b) the polarization integrated from the areas under the switching current–time curves for composition 1

the switching It must be remembered that the switching here is different from the polarization reversal in ferroelectric crystals There is no domain wall movement but there is a phase boundary movement during the switching It may be possible to observe a phase-boundary-controlled switching region if the applied field can be greatly increased However. the amplitude of the voltage is limited by the maximum voltage of the high-power pulse generator and some other experimental difficulties The activation field calculated from ln (1/t,) vs 1/E is 200 kV cm while that calculated from ln $(I_{max})$ vs 1/E is 150 kV/cm Although. there is no perfect agreement, it is believed that the activation field falls into the range from 150 to 200 kV cm. The activation fields for the polarization reversal in the PLZT and PZT family of ferroelectric ceramics ha e been reported by L. et al [12] The activation field for PLZT 8 65, 35 is about 5 kV cm and that for Nb-doped PZT is about 10 kV cm The activation field here is much higher compared to those observed for ferroelectric ceramics, which indicates that the nucleation of a new phase is more difficult than the nucleation of new domains

B) *Composition 1*    The switching current–time curves at various electric fields for composition 1 are shown in Fig. 10(a) It is observed that the area under the switching current under low electric field is significantly less than that under the higher field. The polarization induced by the switching is shown in Fig 10(b) It may be seen that the polarization increases with increasing electric field until 35 kV cm In the 1/t, vs E plot shown in Fig 11(a), a minimum value for 1/t, occurs in the medium level of applied electric field Below the field for this minimum, 1/t, decreases with increasing field This field range corresponds well with the field range in Fig 11(b) within which the polarization switched increases with increasing applied field Because this ceramic has a diffused transition field, the activation field should also be diffuse in nature If the field is not high enough to switch the whole system but high enough to switch lower activation field

components, the switching time can be shorter Above the field for the minimum the system begins to switch as a whole and the increase in the applied field should reduce the switching time For this composition. the activation field cannot be determined in the same manner as that for composition 5 because the activation field is distributed over a range. Figure 11(b) shows a plot of $I_{max}$ vs E It is observed that $I_{max}$ increases with increasing applied field without a minimum in the middle This is due to the fact that more polarization is induced under increased applied field.

### (3)  Effect of Hydrostatic Pressure

Figure 12(a) shows the switching current–time curves under different hydrostatic pressure for composition 5 It is observed that the peak switching current $I_{max}$ decreases under increasing hydrostatic pressure. Figure 12(b) shows the switching time and the reciprocal switching time as a function of the hydrostatic pressure. It is observed that the switching time increases with increasing hydrostatic pressure. This is just opposite to the effect observed in ferroelectric PZT ceramics.[12] In ferroelectric PZT. hydrostatic pressure favors the smaller-volume paraelectric state and lowers the Curie temperature and the coercive field, therefore the switching time decreases with increasing hydrostatic pressure In the antiferroelectric. the hydrostatic pressure favors smaller-volume antiferroelectric and increases the transition field. therefore, the switching time increases with increasing hydrostatic pressure

### (4)  Fatigue Effects

Unfortunately. a fatigue effect is found in this family of antiferroelectric ceramics when they are driven electrically through the phase change repeatedly

Figure 13(a) shows the polarization–electric field hysteresis loops for different driving cycles for composition 5. It is observed that the hysteresis loop changes from a square shape in the virgin state to a diffused one in the fatigued state. The induced
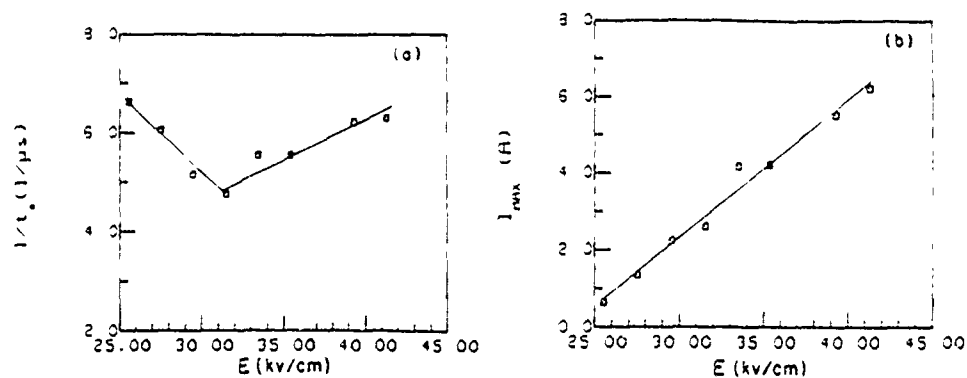
Fig. 11. (a) $1/t_s$ vs $E$ and (b) $I_{max}$ vs $E$ for composition 1
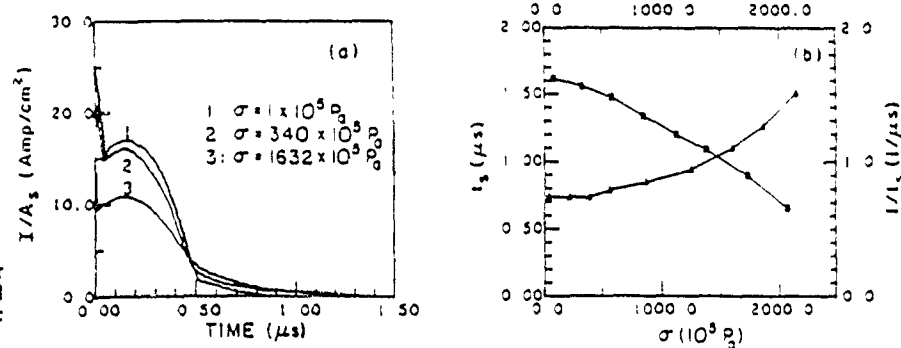
Fig. 12. (a) Switching current-time curves under different hydrostatic pressures and a fixed applied electric field and (b) $t_s$ and $1/t_s$ vs hydrostatic pressure for composition 5

polarization decreases and the transition field is diffused Figure 13(b) shows the induced polarization (normalized to that of the initial state) versus the switching cycles. It is observed that the induced polarization and strain decrease with the switching cycles up to about 500 000 cycles and then the value stabilizes at 90% of the initial polarization and 80% of the initial strain. If the fatigued sample is annealed at 300°C, the induced polarization and strain may be nearly recovered. We believe that for this composition within switching cycles attempted, the degradation effects come mainly from the modified mechanical boundary conditions of the grains in the ceramic system or the modified field distribution due to the redistribution of space charges. When the randomly oriented grains in ceramics deform under the applied electric field, they deform differently because of the dielectric and electromechanical anisotropy of the individual grains. Therefore, larger and larger internal stresses are introduced as the switching continues. Some regions may be subject to tensile stresses while other regions may be subject to compressive stresses. These internal stresses modify the transition field of different regions. The transition field is therefore diffused over a range. Some regions may become so compressive that these regions no longer are able to switch and the induced polarization therefore decreases. Under a high driving electric field, current injection from the electrode and space charge or defect redistribution within the bulk of the ceramic may also modify the local electric fields of the ceramic, giving rise to the observed fatigue effects. High-temperature annealing can relieve the internal stresses, redistribute the defects and space charges, and hence restore the original properties.

For composition 4, the fatigue effect is very severe. The induced polarization and strain as a function of switching cycles are shown in Fig. 14(a). There may also be stable $\tau$, or $P$ values for composition 4 as suggested by the plot. But these are greatly reduced with respect to the initial values. The polarization and strain hysteresis loops of a fatigued sample for composition 4 are shown in Fig. 14(b). These hysteresis loops are of completely different shape from the ones observed initially. High-temperature annealing at 300°C increases the induced polarization partly but
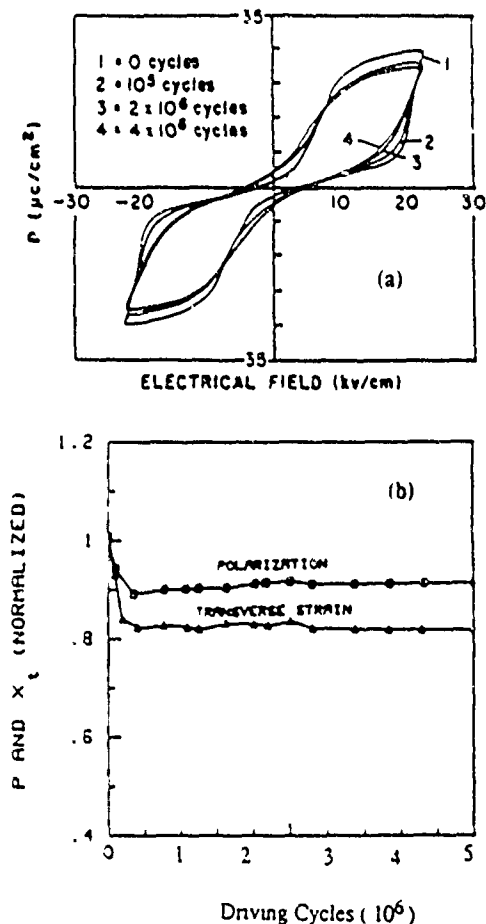
Fig. 13. (a) Polarization-electric field hysteresis loops after different switching cycles and (b) the field-induced polarization and transverse strain (normalized to the initial values) versus switching cycles for composition 5.
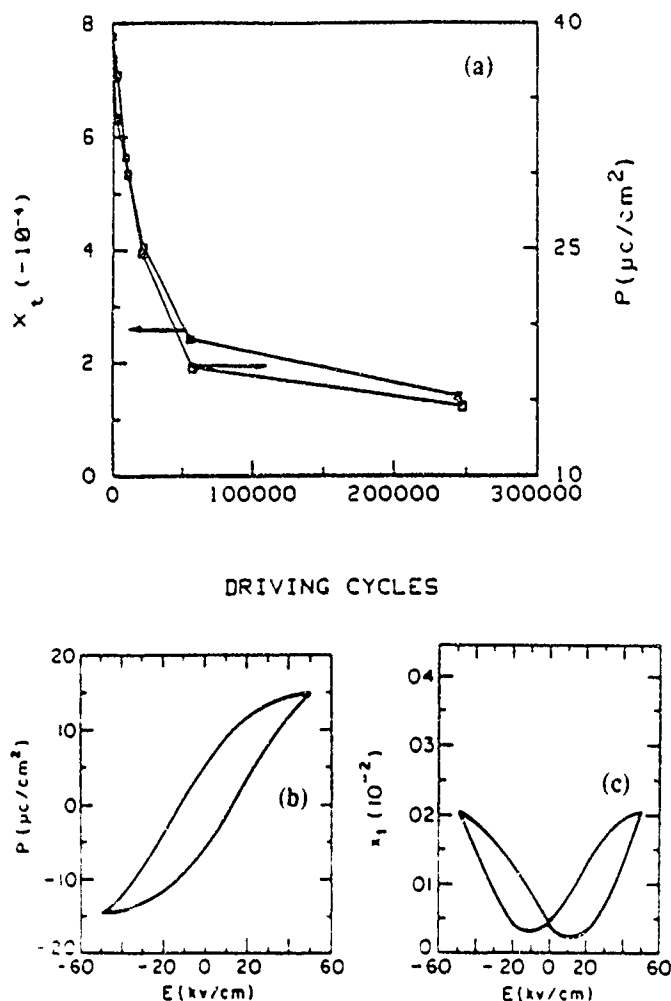
DRIVING CYCLES



Fig. 14. (a) Field (52 kV/cm) induced polarization and transverse strain as a function of switching cycles. (b) the polarization–electric field, and (c) transverse strain–electric field hysteresis loops for fatigued composition 4

the double hysteresis loop could not be recovered. It is believed that microcracks developed within the bulk of the ceramic because of the large internal stresses due to the mismatch between the grains An electron microscope study of the development of the microcracks has also been reported in fatigued doped $PbTiO_3$ ceramics [1]

## IV. Summary and Conclusions

Large field-induced longitudinal strain up to 0.85% and volume expansion of 0.95% are observed in the modified lead zirconate titanate stannate family of switchable antiferroelectric ceramics The switching is controlled by a phase nucleation process up to very high applied field level and the activation field observed is on the order of 200 kV/cm For composition 5 the switching time may be less than 1 $\mu$s if a field level above 30 kV/cm is applied. Hydrostatic pressure increases both the transition field and the switching time But the maximum induced strain and polarization are unaffected by hydrostatic pressure when the applied field is much larger than the transition field

For actuator applications, the antiferroelectric ceramics show the advantage of having large field-induced strains, especially the volume expansion The kinetics of the phase transition is fast enough to make these materials useful for most of the potential applications However, the materials show a fatigue effect when used in ceramic form, especially if the field-induced strain

involved is very large The fatigue effect should be overcome before the advantage of the large field induced strain characteristics can be utilized

## References

[1] B Jaffe, W R Cooke, Jr and H Jaffe, Piezoelectric Ceramics, pp 135-81 Monographs on Non-metallic Solids Edited by J P Roberts and P Popper Academic Press, London, 1971

[2] D Berlincourt, H H Krueger, and B Jaffe, "Stability of Phase in Modified Lead Zirconate with Variation in Pressure, Electric Field, Temperature and Composition." *Phys Chem Solids*, 25, 659-74 (1964)

[3] D Berlincourt, H Jaffe, H H A Krueger, and B Jaffe, "Release of Electric Energy in $PbNb(Zr, Ti, Sn)O_3$ by Temperature and by Pressure-Enforced Phase Transitions," *Appl Phys Lett* 3, 90-98 (1963)

[4] L E Cross, Antiferroelectric-Ferroelectric Switching in Simple Kittle Antiferroelectrics," *J Phys Soc Jpn* 23, 77-82 (1967)

[5] K Uchino and S Nomura, Shape Memory Effect Associated with the Forced Phase Transition in Antiferroelectrics *Ferroelectrics* 50, 51*-21 1983)

[6] D Berlincourt, "Transducers Using Forced Transitions between Ferroelectric and Antiferroelectric States, *IEEE Trans Sonics Ultrason* 13, 116-24 (1966)

[7] W Pan, Q M Zhang, A S Bhalla, and L E Cross, Field Induced Strain in Single Crystal $BaTiO_3$, *J Am Ceram Soc* 72 [6] C-302-C-305 (1988)

[8] W Y Pan, Q M Zhang, Q Y Jiang, and L E Cross, 'Field Induced Strain in PLZT Ceramics near the Tetragonal–Rhombohedral Phase Boundary to be published in *Ferroelectrics* 89 (1989)

[9] Q M Zhang, W Y Pan, and L E Cross, Laser Interferometer for the Study of Piezoelectric and Electrostrictive Strains *J Appl Phys* 63 2492-96 (1988)

[10] W J Merz Switching Time in Ferroelectric $BaTiO_3$ and Its Dependence on Crystal Thickness, *J Appl Phys* 27 938-43 (1956)

[11] C F Pulvari Ferrelectricity *Phys Rev* 120 1670-73 (1960)

[12] Q Li, W Y Pan, and L E Cross Effect of Hydrostatic Pressure on Polarization Reversal in Soft Nb PZT Ceramics, *J Wave Mater Interact* 1 [3] 257-64 (1986)

[13] K Carl, Ferroelectric Properties and Fatiguing Effect of Modified $PbTiO_3$ Ceramics *Ferroelectrics* 9 23-32 (1975)

APPENDIX 37

# TRANSITION SPEED ON SWITCHING FROM A FIELD-INDUCED FERROELECTRIC TO AN ANTIFERROELECTRIC UPON THE RELEASE OF THE APPLIED ELECTRIC FIELD IN (Pb,La)(Zr,Ti,Sn)O$_3$ ANTIFERROELECTRIC CERAMICS

W. Y. PAN, W. Y. GU and L. E. CROSS

*Materials Research Laboratory, The Pennsylvania State University. University Park, PA 16802. USA*

A technique is developed to measure the transition speed from a field-induced ferroelectric to an antiferroelectric phase upon the release of the applied electric field in the antiferroelectric ceramics The transition speeds of three members in the antiferroelectric (Pb.La)(Zr.Ti.Sn)O$_3$ family were investigated Switching current-time curves similar to those observed in the normal square pulse forward switching technique were found A switching time as short as 2 µSec. was found in one of the antiferroelectric compositions The switching time increases as the ferroelectric to the antiferroelectric transition field decreases Under a continuous high frequency driving field, the ferroelectric to antiferroelectric transition field is increased and the induced ferroelectric polarization is decreased due to the hysteretic heating.

## INTRODUCTION

Ceramics in the Lead Lanthanum Zirconate Titanate Stannate antiferroelectric family have been studied extensively in the past 20 years for many actual and potential applications in energy conversion.[1,2] More recently, field induced strain and kinetics of the field-forced antiferroelectric to ferroelectric phase transition were investigated.[3] A large field induced strain ($\sim 8 \times 10^{-3}$) makes this family of ceramics interesting for displacement transducer applications. However, there are controversies in the literature regarding the kinetics of the phase switching between the ferroelectric and antiferroelectric forms. A very long time (up to 0.1 Sec) was declared in an earlier paper for the field induced strain.[4] In contrast, a very short antiferroelectric to ferroelectric switching (this switching will be referred to as forward switching) time ($<1$ µsec.) under high over electric field was reported in a recent paper.[3] However, in this paper,[3] the induced ferroelectric back to the stable antiferroelectric phase switching time (this switching will be referred to as the backward switching) was not measured. As evident in the earlier work, the forward switching time may be improved dramatically by applying a large over voltage, i.e., an electric field well above the forward transition field. Clearly, an over applied electric field should not improve the backward switching speed because the forward electric field favors the ferroelectric phase. Thus, one may expect a different speed for the backward switching, depending upon the reverse field applied.

In this paper. we report a technique for measuring the speed of the backward switching under zero field and the experimental results on three members of (Pb.La)(Zr.Ti.Sn)O$_3$ antiferroelectric ceramics. These data are important for several types of actuators. In a later paper. we will report the behavior under limited reverse bias fields.

## CERAMIC SAMPLES AND PREPARATION

The ceramic compositions chosen for study were:

(1)  Pb$_{0.9}$-La$_{0.02}$ (Zr$_{0.66}$ Ti$_{0.09}$ Sn$_{0.25}$)O$_3$
(2)  Pb$_{0.9}$-La$_{0.02}$ (Zr$_{0.68}$ Ti$_{0.09}$ Sn$_{0.23}$)O$_3$
(3)  Pb$_{0.97}$La$_{0.02}$ (Zr$_{0.53}$ Ti$_{0.12}$ Sn$_{0.35}$)O$_3$

The different compositions were made up from reagent grade mixed oxides  The calcining temperatures were in the range of 750°C–900°C. Disks 1″ in diameter by 0.2″ thickness were cold pressed using a small amount of PVA binder and fired at 1280°C in a PbO atmosphere provided by excess PbZrO$_3$ in closed containers.

The dielectric hysteresis loops of these three compositions are displayed in Figure 1. The forward switching field $E_{fr}$ and the backward switching field $E_{a}$ are designated in Figure 1(a). It is observed that the $E_{a}$ values for all three compositions are greater than zero. i.e.. the antiferroelectric phase recovers before the electric field goes to zero. but the value decreases as the composition changes from (1). (2) to (3).

## MEASUREMENT TECHNIQUE

The principle utilized in the measurement is to induce a ferroelectric polarization by applying an electric field above $E_{fr}$. then to quickly release the electric field and measure the current due to the discharge of the sample as a function of time. The block diagram for the measuring system is shown in Figure 2. The transistor used was a SIPMOS power field effect transistor (FET) with a drain-source break down voltage of 1000 volts. a "on" resistance 5Ω and a "turn on" time of 45 nano seconds.
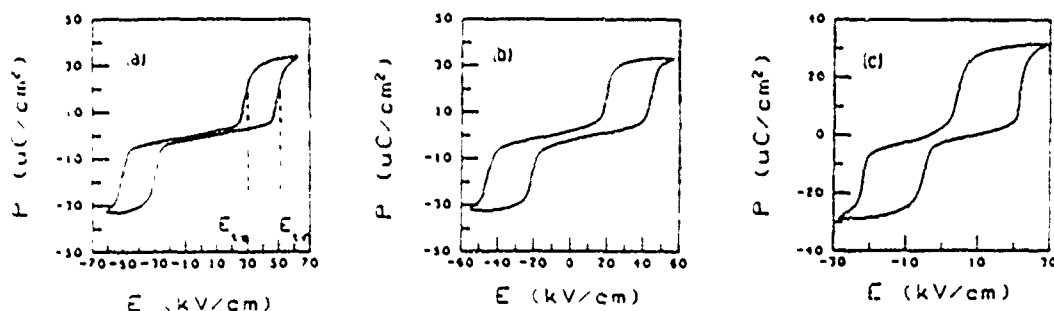


FIGURE 1   P-E hysteresis hysteresis loops under AC field frequency 0 5 Hz. (a) composition (1) (b) composition (2) and (c) composition (3)
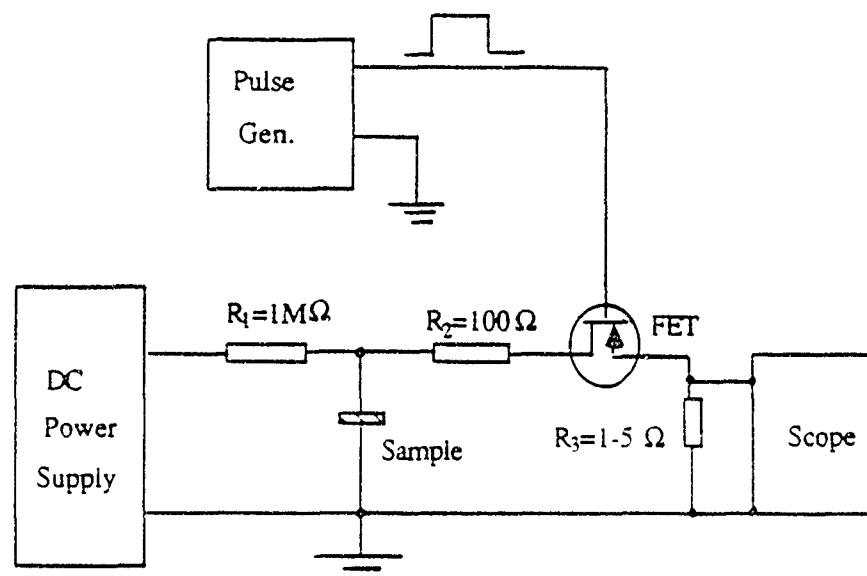
FIGURE 2   Block diagram for the measuring system

The oscilloscope used for the measurement was a Nicolet 204 A digital oscilloscope with a bandwidth of 20 MHz. The pulse generator used was a Hewlett Packard type 214 B pulse generator with a rise time of 20 nano seconds. When no voltage is applied to the gate and ground of the FET, the FET is "off" and thus the applied voltage drops across the sample to induce a large ferroelectric polarization. When the pulse generator is manually triggered, a square pulse is applied to the gate-source junction to turn the FET "on" and the field across the sample is reduced to nearly zero. The discharge, then, takes place through the small resistor $R_3$. It must be remembered that the discharge may also take place through the loop involving the DC powder supply and $R_1$. However, since the resistance of $R_1$ was large compared to $R_3$, so the current flow could be neglected. The purpose of putting the resistor $R_2$ in the discharging loop is to damp the high frequency piezoelectric resonance modes.[5] After $R_2$ is placed in the circuit, the area of sample is limited by the time constant of the sample capacitance and the resistors in the discharging loop. Figure 3 illustrates this fact. Curve (b) is the discharge current-time curve of composition (1). The area of the sample was 0.14 cm$^2$ and the applied field was 70 kV/cm. Curve (a) is the discharging current-time curve of a linear capacitor charged to same amount of charge under the same applied voltage. Clearly, the sample discharged slower and has a second current maximum. Evidently, the first peak is due to the discharge when the field is reduced from the applied field to backward switching field $R_s$, and the second part is due to the backward phase switching. The shape of the curve is very similar to that of forward switching.[3] When the area of the sample was reduced, two effects were observed: the height of the second maximum decreased and the time of the maximum moved toward the left. Apparently, the decrease of the height is caused by the reduced induced polarization charges, and the movement to the left is due to the decrease of the RC time constant caused by the decrease of the sample area.
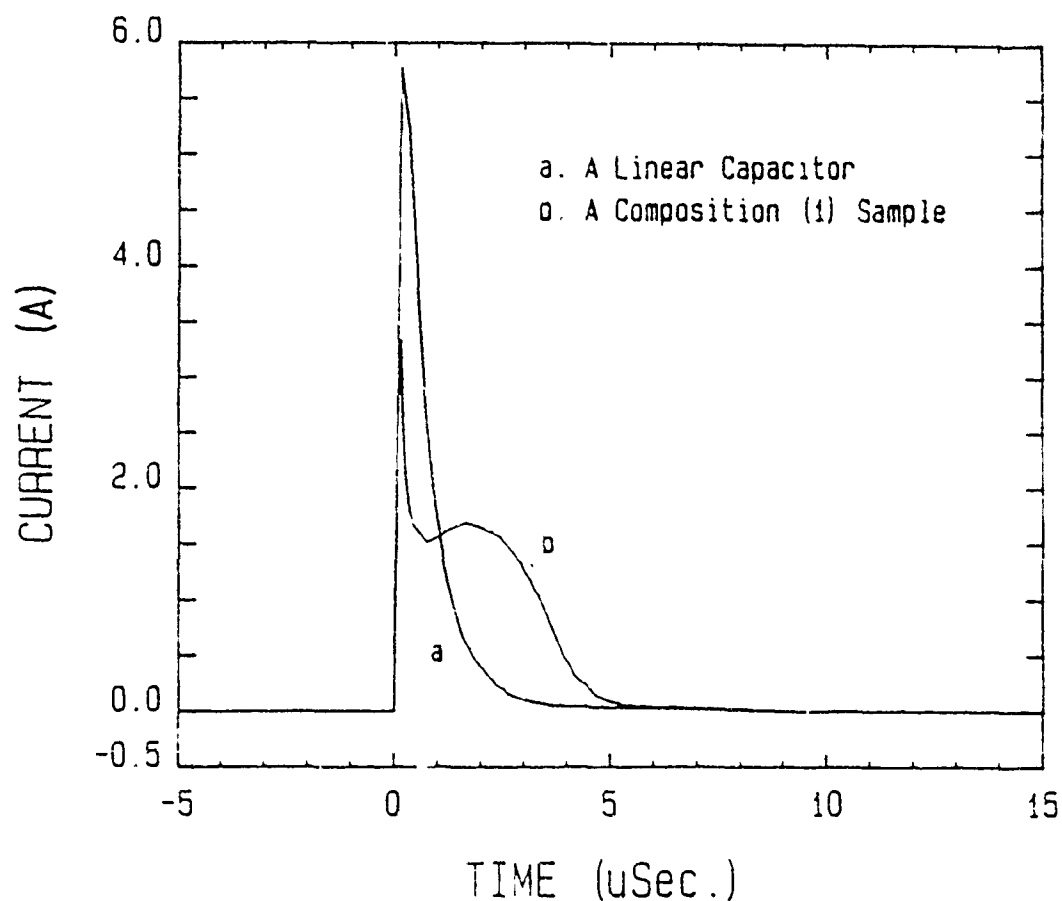
FIGURE 3   A comparison of discharge current-time curves of (a) a charged capacitor and (b) a composition (1) ceramic sample with area of 1.14 cm². The applied voltages a, 100 volts, and total induced polarization charges are the same for both ceramic sample and the linear capacitor.

However, when the sample area was reduced to a certain limiting value, further decrease did not cause the second current maximum to move to the left, but only to reduce its height. Under this condition, it may be said that the time constant in the discharge loop no longer affects the backward switching time. It was for this reason that the areas of the samples were kept under 0.03 cm² so that the backward switching speeds of all three compositions were not affected. The maximum allowed gate-source voltage was 20 volts, this value limited the resistance value of $R_1$. If $R_1$ is too large, the voltage across $R_1$ may go higher than the gate voltage, causing the FET to turn "off." Since $R_1$ can not be larger than 5Ω, minimum area below 0.03 cm² was set by the signal-to-noise ratio.

## EXPERIMENTAL RESULTS AND DISCUSSIONS ON (Pb,La)(Zr,Ti,Sn)O₃ ANTIFERROELECTRIC CERAMICS

The backward switching currents of composition (1) for three different applied fields is shown in Figure 4(A). Similar to that in the earlier work,[*] the switching time $t_s$ in this work is defined as the time at which the current decreases to 10%
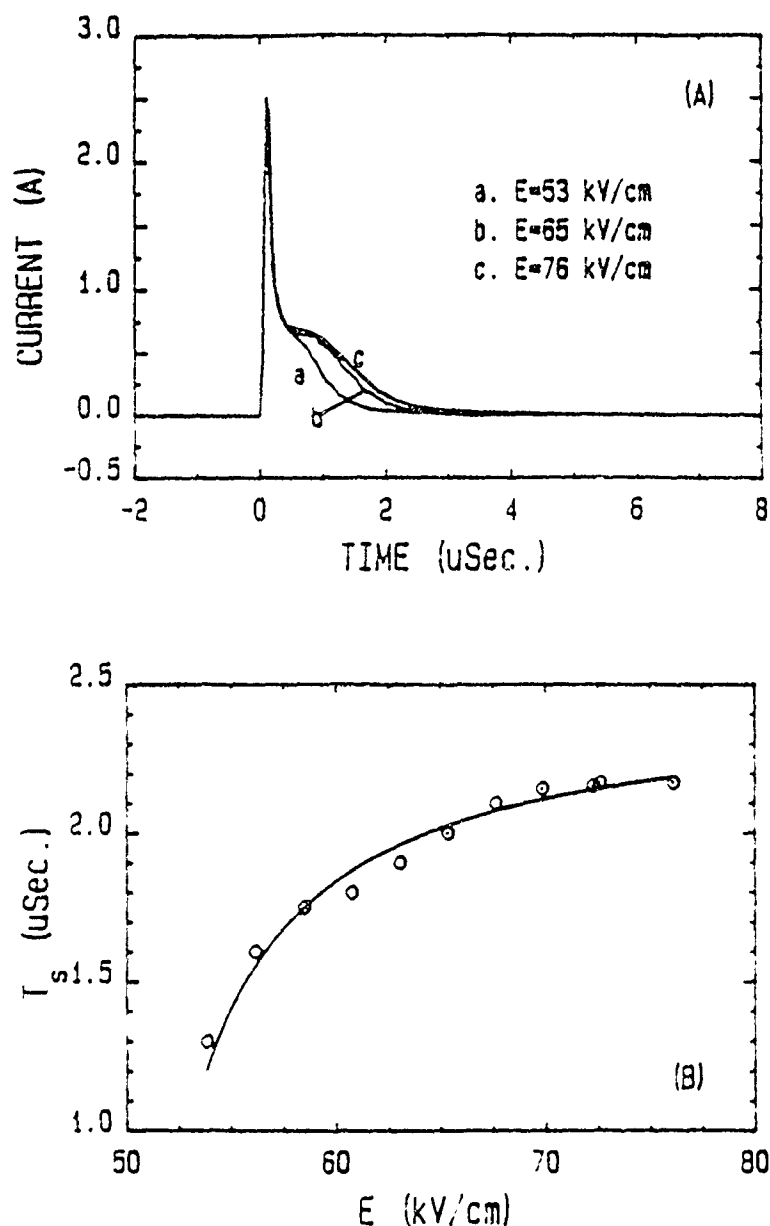
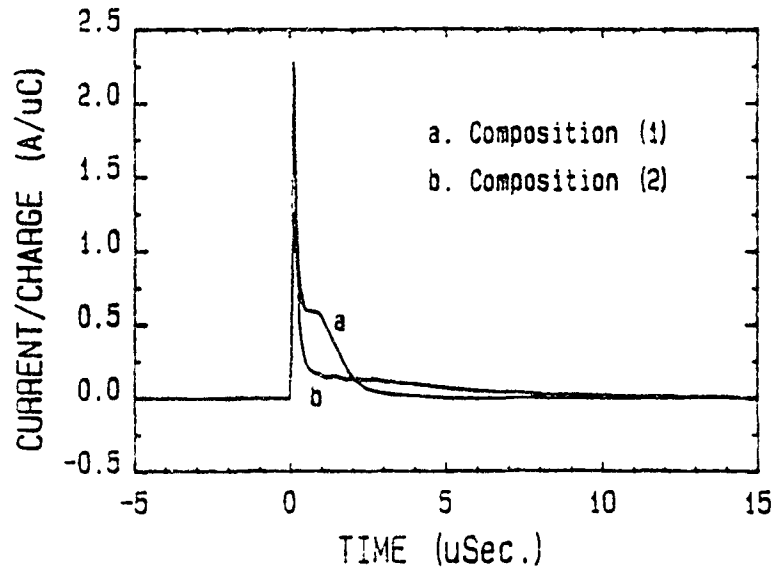FIGURE 4   (A) Backward switching current-time curves of composition (I) for different applied fields (a) 53 kV cm, (b) 65 kV cm and (c) 76 kV cm  (B) Backward switching time $\tau_s$ vs the applied electric field of composition (I)

of the value at the second maximum. The switching time as a function of the applied field is shown in Figure 4(B). It is observed that the switching time increases with the applied field and then reaches an almost constant value at about 70 kV cm. When the applied field is below 70 kV cm, the area under the switching current-time curve, a measure of the total induced charges, decreases appreciably with decreasing applied field. In Figure 4(A), for example, the area for an applied field of 53 kV cm is significantly less than those for higher applied fields. Accordingly, in Figure 1(a), the total ferroelectric polarization is not fully induced at 53 kV cm. Above the field of 70 kV cm, when an almost constant switching time is observed

in Figure 4(b). the induced ferroelectric polarization may also be expected not to increase significantly with increasing applied electric field as shown in Figure 1(a) The initial increase and the subsequent "level off" of the switching time with the applied field may be explained by the sharpness of the forward transition field. In Figure 1(a). the forward transition field $E_,$ is not perfectly defined and distributed over a field range instead. In this field range. the ferroelectric polarization is not fully induced and the ferroelectric phase is not fully stabilized. One may image that the stability of the ferroelectric phase increases with increasing applied field and thus the energy barrier for the recovery of the antiferroelectric phase increases with the increasing applied field within this field range. As a result. the switching time increases with increasing applied field. When the applied field is high enough to complete the antiferroelectric to ferroelectric phase transition. further increase in the applied field would not increase the stability of the induced ferroelectric phase significantly and thus the switching time levels off with increasing applied field.

The backward switching currents for composition (2) under different applied electric fields are shown in Figure 5. The switching behavior is basically the same as that for composition (1). But the second maximum for this composition is not very distinct and therefore the switching time as a function of the applied field is difficult to plot. It may also be seen from the figure that the switching current value goes to zero for times greater 10 μSec.. which is significantly longer than that for composition (1).

Figure 6 shows a comparison of the switching current curves of composition (1) and composition (2). The applied field for composition (1) is 75 kV cm and 67 kV cm for composition (2). It may be seen trom Figure 1 that under such applied field levels. the ferroelectric polarizations for both compositions are fully induced Since the total charges induced for two compositions are different because the ferro-
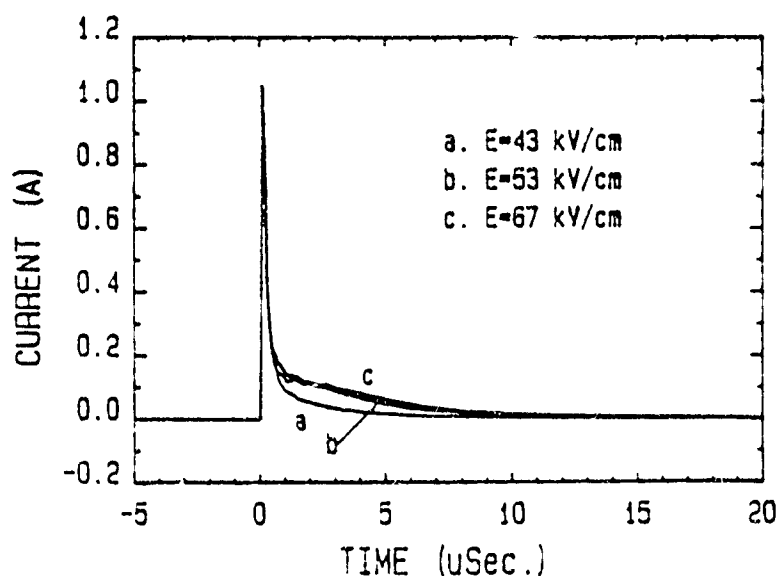


FIGURE 5    Backward switching current-time curves of composition (2) for different applied fields (a) 43 kV cm. (b) 53 kV cm. and (c) 67 kV cm

FIGURE 6   A comparison of backward switching current-time curves for composition (1) and (2) (the currents for two compositions were divided by their respectively total charges The applied field for composition (1) is 75 kV cm and that for composition (2) is 67 kV cm).

electric polarization values as well as sample areas for the two compositions were not the same. The switching current is, for the purpose of comparison, divided by the total charge induced. It may be seen that areas under the switching current-time curves for these two compositions are roughly equal, however, the switching time for composition (2) is much longer. The same measurement was also carried out on composition (3). The situation was even worse. The switching current was so spread out on the time axis that the real switching time could not be ascertained by the present technique.

In the forward switching, the switching time decreases as the over electric field $E_{app} - E_{ft}$ increases.[3] In the backward switching, on the other hand, the switching time may be expected to increase as the over electric field $E_{ta}$ ($E_{ta} - 0$) decreases. Thus the increase of the switching time as the composition changes from (1), (2) to (3) should be due to the decrease in backward switching field since the backward switching field decreases from 30 kV cm, 20 kV cm to 5 kV cm as the composition changes from (1), (2) to (3). Clearly, the difference between the backward switching field and the zero field is the driving force for the recovery of the antiferroelectric phase from a field induced ferroelectric phase upon the release of the applied electric field. The higher the $E_{ta}$, the larger the driving force for the backward switching and the shorter the switching time. For composition (3), if the applied field is suddenly reduced to a negative value, but not too negative to pass the $E_{ft}$ value in the negative direction, the driving force for the recovery of the antiferroelectric phase may be increased and the switching time may be shorter.

The switching times presented above were all obtained from "single shot," i.e., the transition from the ferroelectric phase to the antiferroelectric phase just occurred once. When the sample is driven continuously by an AC field, the P-E hysteresis effect will generate heat, modifying the original switching behavior. Figure 7 shows the P-E hysteresis loops under three different AC field frequencies. Figure 3 shows the forward switching field and backward switching field as a
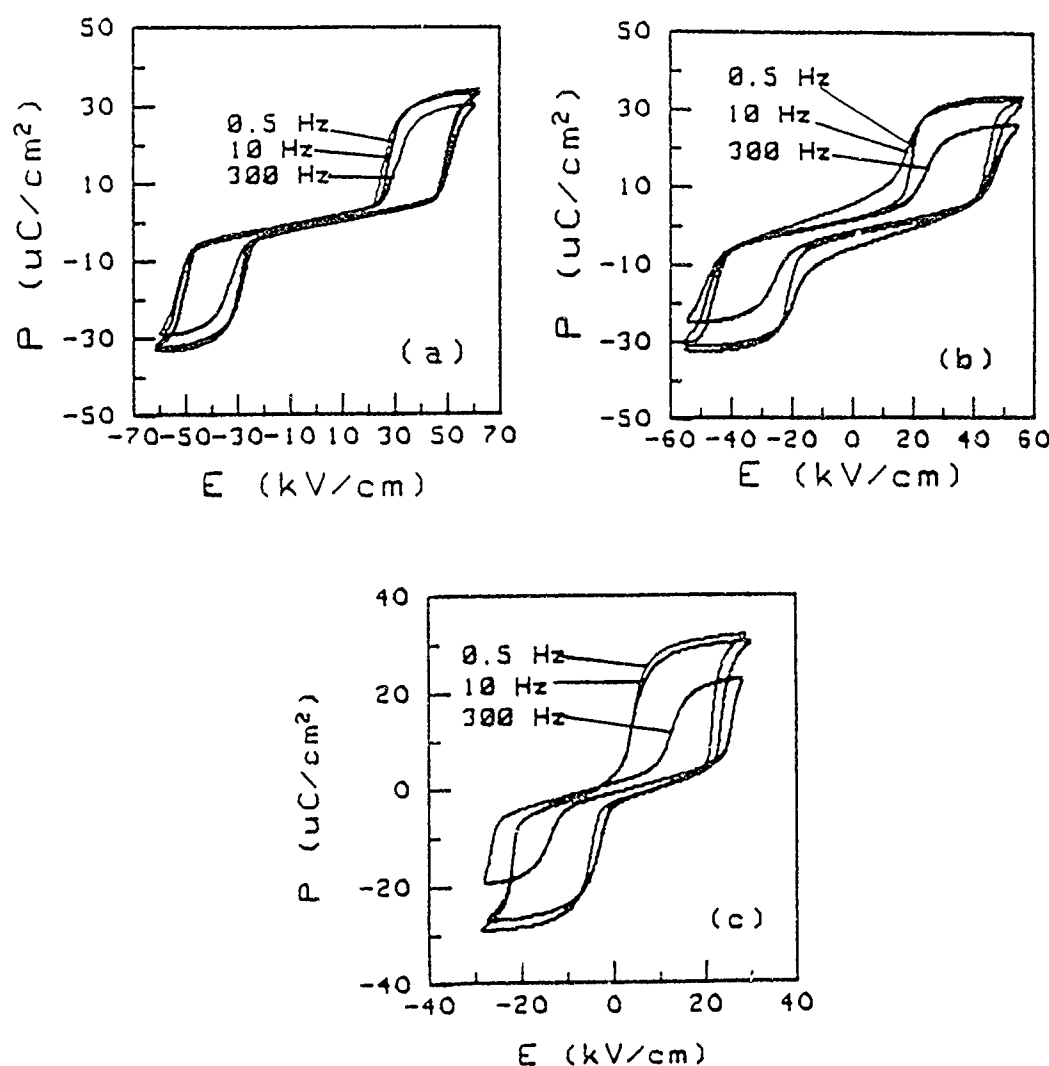
FIGURE ~   P-E hysteresis loops under different driving frequencies (a) composition (1), (b) composition (2) and (c) composition, (3), (the frequencies are as illustrated)

function of the driving field frequency. For all three compositions, the forward switching field increases slightly with increasing driving frequency, while the backward switching field decreases slightly with driving field frequency up to 10 Hz and then increases with the increasing driving field frequency. For the hysteresis loops of 300 Hz, the $E_{ra}$ values are increased greatly and ferroelectric polarization values decreased appreciably with respect to those of 0.5 and 10 Hz. Clearly these phenomena can not be explained by the kinetics of the phase switching. It was observed in the earlier work' that well below room low temperature, this family of antiferroelectrics transforms into ferroelectrics, and within the antiferroelectric phase temperature range, the transition fields, especially $E_a$, increase with increasing temperature under constant driving field frequency (0.1 Hz). Because the hysteretic heating effect increases with increasing driving frequency, the high driving frequency in this work is equivalent to the high temperature in the earlier work. Thus, the dielectric parameters observed in the high frequency dielectric hysteresis loops
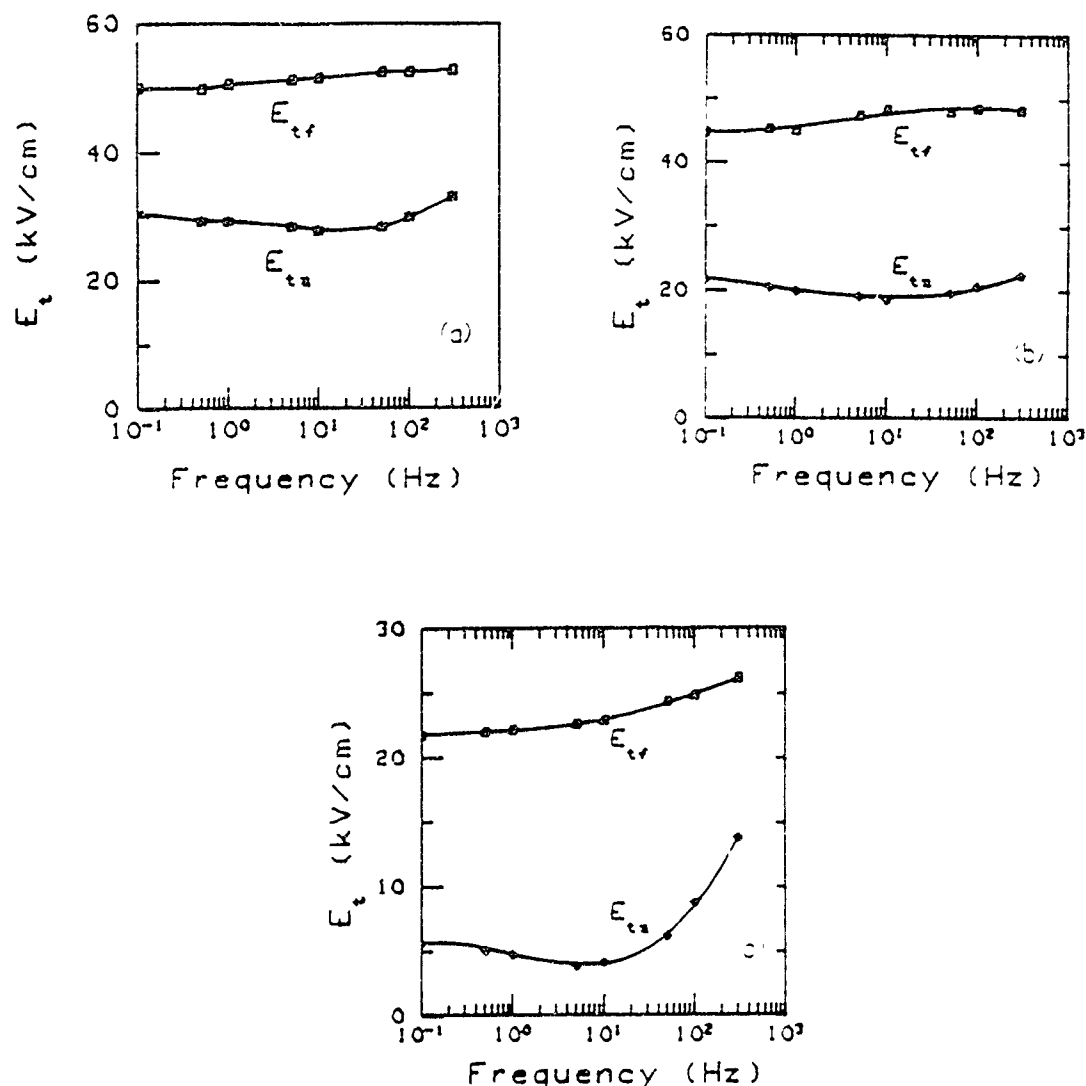
FIGURE 3  Forward switching field $E_{tf}$ and backward switching field $E_{ta}$ vs driving frequency (a) composition (1), (b) composition (2) and (c) composition (3)

are not the intrinsic properties at room temperature. It was also observed that the variation of the hysteresis loop parameters with temperature was most pronounced near to the antiferroelectric to ferroelectric phase transition temperature. Composition (3) has the lowest $E_{tf}$ and $E_{ta}$ values compared with composition (1) and (2), thus its antiferroelectric to ferroelectric phase transition temperature may be expected to be more close to room temperature than those for composition (1) and (2). This may be reason why Figure 8(c) shows the most pronounced increases of $E_{ta}$ with the driving field frequency. Apparently, a slim loop antiferroelectric as suggested by Berlincourt is preferred to overcome the hysteretic heating effect for the continuous driving applications.

REFERENCES

1  B Jaffe, W R Cook, Jr and H Jaffe. *Piezoelectric Ceramics*, Academic Press London Monographs on Non-metallic Solids (1971)

2. D  Berlincourt, H. H  Krueger and B  Jaffe. *Phys  Chem  Solids*, **25**, 659 (1964)
3  W  Y  Pan, Q  M  Zhang, A  S  Bhalla and L  E  Cross (will be published in the next issue of Journal of Amer  Cer  Soc )
4  K  Uchino and S  Nomura. *Ferroelectrics*, **50**, 517 (1983)
5  Q  Li, W  Y  Pan and L  E  Cross. *J  of Wave Materials Interaction*  **1**, 258 (1968)
6  E  Fatuzzo and W  J  Merz. *Physic Review*  **116**, 61 (1959)
7  D  Berlincourt. *IEE transactions on Sonic and Ultrasonic*, **13**, 116 (1966)

Associated   Program

J.H. Jeng, X. Bao, V.V. Varadan, V.J. Varadan

Design and Analysis of PZT/Polymer 1:3 Type Composites.

Work on this program has been focused upon a detailed analysis of the 1:3 type PZT/Polymer composite transducer interacting with a fluid medium.   A finite element analysis of the problem has been carried out and is reported in detail in appendices 38 and 39.

In a second study, numerical simulations were compared to experimental data from earlier published work and from new measurements performed in the Center for Engineering of Electronic and Acoustic Materials.   Parametric studies involving systematic variation of fiber geometry and volume fraction are now being completed. The formulation used takes advantage of some new 3-D piezoelectric elements incorporated in the ANSYS computational package and represents a powerful new design tool for composite transducers.

APPENDIX 38

# DESIGN AND ANALYSIS OF THE PERFORMANCE OF PZT/POLYMER COMPOSITE TRANSDUCERS

J.H. Jeng, V.V. Varadan and V.K. Varadan

Center for the Engineering of Electronic & Acoustic Materials,

Department of Engineering Science and Mechanics,

The Pennsylvania State University, University Park, PA 16802

## SUMMARY

In this report we have conducted a detailed parametric study using the finite element formulation including the effect of fluid loading for the design of composite piezoelectric transducers by varying a) diameter of piezoelectric fibers relative to transducer thickness (b) properties of filler material. Results from numerical modeling were compared with earlier composite samples prepared by Gururaja et al and two new samples prepared at the Center. Very good agreement was obtained between predicted and observed performance. Parametric studies varying the volume fraction of the piezoelectric phase ( inter fiber spacing ), non–circular fibers - square, rectangular, elliptical as well as fibers of varying cross=sectional diameter such as a conical frustum are being investigated. Results should be available in the next few months. A new formulation that can take advantage of certain new 3-D piezoelectric elements incorporated into the ANSYS package are also under development. A powerful tool has been developed for computer aided transducer design.

## I. INTRODUCTION:

PZT/polymer composite materials have been widely used in ultrasonic applications due to their desirable material properties such as high electromechanical coupling and low acoustic impedance. An ultrasonic probe that has broadband performance and high sensitivity characteristics is considered in this report. In order to properly evaluate the performance and realize a good design, we need both experimental verification and analytical simulation. The finite element approach has been used to simulate the vibrations of a composite disk containing piezoelectric elements in the form of rods. The detailed derivation and formulation has been reported before, and is enclosed again as an Appendix to this report. In these studies, the effect of fluid loading and material damping was considered. The advantages of this formulation are that (1) the details of the modal information for different microstructures are given, (2) the effect of fluid loading on transducer performance can be easily included via the effective modal force on the transducer face, (3) the effect of matching layer,

the electric impedance, and the internal losses are included in the computation.

## II. NUMERICAL RESULTS AND DISCUSSIONS:

The numerical results presented are the normalized frequency spectra and the normalized electric conductance spectra. In addition, the frequency constant is tabulated for different designs. As mentioned, the width to the thickness ratio w/t, is an important factor in designing and fabricating PZT/Polymer probes. We proposed several different microstructures and different host matrix materials in the computation to study this effect. In all cases the fiber cross section is square. These cases are

(A) Host Material is Spurr Epoxy which has acoustic impedance as $2.27*E06$ kg/m²-sec:
   (1). w/t=1/10, (2) w/t=1/5, (3) w/t=1/2.5, (4) w/t=1/2,

(B) Host Material is RE2039/HD3475 which has acoustic impedance as $3.117*E06$ kg/m²sec:
   (1). w/t=1/10, (2) w/t=1/5, (3) w/t=1/2.5,

(A) Host Material is Insulcast 135 which has acoustic impedance as $4.707*E06$ kg/m²-sec:
   (1). w/t=1/10, (2) w/t=1/5, (3) w/t=1/4, (4) w/t=1/3.

As we can see, these cases cover a wide range of design parameters that can be used in designing the 1-3 composite transducer. Concerning the choice of a host medium, for instance, we have computed cases with a low acoustic impedance $2.27E06$ kg/m²-sec, as well as a higher acoustic impedance, $4.71E06$ kg/m²-sec. Most of the commercial epoxy which are suitable for using as the host medium are located in this range. Based on computations, we are able to decide the width to thickness ratio, the operating frequency and the matching impedance for special purposes.

Two tables are presented. Table I lists the acoustic properties of the three host materials. The Spurr epoxy is an acoustically soft material and the Insulcast 135 is an acoustically hard material in contrast. Table II lists the frequency constants for the composite disk if operating in air and when operating in a water medium. The water loading lowers the frequency constant by about 10 % and can be considered as an external damping effect. From Table II, it can be concluded that the higher the acoustic impedance of the host medium, the higher the frequency constant. It implies that the operating frequency of a transducer can be increased for the same thickness of the composite disk by varying the acoustic impedance of the host medium. Furthermore, the results show that acoustically hard materials operate with a smaller w/t ratio than acoustically soft materials for getting a clear thickness vibration mode..

Figures 1 to 7 present the frequency spectrum, which is the transmission efficiency vs.

normalized frequency. The transmission efficiency is defined as the amount of acoustic pressure, which is generated by a unit driving voltage, radiated into the fluid medium. Figures 1a, 2a, and 3a present results considering only the fluid loading effect while Figures 1b,2b, and 3b present results which include both the fluid loading effect and the material damping effect. For Spurr epoxy, a coupled vibration mode can be observed in Figure 3 with w/t ratio equal to 1/5. The wave spectrum was distorted and showed two peaks. Thus, the optimized w/t ratio we suggest is 1/4.5. For Insulcast 135, the coupled mode appears for a w/t ratio equal to 1/3, see Figure 7, which is a higher value than that of Spurr epoxy. For the same saw cut slot. w, the Insulcast 135 can be fabricated as a thinner disk and realize a higher frequency constant. For RE2039/HD3475. the frequency spectrum shows characteristics similar to the Spurr Epoxy but with higher w/t ratio, as shown in Figure 6.

The material damping ratio, $\xi$, is equal to 0.06 for Spurr Epoxy. It is determined by measuring the mechanical Q of the composite disk in air which has a value of 8.4. From the computation, the mechanical Q of the composite disk is calculated as 7.06 for w/t=1/10 by considering only the fluid loading effect. The two Q values, one for the damping effect and the other for the fluid loading effect, are very close to each other. This shows that the fluid loading and the material damping have an equal effect on transducer performance and both cannot be neglected in transducer design simulation programs.

The maximum peak value decreases when the w/t ratio increases, as shown in Figures 3 to 7. It can be interpreted as the strong coupling between the lateral vibration and the thickness vibration as the w/t ratio increases. We also notice that the lateral vibration results in a distortion of the main spectral peak. The distortion in some cases, eg. w/t=1/5 in Fig.4, can broaden the spectrum, however, it can also suppress the resonance band to several resonance peaks as shown in Fig. 3, 5 and 7. Thus,we can achieve an optimized design by varying the w/t ratio according to the matrix material to have a broadband response, low mechanical Q, and a smooth spectrum.

Figures 8 to 13 show the the normalized conductance, G, vs the normalized frequency. Figure 9, reveals that the first lateral mode, $f_{t1}$, which occurs at f=1.68, has a very strong electric coupling. This coupling enhances the broadband characteristics in the frequency spectrum. It means that the effective coupling factor is enlarged. However, the electric impedance of the transducer is also increased.

## III. EXPERIMENTAL RESULTS:

First the numerical simulation was used to compare with the results obtained by Gururaja et

al with relatively lower frequency PZT – polymer composite transducers. Sample #101 of their paper [1] has w= 45mm, t = 1.95 mm and periodicity is 1.27 mm. The volume fraction of PZT is 10%. The experimental results and the simulation values ( number in parentheses ) agree quite well:

> Thickness mode frequency   640 kHz ( 599 kHz )
>
> First lateral mode frequency   804 kHz ( 813 kHz)
>
> Second lateral mode frequency  1096 kHz ( 960 kHz)

Discrepancies can be attributed to inaccuracies in the input values of material constants in the computer program and alignment of the PZT rods.

Two new samples were also made. They were composite disks made for further experimental verification of theory. These samples were fabricated by the dicing and filling technique in which a PZT disk was saw-cut to resemble a periodic arrangement of pillars or straight fibers protruding from a solid disk, the inter fiber spaces was filled with a polymer and the solid base was then machined off. Spurr Epoxy was considered as the filling material. Its longitudinal and transverse wave velocities were measured to be 2060 m/sec and 1150 m/sec respectively. The acoustic impedance is 2.27E+06 kg/m²-s and the density is 1100. kg/m³.

The width or diameter of fiber (w) to thickness of the transducer (t) ratio, w/t, is 1/10 for Sample 1 and is 1/4.1 for sample 2. The volume fraction is 25% since the fiber diameter is equal to the periodic interfiber spacing. The frequency spectra measured in water, are plotted in Figures 14 and 15 for sample 1 and 2 respectively. The mechanical Q for the two samples has the value of 3.6 and 8.4 in air and 3.75 and 3.4 in water. A small distortion is noticed in Figure 15 due to the effect of the first lateral resonance mode. The experiment results show that the composite disk has good impedance matching with the fluid medium compared with pure PZT disk for which the Q value is around 30 in water. The measured frequency response also agrees very well with the predicted frequency response in Figures 1 and 2 ( note this is for w/t=1/5, whereas sample has w/t=1/4.1)

## IV. CONCLUSION:

In this study, we have performed an experimental and analytical study of composite transducer design. The numerical simulations were verified by the experimental measurement and the published data on the literature. Based on the experimental analysis, we can gain practical insight into manufacturing difficulties. Currently non-availability of proper cutting technology for ceramics limits the upper limit for the frequency. In this report, we have presented two Tables and

fifteen figures which provide adequate guidance for the designer to design a 1-3 PZT/epoxy transducer for different purposes. Parametric studies varying the volume fraction of the piezoelectric phase ( inter fiber spacing ), non–circular fibers - square, rectangular, elliptical as well as fibers of varying cross=sectional diameter such as a conical frustum are being investigated. Results should be available in the next few months. A new formulation that can take advantage of certain new 3–D piezoelectric elements incorporated into the ANSYS package are also under development. A powerful tool has been developed for computer aided transducer design.

REFERENCE
T.R. Gururaja, W.A. Schulze, L.E. Cross, R.E. Newnham, B.A. Auld and Y.J. Wang, IEEE – Sonics and Ultrasonics, SU 32, 1985

Table I. Material constants for matrix medium:

| | Spurr Epoxy | RE2039/HD3475 | Insulcast 135 |
|---|---|---|---|
| Mass density | 1110. kg/m3 | 1153. | 1585. |
| Acoustic Impedance 10E06 | 2.27 kg/m2 s | 3.1169 | 4.7073 |
| C11 *E10 N/m2 | 0.471 | 0.84262 | 1.398 |
| C44 *E10 N/m2 | 0.147 | 0.19384 | 0.357 |

Table II. Frequency Constant:

Spurr Epoxy:

| w / t ratio | 1/10 | 1/5 | 1/2.5 | 1/2 |
|---|---|---|---|---|
| f*t (MHz.mm) air | 1.745 | 1.69 | 1.40 | 1.273 |
| f*t water | 1.59 | 1.58 | **** | **** |
| Acoustic Z kg/m2-s (10E6) | 9.605 | 9.30 | **** | **** |

RE2039/HD3475:

| w / t ratio | 1/10 | 1/5 | 1/2.5 | |
|---|---|---|---|---|
| f*t (MHz.mm) air | 1.8455 | 1.8265 | 1.68 | |
| f*t water | 1.68 | 1.6954 | **** | |
| Acoustic Z kg/m2-s (10E6) | 10.158 | 10.05 | **** | |

Table II. Frequency Constant (continued):

Insulcast 135:

| w / t ratio | 1/10 | 1/5 | 1/4 | 1/3 |
|---|---|---|---|---|
| f*t (MHz.mm) air | 1.87 | 1.854 | 1.84 | **** |
| f*t water | 1.7145 | 1.7145 | 1.722 | **** |
| Acoustic Z kg/m2-s (10E6) | 10.29 | 10.20 | 10.125 | **** |

PZT-5H:

| | |
|---|---|
| f*t (MHz.mm) air | 2.1 |
| Acoustic Z kg/m2-s (10E6) | 32.25 |
| Density Kg/m3 | 7678.8 |

Fig. 1    Spectrum of Transmission Efficiency in Water for PZT Fibers
          Embedded in Spurr Epoxy

Fig. 2    Spectrum of Transmission Efficiency in Water for PZT Fibers
Embedded in Spurr Epoxy
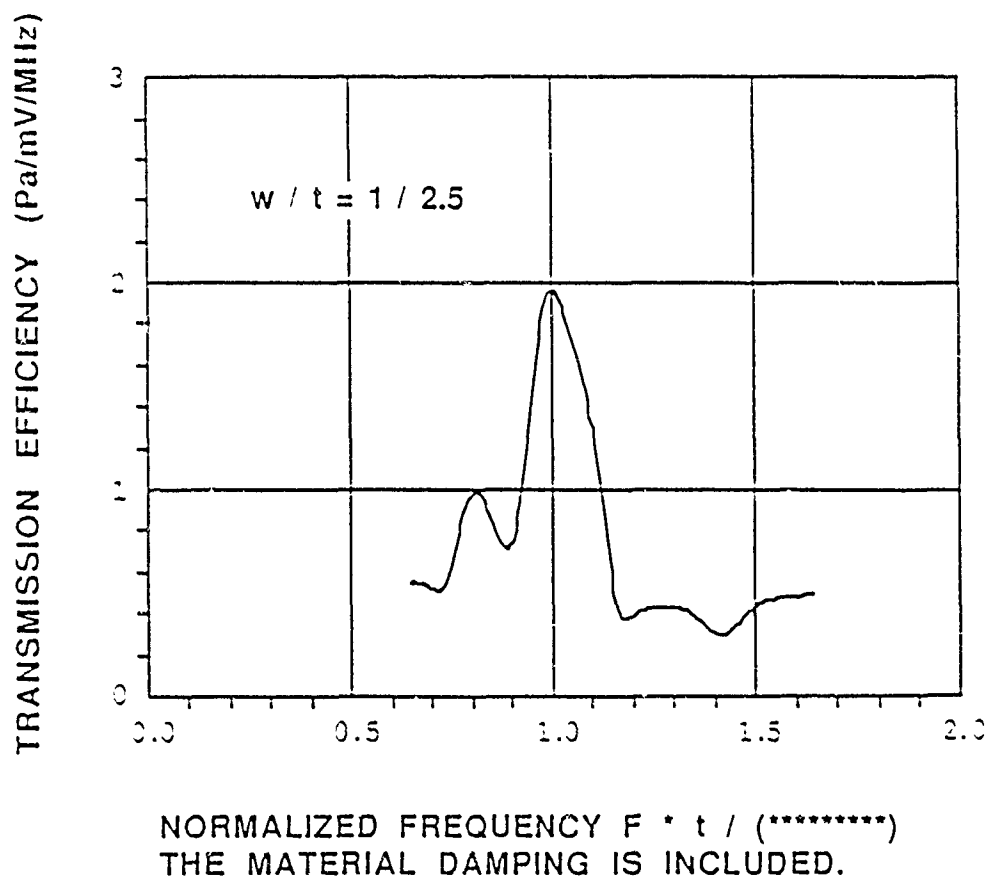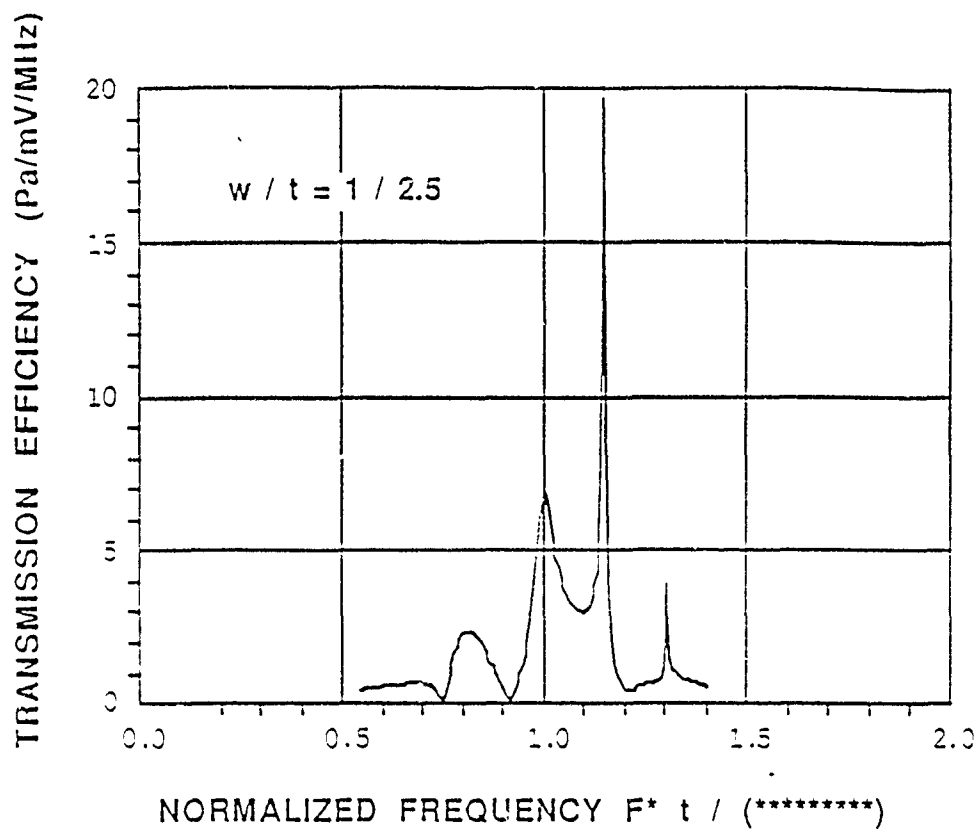
Fig. 3   Spectrum of Transmission Efficiency in Water for PZT Fibers
Embedded in Spurr Epoxy
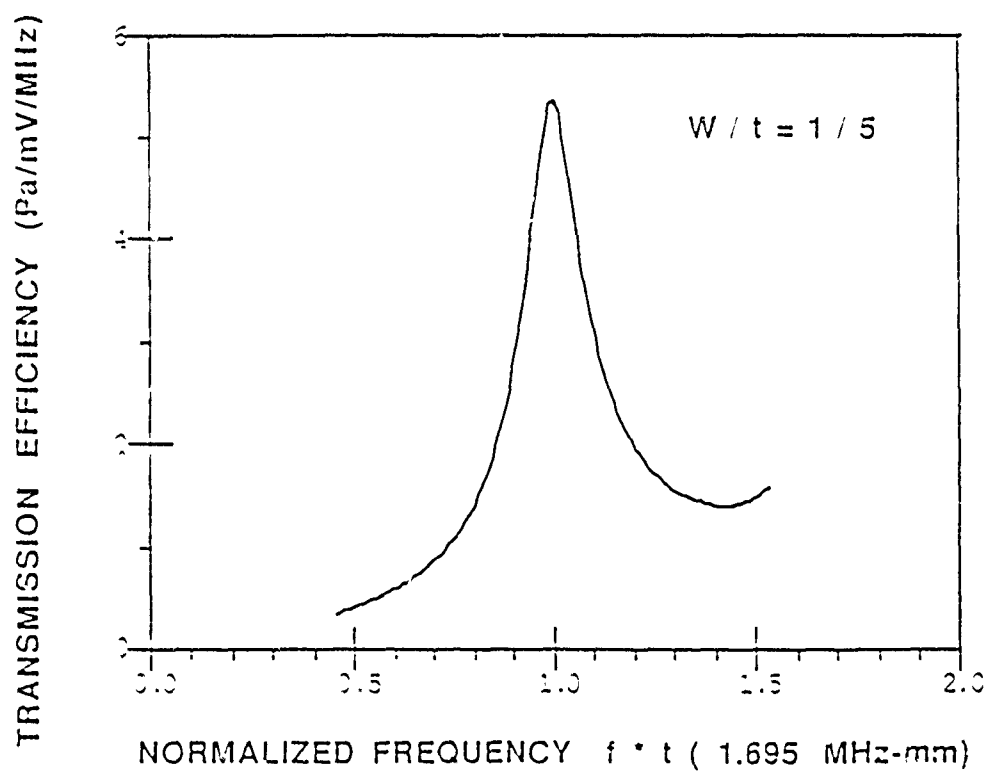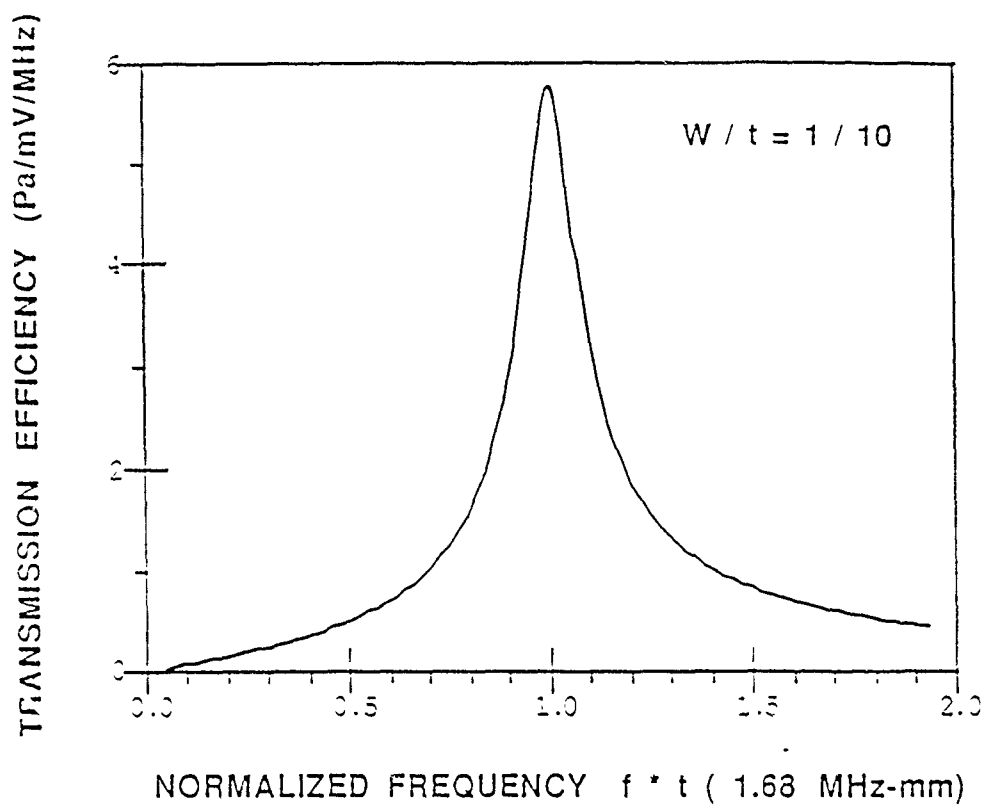
Fig. 4   Spectrum of Transmission Efficiency in Water for PZT Fibers Embedded in RE2039/HD3475
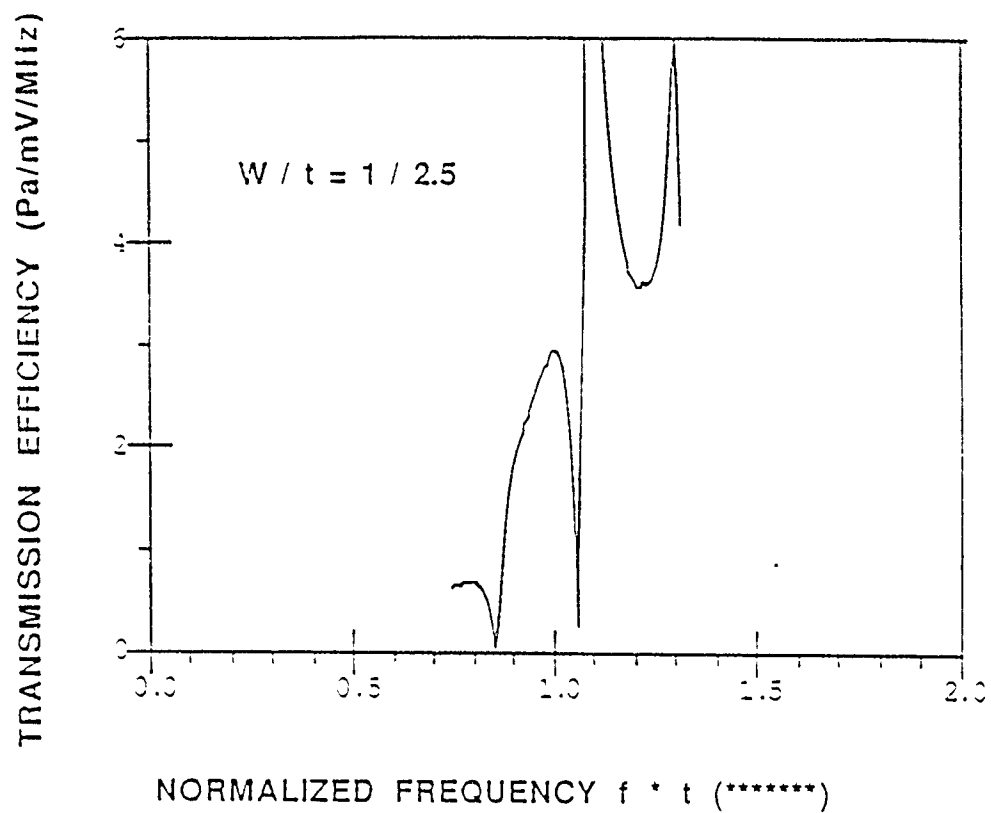
Fig. 5   Spectrum of Transmission Efficiency in Water for PZT Fibers
Embedded in RE2039/HD3475
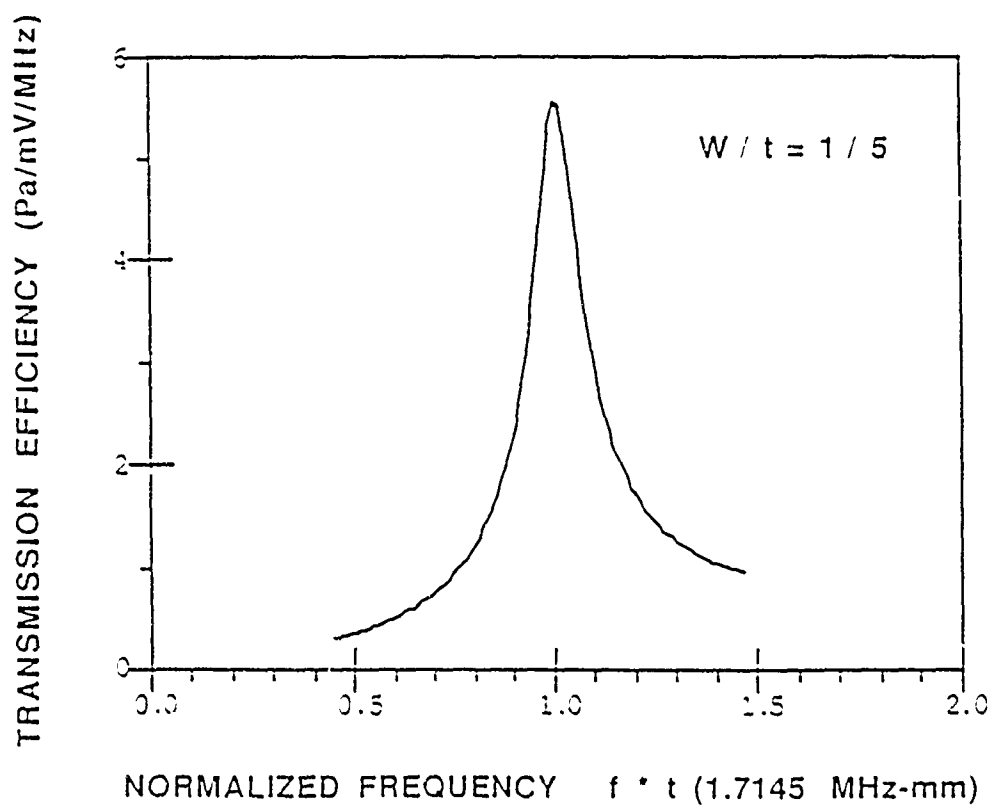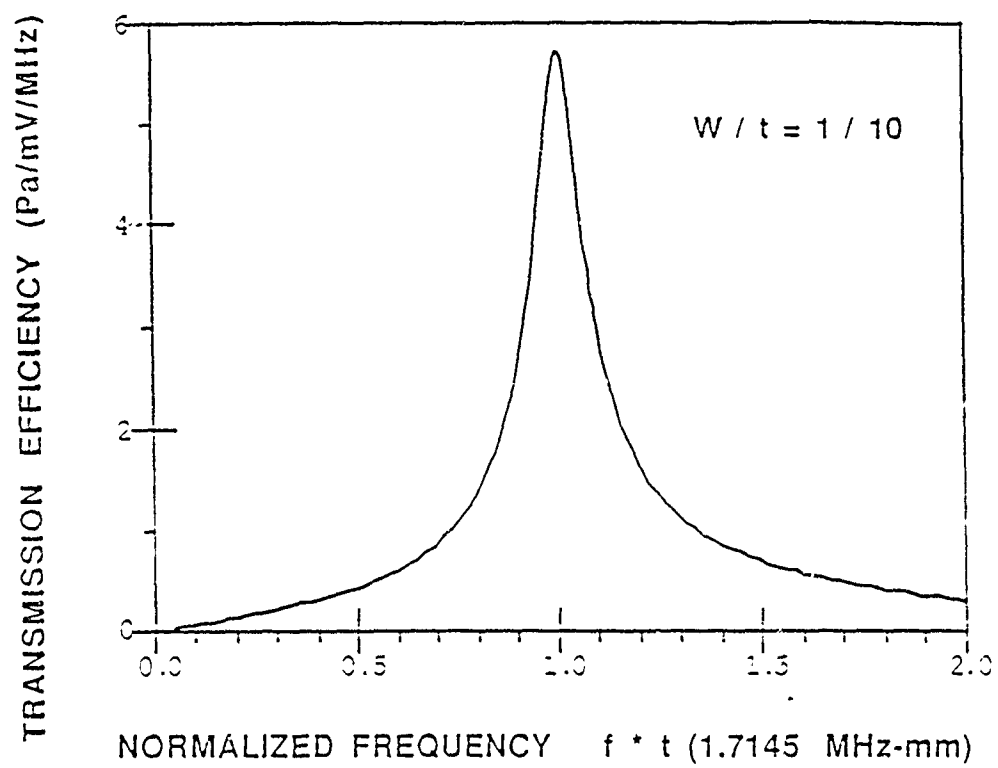
Fig. 6    Spectrum of Transmission Efficiency in Water for PZT Fibers
          Embedded in Insulcast 135
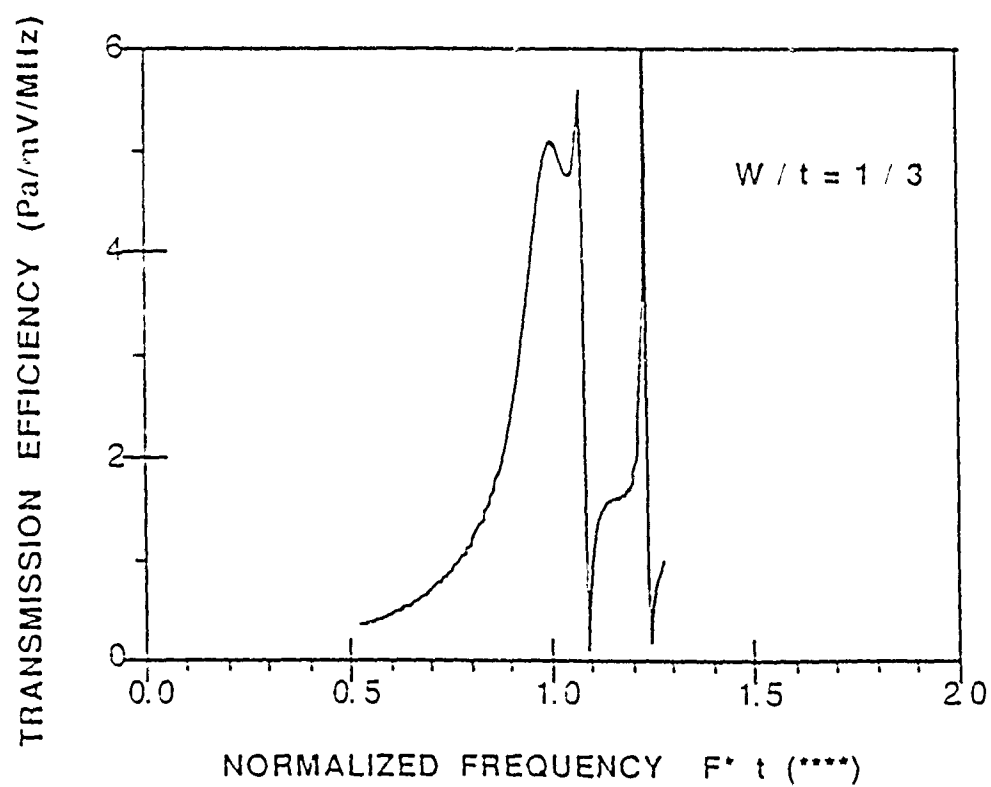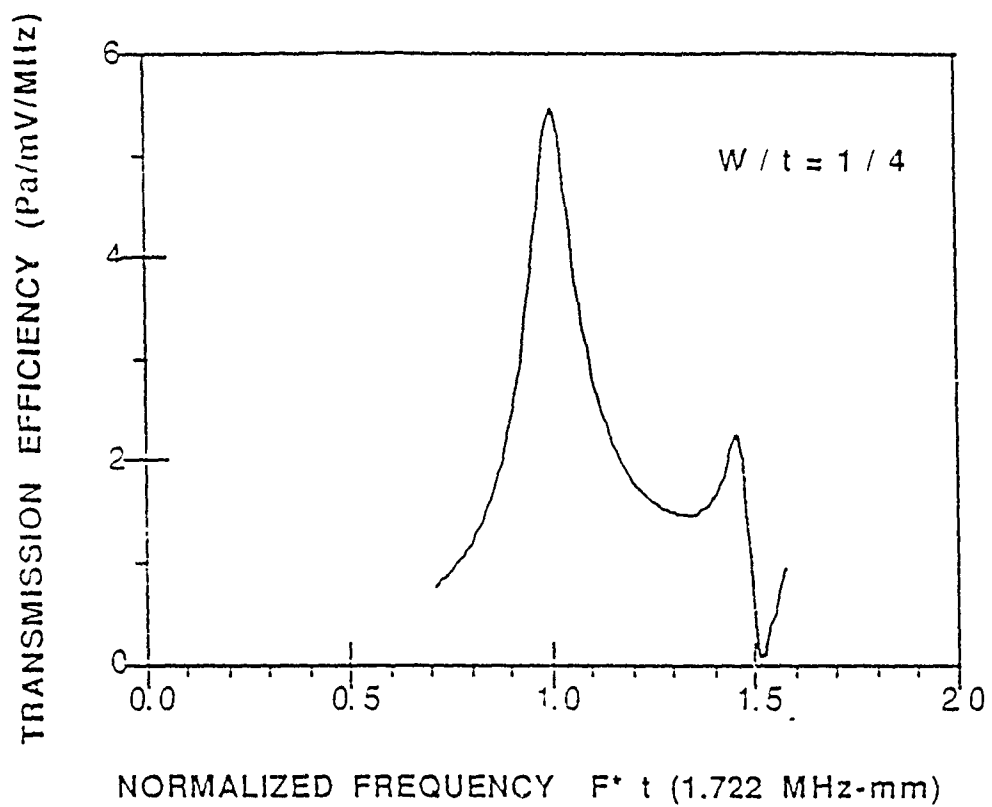
Fig. 7 Spectrum of Transmission Efficiency in Water for PZT Fibers
Embedded in Insulcast 135
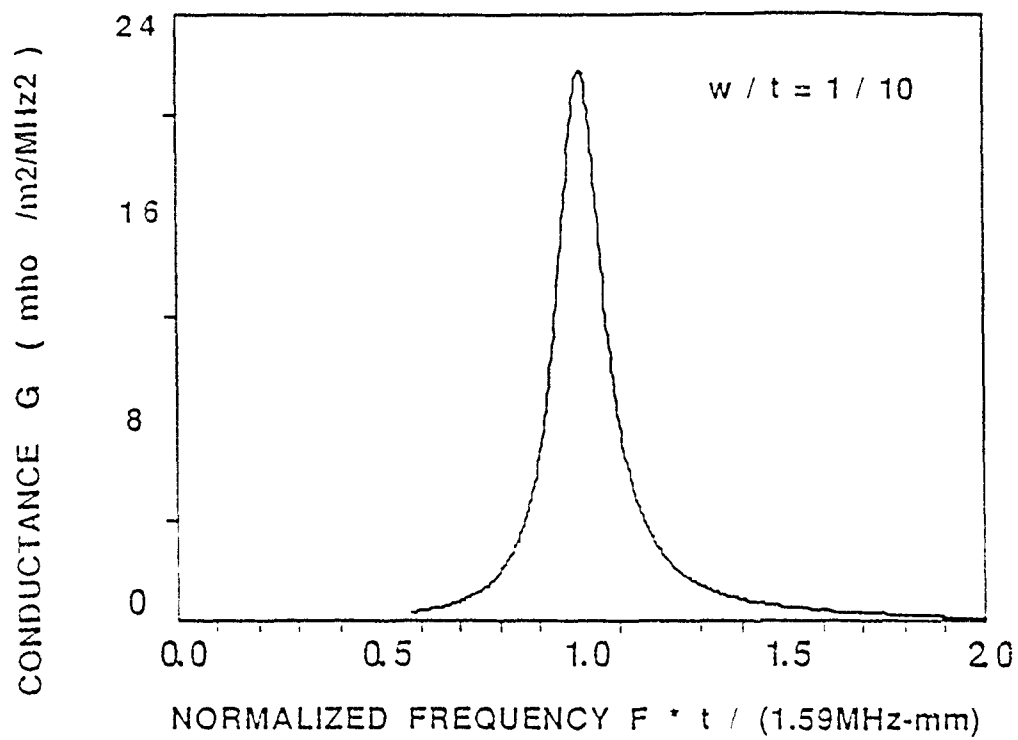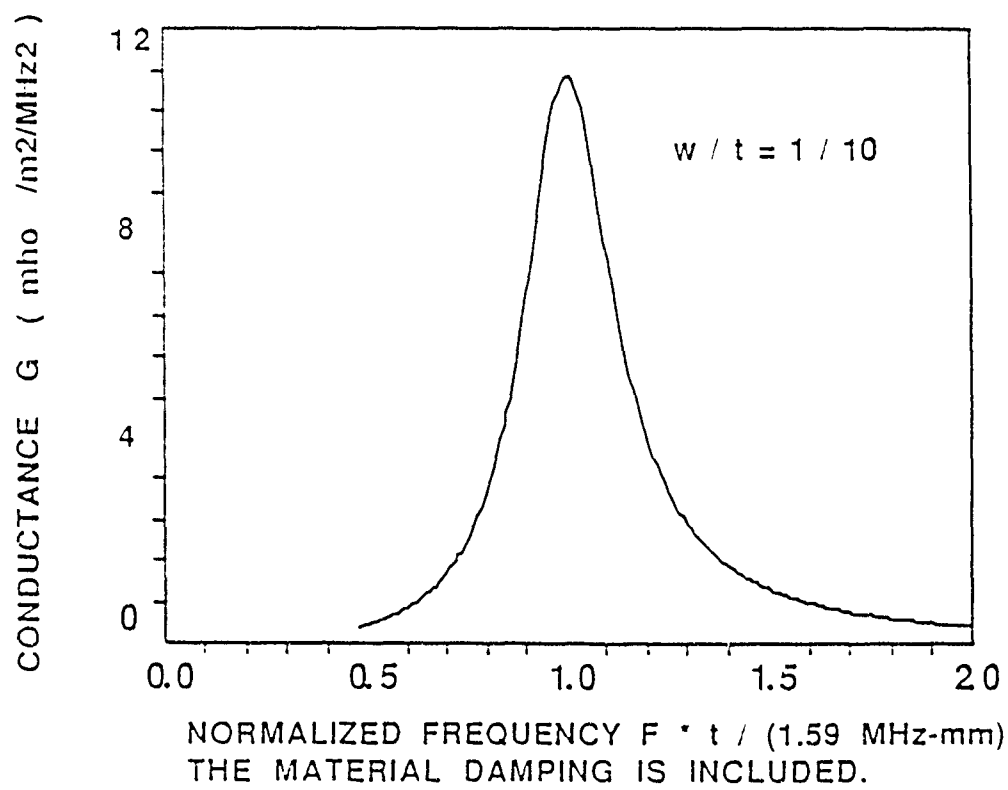
Fig. 8　Conductance Spectrum for PZT Fibers Embedded in Spurr Epoxy
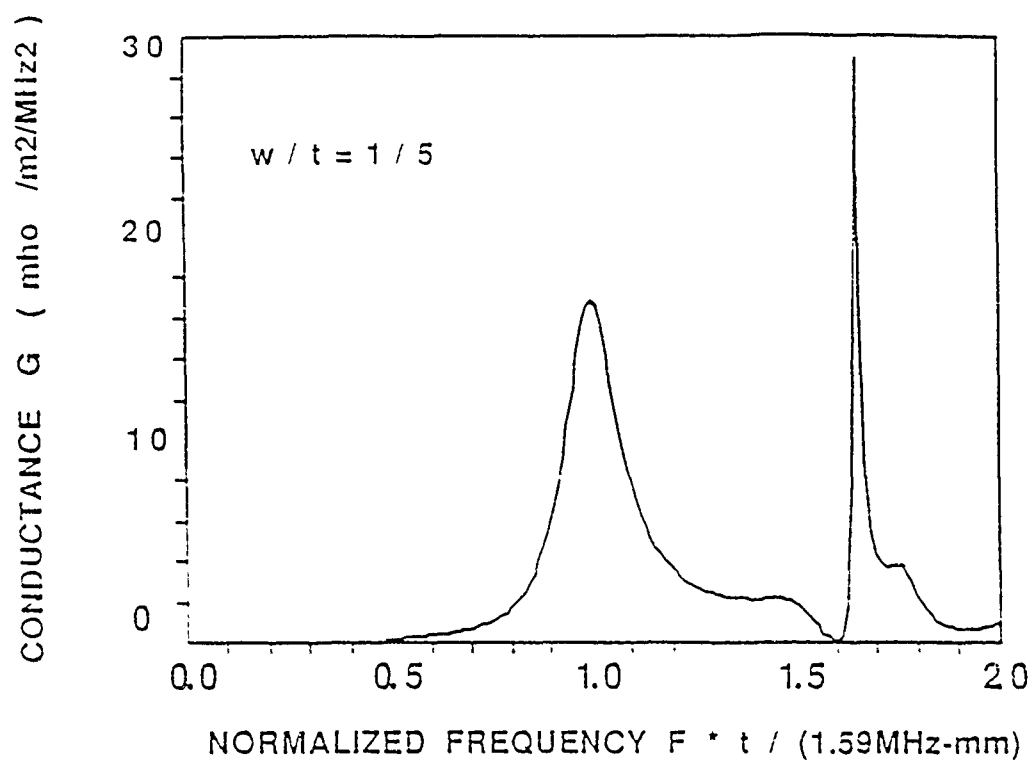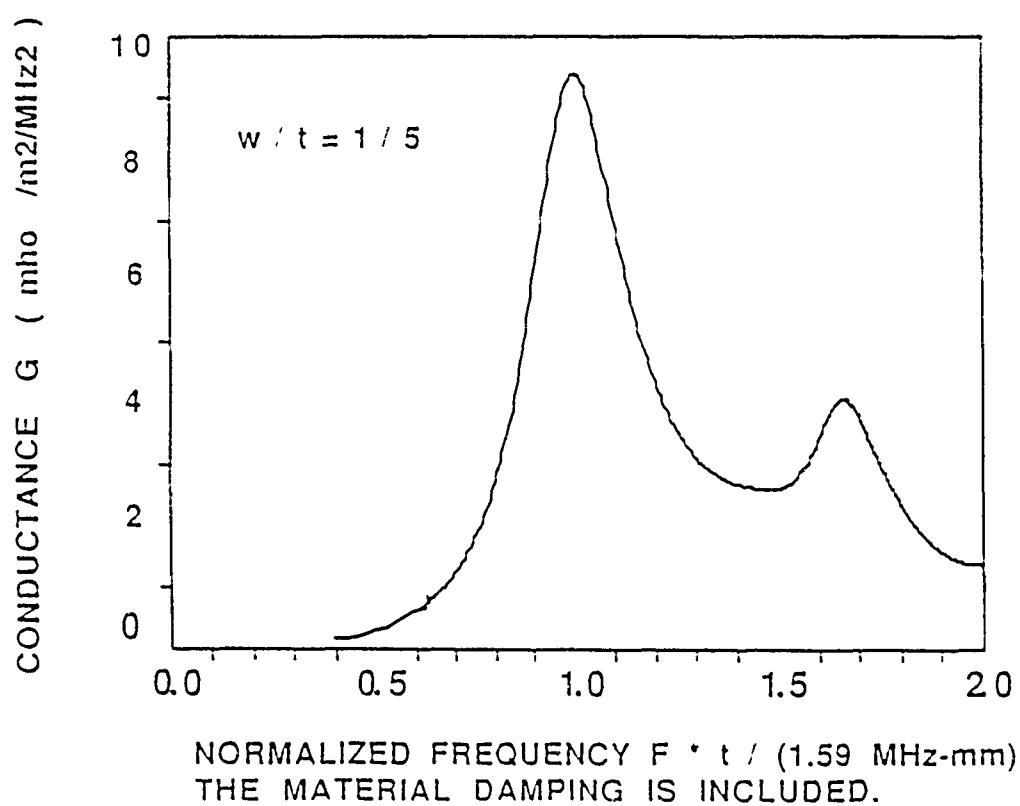
Fig. 9 Conductance Spectrum for PZT Fibers Embedded in Spurr Epoxy
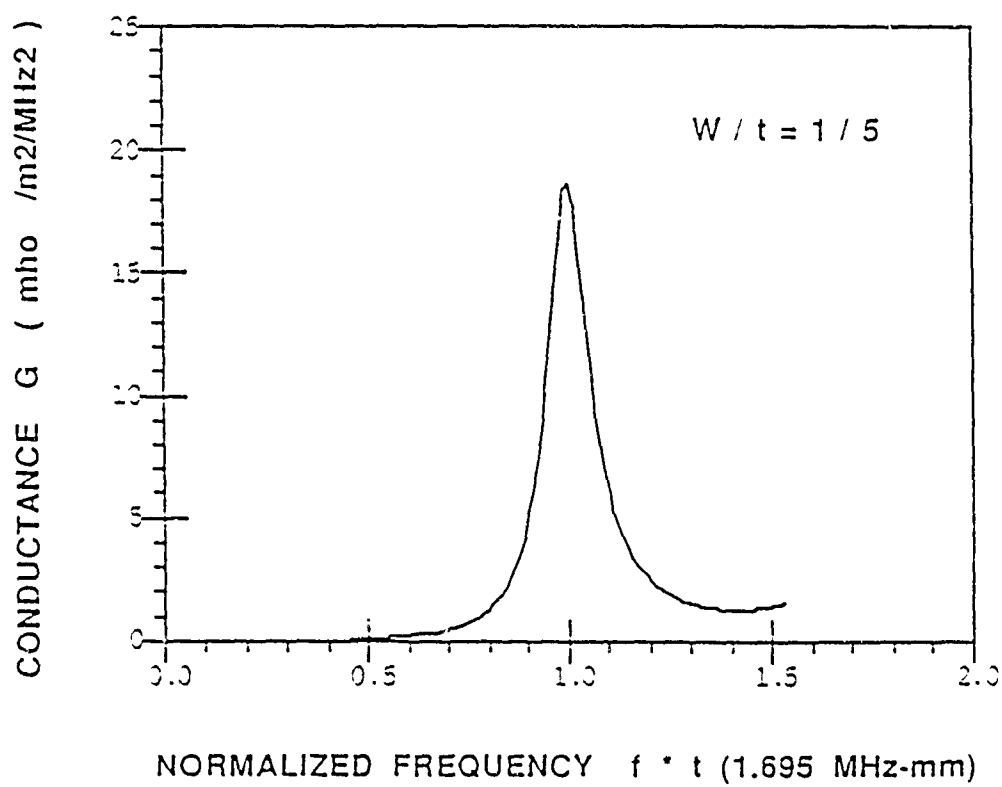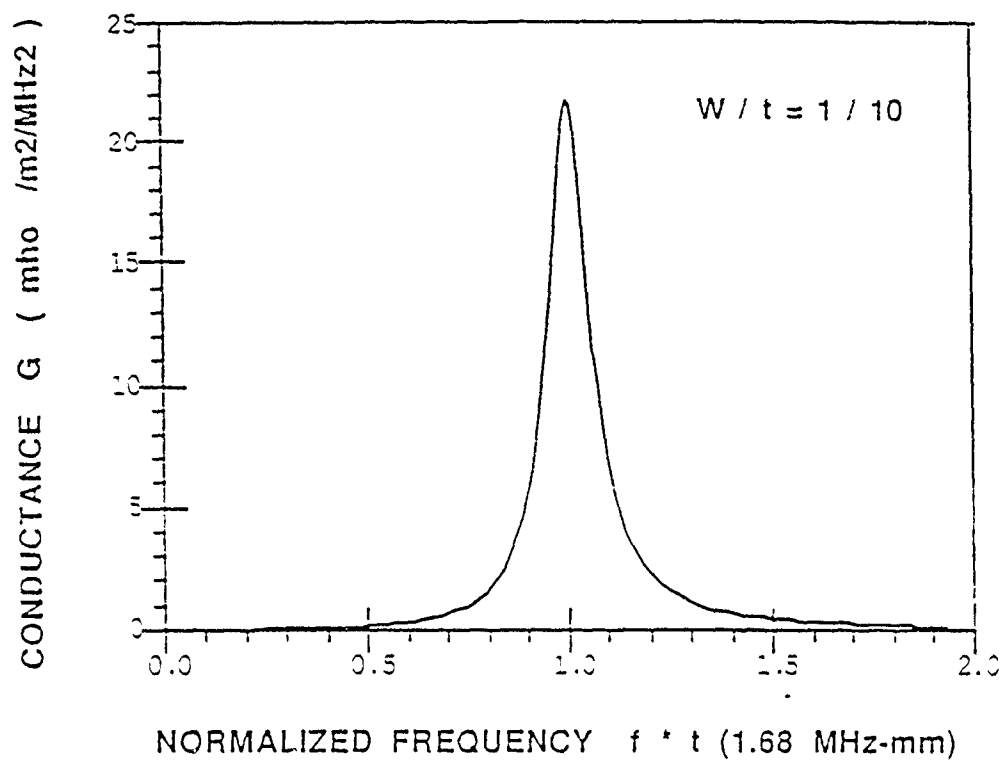
Fig. 10 Conductance Spectrum for PZT Fibers Embedded in RE2039/HD3475
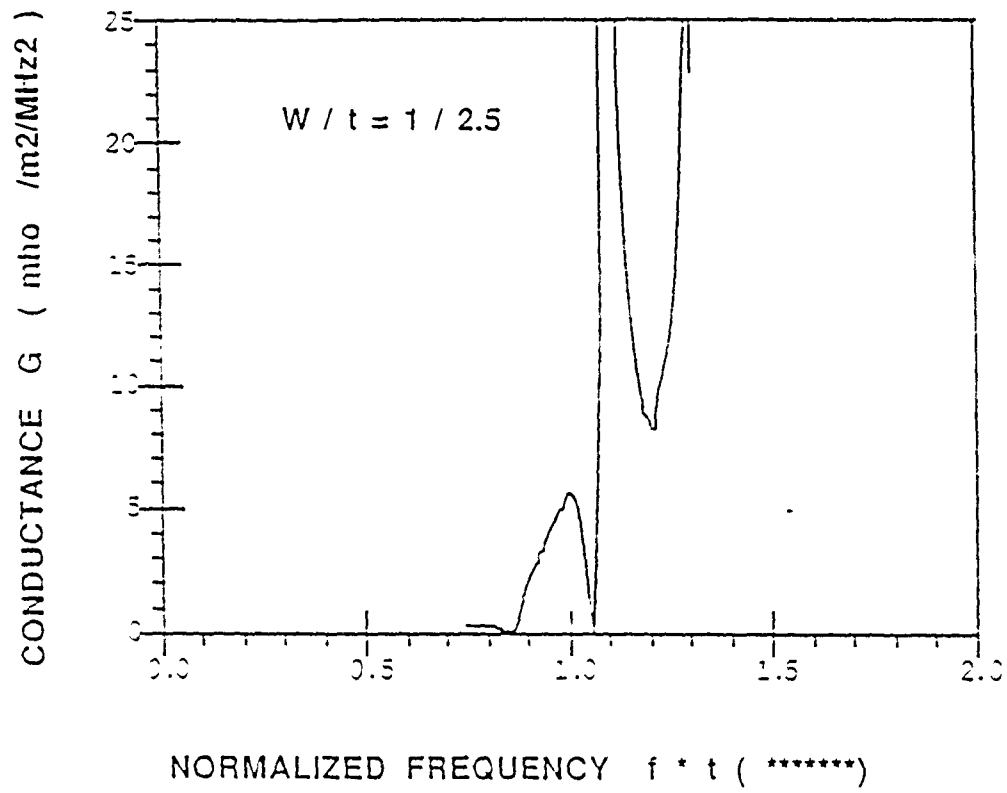
Fig. 11  Conductance  Spectrum  for  PZT  Fibers  Embedded  in RE2039/HD3475
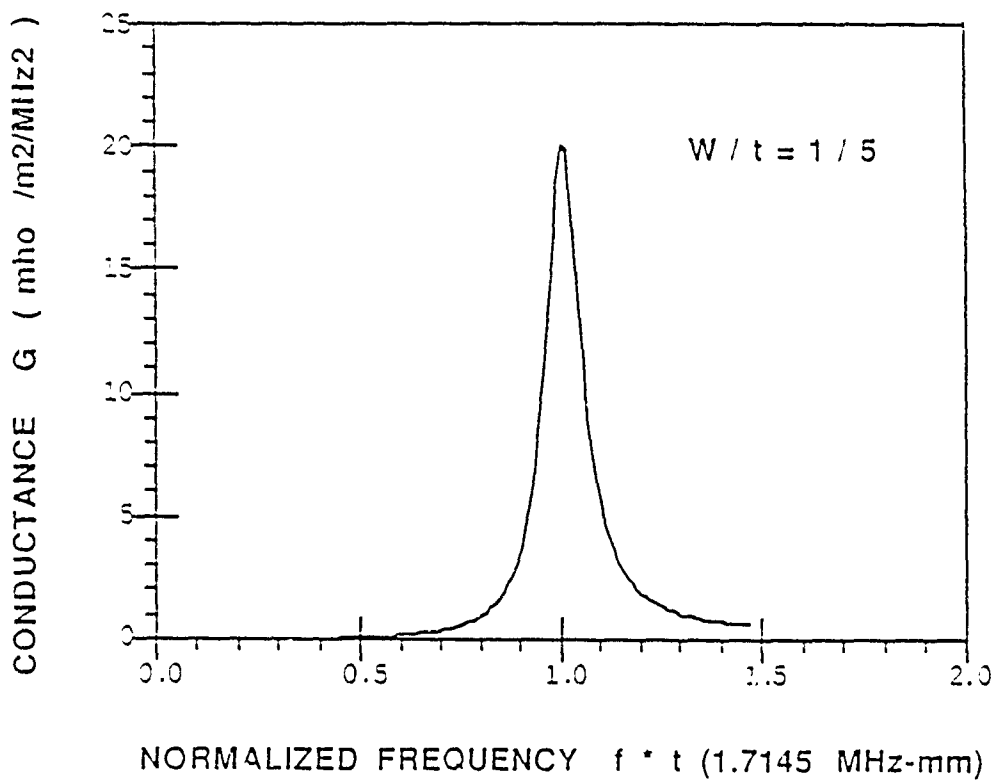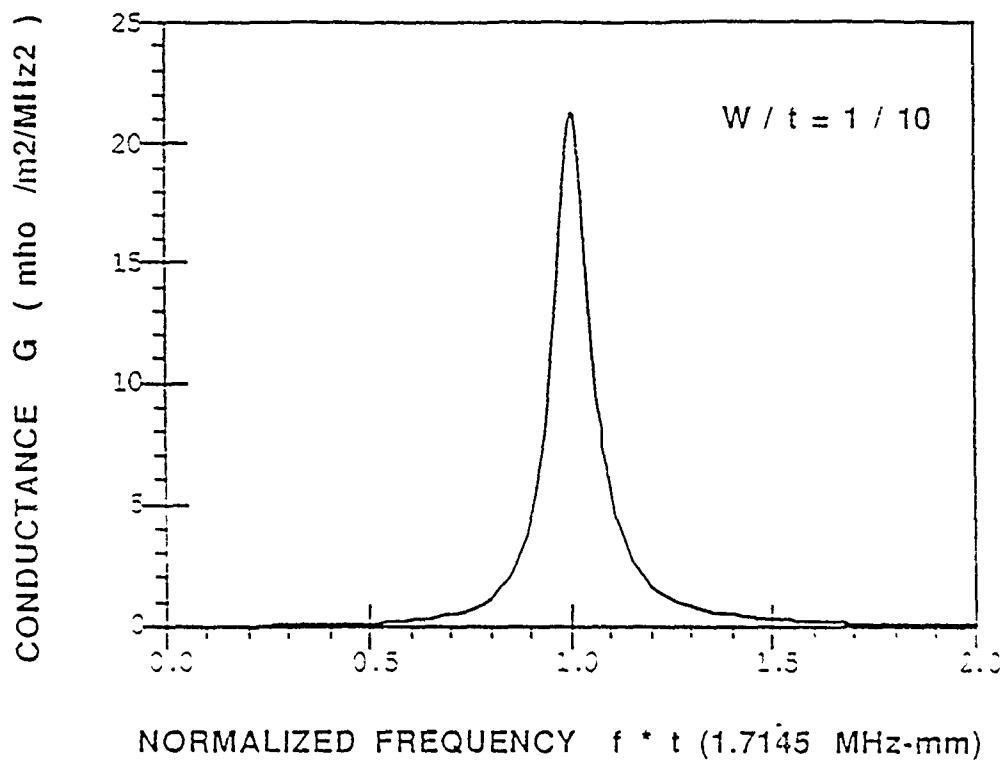
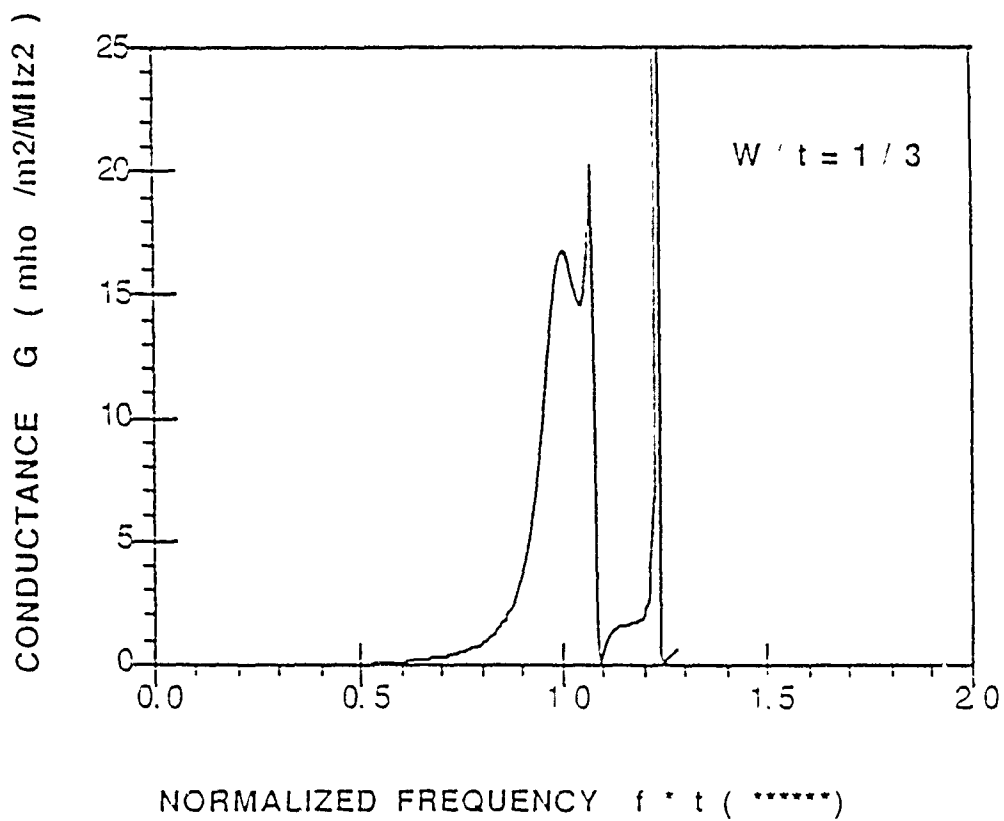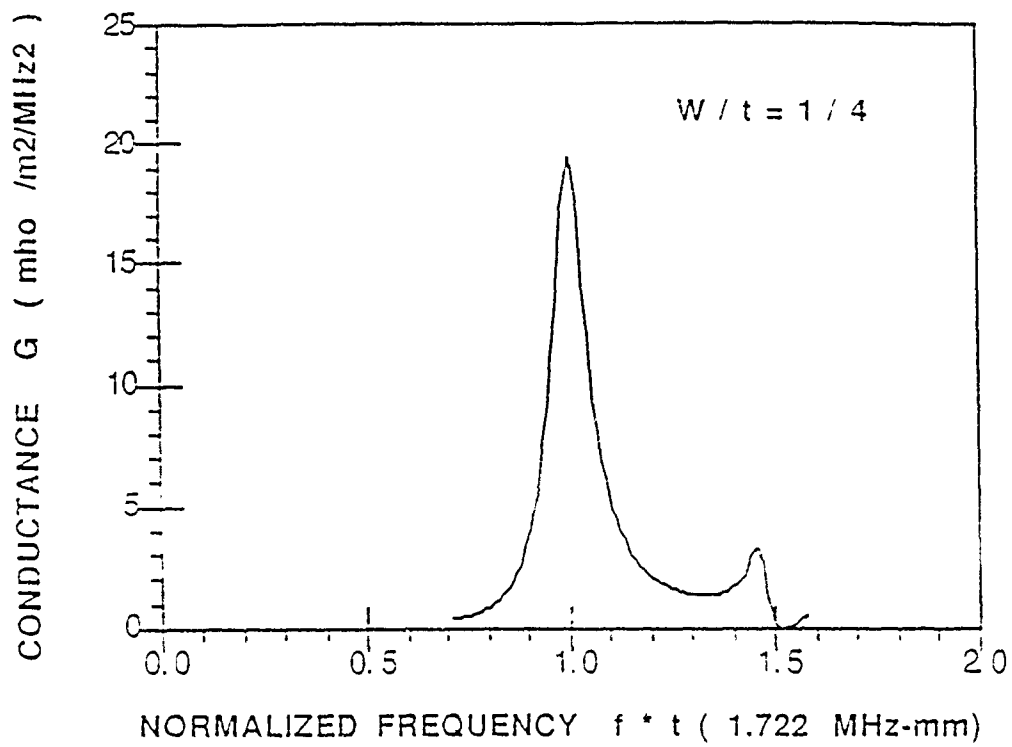Fig. 12  Conductance Spectrum for PZT Fibers Embedded in Insulcast
135

Fig. 13  Conductance Spectrum for PZT Fibers Embedded in Insulcast
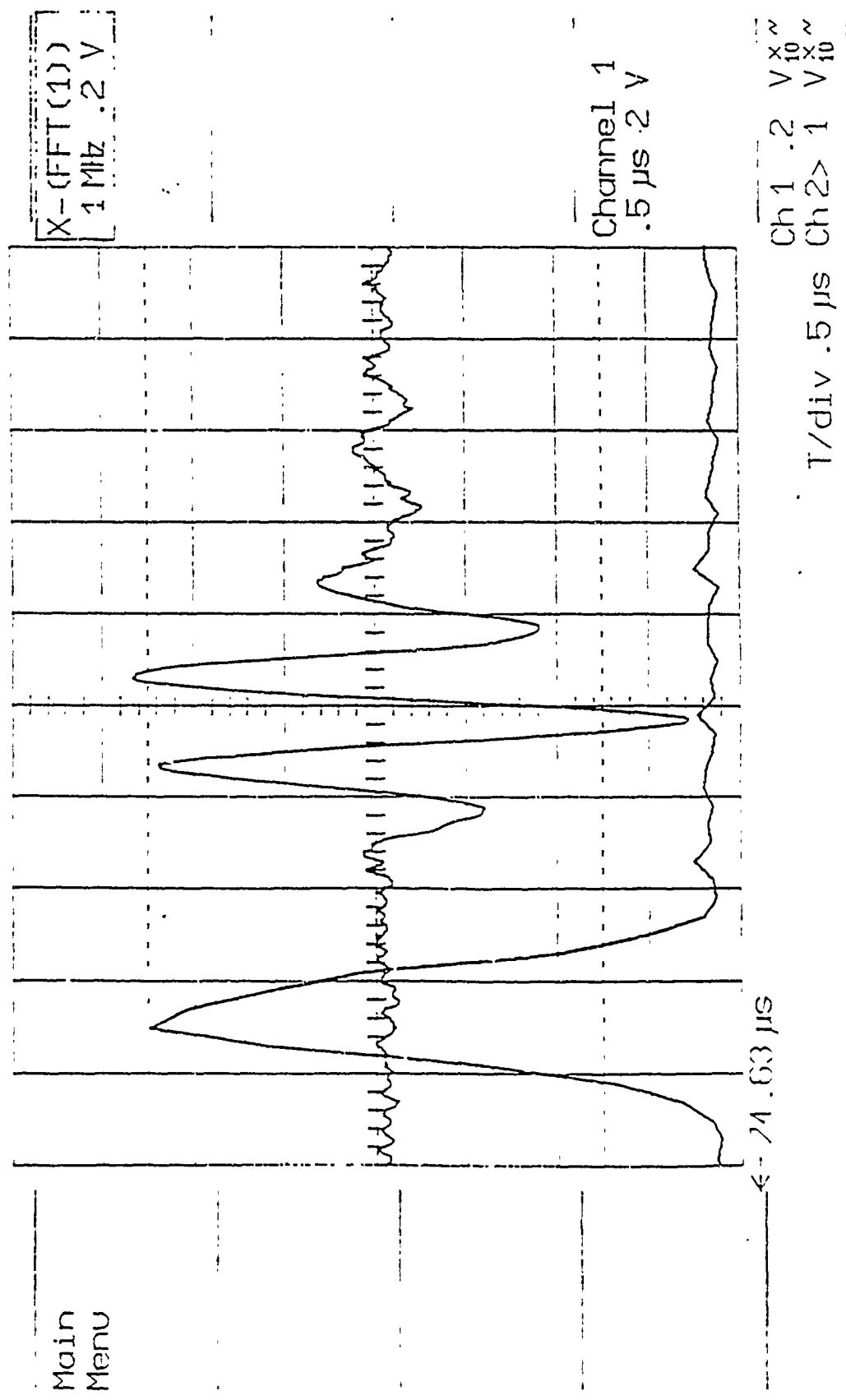135

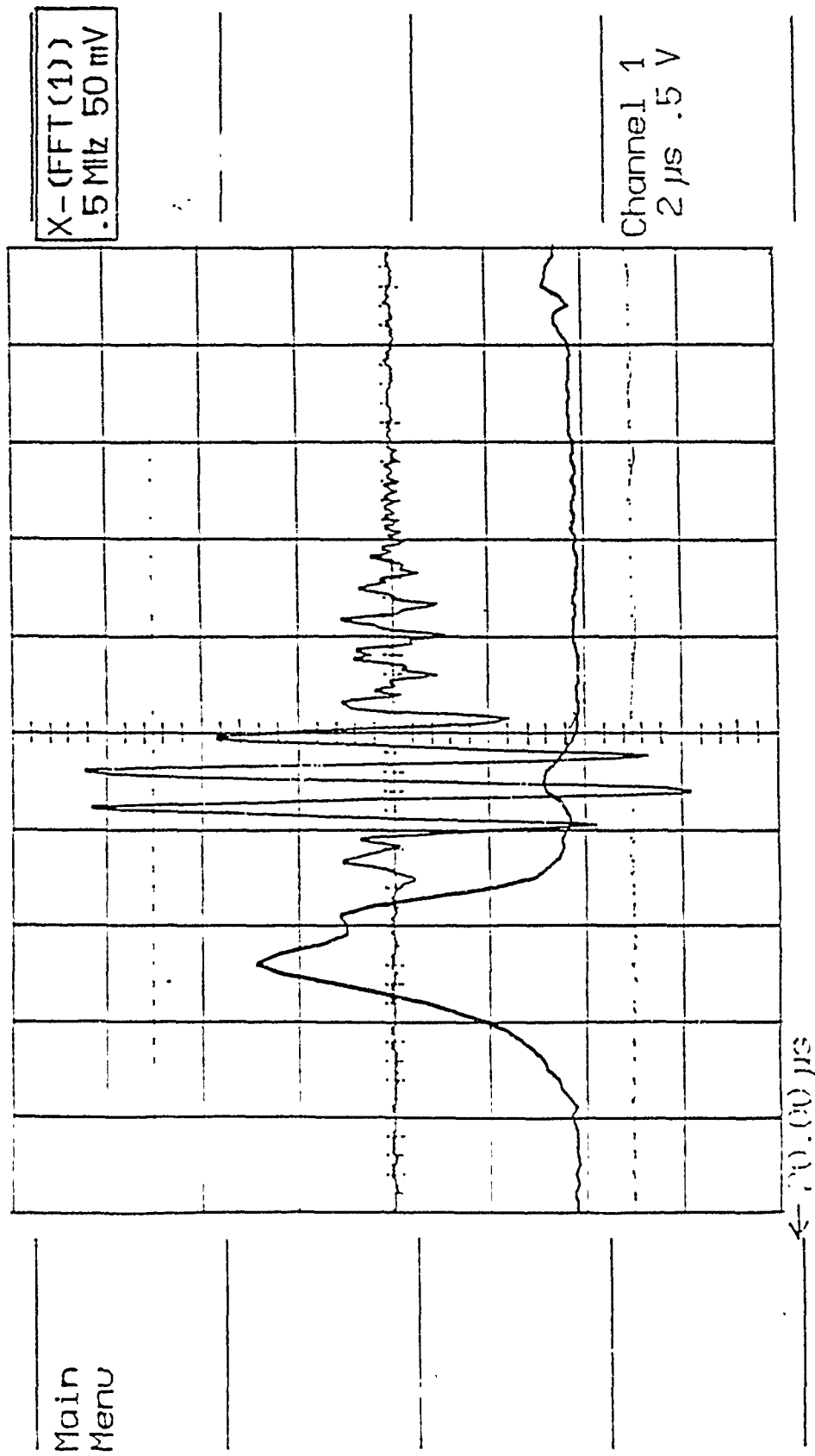Fig. 14 Frequency Spectrum for Sample #1, w/l = 1/10 Measured in Water

Fig. 15 Frequency Spectrum for Sample #2, w/t/ = 1/4.1 Measured in Water

APPENDIX  39

# FINITE ELEMENT - EIGENMODE ANALYSIS FOR
# THE DESIGN OF 1-3 COMPOSITE TRANSDUCERS
# INCLUDING THE EFFECT OF FLUID LOADING

Jiann-Hwa Jeng, Xiaoqi Bao, Vasundara V. Varadan and Vijay K. Varadan

Research Center for the Engineering of Electronic and Acoustic Materials

The Pennsylvania State University

University Park, PA 16802

## Abstract

A finite element – eigenmode analysis is presented for analyzing the dynamic performance of a composite transducer interacting with a fluid medium. The composite transducer contains a periodic distribution of piezoelectric rods forming a 1-3 composite. The mathematical model proposed reduces the boundary value problem to a typical forced vibration problem. Thus, the damping of the composite slab can be easily introduced into the formulation. Based on the analysis, the resonance spectrum and the electrical admittance spectrum are calculated. The analysis can be used to simulate transducer performance under fluid loading and becomes a powerful design tool.

## I. Introduction

The analytical problem of the response of a piezoelectric plate in contact with water to applied stresses or voltage is analogous to the problem of acoustic wave interaction with a fluid-loaded anisotropic plate. Both problems are of considerable practical importance and have been solved by several different mathematical techniques. For instance, many authors have developed a complete procedure for obtaining analytical solutions for thin-or multi-layered plates immersed in a fluid medium, provided that each layer is isotropic. This solution has many applications, such as impedance matching layer design, quarter wave transformer design etc.[1]. Recently, piezoelectric composite materials have been widely used due to their desirable material

1

properties such as high electromechanical coupling and low acoustic impedance [2-4]. These advantages are of value in ultrasonic applications. Due to their high electromechanical coupling and good impedance matching with water, piezo-composite material have been considered for acoustic-wave absorbing purposes as well as in transducer design. For these composite transducers, the problem is further complicated by the strong coupling of the fields at the interface. Analytical solutions are not available for composite slabs having arbitrary microstructure which in this case is also anisotropic. In order to properly describe the dynamic properties of the transducer in the presence of fluid loading, a numerical approach is necessary.

In references [5-8], a finite element analysis has been presented for the fluid-structure interaction problem of a single, isotropic and homogeneous body immersed in a fluid. The vibrations of a composite disk containing piezoelectric elements in the form of rods have been studied by some authors [9,10] using a finite element approach. In these studies, the effect of fluid loading was not considered and further the analysis was restricted to a study of the eigenmodes of vibration. Other than the finite element analysis, electrical equivalent circuits have also been used to evaluate a piezoelectric resonator. Smith et al.[11] treated the 1-3 type of composite as a transmission line model to study the transmitting and receiving sensitivity. The material parameters in their model were determined by fitting the electric impedance curve measured near the thickness resonance with one face of the composite disk in water. Ih et al.[12] extended the model in terms of five effective parameters with consideration of internal losses. Again, these effective model parameters were obtained from experiments. In their simulation, a sample should be properly fabricated to specification and the requisite measurements have to be made. Thus, these methods cannot be used for transducer design.

Recently, Angel and Achenbach [13,14] studied the reflection and transmission of elastic waves by a periodic array of cracks. Due to the periodicity of the geometry, only a typical element of the solid which contains half of a single crack is considered in their calculations. Varadan et al. [15] have developed an analytical approach for the transmission and reflection study of SH waves incident on a bimaterial slab, inside which identical cylinders with parallel

orientation (axes parallel to the surface) are periodically distributed. The approach is based on Fourier-Bessel expansion and T-matrix technique.

Both these approaches could be applied to the problem at hand, but are limited to isotropic microstructure. Arbitrary geometry of the substructure necessitates an approximation for the shape and field representation. As mentioned above, to properly describe the microstructure and to simplify the computation for various problems, a finite element technique combining the eigenmode expansion analysis is introduced. The advantages of this method are that (1) the details of the modal information for different microstructures are given, (2) the computation of the eigenmode expansion technique is a standard procedure and can be easily applied, (3) the effect of the matching layer and the internal losses are included in the computation without any further modification.

In the formulation, the boundary-value problem of wave interaction with a solid structure can be recast as a typical forced vibration problem. The damping effect can then be automatically included in the dynamic equation [16]. Due to the periodicity of the structure, the mathematical model is further simplified by employing Floquet's theorem and symmetric boundary conditions. Representing the field with suitable eigenmodes and imposing appropriate boundary conditions on the interfaces, eigenmodes and eigenfrequencies can be computed. Since the dynamic equation is well defined, the method of solution is simple.

## II. Formulation of the Problem

The geometry, as shown in Fig.1, has three regions in which the fields need to be described. The composite disk, namely region (III), separates the infinite homogeneous medium into two regions, (I) and (II), thus forming the two planar interfaces $S_I$ and $S_{II}$. The composite slab, considered here, contains a periodic array of rods made of a piezoelectric material which are embedded in rubber. The period of the array is 2a and 2b in the x- and y- directions respectively.

### (a) Mathematical Model

The composite slab in region III is characterized by using the finite element analysis. For

3

an elastic medium, a discrete model for vibration analysis is set up as follows:

$$( K - i\omega C - \omega^2 M ) \vec{U} = \vec{F} \qquad (1)$$

where

K — is the stiffness matrix,

C — is the damping matrix,

M — is the mass matrix,

U — is the displacement vector, and

F — is the force vector

By solving a homogeneous undamped system with appropriate boundary conditions:

$$( K - \omega^2 M ) \vec{d} = 0 \qquad (2)$$

we obtain the eigenvalues and eigenvectors which describe the normal modes of the system.

Thus, we have

Eigenvalues $\quad \omega_1 < \omega_2 < \;\ldots\ldots\; < \omega_n$

Eigenvectors $\quad d_1, \quad d_2, \quad \ldots\ldots, \quad d_n$

and the eigenvectors satisfy the orthogonality relation

$$\int_V \vec{d}_i \, \rho \, \vec{d}_j \, \partial V = \begin{cases} 0, & i \neq j \\ 1, & i = j \end{cases} \qquad (3)$$

Based on the modal analysis, namely, the normal mode summation method, the displacement of the structure under forced excitation is represented by the sum of a finite number of normal modes of the system multiplied by the generalized coordinates. The displacement field can then be expanded as

$$\vec{U} = \sum_{i=1}^{n} q_i \vec{d}_i \qquad (4)$$

with unknown weighting $q_i$. The summation is truncated to the first N terms for numerical purposes. Substituting Eq. (4) into Eq. (1) and using the orthogonality condition Eq. (3), the equations of motion can be uncoupled into 'N" algebraic equations. Thus, we have

$$( \omega_i^2 - 2i \, \xi_i \omega \omega_i - \omega^2 ) \, q_i = f_i \qquad (5)$$

where $\xi_i$ is the modal damping ratio; $f_i$ is the effective force.

4

(b) Piezoelectric Phase

In many practical problems, due to the enormous difference in the speed of propagation of elastic waves and electromagnetic waves, the quasi-static approximation is made. Usually the frequencies relevant to elastic waves in solids or acoustic waves in fluids are less than 10 MHz. At these frequencies, the wavelength of electromagnetic waves is quite large and it is reasonable to assume that the electric field is a quasi-static field [17]. It is important that the distinction between static and quasi-static is retained. In the quasi-static approximation, a constitutive equation is derived in invariant form relating the stress and strain tensors that includes the piezoelectric coupling coefficients.

Hence, for a piezoelectric material, the stiffness matrix K can be formulated as that of a elastic solid by substituting the stiffened elastic constants which include the piezoelectric coupling effect [18]. This simplification is valid for the case in which the piezoelectric material is shaped as a long rod [17]. Thus, elements listed in the ANSYS library [19] can be used to describe the behavior of the piezoelectric phase.

Next , we should consider the discretization of the equation for a piezoelectric material. A further simplification can be made when the piezoelectric material is fabricated into a long-bar shape which satisfies a constant D-field approximation. In such approximation, the D-field along the z-axis of a PZT- bar is constant as shown in Fig.2. The D-field which is proportional to the charges distributed on the electrodes is represented as

$$D_X = 0, \ D_Y = 0, \ D_Z = \frac{Q}{A_Z} \ \Rightarrow \ D = \psi_D^* Q \qquad (6)$$

By using the constitutive equations of a piezoelectric material which have the form as

$$T = C^D S - h \, D$$
$$E = h^* S + \beta^S D \qquad (7)$$

and applying a variational principle, a discrete finite element equation for the long-bar piezoelectric material can be expressed as

$$( K^D - i\omega C - \omega^2 M ) U = PQ + F$$

$$V = - P^* U + \frac{1}{C_0} Q \qquad (8)$$

where

$$P = \int B^* \, h \, \psi_D \, dV$$

$$\frac{1}{C_0} = \int \psi_D^* \, \beta^S \, \psi_D \, dV$$

$C^D$ is the elastic constant with D-constant; h is the piezoelectric coupling constant and $\beta^s$ is the constant strain dielectric constant.

By using the orthogonality condition of the normal modes representation, Eqs.(3), (4), Eq. (8) can also be uncoupled into a group of algebraic equations.and is expressed as

$$\Omega q = X Q + D_{ei}^* F$$

$$V = - X^* q + \frac{Q}{C_0} \qquad (9)$$

where $D_{ei}$ are the eigenvectors, further

$$\Omega_i = \omega_i^2 - 2 i \, \xi_i \omega \, \omega_i - \omega^2 \; ; \quad X = D_{ei}^* P \qquad (10)$$

where $\omega$ is the operating frequency; $\omega_i$ is the eigenvalue; and $\xi_i$ is the modal damping ratio.

(c) Effect of Fluid Loading

The effect of the fluid loading can be formulated as part of the exciting force acting on the transducer surface which is the F term as shown in Eq.(7). Due to the periodicity and symmetry of the substructure, only a portion of the composite slab needs to be considered. As shown in Fig. 3 the unit cell contains one quarter of the rod which is of dimension 'a' and 'b' along the x- and y- axis respectively. This domain will be described by the finite element approximation. The normal displacements on the x=0, x=a, y=0, and y=b plane are equal to zero due to the four fold symmetry in the geometry.

6

In regions I and II, the field must be represented by a periodic function in the x-y plane due to the periodic distribution of the rods in the composite disk. Floquet theorem is used to describe periodicity in terms of the Floquet modes [15] and is given as

$$\vec{W}_{mn} = \sum_{mn} [A_{mn} e^{-ik_{zmn}z} + B_{mn} e^{ik_{zmn}z}] e^{ik_{xm}x} e^{ik_{yn}y} e^{-i\omega t} \quad (11a)$$

where

$$k_{xm} = \frac{m\pi}{a} + k \sin \theta_x \quad (11b)$$

$$k_{yn} = \frac{n\pi}{b} + k \sin \theta_y \quad (11c)$$

and

$$k_{zmn} = \sqrt{(\frac{\omega}{c})^2 - (k_{xm})^2 - (k_{yn})^2} \quad (11d)$$

where 'c' is the acoustic speed in water.

Employing the Floquet condition for the field radiating into the infinite regions I and II, the total geometry, region III, is broken up into an infinite number of unit cells with a length 2a along the x- axis and a length 2b along the y- axis. Eq. (6) can be modified further and has the form

$$\vec{W}_{mn} = A_{mn} \cos (k_{xm} x) \cos (k_{yn} y) e^{i(K_{zmn} z - \omega t)} \quad (12)$$

There is a cutoff frequency for this periodic substructure

$$\lambda_{cut\,off} = \frac{c}{f_{cut\,off}} = Max\,(\,2a, 2b\,) \quad (13)$$

The cutoff frequency is a function of geometry of the substructure and is an important design factor. Whether a mode $W_{mn}$ can propagate or not, depends on the value of $k_{zmn}$. If the value is real, then $W_{mn}$ is a propagating mode, otherwise, $W_{mn}$ is a decaying or evanescent mode.

Defining a set of functions $\psi_{mn}$ in the form as:

$$\psi_{mn} = \cos (\, k_{xm} x) \cos (\, k_{yn} y) \quad (14)$$

the displacement field $U_1$ and the radiating pressure field , $P^r$ in region I are represented as

7

$$\vec{U}_1 = \sum_{mn} D_{mn1}\, \psi_{mn}\, e^{\,i\,k_{zmn}z} \qquad (15)$$

$$\vec{P}^r = \sum_{mn} \alpha_{mn}\, \psi_{mn}\, e^{\,i\,k_{zmn}z} \qquad (16)$$

The radiating pressure field is the acoustic pressure on the surface due to vibrations of the elastic body.

In region II, the displacement field $U_2$ and the transmitted pressure field $P^t$ have the same form as

$$\vec{U}_2 = \sum_{mn} D_{mn2}\, \psi_{mn}\, e^{\,-\,i\,k_{zmn}\,z} \qquad (17)$$

$$\vec{P}^t = \sum_{mn} \beta_{mn}\, \psi_{mn}\, e^{\,-\,i\,k_{zmn}\,z} \qquad (18)$$

As we know, either the displacement field or the pressure field is enough to describe the infinite fluid medium. The set of unknown coefficients in both displacement and pressure fields are related. Based on the displacement-pressure relation

$$\rho\, \frac{\partial^2 \vec{U}}{\partial t^2} = -\,\nabla \vec{P} \qquad (19)$$

the dependence of the unknown coefficients in Eqs. (15), (16) and in Eqs. (17), (18) are obtained as

$$\alpha_{mn} = -i\, D_{mn1}\, \rho\omega C_{mn} \qquad (20)$$
$$\beta_{mn} = i\, D_{mn2}\, \rho\omega C_{mn} \qquad (21)$$
$$\beta_{mn} = i\, D_{mn2}\, \rho\omega C_{mn} \qquad (21)$$

where $C_{mn}$ is the velocity of the m–n th mode.

The unknown coefficient can be computed by matching the boundary condition across the interface which require the normal displacements to be continuous. For computational convenience, the surface field represented in a normal mode expansion is transformed to the Fourier series representation as follows

$$\vec{U}_{surface} = \sum_{mn}\sum_{i} A_{mni}\, q_i\, \psi_{mn}\,(x,y) \qquad (22)$$

where $A_{mni}$ are Fourier expansion coefficients. Thus

$$D_{mni} = \sum_{mn} \sum_i A_{lmni} \, q_i \qquad (23)$$

and

$$\alpha_{mn} = \sum_i -i \, q_i \, A_{lmni} \, \rho\omega \, C_{mn} \qquad (24)$$

Here, we have assumed that the pressure field radiates only into region I because only one side of the transducer is active. The modal pressure field is defined as

$$D^*_{ei} F = \int_{SI} - \, d_{i \,(On \, SI)} \vec{P} \, dS \qquad (25)$$

and can be rewritten as the known Fourier expansion coefficients $A_{mni}$ and the unknown weighting coefficients $q_i$ as follows:

$$D^*_{ei} F = \sum_i q_j \, Z_{ij}$$

$$= \sum_i \sum_{mn} -i\rho\omega C_{mn} \, \eta_{mn} \, A_{mni} \, A_{mnj} \, q_j \qquad (26)$$

$\eta_{mn}$ is the normalized constant.


III. Method of Solution

The model used for computation was a disk with diameter $D \gg \lambda$ (wavelength), so it can be thought of as an infinite slab in the x-y plane. Thus, it can be broken up into an infinite number of unit cells and the plane wave field can be represented in terms of the Floquet modes.

The eigenmodes for the computations can be obtained by the finite element analysis. The finite element package ANSYS, installed in a VAX 11/780 was chosen for the this purpose. The reasons for using this package are as follows. The ANSYS uses a Householder procedure to solve the problem of free rigid body motion. Due to the symmetric boundary condition in our problem, we require rigid body motion only in the z- direction. Also, ANSYS allows us to define a damping ratio $\xi$ for a material dependent damping constant in the modal analysis. Thus,

an effective damping ratio, $\xi_i$, based on a material weighted strain energy average for each mode is calculated as,

$$\xi_i = \frac{\sum_m \xi_m E_m^i}{\sum_m E_m^i} \qquad (29)$$

where $E_m^i$ and $\xi_m$ are the strain energy and damping ratio for the $m^{th}$ element in the $i^{th}$ mode respectively. The $\xi_i$ obtained from Eq. (29) is in fact the modal damping ratio described in Eq. (9).

The '3-D anisotropic solid element' [19] was chosen to model the solid structure. The behavior of an element is defined by eight nodal points each of which has three degrees of freedom: translation in the x, y, and z directions. In all the computations, 66 elements with 124 nodal points are used to mesh a symmetric quadrant of the unit cell.

In real applications, it is important to know the transmitting sensitivity of a projector and the receiving sensitivity of a sensor. In order to evaluate the transmitting sensitivity, a voltage of fixed amplitude is applied to the transducer. For a given voltage supply, using Eq.(26), Eq.(9) can be rewritten as

$$( \Omega_{ij} + Z_{ij} - X_i X_j C_0 ) q_j = X_i C_0 V \qquad (27)$$

$$Q = C_0 V + X_j q_j C_0 \qquad (28)$$

the only unknown shown in Eq.(27) is $q_j$ and can be easily solved. While $q_j$ is given, the charge distribution Q can be calculated from Eq.(28).


IV. Numerical Results and Discussion

The numerical results presented are the resonance spectrum and electric conductance spectrum of a disk.

To assess the feasibility of the numerical formulation, we first consider the simple case of a uniform isotropic steel plate immersed in an infinite fluid medium. The calculations were made

10

to examine the effect of the fluid loading with a normal incoming acoustic wave acting on the plate. The steel plate has longitudinal wave velocity $V_p = 5220$ m/sec and thickness h=5 cm, thus, the first thickness mode occurs at 52.2 KHz. The reflection coefficient and transmission coefficient are plotted versus frequencies in Fig. 4. In this figure, both the numerical results and exact results are plotted. The reflection coefficients approach unity below the first thickness mode, 52.2 KHz, due to the high impedance mismatch at the water-steel interface. The damping of the steel is neglected in the computation for comparison purposes. The data shows that these two results agree with each other exactly. The comparison is a good indication of the appropriateness of the numerical approach.

Based on the simulation, the performance of two different disks will be presented. One is the pure PZT-5 disk, the other is the 1-3 composite disk. For the second case, spurrs epoxy was considered as the filler matrix. Its longitudinal and transverse wave velocities were measured to be 2060 m/sec and 1150 m/sec respectively.

Figure 5 presents the resonance frequency spectrum, i.e. the transmission efficiency vs. frequency for both the pure PZT and composite PZT disks, which are driven with the same voltage and radiate acoustic waves into the water. The solid line in the figure is for the PZT-5 disk. It shows that the pure disk transducer has a very high Q factor compared with the composite transducer. We can see that the amplitude value near the resonance are close for both cases. We can infer from this result that the composite transducer has similar transmission efficiency as the pure PZT disk under the fluid loading condition. We also notice that the lateral vibration results in little distortion of the main broadband signal in the composite transducer.

Figures 6 and 7 show the real and imaginary part of the conductance curve respectively. Both figures are in general agreement with the known behavior of a pure PZT disk under fluid loading.

V. Conclusions

Based on the theoretical derivation and the computed results, it is concluded that this technique is capable of solving a problem involving complex geometry and material anisotropy.

11

In addition, the analysis provides detailed mode information describing the composite disk. This information contributes to the understanding of the mechanisms of wave-material interaction. With the basic understanding of the wave motion and vibrations in the piezoelectric structure, it is possible to optimize the design of transducers for specific purposes. The damping effect also has been introduced in the normal mode expansion analysis. As a conclusion, the analysis can be used to simulate transducer performance under fluid loading and becomes a powerful design tool.

## Acknowledgement

# Reference

1. V. M. Ristic, *Principles of Acoustic Devices*, Wiley, New York (1983).

2. R. E. Newnham, L. J. Bowen, K. A. Klicker and L. E. Cross,"Composite Piezoelectric Transducer," Mater. Eng., Vol. 2, (1980).

3. T.R.Gururaja, W.A.Schulze, L.E.Cross, R.E.Newnham, B.A.Auld, and Y.Wang,"Piezoelectric Composite Materials for Ultrasonic Transducer Applications, Pa— I: Resonant Modes of vibration of PZT rod - polymer composites," IEEE Trans. Sonic. Ultrason., Vol. SU-32, 1985.

4. H.Takeuchi and C.Nakaya,"PZT/Polymer Composites for Medical Ultrasonic Probes," Ferroelectrics, Vol. 68, 1986.

5. X. Q. Bao, V. V. Varadan, V. K. Varadan, Q. C. Xu and Wang, T. C.,"A Hybrid Finite/Boundary Element and Modal Analysis Procedure for Acoustic Wave Scattering by Finite Elastic Obstacles in Water," J. Wave-Material Interact.,Vol. 3, (1988).

6. V. V. Varadan, K. Eswaran and V. K. Varadan," Hybrid FEM-T matrix Technique for Analysis of Acoustic Wave Scattering by Elastic Shells of Revolution," J. Wave-Material Interact., Vol. 1, (1986).

7. J. T. Hunt, M. R. Knittel, C. S. Nichols and D. Barach,"Finite-Element Approach to Acoustic Scattering from Elastic Structure," J. Acoust. Soc. Am., Vol. 57, (1975).

8. H. Allik, K. M. Webman and J. T. Hunt,"Vibrational Response of Sonar Transducers Using Piezoelectric Finite Elements," J. Acoust. Soc. Am., Vol. 56, (1974).

9. Y. Kagawa and T. Yamaguchi,"Finite element Simulation of a Composite Piezoelectric Ultrasonic Transducer," IEEE Trans. Sonics and Ultrasonics, SU-2, 81 (1979).

10. D. Boucher, M. Lagier and C. Maerfeld,"Computation of the Vibrational Modes for Piezoelectric Array Transducers Using a Mixed Finite Element-Perturbation Method," IEEE Trans. Sonics and Ultrasonics, SU-28, 318 (1981).

11. W.A.Smith, A.A.Shaulov, and B.M.Singer,"Properties of Composite Piezoelectric Materials for ultrasonic transducer,"Proc. IEEE Ultrasonic Symposium, 1984.

12. J.H.Ih and B.H.Lee,"Performance Analysis of Piezoelectric Composite Plates with Consideration of the Internal Losses,"IEEE Trans. Ultrason. Ferroelectrics and Frequency Control, Vol. 35, 1988.

13. Y. C. Angel and J. D. Achenbach,"Reflection and Transmission of Elastic Waves by a Periodic Array of Cracks," J. Appl. Mech., 52, 33, (1985).

14. Y. C. Angel and J. D. Achenbach,"Reflection and Transmission of Elastic Waves by a Periodic Array of Cracks: Oblique Incidence," Wave Motion, 7, (1985).

15. V. V. Varadan, A. Lakhtakia and V. K. Varadan,"Transmission of SH waves Through a Periodic Array of Elastic Cylinders," J. Vibration, Acoustic, Stress, and Reliability in Design, 109, 43, (1987).

16. W. T. Thomson,*Theory of Vibration with Applications*, Prentice-Hall, NJ (1972).

17. V. V. Varadan, J. H. Jeng and V. K. Varadan,"Form Invariant Constitutive Relations for Transversely Isotropic Piezoelectric Material," J. Acoust. Soc. Am. Vol. 82 (1987).

18. B. A. Auld, *Acoustic Fields and Waves in Solids*, Wiley, New York (1973).

19. *ANSYS User's Manual* , Vol.1 and 2, Swanson Analysis System Inc, (1985).

Figure Captions

Figure 1. Geometry of the problem

Figure 2. Constant D field along Z-axis.

Figure 3. Symmetric boundary conditions for a unit cell

Figure 4. The reflection coefficient vs. Frequency, Hz, _____ and the transmission coefficient vs. Frequency, Hz, - - - - - - - for steel slab immersed in water.

Figure 5. Transmission efficiency vs. frequency; Solid line is for the pure PZT-5 disk, dash line is for the 1-3 composite disk.

Figure 6. Admittance curve (solid line) and susceptance curve (dot line) Vs. frequency for pure PZT-5 disk.

Figure 7. Admittance curve (solid line) and susceptance curve (dot line) Vs. frequency for 1-3 composite disk.

$P^R$

REGION I

FLUID

REGION III

COMPOSITE

SLAB

$P^T$

REGION II

FLUID
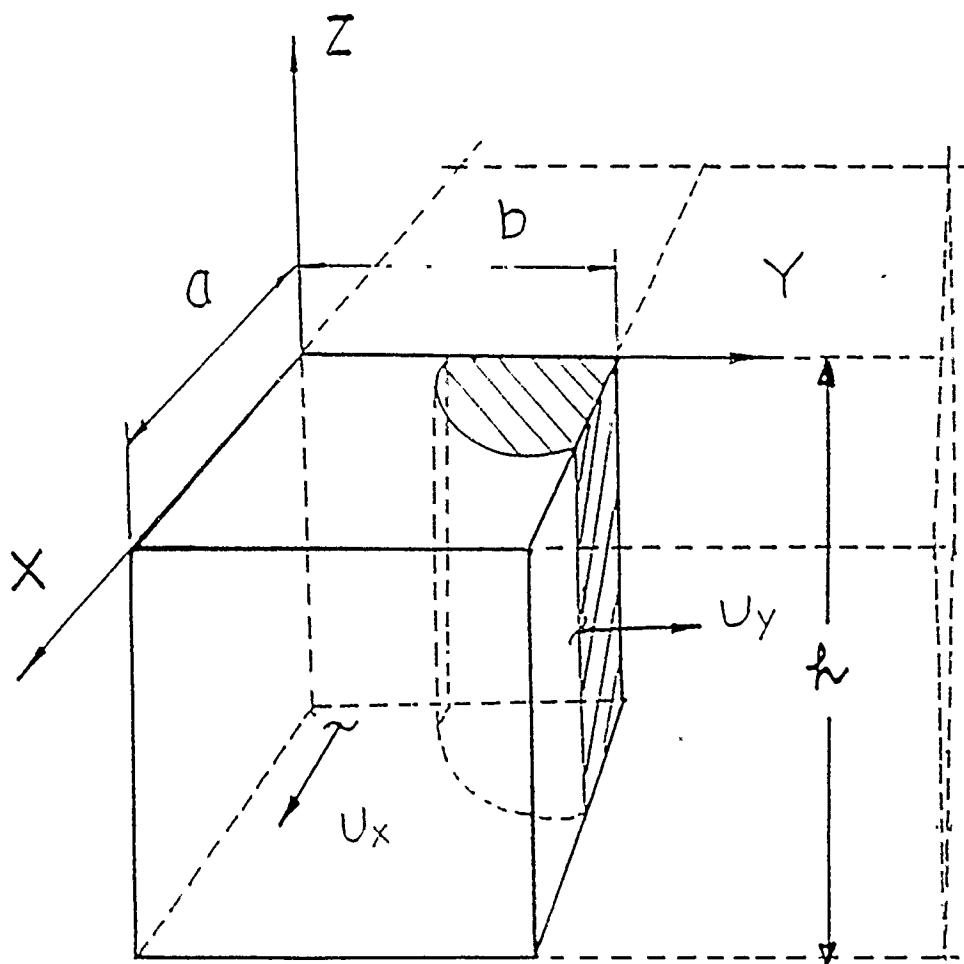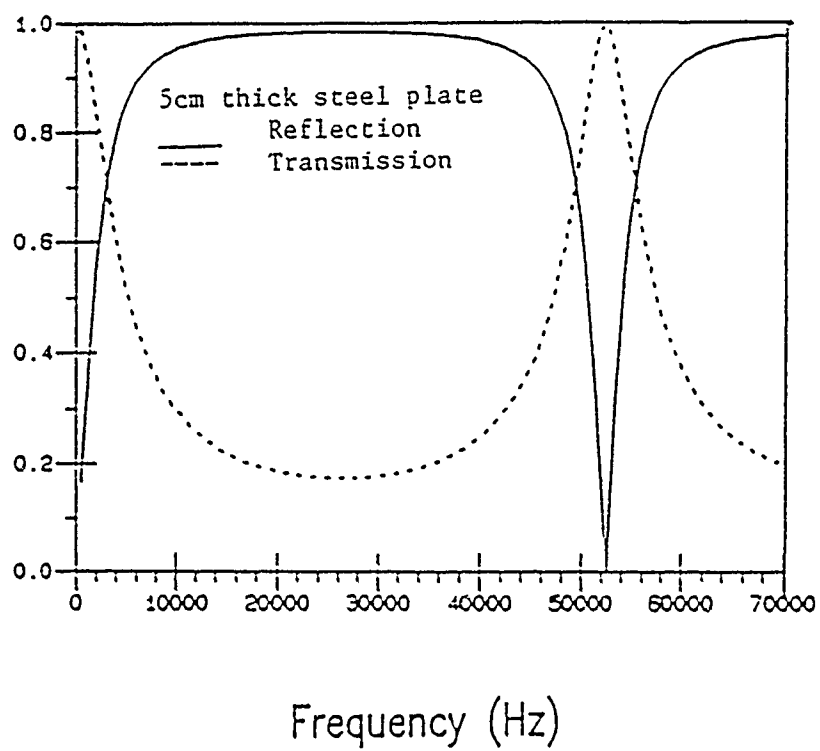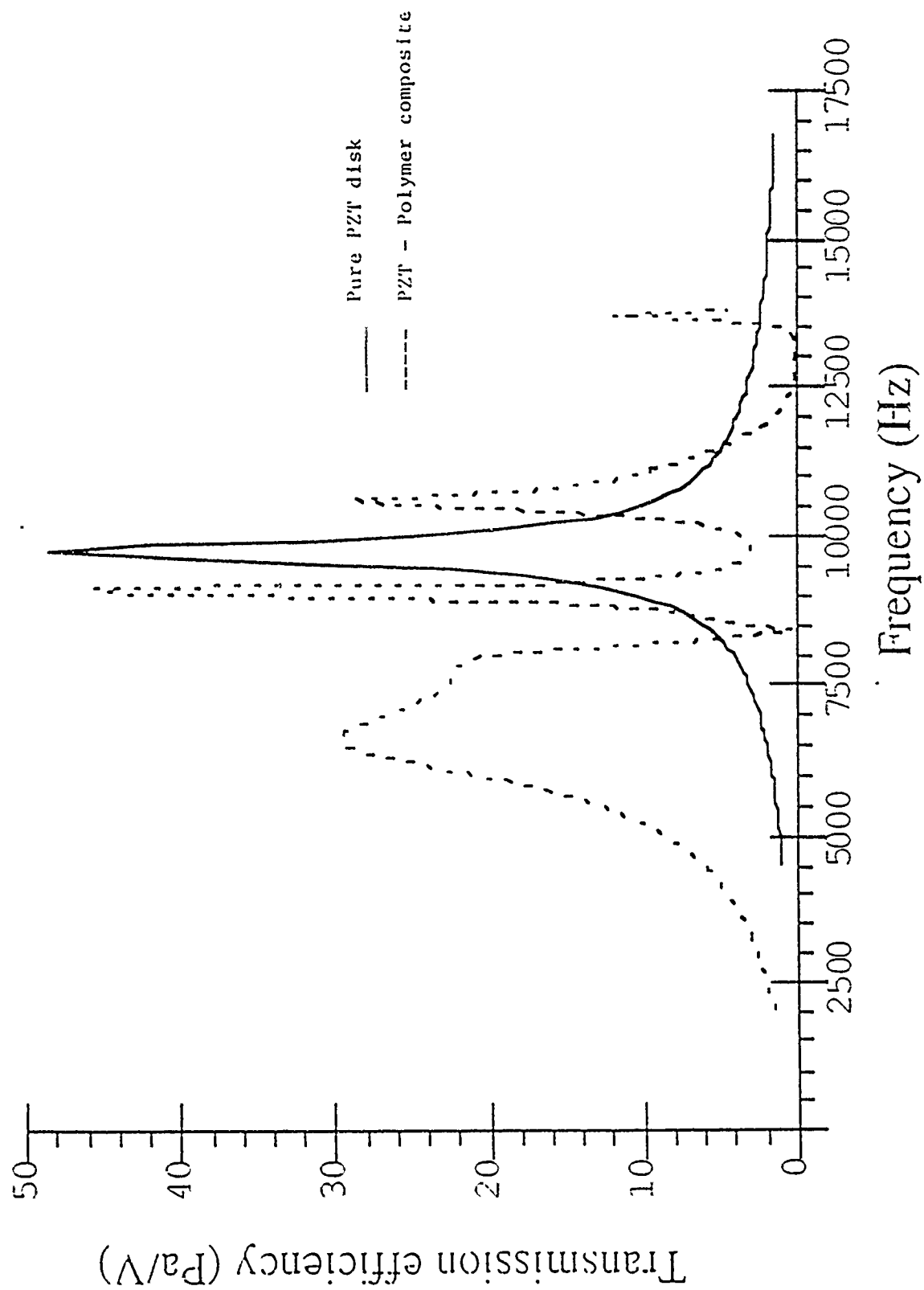


$2R$

$h$
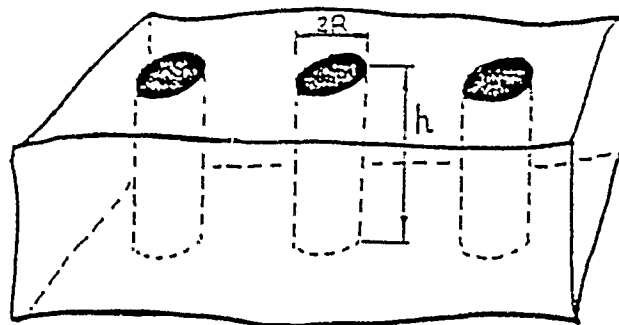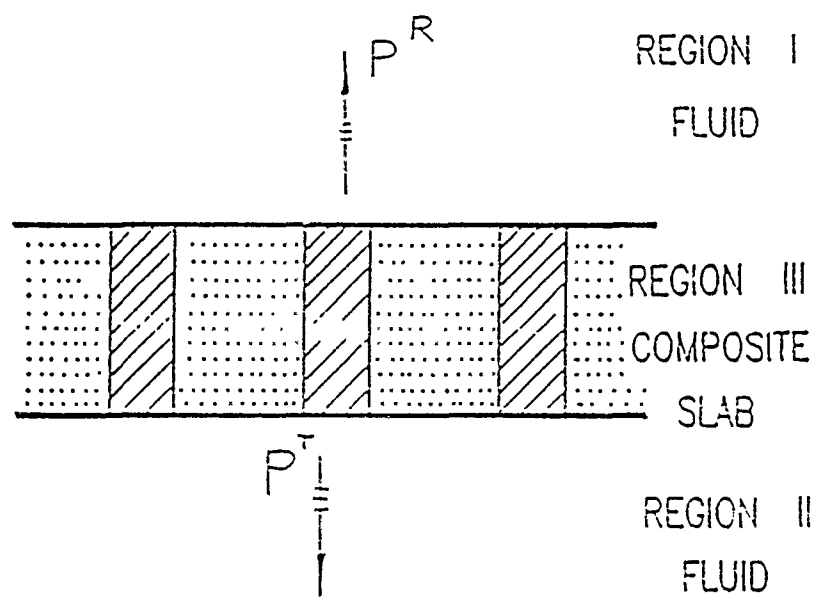
Figure 1. Geometry of the problem
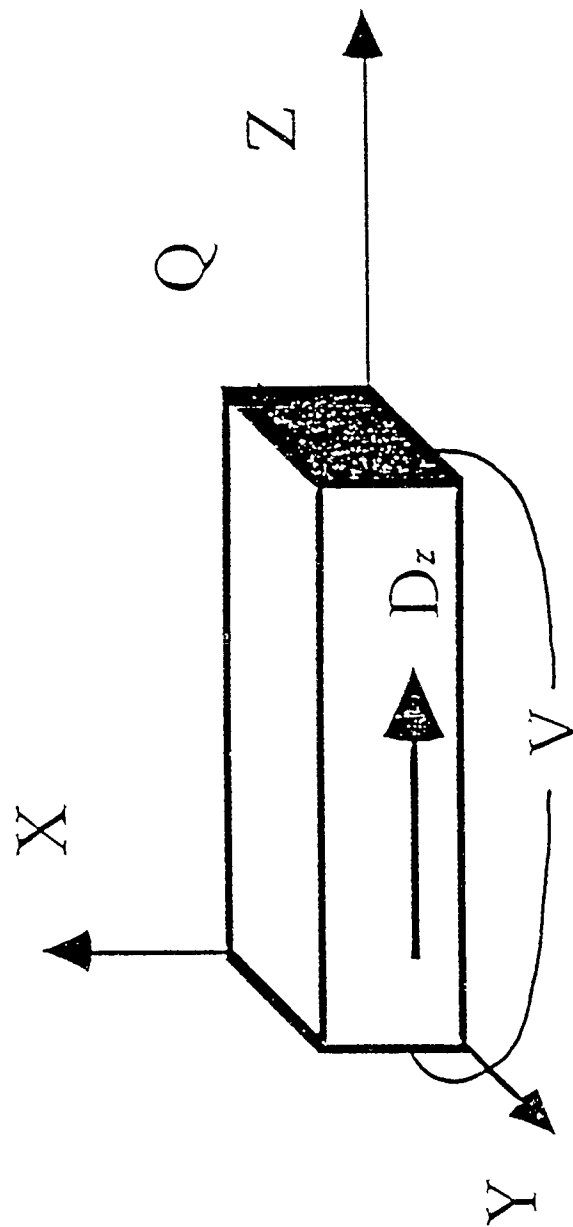
Figure 2. Constant D field along Z-axis.

Boundary conditions:
(Normal displacement equals
to zero at four side walls)
$U_x = 0$, at $X = 0$ and $X = a$
$U_y = 0$, at $Y = 0$ and $Y = b$

Figure 3. Symmetric boundary conditions for a unit cell

Figure 4. The reflection coefficient vs. Frequency, Hz, _____ and the transmission coefficient vs. Frequency, Hz, - - - - - - - for steel slab immersed in water.

Figure 5. Transmission efficiency vs. frequency; Solid line is for the pure PZT-5 disk, dash line is for the 1-3 composite disk.
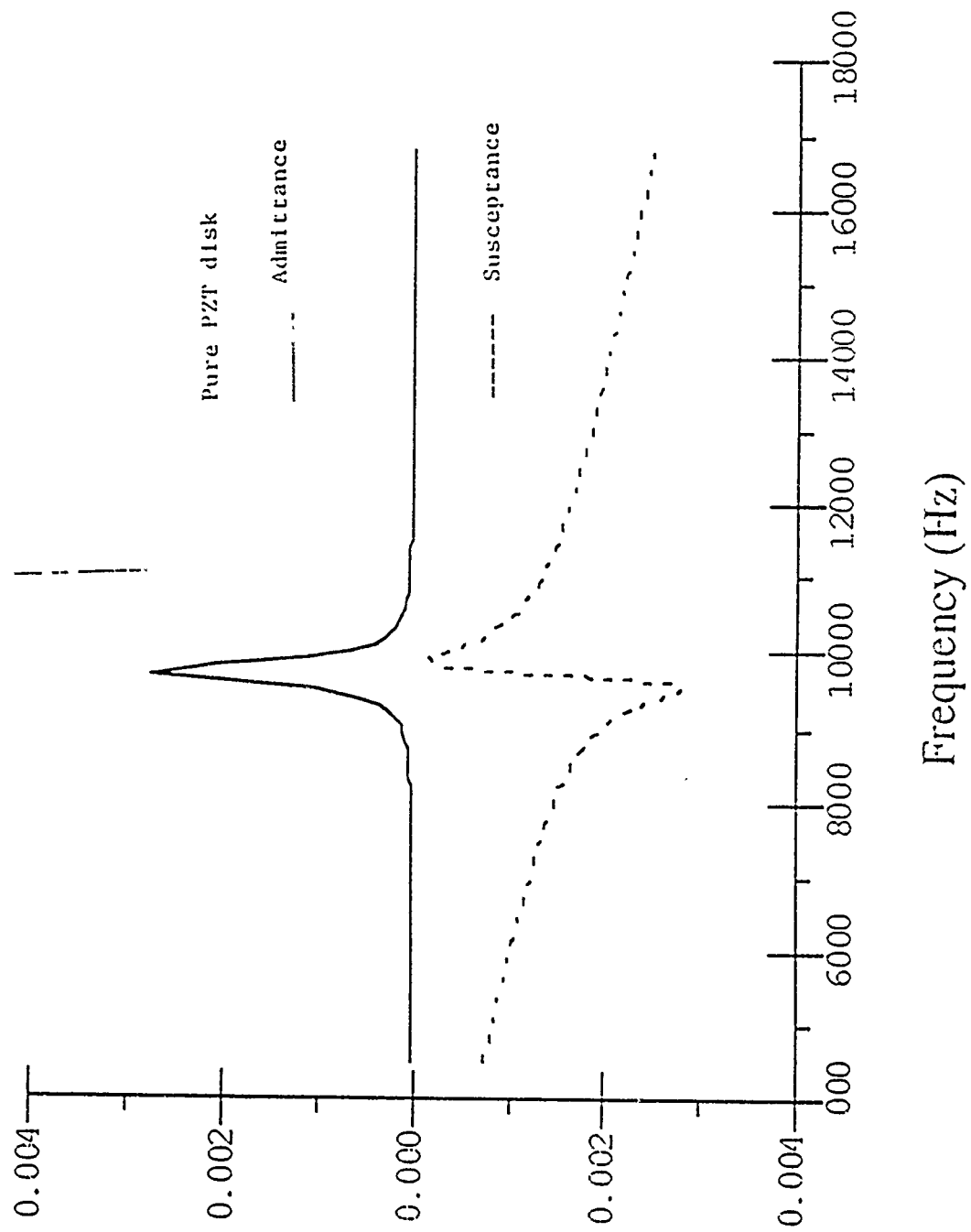
Figure 6. Admittance curve (solid line) and susceptance curve (dot line) Vs. frequency for pure PZT-5 disk.
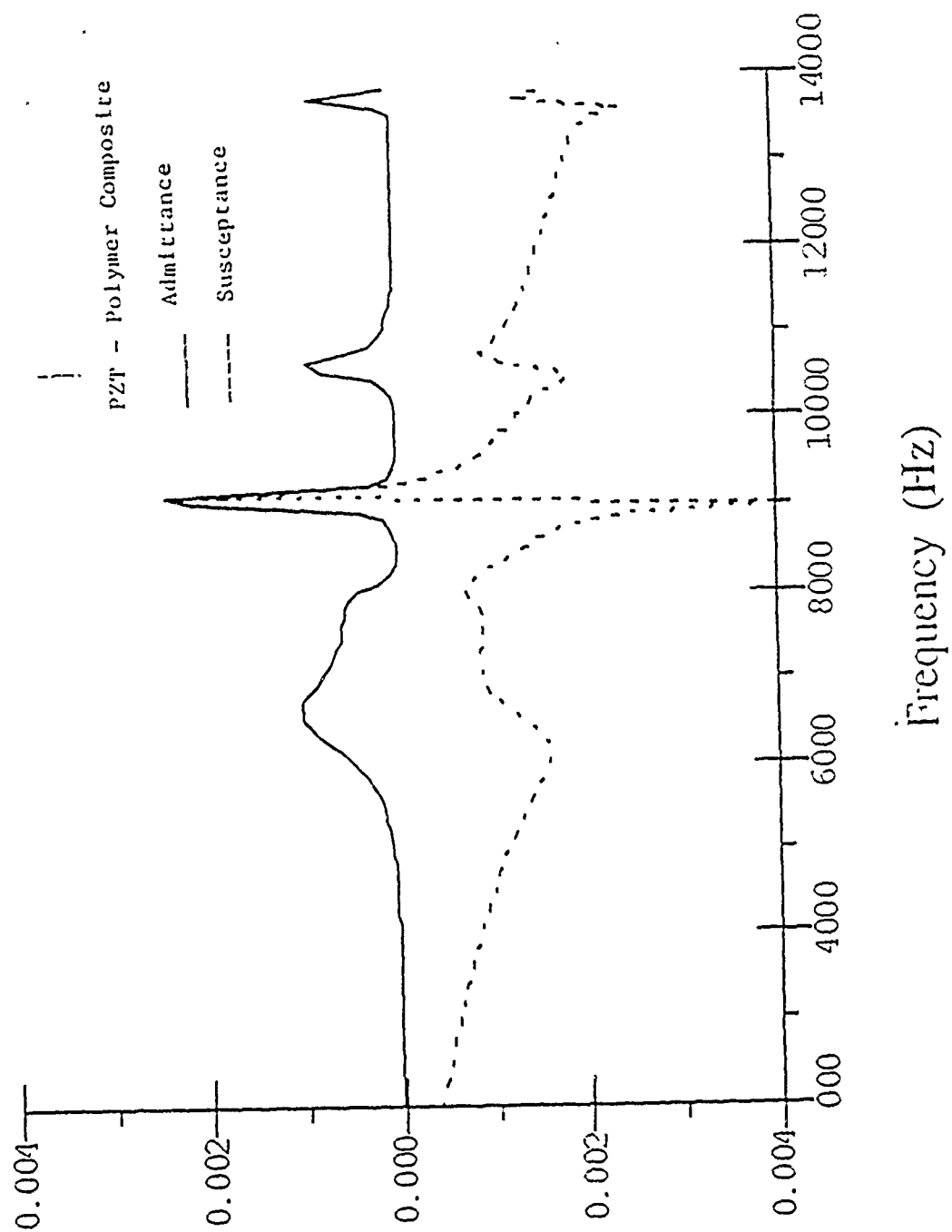
Figure 7. Admittance curve (solid line) and susceptance curve (dot line) Vs. frequency for 1-3 composite disk.

# AD-B193 955

# AN ABSTRACT COMPILATION OF
# THE LITERATURE ON
# HIGH TEMPERATURE OXIDATION
# OF METALS

*by*

W. MARTIN FASSELL, JR.
MARTHA S. CHAMBERLAIN
ROBERT C. PETERSON

"DTIC USERS ONLY" TECHNICAL REPORT

NUMBER III

PART I

94-24568

ARMY ORDNANCE CONTRACT
04 - 495 - ORD -

94 8 19 040

DEPARTMENT OF METALLURGY
UNIVERSITY OF UTAH
SALT LAKE CITY